

Micromechanical finite element modeling of long fiber reinforced thermoplastics

Zur Erlangung des akademischen Grades
Doktor der Ingenieurwissenschaften
der Fakultät für Maschinenbau
Karlsruher Institut für Technologie (KIT)

genehmigte

Dissertation

von

Dipl.-Ing. Sascha Fliegener

Tag der mündlichen Prüfung: 22.09.2015

Hauptreferent: Prof. Dr. rer. nat. Peter Gumbsch

Korreferent: Prof. Dr.-Ing. habil. Thomas Böhlke

Vorwort

Diese Arbeit entstand während meiner wissenschaftlichen Tätigkeit von 2011 - 2015 am *Fraunhofer-Institut für Werkstoffmechanik (IWM)* in Freiburg.

Prof. Peter Gumbsch danke ich für seine Bereitschaft, das Hauptreferat zu übernehmen, sein hohes Interesse an dieser Arbeit und die sehr guten Diskussionen und Anregungen.

Prof. Thomas Böhlke möchte ich danken für die Übernahme des Korreferats.

Dr. Michael Luke hat sich für enorme Freiräume bei der Themenfindung und -ausarbeitung eingesetzt, ohne die diese Arbeit in der vorliegenden Form nicht hätte entstehen können.

Dr. Jörg Hohe war für mich insbesondere in der letzten Phase der Arbeit durch kritische Diskussionen und wertvolle Anregungen eine große Hilfe.

Dr. Hanna Paul danke ich für zahlreiche Diskussionen und Kontakte,
Dr. Melanie Senn für wertvolle Tipps zum Programmieren,
Michael Burdack für seine Ratschläge während meiner ersten Schritte in HyperMesh,
Dr. Achim Neubrand und Georg Falkinger für inspirierende Gespräche,
Michael Deissenbeck, Gerhard Stöhr für ihre Hilfe bei experimentellen Fragen und
Christian Eichheimer für eine grobe Einführung in Krylov-Unterraumverfahren.

Des Weiteren möchte ich folgenden Wissenschaftlerinnen und Wissenschaftlern danken, die ich im thematischen Umfeld kennengelernt habe und die alle auf ihre individuelle Weise zum Gelingen dieser Arbeit beigetragen haben:

Dr. Francesca Garesci (*Universität von Messina*),
Benjamin Hangs und Manfred Reif (*Fraunhofer-Institut für Chemische Technologie*),
Dr. Ralf Schlimper (*Fraunhofer-Institut für Werkstoffmechanik, Halle*),
Dr. Kay André Weidenmann und Dr. Benedikt Haspel (*Karlsruher Inst. für Technologie*),
Prof. Thomas Seifert (*Hochschule Offenburg*),
Dr. Matthias Kabel (*Fraunhofer-Institut für Techno- und Wirtschaftsmathematik*).

Nicht zuletzt möchte ich an dieser Stelle die damaligen Studenten Diego Elmer und Martin Kilb erwähnen, die mir durch ihren hohen Einsatz eine große Hilfe waren.

Meinen Eltern Inge und Winfried, die mich jederzeit unterstützt haben, gilt besonderer Dank, genauso wie Karolina, die mir in den letzten Jahren sehr viel Kraft gegeben hat.

Freiburg, den 18. November 2015

Sascha Fliegener

Kurzfassung

Langfaserverstärkte Thermoplaste (LFT) bieten ein hohes Potential, um großserienfähigen Leichtbau im Automobilbereich zu ermöglichen. Sie können effizient mit den Fertigungsverfahren Spritzgießen oder Fließpressen verarbeitet werden, woraus eine komplexe, vom Herstellungsprozeß abhängige und örtlich variierende Mikrostruktur des diskontinuierlichen Wirrfasergerüsts resultiert. Um die mikrostrukturabhängigen Materialeigenschaften vorhersagen zu können, wurde im Rahmen dieser Arbeit eine neuartige Methode zur Generierung eines repräsentativen Volumenelements (RVE) für LFT und Materialien mit einer ähnlichen Mikrostruktur erstellt. Die Methode ist anwendbar für Werkstoffe mit einem Faseraspektverhältnis bis ca. 5000 und einem Faservolumenanteil bis ca. 25 %. Die Mikrostruktur des Wirrfasergerüsts wird basierend auf der planaren Faserorientierungsverteilung, der Faserlängenverteilung, sowie dem Faservolumengehalt erzeugt. Das Netz für Simulationen mit der Methode der finiten Elemente beschreibt die Mikrostruktur mit einer relativ geringen Elementzahl, wobei die Fasern mit einem einzigen Element über ihren Querschnitt aufgelöst werden. Somit wird die Berechnung vergleichsweise großer Strukturen, die das komplette Faserlängenspektrum enthalten, ermöglicht. Des Weiteren berücksichtigt die Modellierungsmethode den Pressprozeß bei der Herstellung des Materials. Die resultierende Faserwellung, sowie mikromechanische Interaktionen zwischen den Fasern werden vom Modell erfasst.

Drei LFT-Materialien mit unterschiedlichen Faseranteilen wurden experimentell charakterisiert, um das Modell zu validieren. Die elastische Steifigkeit als fundamentale mechanische Eigenschaft wurde zuerst untersucht. Die Modellvorhersagen sind in sehr guter Übereinstimmung mit den experimentellen Daten, sowie den mit einem analytischen Modell berechneten Werten. Um den Anwendungsbereich des Modells zu erweitern, wurden Kriechszenarios untersucht, die für die Anwendung des Materials unter erheblichen statischen Lasten wichtig sind. Um das experimentell beobachtete nichtlinear viskoelastische Verhalten der Matrix zu berücksichtigen, wurde ein klassisches Modell modifiziert und in die Simulationssoftware implementiert. Die Modellvorhersagen für den LFT-Verbundwerkstoff stimmen gut mit den experimentellen Ergebnissen überein. Der Vergleich mit einer alternativen Modellformulierung zeigt, dass die Spannungs- und Umverteilung aufgrund des nichtlinear viskoelastischen Verhaltens der Matrix tatsächlich einen erheblichen Einfluß auf das globale Deformationsverhalten hat. Als weiterer Anwendungsfall wurde schließlich das Deformations- und Schädigungsverhalten von LFT unter Berücksichtigung verschiedener Mechanismen untersucht. Diese sind die plastische Deformation der Matrix, die Faser-Matrix-Grenzflächenschädigung, die Reibung beim Faserauszug und der Spröbruch der Fasern. Das numerische Modell kann die experimentell beobachtete Spannungs-Dehnungskurve des LFT mit hoher Genauigkeit wiedergeben und ermöglicht die mechanismenbasierte Interpretation dieser.

Abstract

Long fiber reinforced thermoplastics (LFT) are considered as very promising for the mass production of automotive components with a high lightweight potential. Cost-efficient manufacturing is enabled by the application of the technologies of injection or compression molding, resulting in a complex, locally varying microstructure of the discontinuous fibers. In order to predict the microstructure-dependent material properties, a novel procedure for the generation of a representative volume element (RVE) for LFTs and materials with a similar microstructure was developed within this work. The method is applicable to materials with a maximum fiber aspect ratio of up to approx. 5000 and a maximum fiber volume fraction up to approx. 25 %. The microstructure generation is based on characteristic values, describing the microstructure in a statistical sense, which are the planar fiber orientation distribution, the fiber length distribution and the fiber volume fraction. The resulting mesh for finite element analysis represents the microstructure by a relatively low element count, modeling each fiber by a single element over its cross section. Hence, the analysis of comparably large structures which include the complete fiber length spectrum is possible within computational limits. Furthermore, the modeling procedure accounts for the pressing process as applied during fabrication of the material. Thus, microstructural features like fiber waviness and micromechanical interactions between the fibers are inherent to the model.

Three LFT materials with varying fiber fractions were characterized experimentally and are used to validate the model. The elastic stiffness as the fundamental mechanical property was investigated at first. The model predictions were found to be in very good agreement with the experimental results and those of an established analytical model. To widen the range of application, creep scenarios were also studied which are important for the application of the material under significant static loads. To account for the experimentally observed nonlinear viscoelastic behavior of the matrix, a classical model was modified and implemented into the finite element framework. On the composite level, good agreement between numerical and experimental data was found for all investigated load cases. A variation of the model formulation revealed that the effects of stress redistribution within the matrix due to its nonlinear viscoelastic behavior are indeed significant. Finally, the deformation and damage behavior was investigated under consideration of different mechanisms, which are the plastic deformation of the matrix, the fiber-matrix interface debonding, the post debonding friction between fibers and matrix and the brittle fiber fracture. The numerical model was shown to be suitable for the accurate reproduction of the effective stress-strain curve, determined by experimental tensile tests. This enables a mechanism-based interpretation of the deformation behavior of LFT.

Contents

- Contents** **5**

- Nomenclature** **9**

- 1 Introduction** **12**
 - 1.1 General introduction and background 12
 - 1.2 Structure of the thesis 13
 - 1.3 Notational conventions 17

- 2 Literature review** **18**
 - 2.1 Material and process 18
 - 2.1.1 Nomenclature and differentiation 18
 - 2.1.2 Direct compounding process 19
 - 2.1.3 Compression molding 20
 - 2.1.4 Effects of fiber length 21
 - 2.1.5 Thermoplastic matrix material 24
 - 2.2 Micromechanics and homogenization 25
 - 2.2.1 Concept of homogenization 25
 - 2.2.2 Classical stiffness prediction and homogenization methods 25
 - 2.2.3 Advanced nonlinear modeling approaches 26
 - 2.2.4 Representative volume element 27
 - 2.2.5 Microstructure generation of discontinuous fiber composites 29

- 3 Experimental methods** **32**
 - 3.1 Material and microstructure 32
 - 3.1.1 Processing conditions 32
 - 3.1.2 Fiber orientation distribution 32
 - 3.1.3 Fiber length distribution 34
 - 3.1.4 Fiber volume fraction 35
 - 3.2 Tensile tests 36
 - 3.2.1 Matrix specimens 36
 - 3.2.2 LFT specimens 36
 - 3.3 Creep tests 38
 - 3.3.1 Matrix specimens 38
 - 3.3.2 LFT specimens 38
 - 3.4 Fiber push-out tests 38

4	Modeling techniques	40
4.1	Viscoelastic matrix model	40
4.1.1	Modeling strategy	40
4.1.2	Burgers four parameter model	41
4.1.3	Differential equation	42
4.1.4	Hereditary integral	42
4.1.5	Incremental form	43
4.1.6	3D generalization	43
4.1.7	Nonlinear modification and range of validity	47
4.1.8	Numerical implementation of nonlinearity	49
4.2	Plastic matrix model	53
4.3	Interface model	55
4.3.1	Simulation of fiber push-out	55
4.3.2	Traction-separation law	56
4.3.3	Contact formulation	57
4.4	Unidirectional fiber arrangement	58
4.5	Multidirectional LFT structure	60
4.5.1	Generation of a fiber stack	61
4.5.2	Fiber compression	63
4.5.3	Meshing and boundary conditions	65
4.5.4	Elasticity	68
4.5.5	Viscoelasticity	70
4.5.6	Plasticity and damage	70
4.6	Analytical homogenization	72
4.6.1	Halpin-Tsai equations	73
4.6.2	Orientation tensor	74
4.6.3	Orientation averaging	76
4.6.4	Length averaging	77

5	Results	78
5.1	Material and microstructure	78
5.1.1	Fiber orientation distribution	78
5.1.2	Fiber length distribution	78
5.1.3	Fiber volume fraction	80
5.1.4	Fracture surfaces	80
5.2	Viscoelastic matrix model	82
5.2.1	Model calibration	82
5.2.2	Model validation	84
5.2.3	Modified parameters	86
5.3	Plastic matrix model	89
5.4	Interface model	90
5.5	Unidirectional fiber arrangement	91
5.6	Multidirectional LFT structure	94
5.6.1	Nomenclature and microstructure characteristics	95
5.6.2	Elasticity - general	97
5.6.3	Elasticity - variation of RVE size	98
5.6.4	Elasticity - variation of fiber length	99
5.6.5	Elasticity - variation of FE mesh	100
5.6.6	Viscoelasticity - general	102
5.6.7	Viscoelasticity - variation of RVE size	106
5.6.8	Viscoelasticity - variation of fiber length	107
5.6.9	Viscoelasticity - variation of model formulation	108
5.6.10	Viscoelasticity - contour plots	110
5.6.11	Plasticity and damage - deformation and damage mechanisms . . .	112
5.6.12	Plasticity and damage - experimental scatter	114
5.6.13	Plasticity and damage - variation of RVE size	116
5.6.14	Plasticity and damage - variation of fiber length	117
5.6.15	Plasticity and damage - contour plots	118

6	Discussion	119
6.1	Microstructural aspects	119
6.1.1	Fiber volume fraction	119
6.1.2	Fiber orientation distribution	120
6.1.3	Fiber length distribution	122
6.1.4	Correlation between fiber orientation and length distribution	122
6.1.5	Microstructure generation	123
6.2	Constitutive models	124
6.2.1	General aspects	124
6.2.2	Viscoelastic matrix model	125
6.2.3	Plastic matrix model	131
6.2.4	Fiber fracture model	132
6.2.5	Interface model	132
6.3	Multidirectional LFT structure	133
6.3.1	General aspects	133
6.3.2	Effects of RVE size	136
6.3.3	Effects of fiber length	139
6.3.4	Effects of the finite element mesh	142
6.3.5	Deformation and damage mechanisms	143
6.3.6	Current limitations and future developments	147
7	Conclusions	149
	References	150
A	Appendix	159
A.1	Derivation of viscoelastic matrix model	159
A.1.1	Differential equation	159
A.1.2	Hereditary integral	160
A.1.3	Incremental form	160
A.2	Additional fiber length data	164
A.3	Variation of matrix strain rate	164

Nomenclature

Abbreviations

2D	Two dimensional
3D	Three dimensional
AR	Aspect ratio
BC	Boundary condition
BSE	Back scattered electrons
CAD	Computer aided design
CT	Computer tomography
DMA	Dynamical mechanical analysis
DOF	Degree of freedom
FE	Finite element
FFT	Fast Fourier transform
GMT	Glass mat reinforced thermoplastic
LFT	Long fiber reinforced thermoplastic
MSP	Modified superposition principle
ODE	Ordinary differential equation
RSA	Random sequential adsorption
RVE	Representative volume element
SEM	Scanning electron microscope
UD	Unidirectional
UMAT	User subroutine for material models

Greek symbols

α_c	Class of fiber angle
α_f	In-plane fiber angle
δ_{ij}	Kronecker delta
δ	Separation vector of traction-separation law
Δt	Time increment
Δl	Length interval
ε	Strain
ε^e	Elastic strain
ε'	Deviatoric strain
ε'_{eq}	Equivalent deviatoric strain
ε_H	Hydrostatic strain
ε^p	Plastic strain

ε^{tot}	Total strain
ε^{v}	Viscous strain
ε^{ve}	Viscoelastic strain
η	Viscosity
η_{HT}	Parameter of Halpin-Tsai equations
Λ	Proportionality factor
ν	Poisson's ratio
ϕ	Spherical fiber coordinate
ψ	Probability density function
ψ_t	Reduced time
ρ	Mass density
ρ_f	Fiber mass density
ρ_m	Matrix mass density
σ	Stress
$\boldsymbol{\sigma}'$	Deviatoric stress
σ_{H}	Hydrostatic stress
σ_{M}	Von Mises equivalent stress
$\bar{\sigma}_{\text{Y}}$	Yield stress
τ_{r}	Relaxation time
θ	Spherical fiber coordinate
ζ_{HT}	Geometry factor of Halpin-Tsai equations

Latin symbols

\mathbf{a}	Second order fiber orientation tensor
\mathbf{A}	Fourth order fiber orientation tensor
B	Bulk compliance
B'_i	Parameter of orientation averaging
\mathbf{C}	Stiffness matrix
$C(t)$	Creep compliance
D	Degradation factor
E	Elastic stiffness
F	Force
f_{v}	Fiber volume fraction
f_{w}	Fiber weight fraction
G	Shear modulus
J	Shear compliance
J'_i	Invariant of deviatoric stress tensor
K	Stiffness of traction-separation law

\mathbf{K}	Stiffness matrix
L_0	Reference length
$L(\alpha_c)_{\text{des}}$	Desired fiber orientation distribution
l_c	Class of fiber length
l_f	Fiber length
L_{KT}	Critical fiber length after Kelly and Tyson
L^*	Fiber length per layer
$L(l_c)_{\text{des}}$	Desired fiber length distribution
L_{macro}	Macroscopic characteristic length
L_{micro}	Microscopic characteristic length
\bar{l}_n	Mean fiber length (number average)
L_{RVE}	RVE length
L^{sat}	Fiber length of saturation
L_{tot}	Total fiber length
\bar{l}_w	Mean weighted fiber length (length average)
\mathbf{M}	Coupling matrix
\mathbf{n}	Normal vector
o	Re-orientation limit
P	Elastic property (Halpin-Tsai equations)
p	Re-position limit
\mathbf{p}	Vector of fiber orientation
\mathbf{r}	Residual vector
\mathbf{S}	Compliance matrix
\mathbf{t}	Traction vector of traction-separation law
t	Time
u	Displacement
u_{max}	Maximum displacement of pressing plates
U	Strain energy
v	Velocity
V	Volume
$x_{1,2,3}$	Cartesian coordinates
x_e	Fiber end point
X	Longitudinal RVE dimension
x_s	Fiber start point
Y	Transverse RVE dimension
y_e	Fiber end point
y_s	Fiber start point
z	Layer coordinate

1 Introduction

1.1 General introduction and background

As matters of energy efficiency and sustainability gain steadily in importance, a significant need exists for medium to high performance, cost-efficient composites which can be manufactured on a mass-production scale e.g. for lightweight automotive components. Thermoplastic composites are in general suitable to reduce the cycle times in the manufacturing process since no time-consuming curing step is needed in contrast to thermosetting matrix systems. Due to the reversibility of solidification process, they are predestined for the recycling of the material. Long fiber reinforced thermoplastics (LFT) are extremely promising for a cost-efficient manufacturing of structural parts since they can be efficiently processed by injection or compression molding and they provide a sufficiently high fiber length which is essential for structural application. In order to create material designs which are precisely adapted to their respective application, microstructural models to predict the effective material performance based on the mechanical properties of the constituents and the characteristics of the microstructure are of crucial importance. Such models can also provide information about the active mechanisms at the microstructural level and how they influence the global deformation and/or damage behavior. Effective mechanical models of the material on the homogenized level, which account for the observed micromechanical mechanisms, can then be developed in the following step. These models will allow the simulation of LFT components as mandatory requirement for their industrial application.

To achieve this goal, precise, three dimensional models of the complex microstructure of LFT are essential. The arising challenges are enormous, mostly due to the extreme fiber aspect ratio of these materials and the associated size of the models. Hence, significant simplifications are mandatory in order that the models are computable. Motivated by this situation, the key approach of this work is to close the gap between the existent type of models: Conventional three dimensional finite element (FE) models of discontinuous fiber composites, in which the fibers are depicted by a multitude of elements over their cross section, result in an extensive element count and related computational cost. On the other hand, very simplified two dimensional methods are available, which use truss elements for the fibers, permit interpenetration between them and are not suitable for the modeling of the complex micromechanical interactions of LFTs. The degree of detail of the proposed model is therefore chosen between both conventional approaches by means of a fully three dimensional representation of the structure, but a rather coarse description of the fibers by a single element over their cross section.

The core of this work is the development of an adapted structure generation procedure, suitable for the reproduction of the LFT fiber structure in the form of a FE mesh. This

is addressed by modeling a fiber compression procedure in analogy to the manufacturing process of the material by the technology of compression molding. The modeling is based on microstructural data in the form of fiber orientation and length distributions as well as values of fiber volume fraction. The applicability of such generated structures to industrial relevant load scenarios is investigated in order to assess the potential of the modeling approach. The accuracy of the model with respect to predicting the elastic stiffness as the most fundamental material property is investigated at first by comparison to experimental data as well as to evaluations of an established analytical approach. Then, the range of application is widened to the modeling of a creep scenario, accounting for the viscoelastic behavior of the thermoplastic matrix. Consideration of such load scenarios is crucial for the dimensioning of structural parts under significant static loads and particularly important for thermoplastic materials due to their inherent tendency to creep. At last, virtual tensile tests of the material are modeled accounting for different deformation and damage mechanisms, which are in detail the plastic flow of the matrix, the fiber-matrix debonding at the interface, the post-debonding friction between fiber and matrix during fiber pullout and the brittle fracture of the fibers.

1.2 Structure of the thesis

The flow of data and interaction between the modeling techniques and experimental methods is illustrated in Fig. 1. The flowchart is divided into five blocks which represent the main categories of the applied methods. Both modeling techniques (finite element modeling and analytical homogenization) are fed by *structural data* (dotted grey lines), describing the LFT microstructure in an statistical sense and by *material data* (dashed grey lines) in the form of constitutive laws of the components fiber, matrix and interface. The effective LFT properties (elasticity, viscoelasticity, plasticity and damage) labeled as *merged data* (full grey lines) are obtained as output from the models and interact with respective validation experiments. Besides the hierarchical structure of input data at the first level (top of the flowchart), modeling procedures at the second level (middle) and output data at the third level (bottom), there exist several cross-links between specific components which are highlighted by bold, double-sided arrows, labeled as *interaction* (e.g. validation of data against each other).

Microstructure characteristics

The LFT microstructure is described by the fiber volume fraction (calculated from the mass flow rates of the manufacturing process), the fiber length distribution (obtained by image analysis of the fiber structure of an incinerated specimen) and the fiber orientation distribution (extracted by image correlation from CT scans). The applied methods are specified in Section 3.1. The results are presented in Section 5.1.

Constitutive models

Due to their fundamental character, the elastic properties of fiber and matrix are not elaborated by a separate chapter. The respective values used as input for the microstructural models are specified in conjunction with the modeling results (e.g. Section 5.6.2). The derivation of the viscoelastic matrix model is described in Section 4.1. A Burgers four parameter model was modified to account for nonlinear viscoelastic effects as observed experimentally. The results, divided into the calibration of the model with experimental data, the validation with respect to reproduction of an exemplary load history and the three dimensional behavior as well as the derivation of modified model parameters to partially compensate mesh effects are presented in Section 5.2. The plasticity of the matrix was experimentally characterized with substance specimens and is numerically described by application of a classical von Mises plasticity model. The methodology is described in Section 4.2, whereas the calibration with experimental data is presented in Section 5.3. Fiber damage was implemented by means of a brittle fracture model with a value of failure stress from the literature. The value is specified in conjunction with the modeling results in Section 5.6.11. The damage behavior of the fiber-matrix-interface was investigated by single fiber push-out tests. Reverse determination of the interface parameters is performed by FE simulation of the push-out scenario. The experimental details are specified in Section 3.4, whereas the modeling is described in Section 4.3. The results are given in Section 5.4.

Finite element modeling

Based on the structural data (fiber volume fraction, fiber orientation distribution, fiber length distribution), a representative volume element (RVE) of the LFT material is formed. The RVE generation procedure, mimicking the compression of the fibers in analogy to the manufacturing process of the material, is detailed in Section 4.5. Several RVEs were studied under variation of fiber volume fraction, orientation distribution, fiber length and RVE size. The characteristics of the investigated structures are given in Section 5.6.1 and compared to the microstructural input data. The multidirectional RVEs, representing the LFT material, are analyzed by finite element simulations with respect to different mechanical properties, which are the elastic and viscoelastic properties as well as the deformation and damage behavior. The elastic properties were studied by implicit simulations using the elastic material data for fibers and matrix. The viscoelastic properties were investigated by implicit simulations under consideration of elastic fiber properties and the viscoelastic model of the matrix. The deformation and damage behavior was analyzed by explicit simulations and the application of the plastic matrix model, the interface model and a brittle fiber failure criterion. The details of each numerical study are specified in Section 4.5. The results are presented in conjunction with those of the validation experiments in Section 5.6. The elastic results of the multidirectional

RVEs were validated against the effective LFT properties from analytical homogenization (Section 5.6.2). The single fiber push-out scenario was modeled to extract the interface characteristics. Fiber-matrix-debonding is represented numerically by cohesive zone elements between the fibers and the matrix. The parameters of the traction-separation law to describe the decohesion are reversely determined by simulation of the fiber push-out scenario (Section 4.3). The parameters (Section 5.4) then flow into the multidirectional RVEs in order to analyze the deformation and damage behavior of LFT. Several variants of an unidirectional (UD) fiber arrangement were studied to investigate the principle relation between fiber length, elastic and viscoelastic properties. The methodology is described in Section 4.4, whereas the results are presented in Section 5.5. Furthermore, the elastic UD model was validated against the Halpin-Tsai equations.

Analytical homogenization

Analytical homogenization of the elastic properties of LFT was performed by multiple steps, which are described in Section 4.6. At first, the transversely isotropic compliance matrix of a unidirectional reference composite of uniform fiber length is calculated by application of the Halpin-Tsai equations. Structural data in the form of fiber volume fraction and material data in the form of elastic properties of fibers and matrix flow into the model. The results are compared to those of the finite element models of a unidirectional fiber arrangement in Section 5.5. In the next step, the fiber orientation distribution is converted into second and fourth order orientation tensors in order to apply the orientation averaging scheme. So-called orientation averaged pseudo-grains of uniform aspect ratio are formed before averaging over these pseudo-grains is carried out to account for the fiber length distribution. The homogenized LFT properties (orientation and length averaged) are compared with the results from finite element modeling in Section 5.6.2.

Effective LFT properties

The results from finite element modeling (multidirectional RVEs) and analytical homogenization are compared to respective validation experiments in Section 5.6. The finite element results include elasticity / viscoelasticity as well as plasticity and damage. The analytical results are restricted to elasticity. The methodology of the validation experiments is described in Section 3.2.2 and 3.3.2. To validate the elastic properties, tensile tests in the elastic range were carried out on LFT specimens with varying fiber volume fraction. Three loading-unloading cycles in the elastic range were performed to ensure that no effects of material degradation or plasticity are active. The viscoelastic properties are validated with creep experiments under variation of fiber volume fraction, load direction and stress level. The deformation and damage behavior is validated with quasi-static tensile tests until fracture. Only the material with the highest fiber volume fraction was tested in this respect.

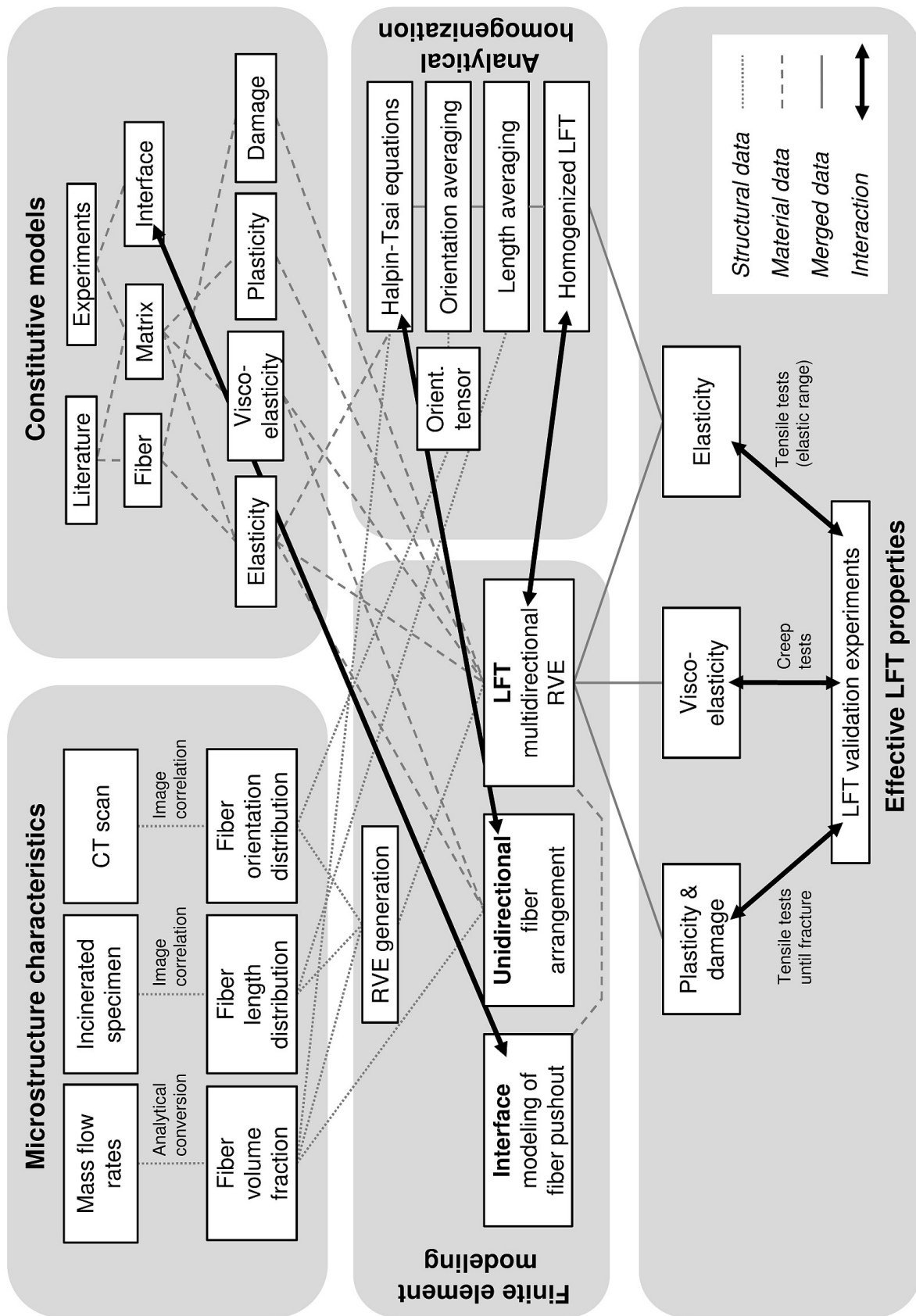


Figure 1: Flow of data and interaction between the applied modeling procedures and experimental techniques.

1.3 Notational conventions

Vectors, tensors or matrices are highlighted either by the use of the index notation (a_{ij} , A_{ijkl}) or printed in bold face (first and second order in lower case - \mathbf{a} , fourth order in upper case - \mathbf{A}), e.g.

$$\mathbf{a} = \begin{bmatrix} a_{11} & a_{12} & a_{13} \\ a_{21} & a_{22} & a_{23} \\ a_{31} & a_{32} & a_{33} \end{bmatrix} . \quad (1)$$

Einstein's summation convention implies that if an index appears twice in a single term, summation of that term over all the index values is carried out:

$$a_i b_i = \sum_{i=1}^3 a_i b_i = a_1 b_1 + a_2 b_2 + a_3 b_3 . \quad (2)$$

The Kronecker delta δ_{ij} returns zero or one depending on the equality of the indexes:

$$\delta_{ij} = \begin{cases} 0 & \text{if } i \neq j \\ 1 & \text{if } i = j \end{cases} . \quad (3)$$

The \otimes sign represents the dyadic product between two vectors, e.g. (in 2D)

$$\mathbf{a} \otimes \mathbf{b} = \begin{bmatrix} a_1 b_1 & a_1 b_2 \\ a_2 b_1 & a_2 b_2 \end{bmatrix} . \quad (4)$$

The trace of a tensor or matrix is defined as

$$\text{tr}(\mathbf{a}) = a_{kk} = a_{11} + a_{22} + a_{33} . \quad (5)$$

The $|\cdot|$ sign represents the absolute value of a scalar variable, whereas $\|\cdot\|$ means the Euclidean norm of a vector, e.g.

$$\|\mathbf{a}\| = \sqrt{a_1^2 + \dots + a_n^2} . \quad (6)$$

The time derivative is marked by dots (Newton's notation). The use within this work is restricted to small deformation theory with a fixed coordinate system:

$$\dot{x} = \frac{dx}{dt} , \quad \ddot{x} = \frac{d^2x}{dt^2} . \quad (7)$$

The $f(\cdot)$ -operator represents a function with the dependent variable y and the independent variables $x_1 \dots x_n$ and is used as abbreviation in flowcharts to avoid an explicit specification of the function:

$$y = f(x_1 \dots x_n) . \quad (8)$$

2 Literature review

2.1 Material and process

2.1.1 Nomenclature and differentiation

A variety of materials can be considered to be associated with the class of long fiber reinforced thermoplastics. Differentiation in particular to short fiber reinforcements is not consistent in the literature, since some overlap exists between the different material classes with respect to the fiber length. In Fig. 2, the most common materials are arranged under consideration of their semi-finished product, their manufacturing process and their characteristic fiber length according to Henning *et al.* [Hen05].

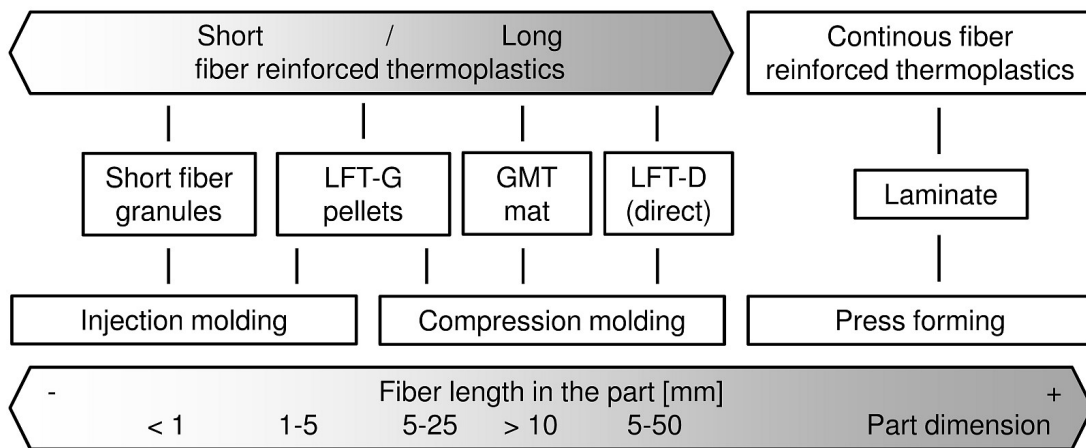


Figure 2: Nomenclature and differentiation of short, long and continuous fiber composites based on semi-finished product, manufacturing process and characteristic fiber length according to Henning *et al.* [Hen05].

Short fiber reinforced thermoplastics are exclusively processed by injection molding. The polymer granules contain the pre-impregnated fibers and are plasticized in a single screw extruder to avoid fiber attrition. The fiber length within the granules is well below 1 mm and further decreasing during injection into the mold. If LFT-G pellets instead of short fiber granules are processed by injection molding, the fiber length can be kept at several millimeters within the part. A more gentle processing of the pellets is available with the technology of compression molding. Instead of injection into a closed mold with fixed walls, a strand of the plasticized mass of molten pellets is positioned into an open mold with moving walls which is then closed by a hydraulic press during the compression. Due to the omission of high-pressure injection, fiber attrition is reduced and the characteristic fiber length within the part can be kept even longer. Glass mat reinforced thermoplastics (GMT) are processed in a similar manner. Instead of the plasticized mass as output from the extruder, the GMT blanks are cut into a shape close to the part dimensions before heating and stacking the blanks in the mold by a robot. Although the

achievable fiber length of the GMT process is very high, the process lacks in adaptability to fully three dimensional shaped parts due to the somewhat limited formability of the blanks. The direct LFT process (LFT-D) combines the flexibility for complex part designs (an attribute of all processes which are based on injection or compression of a plasticized mass) with a very high characteristic fiber length due to omission of a semi-product and direct part manufacturing from the constituents (fiber rovings, polymer granules and additives). The investigated material of this work was manufactured by application of the direct compounding (LFT-D) scheme and compression molding. These two technologies are therefore described in detail in the following sections.

From a modeling point of view, long fiber reinforced thermoplastics are in particular problematic because of their huge fiber aspect ratio in the region of several thousand and the resulting data amount. For typical thin-walled structures, the characteristic fiber length is significantly larger than the wall thickness, resulting in a layered structure with the layers parallel to the part surface [Adv87]. Therefore, a two dimensional description of the fiber orientation and a semi 3D or so-called 2.5D modeling procedure is sufficient to represent the microstructure for most cases. In contrast, short fiber composites with a typical fiber length well below the wall thickness can feature a significant component of orientation in thickness direction and therefore a fully three dimensional description of the fiber orientation and modeling is mandatory. A differentiation with respect to modeling features is presented in Table 1.

Criterion	Short fibers	Long fibers
Typical fiber length	0.2 - 1 mm	2 - 100 mm
Aspect ratio	10 - 50	100 - 5000
Relative fiber length	fiber length < wall thickness	fiber length >> wall thickness
Fiber orientation	3D	2D layers
Modeling approach	fully 3D	semi 3D, 2.5D
Data amount	medium	high

Table 1: Differentiation between short and long fibers from a modeling point of view.

2.1.2 Direct compounding process

Fig. 3 illustrates the compounding process of a LFT-D material with two twin-screw, co-rotating extruders (compounding extruder, horizontal / mixing extruder, vertical) and direct introduction of the fiber rovings into the mixing extruder [Hen05, Kra03, Rad08, Tro03]. The polymer granules as well as optional additives are fed into the compounding extruder by a gravimetric dosing unit. The additives (e.g. coupling agents, heat stabilizers, antioxidants and colorants) are chosen individually according to the requirements for a specific application with respect to fiber-matrix interface characteristics, thermostability, ultraviolet stability and coloring. The polymer melt is combined with the fiber rovings

by the mixing extruder. The rovings are fed through a pre-heating device and heated up to a temperature below the critical limit where the fiber sizing shows degradation effects. The fiber rovings are then introduced directly into the mixing extruder. Thus, the fibers are cut by the edges of the co-rotating screws with the maximum fiber length defined by the pitch of the thread of the screws. The LFT-D strand (plasticized mass of polymer and fibers) as it is provided by the mixing extruder is finally fed through a slot die to shape its cross-section and then segmented into packages by a cutting unit.

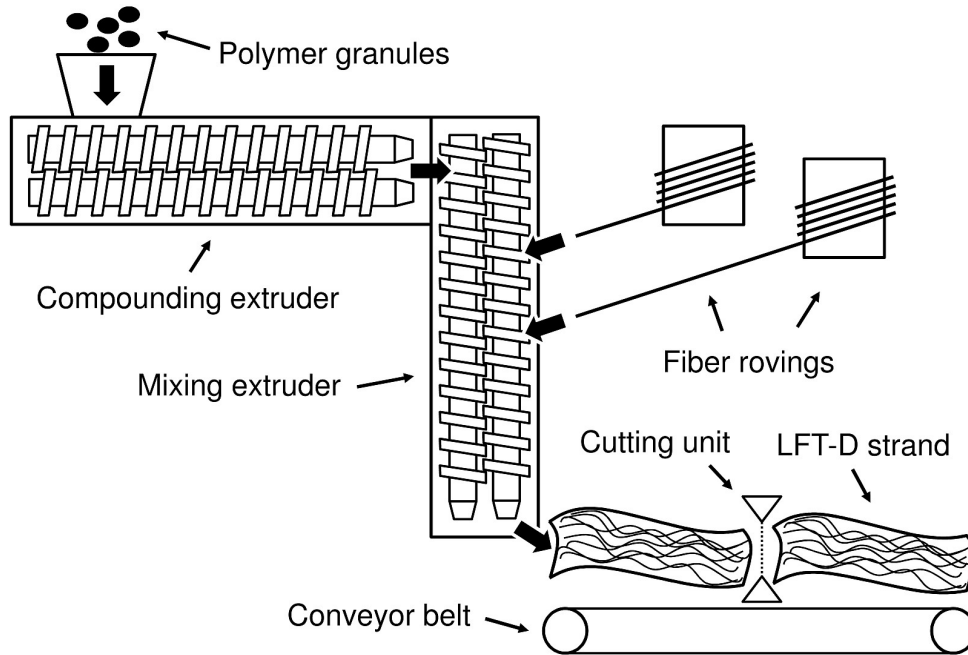


Figure 3: Scheme of the direct LFT process [Hen05, Kra03, Rad08, Tro03].

The material resulting from the direct LFT process is characterized by a broad fiber length distribution reaching from a large amount of fiber fragments with a length well below 1 mm to very long fibers up to approx. 50 mm (depending on the extruder screws). The very high maximum fiber length and the resulting high mechanical properties can be considered as one major advantage of the direct process. Other benefits are its energy and cost efficiency due to omission of semi-finished products, the possibility to introduce a certain amount of recycled material into the process (LFT recycling chips plasticized by a second compounding extruder feeding the mixing extruder) and the adaptability of the polymer properties over a broad range to each individual application [Hen05].

2.1.3 Compression molding

The LFT-D strand as produced by the LFT-D compounding procedure described in the previous section is positioned into one half of the opened mold. This is performed by a handling robot with needle grippers, picking the strand package up from the end of the conveyor belt which enables automatic transportation between the mixing extruder

and the mold. The conveyor belt is covered by a heat tunnel to prevent heat dissipation and to ensure that the strand temperature does not drop below the melt temperature of the polymer. Depending on shape and complexity of the mold, several strand packages might be positioned to different locations within the mold by multiple robots to save process time and to prevent heat losses. The mold is heated to a certain temperature to prevent instantaneous solidification of the strand at the touching area with the mold and sharp temperature gradients resulting in a high degree of distortion after compression and solidification of the part. The mold is then closed by a hydraulic press. This is illustrated in Fig. 4. Shearing edges ensure that no material can flow out of the cavity even in partially closed state. The compression forces the plasticized material to flow toward cavities which were not initially covered by the strand. The streaming conditions within these areas (called *flow region* of the part) cause a higher degree of fiber orientation than it is characteristic within the strand inlay location (called *press region* of the part).

In Fig. 5, the development of the microstructure within an exemplary part geometry is illustrated for the strand inlay position and the flow region.

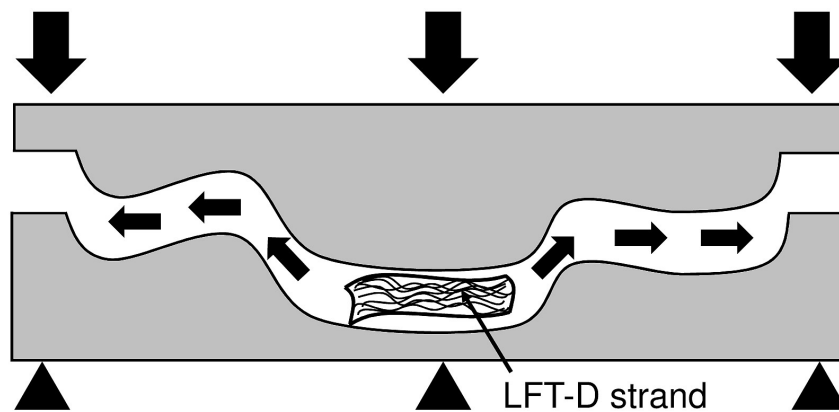


Figure 4: Scheme of compression molding: The LFT-D strand is placed in the cavity (one half of the mold). The mold is then closed by a hydraulic press and the material flows toward uncovered regions.

2.1.4 Effects of fiber length

The principle relationship between the fiber length and the effective mechanical properties is illustrated in Fig. 6 with respect to the elastic stiffness, strength and impact energy. The diagram according to Schemme [Sch03] was constructed based on experimental data of multidirectional laminates of glass fibers in a polypropylene matrix by Thomason [Tho96a, Tho96b, Tho97]. It visualizes the fiber effectiveness, which was defined by Schijve [Sch00] as the degree of contribution of a specific fiber length to the effective property of a discontinuous fiber composite. The saturation length L^{sat} of each individual property is defined as the corresponding fiber length to the saturation threshold of the respective mechanical property.

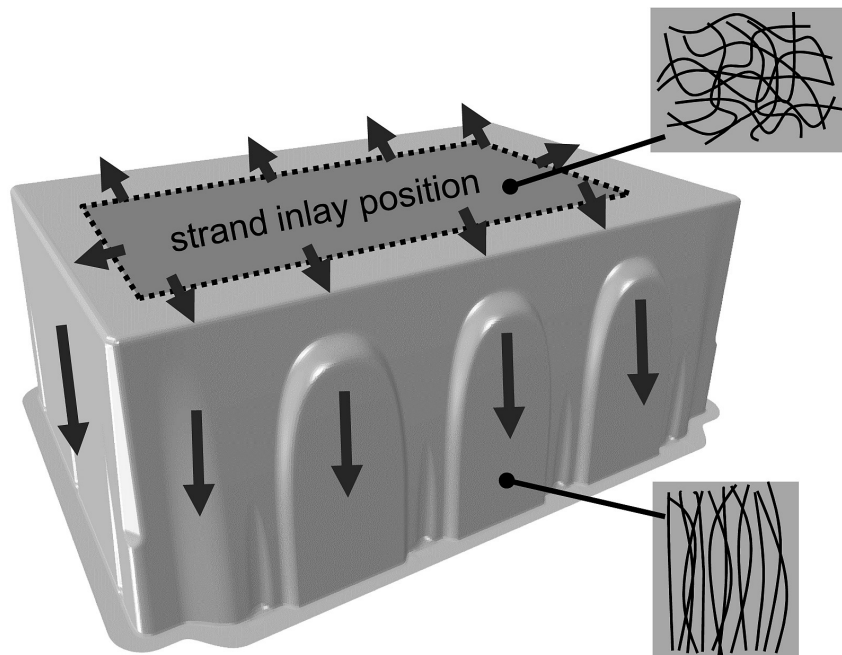


Figure 5: Compression molding of an exemplary part geometry: The arrows show the flow direction within the part. Whereas the fiber orientation is low for the strand inlay position, a more aligned state of the microstructure can be observed for the flow region.

With respect to the elastic stiffness, good agreement of the experimental data to the Cox model [Cox52] (using an extension to account for fiber orientation by Krenchel [Kre64]) was found [Tho96a]. The saturation length and the corresponding aspect ratio for a uniform fiber diameter of $20\ \mu\text{m}$ amount to $L_{\text{Stiffness}}^{\text{sat}} \approx 1\ \text{mm}$ and $AR_{\text{Stiffness}}^{\text{sat}} \approx 50$, respectively. The quasi static strength was compared to predictions of a modified Kelly-Tyson model [Kel65] based on the critical fiber length L_{KT} for which the fiber fracture stress σ_f can be reached by load transfer over the cylindrical circumference area (defined by the fiber diameter D and L_{KT}) of the embedded fiber which has to be large enough to ensure that the interfacial shear strength τ is not exceeded: $L_{\text{KT}} = \sigma_f D / 2\tau$. Based on L_{KT} the model accounts for fibers of sub-critical length which will be pulled out and fibers of super-critical length which will fail in normal tension mode. Thomason extended the model to account for multidirectional fiber orientation to match the experimental data [Tho96b]. The results are strongly dependent on the interface properties influenced by fiber sizing and processing conditions which define the value of the interfacial shear strength τ . The resulting value of saturation length for strength (Fig. 6) is approx. one order of magnitude larger than the value for stiffness with $L_{\text{Strength}}^{\text{sat}} \approx 10\ \text{mm}$ ($AR_{\text{Strength}}^{\text{sat}} \approx 500$).

For further investigation of the experimental impact properties, the Cottrell model [Cot64] was applied which distinguishes between sub- and super-critical fibers in a similar manner as the Kelly-Tyson model [Tho97]. The model is based on the assumption that fiber pull-out is the dominant mechanism for energy dissipation. The predicted impact dissipation energy therefore reaches a maximum at medium fiber length before decreasing toward in-

finite length when all fibers fail in normal mode instead of pullout. This is contradictory to the experimental data, where no such drop of energy for very high fiber length could be observed. A fiber strain energy model was therefore proposed by Thomason which is based on the breakage of debonded fibers [Tho97]. The latter model gives excellent agreement to the experimental data. Now, the impact energy reaches a saturation plateau for very high fiber length in a similar form as observed for the quasi static strength. The saturation value of fiber length for impact resistance amounts to $L_{\text{Impact}}^{\text{sat}} \approx 40$ mm ($AR_{\text{Impact}}^{\text{sat}} \approx 2000$) for the investigated material.

It is worth mentioning that the diagram and the underlying data need to be interpreted as a model to describe the approximate relation between the respective measures. Generality or transferability to other material systems is not proven. Furthermore, no systematic variation of a single characteristic could be performed by the experimental studies, since for example, a variation in fiber length always affects their orientation and local density while manufacturing a new material variant. A more systematic approach would be met by the application of microstructural simulations. Although a variety of numerical methods suitable for such studies is available, there are relatively few publications treating a systematic variation of the fiber length. Some of them, mostly restricted to the prediction of the elastic properties, are cited in Section 2.2.3 and 2.2.5 (e.g. by Hine *et al.* [Hin02]). With respect to rate-dependent fracture, the influence of the fiber length was partially examined by Okabe *et al.* [Oka14, Oka10]. However, no numerical studies of the relation between the impact energy and the fiber length are currently known.

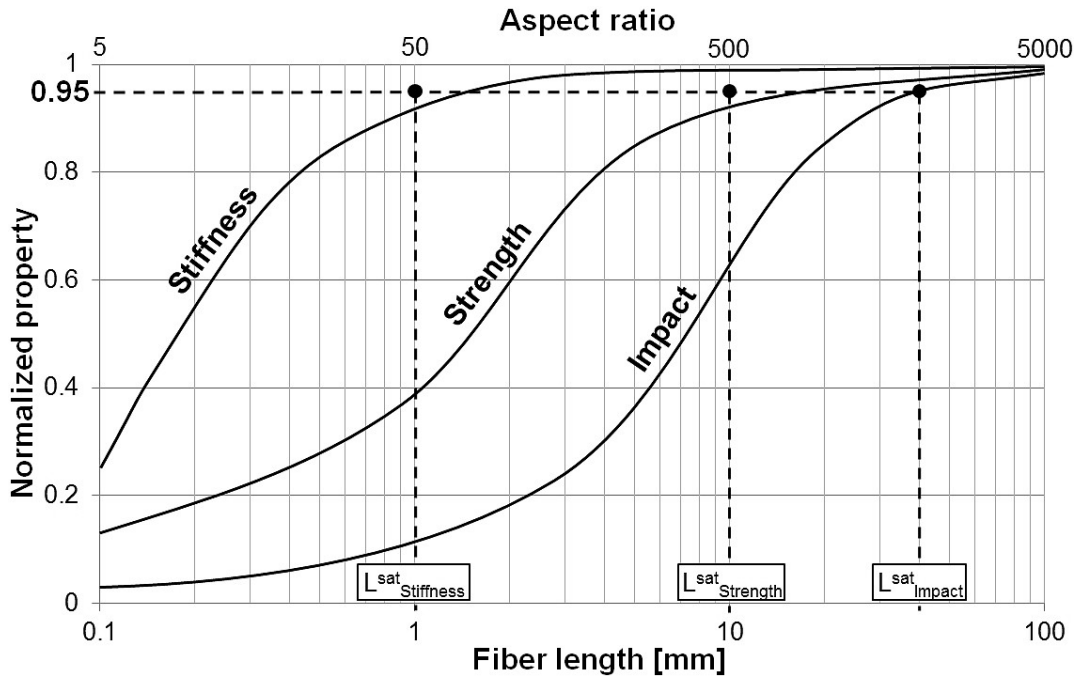


Figure 6: Principle dependence of effective mechanical properties on fiber length / aspect ratio according to Schemme [Sch03]. A fiber diameter of 20 μm was assumed.

2.1.5 Thermoplastic matrix material

Thermoplastics offer certain advantages over thermosets with respect to their application as a matrix polymer. Instead of the time-consuming curing process of a thermoset, the solidification of the thermoplastic melt is usually more time and cost efficient. Furthermore, a certain amount of recycled material can be fed into the process without significant degradation of the material properties. Thermoplastics are therefore well suited for the efficient mass production of structural parts with medium to high mechanical performance and strength-to-weight ratio. Disadvantages of most thermoplastics are their poor thermostability, their low glass-transition temperature, their tendency to creep and their weak bonding to glass fibers due to the nonexistence of covalent bonds. The investigated material of this work features a polypropylene matrix, which is the most universal thermoplastic matrix polymer because of its excellent cost-performance ratio and adaptability by various modifications. Polypropylene is associated with the group of polyolefines which form a semi-crystalline structure during solidification. This structure is characterized by crystalline regions where a spheroidal arrangement of the polymeric chains is formed based on a nucleation process depending on cooling rate, material formulation (additives) and boundary conditions (e.g. the presence of surface tension in the vicinity of a fiber). The remaining regions feature an amorphous structure similar to an undercooled melt (Fig. 7). The resulting mechanical properties are directly influenced by the microstructure. The viscoelastic response is characterized by a spectrum of relaxation times in which each value corresponds to a specific length of a polymeric chain. The inherent creep tendency of most thermoplastics is caused by the lack of a side-chain network that would limit the sliding of the polymeric chains (as existing for thermosets). Whereas inelastic deformation of metals is based on dislocation motion and is therefore in general considered to be independent of hydrostatic stress, such stress is mostly not negligible for thermoplastics because of its effect on the amorphous regions [Gho08, Glo07, Sau74, Mea69].

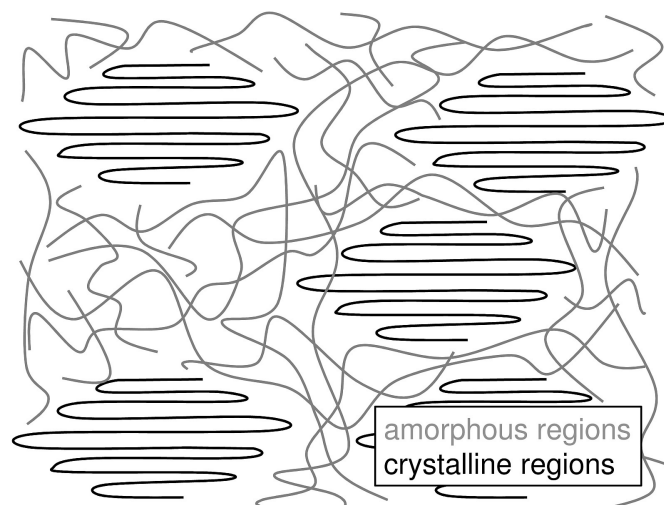


Figure 7: Schematic microstructure of a semi-crystalline thermoplastic.

2.2 Micromechanics and homogenization

2.2.1 Concept of homogenization

The general aim of micromechanics is the prediction of the effective mechanical behavior based on the knowledge of the constituent properties and the geometry of the microstructure. The effective behavior denotes the mechanical response of the homogeneous medium which is equivalent to that of the heterogeneous material. The method to derive the effective behavior of the homogeneous medium from the heterogeneous one is called homogenization. Additional problems often treated are the examination of the microstructural stress-strain state to predict local damage mechanisms or the investigation of arbitrary, often multiaxial load states which are difficult to analyze by experimental techniques. The so-called virtual laboratory can also be helpful to study the effects of various constituents without the necessity to actually produce each material variant. Thus, a virtual material screening for a given application can be performed.

2.2.2 Classical stiffness prediction and homogenization methods

The first analytical approaches provide bounds for the effective elastic moduli of the heterogeneous material under assumption of a constant strain (Voigt upper bound [Voi89]) and a constant stress, respectively (Reuss lower bound [Reu29]) within the composite. More accurate bounds were developed by Hashin and Shtrikman under application of variational principles [Has62]. Eshelby's equivalent inclusion problem [Esh57] at first takes into account the shape of the inclusion by treating an ellipsoidal inclusion in an infinite matrix at dilute concentration. The Mori-Tanaka model [Mor73] extends the Eshelby problem to non-dilute concentrations of the inclusions by considering phase interactions in an approximate way (the so-called *mean field* approach). The elastic constants of a short fiber composite can be determined in this way [Tan84]. Following a different route one can start from Hill's self-consistent scheme [Hil63] and derive the modeling of transversely isotropic composites including the effects of fiber aspect ratio, which leads to the semi-empirical Halpin-Tsai equations [Hal76]. An overview of common methods for stiffness prediction of unidirectional short fiber composites is given by Tucker and Liang [Tuc99]. The effect of a varying fiber orientation can be addressed by averaging the elastic constants of an imaginary transversely isotropic reference composite with respect to the fiber orientation distribution (known as *orientation averaging* according to Advani and Tucker [Adv87]). Since the microstructure is not explicitly depicted, all these approaches require significant simplifications regarding the geometry and the interactions between the fibers or inclusions. However, to predict the elastic properties, the classical models are accurate enough even for modeling LFTs [Ngu08, Gar13], although characteristic geometrical features like fiber waviness resulting from the dense packing and detailed fiber-fiber interactions in regions of high fiber density cannot be addressed.

2.2.3 Advanced nonlinear modeling approaches

The widening of the application range of various models beyond linear elasticity was an important research topic of computational micromechanics in recent years.

One way to overcome the simplifications of the classical approaches is to predict the *full field* at the micro-level by explicit depiction of the microstructure in the form of a surface mesh or a voxel grid which can then be computed e.g. with FE simulations or fast Fourier transform (FFT) solvers. This approach has no inherent limitation with respect to microstructural features and their interaction and is therefore suitable to capture the complex nonlinear and time-dependent behavior of the thermoplastic matrix of LFTs in conjunction with fiber-fiber interactions and fiber-matrix interface debonding phenomena. The major drawback of most *full field* approaches is their high computational cost, which disqualifies them from simulating larger components of industrial relevance.

Gusev *et al.* studied short fiber composites of fixed aspect ratio and volume fraction under variation of the fiber orientation distribution with a *full field* model and found agreement of the elastic properties to the classical approaches within engineering accuracy [Gus02]. The effects of fiber volume fraction, aspect ratio and fiber length distribution on the elastic and thermoelastic properties of short fiber composites were also studied [Hin02]. In a similar spirit, Pan *et al.* created a RVE for random chopped fiber composites with volume fractions up to 35 % and applied the model to predict the elastic properties as well as the damage behavior including fiber-matrix interface debonding [Pan08b, Pan10]. Hoffmann investigated RVEs of short fiber reinforced thermoplastics based on micromechanical values for fiber orientation, length and volume and included the effects of a plastic matrix model accounting for damage [Hof12].

On the other hand, also the *mean field* approaches and purely phenomenological models were further developed for application to nonlinear material behavior. Their benefit is their computational efficiency and therefore their suitability for computations on the component level. However, their accuracy is somewhat limited due to consideration of similar simplifications as the classical approaches or - in the case of purely phenomenological approaches - they are lacking in physical background.

Seelig *et al.* presented an integrative simulation approach with mapping from process to structural simulation using a phenomenological LFT model which accounts for fiber orientation in a simplified way and considers a tension-compression asymmetry [See08]. Fritsch *et al.* applied a phenomenological approach embedded in a FEM framework to investigate the viscoelastic-viscoplastic response of LFT to dynamic loading [Fri09]. Nguyen *et al.* developed an effective elastic-plastic model for injection molded LFTs based on their fiber orientation and length distributions and implemented it into a finite element framework [Ngu09]. The nonlinear deformation behavior was very well reproduced, whereas the validity of the model is restricted to the onset of damage. Therefore, effects

of progressive failure could not be captured. Kammoun included the effects of progressive failure in micromechanical models of short fiber reinforced thermoplastics [Kam11]. In his work, the Eshelby-Mori-Tanaka approach was extended to incorporate a fiber orientation and length distribution by a multiple step homogenization. Fibers with similar orientation and length were assigned to a so-called pseudo grain. At first, homogenization is carried out for each individual pseudo grain before a second homogenization step is performed over all grains with different micromechanical characteristics. The procedure was implemented into a FE framework and validated against experimental data. A similar procedure is commercially available with *Digimat-MF* [Dig14].

2.2.4 Representative volume element

The concept of homogenization is illustrated in Fig. 8 for the sample structure of an unidirectional fiber arrangement. Due to computational cost, it is in general not possible to model the microstructure of the material explicitly within the component to be calculated because the characteristic length of the microstructure is usually several orders of magnitudes smaller than the characteristic component dimension. The microstructure is therefore decomposed into a characteristic sub-unit, the representative volume element. In most cases, the microstructure can be obtained by periodic arrangement of the RVE as depicted in Fig. 8. Homogenization is performed for the RVE sub-unit of significantly reduced dimensions under consideration of appropriate boundary conditions (mostly periodic boundary conditions if applicable). A mathematical description of the constitutive behavior of the effective material is determined which is equivalent to the response of the RVE as a function of the microstructure and the constituent properties (e.g. fiber and matrix). The equivalent, homogenized material behavior is then applied (e.g. by implementation in the form of an effective material law) for calculation of the component without explicitly depicting the microstructure.

The necessary and sufficient condition for the equivalence of the homogenized medium and the heterogeneous one was formulated by Hill [Hil51, Bis51]. Hill's condition ensures the equivalence of strain energy between the heterogeneous and homogenized level. It states that the volume average of the product of microscopic stresses and strains of the composite equals the product of the homogenized stress and strain, as long as the analyzed volume is chosen large enough:

$$\langle \sigma_{ij} \varepsilon_{ij} \rangle = \langle \sigma_{ij} \rangle \langle \varepsilon_{ij} \rangle, \quad (9)$$

where $\langle \cdot \rangle = \frac{1}{V} \int_{(V)} \cdot dV$ denotes the volume average. The RVE acts as a substitute body for the material's microstructure. It has to be large enough to include all representative features on the microscopic scale. If the structure is periodic, the RVE can also be referred to as unit cell. The definition of the RVE dimensions strongly depends on the

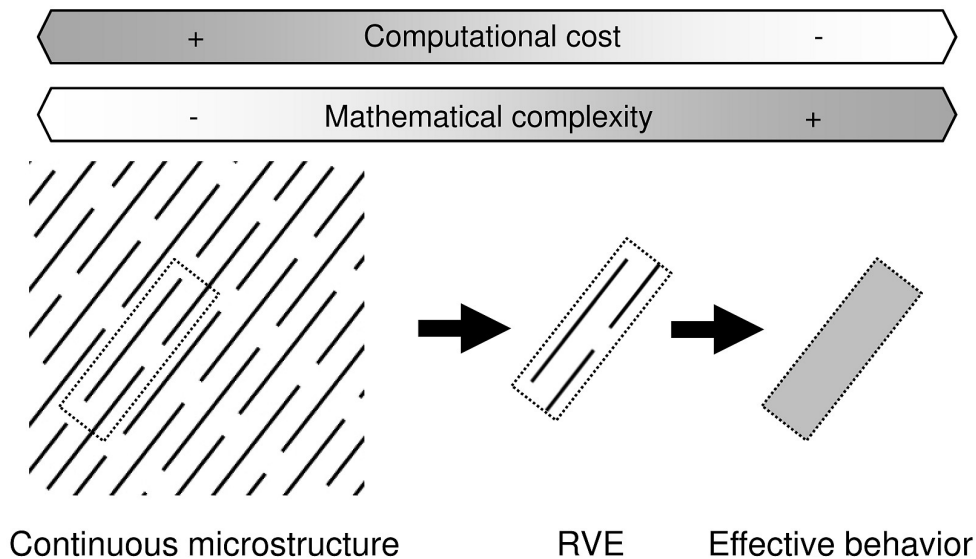


Figure 8: Concept of homogenization: Definition of a periodic sub-unit of the continuous microstructure (RVE) and determination of its effective behavior.

characteristics of the material to be modeled and is often not trivial. In order to be representative in a statistical sense, the characteristic RVE dimension L_{RVE} (e.g. edge length in case of a cubic RVE) must be large compared to the characteristic length on the microstructural level L_{micro} (e.g. the fiber length for discontinuous fiber composites or the cell diameter in case of porous materials or foams) [Hoh05, Dem07]. On the other hand, the RVE must be small compared to the characteristic part dimension L_{macro} (e.g. the wall thickness or lateral dimension of a component):

$$L_{\text{macro}} \gg L_{\text{RVE}} \gg L_{\text{micro}} . \quad (10)$$

Depending on the material, both inequalities might be contradictory and the RVE in a statistical sense might not exist. This is the case for most variants of LFT materials: The characteristic length on the microstructural scale, which can be considered as the maximum fiber length, has a value of several mm ($L_{\text{micro}} = 50$ mm for the material investigated in this work). Most LFT components feature a wall thickness in the region of $L_{\text{macro}} = 5$ mm. As a consequence, the homogenization scheme in a strict statistical sense is not applicable ($L_{\text{micro}} > L_{\text{macro}}$). However, if Eq. 10 is interpreted component-wise, the condition can be met: Most LFT components feature lateral dimensions in the region of or even larger than 1 m, but are very thin, shell-like structures. Because of the thin walls, the fibers are geometrically constrained to be aligned in layers parallel to the wall surface (as discussed by Advani and Tucker [Adv87] amongst others). If L_{micro} in direction of the wall thickness is therefore considered to be the fiber diameter (e.g. 20 μm), the criterion can be met (20 $\mu\text{m} \ll 5$ mm). In the transverse directions, L_{micro} represents the maximum fiber length (e.g. 50 mm) which is often small compared to the lateral part

dimensions (e.g. 1 m). As a consequence, the RVE shape cannot remain cubic and the three RVE dimensions become unequal (e.g. a very flat cuboid). However, a variation of the RVE size should always be performed to ensure that the results are insensitive in this respect.

2.2.5 Microstructure generation of discontinuous fiber composites

Two classical RVE generation procedures which are often referred to in the literature are the random sequential adsorption (RSA) scheme of cylindrical, uncurved fibers and the generation of a FE mesh based on cubic voxels (both illustrated in Fig. 9). The RSA

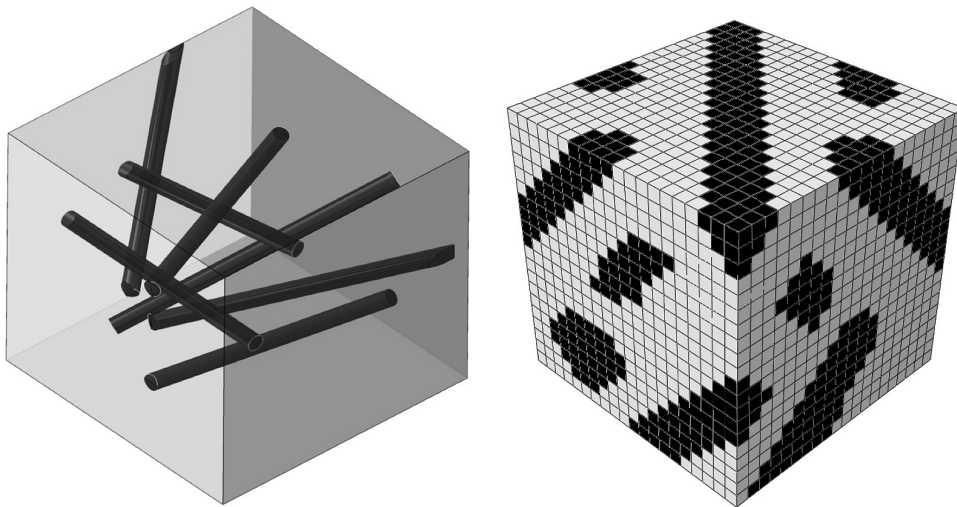


Figure 9: Classical RVE generation procedures: Random sequential adsorption of cylindrical, uncurved fibers (left) and voxel based mesh generation (right).

scheme is mostly based on Monte-Carlo simulations. The position and orientation of cylindrical fibers, described by their starting point and 3D extrusion vector (e.g. Euler angles) is chosen randomly until the desired orientation state and volume fraction is reached. The method can be extended by a shaking or compressing algorithm to reach higher volume fractions with less numerical effort. This procedure was implemented into the structure generation software *Palmyra* [Pal14]. Lu *et al.* presented a modified RSA algorithm by means of an automatic searching and coupling technique and applied it to investigate the elastic properties of random, discontinuous fiber composites over a range of fiber aspect ratios from 20 to 300 for volume fractions up to 15 % [Lu 14]. Wang *et al.* modeled layered fibrous materials with different fiber lengths to investigate the effect of fiber length on through-plane permeability [Wan07]. Dirrenberger *et al.* investigated the behavior of 3D interpenetrating fibrous networks without consideration of a matrix phase toward gigantic RVE sizes [Dir14]. As interpenetration of fibers is not acceptable for a realistic three dimensional model of discontinuous fiber composites, an essential problem of all structure generation methods which are based on cylindrical, uncurved fibers exists in the form of

the so-called jamming limit, describing the dependence of the maximum achievable fiber volume fraction on the fiber aspect ratio. Further investigations of randomly arranged and dispersed, uncurved fibers were carried out by Evans and Toll [Eva86, Tol98] amongst others. Fig. 10 shows the principle dependency. A more detailed analysis and comparison is given by Pan [Pan10]. All analytical and numerical models agree that for (from a LFT point of view) moderate aspect ratio of approx. 80, the maximum achievable volume fraction for an unforced packing of uncurved fibers is well below 0.1 and further decreasing toward higher aspect ratios.

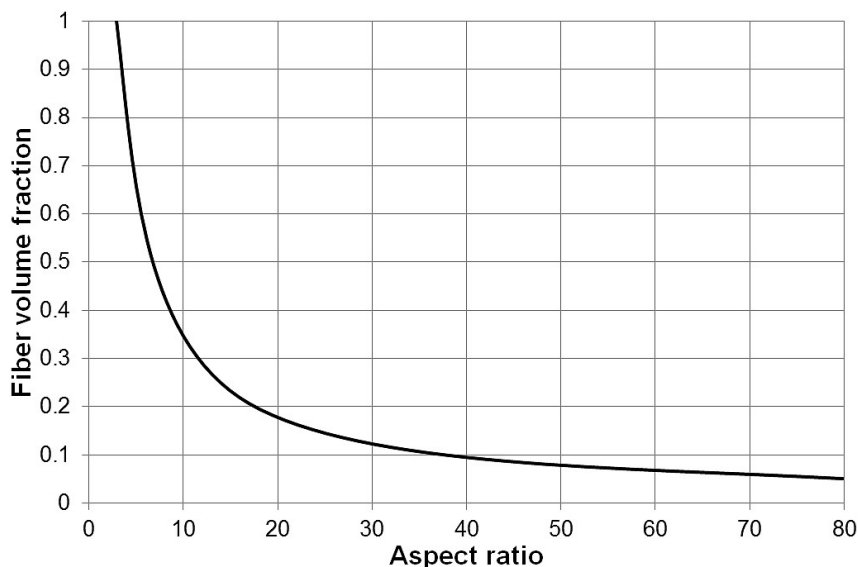


Figure 10: Jamming limit according to Evans and Toll [Eva86, Tol98] describing the maximum achievable volume fraction of randomly arranged and dispersed, uncurved fibers.

To achieve higher volume fractions of discontinuous fiber composites with aspect ratios well above those of short fiber reinforcements, the classical RSA scheme for an unforced packing of uncurved fibers needs to be modified. A suitable method for the modeling of random strand fiber composites with volume fractions up to 35 % was developed by Pan [Pan08a, Pan08b, Pan10]. The fibers are deposited into 2D layers under compliance of a random fiber orientation distribution. If an intersection between two fibers is unavoidable, the fiber extrusion vector jumps to the adjacent layer and bridges the crossing fiber before switching back to the original layer. Pan applied the method to model the elastic properties as well as to describe fiber debonding during quasi static deformation by the inclusion of cohesive zone elements between the fibers and the matrix. The resulting effective elastic properties are in good agreement to experimental results, although the characteristic kinks of Pan's method cannot be considered as realistic. Harper *et al.* modeled discontinuous carbon fiber composites with unlimited volume fraction by representation of the fibers as one dimensional beam elements, embedded in a free or structured matrix mesh [Har12a, Har12b]. Harper systematically investigated the effects of RVE size, boundary conditions, fiber length (up to 10 mm) and volume fraction

(up to 50 %) on the elastic properties of structures with random orientation. The main advantage of the latter method is its ease of implementation as well as its computational efficiency, whereas limitations exist with respect to the modeling of nonlinear material behavior and damage. Soltani *et al.* reconstructed the 3D structure of non-woven fabrics with algorithms applied on 2D slices of their CT voxel data to calculate the permeability of such fiber networks [Sol14]. Each fiber features the exact geometry as observed by the CT scan. However, vast efforts have to be made for such reconstruction mainly due to detailed checks of neighborhood relations for each voxel. For the extremely high aspect ratio of LFT, such detailed reconstruction of CT data can be considered as problematic due to the size of the structures and the related amount of data. With state-of-the-art CT and computational resources, this cannot be considered as currently technically feasible. Faessel *et al.* generated fiber networks based on measured statistical values describing the microstructure (fiber orientation, density, length and curvature) and investigated the effects of thermal conductivity [Fae05]. However, the procedure does not account for any matrix material and permits fiber interpenetration.

Commercial tools are available which use a cubic voxel grid to describe the microstructure (*GeoDict* [Geo14]). Each voxel is either assigned to the matrix or inclusion material properties depending on its position. This is well suited for a stress analysis with FFT solvers as implemented in *GeoDict*, but rather problematic and inefficient for FE analysis of LFT materials with fiber aspect ratios well above 1000 due to the resulting data amount respectively the element count. In detail, each fiber must be depicted by a multitude of elements over its cross section to appropriately model features like fiber crossing, bridging or entanglements. This is illustrated in Fig. 9 (right). To represent the complex LFT structure more efficiently, a free meshing technique should be preferred, where the fiber mesh is swept along the curved fiber axis instead of using a fixed voxel mesh.

The software *Digmat-FE* [Dig14] is in general suitable for the generation of an RVE with discontinuous, curved fibers. However, the generated microstructure is described based on surface geometries by various CAD file formats which then need to be meshed by external software (This procedure is also available in *GeoDict* as an alternative to the voxel grid). For extremely large LFT structures, the indirect way of exporting a surface-based geometrical description can be considered as problematic and meshing of such complex geometry will require enormous computational resources. This issue can be addressed by application of a direct procedure which generates the fiber mesh straight from the statistics, whereas only the matrix mesh needs to be computed by appropriate FE pre-processing software.

3 Experimental methods

3.1 Material and microstructure

3.1.1 Processing conditions

The investigated LFT material consists of a polypropylene matrix (*DOW*[®] *C711-70RNA* [DOW03]) and glass fibers (*TufRov*[®] *4575* [PPG13]). A coupling agent was added to improve the reactivity of the polypropylene with the silane sizing of the glass fibers in order to establish a strong bonding. Furthermore, a heat stabilizer and carbon black inhibit the thermo-oxidative degradation of the matrix. Three material variants PPGF10, PPGF20 and PPGF30 were produced with different fiber weight fractions of 10, 20 and 30 % (corresponding fiber volume fractions of 3.80, 8.16 and 13.22 %) at the *Fraunhofer Institute for Chemical Technology (ICT)*. PPGF30 and PPGF20 are of great interest for structural application and commonly used by the automotive industry, whereas PPGF10 is rather of academic interest to provide additional data for the model validation. Plates with dimensions of 400 x 400 x 3 mm³ were formed by compression molding as described in Section 2.1. The LFT strand as it came out of the extruder was positioned asymmetrically in the mold. The material flow during the compression of the mold generates a rather high degree of fiber orientation everywhere outside the strand inlay position. This so-called *flow region* of the plate was investigated in the following. The specimen plate is illustrated in Fig. 11 with highlighted positions of the tensile and the CT specimens as well as the position of the fiber length analysis section of approx. 100 x 60 mm². Approximate characteristic dimensions are specified in the figure.

The polymer granules were processed on a *Leistritz ZSE-40 HP - 32D* inline compounder and the resulting plasticized mass was mixed with the glass fibers (introduced in the form of continuous rovings) in a *Leistritz ZSG-40 GL - 20D* mixing extruder. The LFT-D strand was then positioned into a flat plaque mold with shear edges with the dimensions of 400 x 400 mm². Compression was performed by a *Dieffenbacher DYL 630/500* hydraulic press with a parallel motion control system and a maximum closing force of 5000 kN. Table 2 shows the parameters of the process.

3.1.2 Fiber orientation distribution

The fiber orientation distribution was extracted by means of image analysis of computer tomographic (CT) scans, which were taken at the *Fraunhofer IWM* in Halle. A *Phoenix nanome|x 180NF* μ CT device was used to acquire the scans with a voxel size of approx. 8 μ m and a resolution of 360³ voxels of the cubic analysis section of 3³ mm³ to screen the specimens over their complete thickness. The scans were taken at a tube voltage of 85 kV and a current of 90 μ A by a flat panel detector with a max. resolution of 512² pixels. The

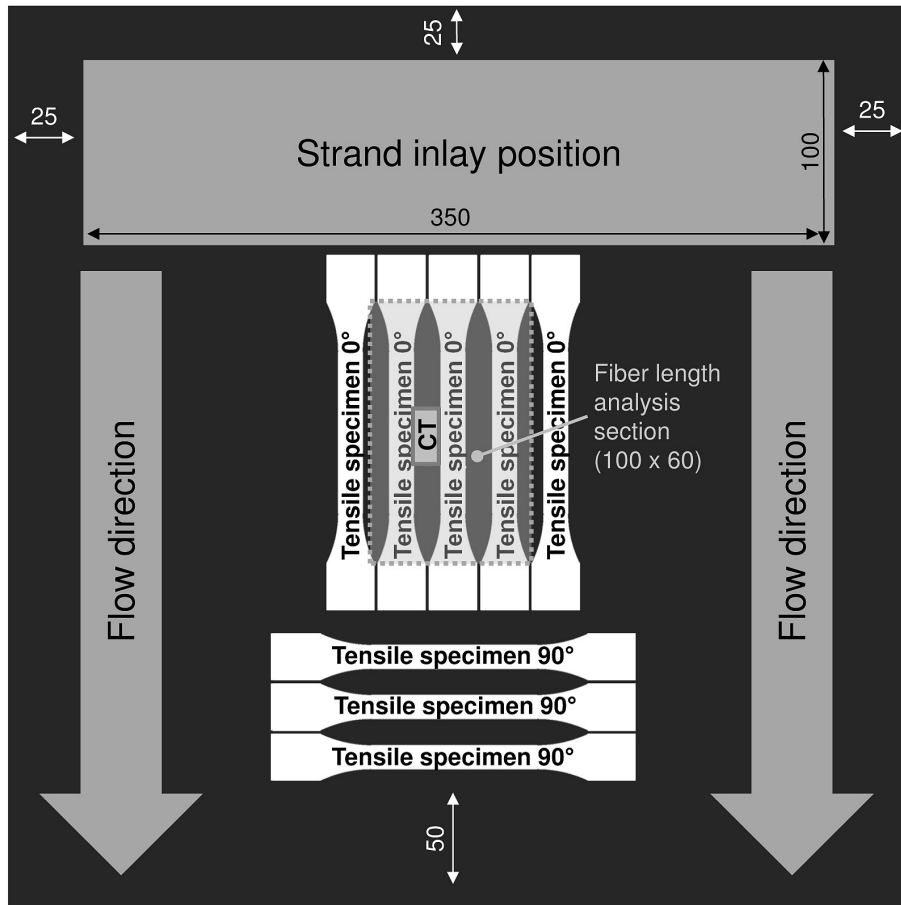


Figure 11: LFT specimen plate with the dimensions of $400 \times 400 \times 3 \text{ mm}^3$ manufactured by compression molding. The positions of the tensile and CT specimens as well as the position of the fiber length analysis section are highlighted in the figure.

Parameter	Value	Unit
Pressing force	3200	kN
Temperature mold (top)	60	°C
Temperature mold (bottom)	65	°C
Temperature mixing extruder	240	°C
Temperature heat tunnel	260	°C
Temperature conveyor belt	250	°C
Polymer mass flow	30	kg/h
Revolution speed of mixing extruder	71	rpm
Density of rovings	2400	tex
Number of rovings (PPGF30, 13.2 vol-%)	14	
Number of rovings (PPGF20, 8.2 vol-%)	8	
Number of rovings (PPGF10, 3.8 vol-%)	4	

Table 2: Parameters of the LFT-D manufacturing process of the investigated material.

specimens were taken from the same region of the LFT plate as the 0° tensile specimens (Fig. 11). In the following, the CT data was analyzed by the plugin *Directionality* of the image processing software *ImageJ* [Fij14]. In order to apply the procedure, the raw CT voxel data was decomposed into 360 slices of 2D images which were binarized before applying the analysis procedure (Fig. 12). The plugin chops each single 2D image into square sections, in which the Fourier transform in the form of its power spectrum in polar coordinates is analyzed for each angle under application of spatial filters proposed by Liu [Liu91]. Therefore, the relative amount of area with a preferred direction is evaluated by means of a probability density function (the planar fiber orientation distribution). The integral orientation distribution as used for the RVE modeling was derived by averaging over all 360 histograms (Fig. 13) of the stack. The distributions are interpreted as fiber length fraction per angle class as the software recognizes the amount of picture area with a preferred direction and does not perform any segmentation of fibers.

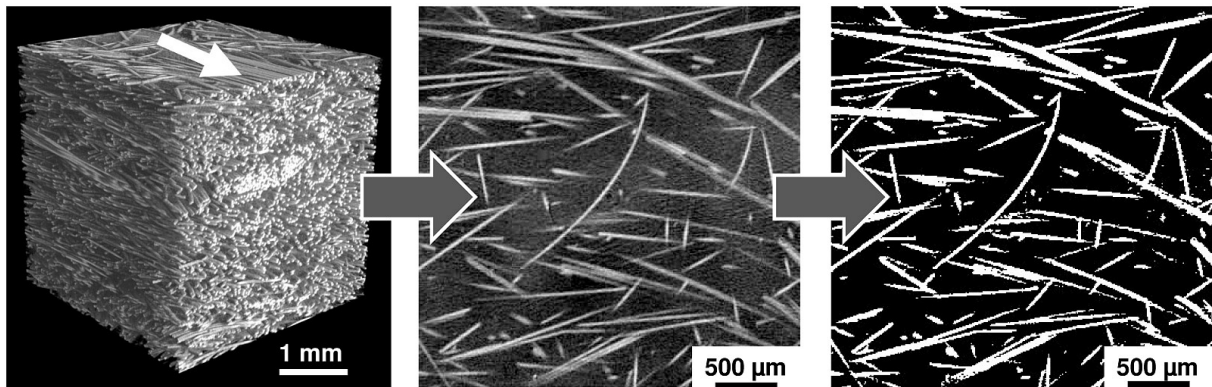


Figure 12: Analysis procedure to extract the fiber orientation distribution from CT scans: Raw CT voxel data (left, the white arrow shows the flow direction), decomposition into a stack of 360 2D images (middle, exemplary image depicted) and binarization and orientation analysis of each 2D image with the plugin *Directionality* [Fij14] of the program *ImageJ* (right). The data of the PPGF30 material (13.2 vol-%) is shown.

3.1.3 Fiber length distribution

The fiber length distribution cannot be determined from the CT scans since this would require identification of the continuity of the fibers which is not currently possible for LFT materials due to the enormous size of such analysis sections and the related data amount. The fiber length distribution therefore was determined by the analysis of the diluted fiber structure of an incinerated specimen by means of automatic image analysis. The specimen was taken from the same region of the plate as the 0° tensile specimens (Fig. 11). To distort the measurement as little as possible, a large specimen area of approx. $100 \times 60 \text{ mm}^2$ was chosen to extract the fiber structure. 8868 fibers were analyzed. The analysis was carried out by the company *xyz high precision* under application of their fiber separation procedure and the analysis software *FASEP*[®] [FAS14, Har09].

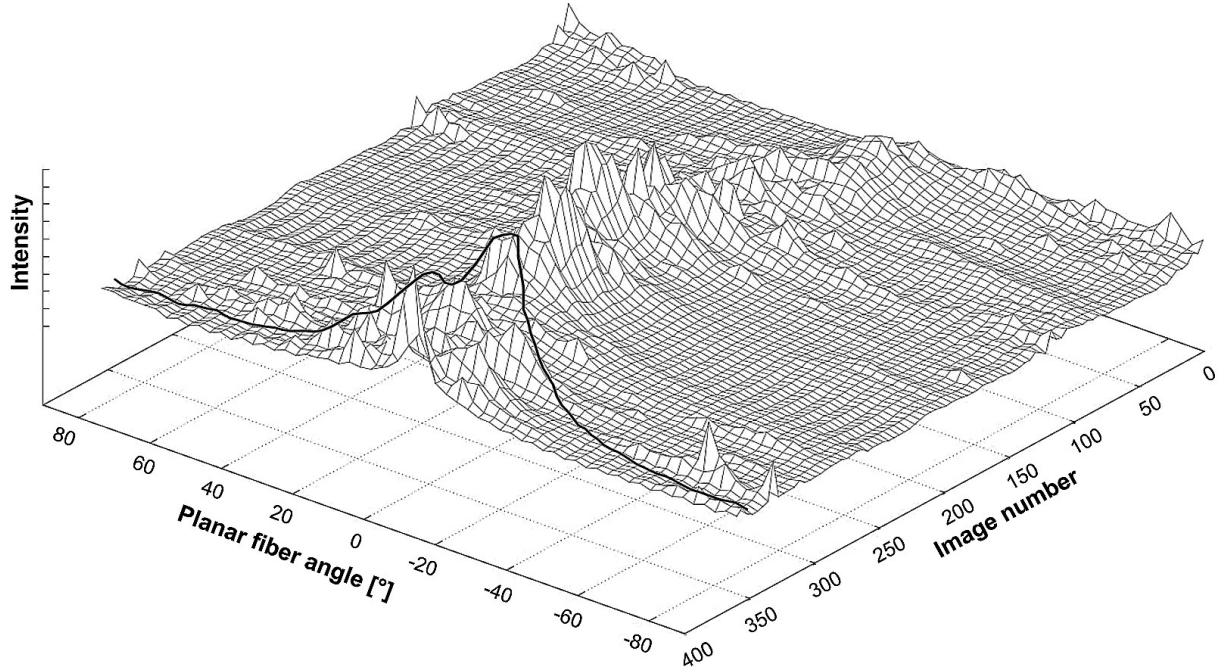


Figure 13: Plot of the fiber orientation distribution over the stack of 360 2D images (PPGF30). The black line represents the integral planar orientation distribution as used for the RVE models, as obtained by averaging over the 360 histograms of the stack.

The mean fiber length as characteristic value of the fiber length distribution can be expressed as the arithmetic mean (number average) \bar{l}_n or alternatively be weighted by fiber length (weight average) \bar{l}_w according to the following equations:

$$\bar{l}_n = \frac{\sum_i n_i l_i}{\sum_i n_i}, \quad (11)$$

$$\bar{l}_w = \frac{\sum_i n_i l_i^2}{\sum_i n_i l_i}, \quad (12)$$

where l_i is the fiber length and n_i the number of fibers with the length l_i .

3.1.4 Fiber volume fraction

The fiber volume fraction f_v was calculated from the weight fraction f_w which results from the mass flow rates of the manufacturing process (Section 3.1.1). The mass density values for fiber ρ_f and matrix ρ_m were taken from the manufacturers data sheet [DOW03,PPG13].

$$f_v = \frac{f_w}{f_w + (1 - f_w) \frac{\rho_f}{\rho_m}} \quad (13)$$

3.2 Tensile tests

3.2.1 Matrix specimens

To determine the elastic-plastic response of the polypropylene matrix, tensile tests on matrix substance specimens were performed. Specimen plates of $500 \times 500 \times 4 \text{ mm}^3$ were manufactured by injection compression molding at the *Fraunhofer Institute for Chemical Technology (ICT)*. The manufacturing process was chosen in order to ensure similar processing conditions as for the compression molding of the LFT specimens (Section 3.1.1). The same additives (coupling agents, UV stabilizers) were added to the matrix polymer (Polypropylene *DOW*[®] *C711-70RNA* [DOW03]) as used to produce the LFT plates.

Quasi-static tensile tests with a cross-head displacement rate of 0.01, 0.1 and 1 mm/s (corresponding strain rates of approx. $7 \cdot 10^{-5}$, $7 \cdot 10^{-4}$ and $7 \cdot 10^{-3}$ 1/s) were carried out with a *Hegewald & Peschke Inspekt 100* testing machine on specimens cut from the 4 mm thick plates. The geometry of the dog bone shaped specimens with a reduced section of $70 \times 10 \text{ mm}^3$ is depicted in Fig. 14. An *Instron*[®] *2620-604* axial clip-on extensometer with a gauge length of 50 mm was used for strain acquisition.

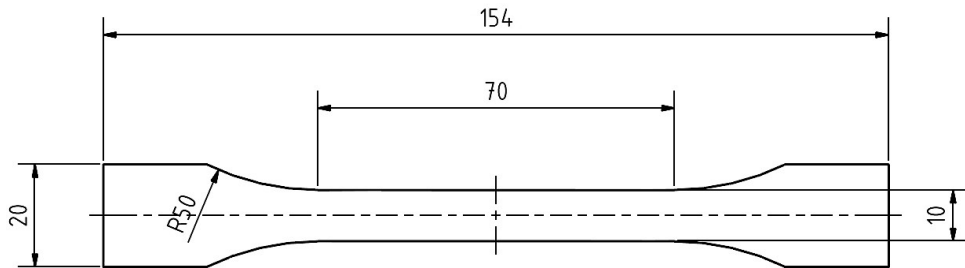


Figure 14: Geometry of multi-purpose tensile specimens according to *DIN EN ISO 3167* [DIN03] (dimensions in mm).

3.2.2 LFT specimens

Elasticity

To measure the elastic properties of the LFT material, quasi-static tensile tests were carried out in a similar manner as in described for the matrix specimens (Section 3.2.1). Exclusively the lowest crosshead displacement rate of 0.01 mm/s (corresponding strain rate of approx. $7 \cdot 10^{-5}$ 1/s) was applied for the elastic testing procedure. The specimens (same geometry as before) were taken from the flow region of the plate under 0° and 90° relative to the material's flow direction (Fig. 11). The stiffness was determined from the initial, linear elastic part of the stress-strain curve, where no effects of plasticity or

damage could be observed (a range up to approx. 10 % of the respective strength for each material variant and fiber orientation). Three loading-unloading cycles were repeated to ensure that no degradation effects were active. At least three specimens per material variant and orientation were tested to obtain the stiffness values in flow direction E_1 and in transverse direction E_2 . The analysis procedure is shown in Fig. 15 for an exemplary stress-strain curve.

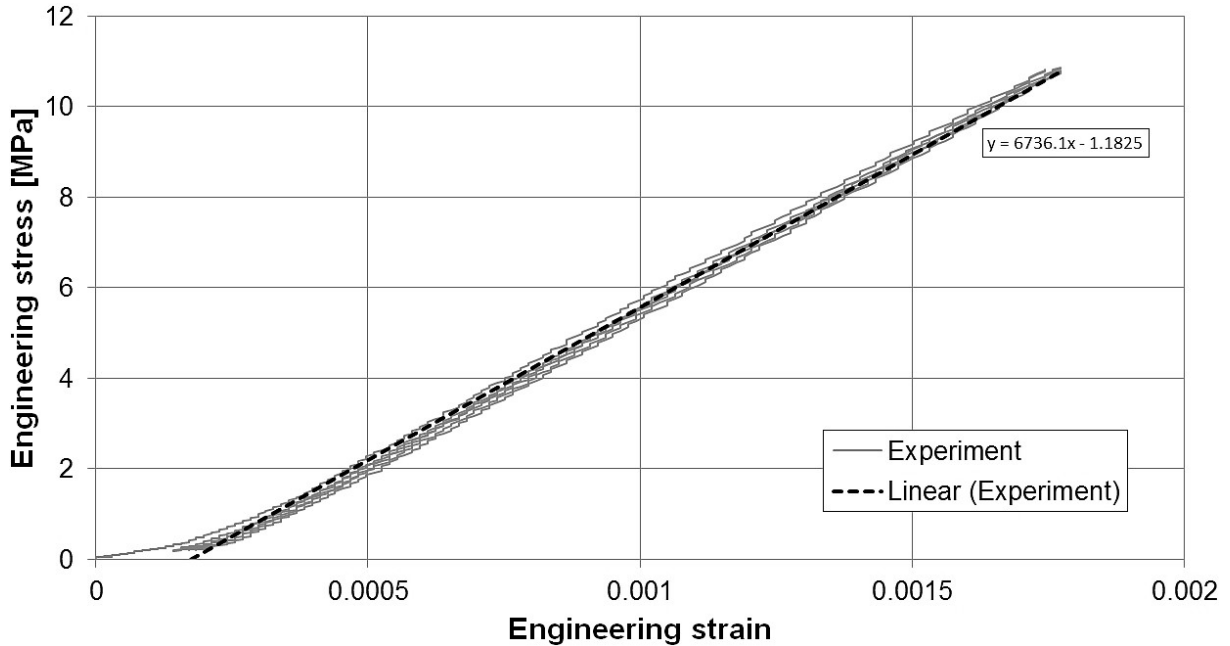


Figure 15: Exemplary stress-strain curve to determine the elastic modulus of a LFT specimen (PPGF30, 13.2 vol-%, 0° load direction). The experimental data is depicted with grey solid lines, whereas the linear least squares fit to extract the stiffness value features a black dashed line.

Plasticity and damage

The deformation and damage behavior of LFT under 0 and 90° load direction was investigated by quasi-static tensile tests with a cross-head displacement rate of approx. 0.05 mm/s (corresponding strain rate of approx. $7 \cdot 10^{-4}$ 1/s). A different specimen geometry (Fig. 16) than the one used for the remaining experiments was chosen in order to ensure that the fracture was localized within the specimen's and extensometer's gauge section, which could not be achieved with the standard geometry (Fig. 14). A *HBM DD1* axial clip-on extensometer with a gauge length of 10 mm was used for strain acquisition. The resulting stress-strain curves presented in Section 5.6.11 were generated under consideration of values of engineering stress ($\sigma = F/A_0$, actual force F divided by original cross section A_0) and engineering strain ($\varepsilon = \Delta l/L_0$ with Δl being the displacement value of the extensometer and L_0 being the original distance between the blades).

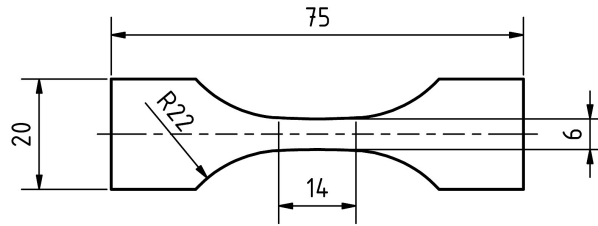


Figure 16: Geometry of LFT specimens for tensile tests until fracture (dimensions in mm).

3.3 Creep tests

3.3.1 Matrix specimens

Creep tests on matrix substance specimens were carried out at standard climate (23 °C temperature, 50 % relative humidity). The specimens are described in Section 3.2.1. At the beginning of the load period of $6 \cdot 10^5$ s, a load defined by the product of specimen cross section and desired nominal stress level was applied in the form of a lead weight. For the lower stress levels up to 5 MPa, the load was directly attached to the specimen clamps, whereas a lever mechanism with a transmission ratio of 10 was used for the higher stress levels. The strain was measured with an *Instron*[®] 2620-604 axial clip-on extensometer with a gauge length of 50 mm. Up to a time period of 3600 s, a recording interval of 1 s was chosen (an interval of 600 s between 3600 and $6 \cdot 10^5$ s) for data acquisition.

3.3.2 LFT specimens

Validation experiments to characterize the creep behavior of LFT were performed under the same conditions as described in the previous section (Section 3.3.1). Specimens of 0° and 90° relative to the materials flow direction (Fig. 11) were tested. The specimen geometry is defined in Fig. 14.

3.4 Fiber push-out tests

To determine the fiber-matrix interface properties, single fiber push-out tests were performed on thin slices of the PPGF30 material at the *Institute for Applied Materials (IAM-WK)* of the *Karlsruhe Institute of Technology (KIT)*. The specimens featuring a multitude of fibers were prepared from the cross section of the LFT plates and were polished with a diamond suspension to a desired thickness of 85 μm. The specimens were prepared with their surface being transversely oriented relative to the flow direction. Thus, a multitude of fibers are aligned in thickness direction of the specimen (Fig. 17). The slice was then placed on a perforated plate with a hole diameter of 60 μm and a

grid distance of 200 μm (Fig. 18). Several fibers were manually selected for indentation under compliance of the criteria that the fibers were located within a hole of the perforated plate and that the fibers were aligned preferably in push-out direction. Numerical studies support that fiber eccentricity and angular misalignment up to 25° from push-out direction rather weakly affect the resulting peak force with a maximum deviation below 10 % [Bry11, Bry10]. Indentation was then carried out with a *Zwick ZHU 0.2* universal hardness testing machine (nominal load capacity of 200 N) using a flat-punch indenter with a tip diameter of approx. 5 μm (Fig. 18). The indents were performed in displacement-controlled mode at a displacement rate of 3 $\mu\text{m}/\text{min}$ up to an indentation depth of approx. 6 to 8 μm measured after the initial contact between indenter and fiber.

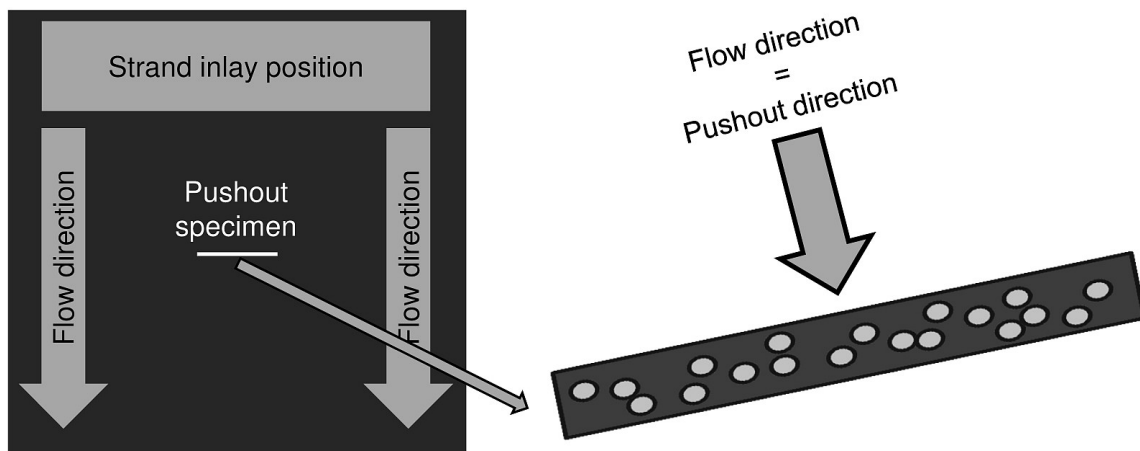


Figure 17: Preparation of the push-out specimens (thickness 85 μm) from the cross section of a LFT plate (PPGF30, 13.2 % fiber volume fraction) with the flow direction being parallel to the thickness direction of the specimen.

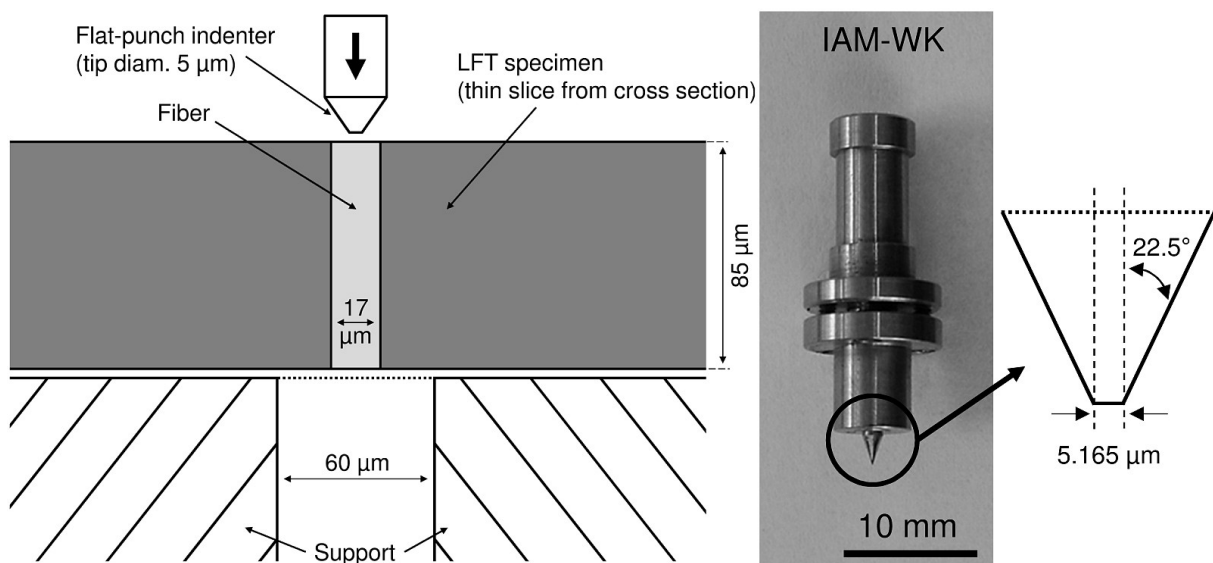


Figure 18: Push-out loading scenario with the specimen bearing on a perforated plate (left), flat-punch indenter (middle) and details of the indenter tip (right).

4 Modeling techniques

4.1 Viscoelastic matrix model

4.1.1 Modeling strategy

The nonlinear viscoelastic matrix model as applied in this work is based on the classical linear viscoelastic Burgers model. The numerical implementation of the linear viscoelastic variant was carried out according to the literature (Section 4.1.2 - 4.1.6). In the following step, the linear model was modified to a nonlinear variant based on the experimental findings (Section 4.1.7 - 4.1.8).

There are several ways of mathematical description of viscoelastic models like the Burgers model. The most general is to derive the ordinary differential equation (ODE, Section 4.1.3) and to solve the ODE either analytically for a specific boundary condition (e.g. a constant stress σ_0) or numerically for an arbitrary load history.

A more elegant and computational efficient way is based on the hereditary form, where the time-dependent creep compliance (as obtained from the analytical solution of the ODE for a constant stress) is combined with an arbitrary load history by means of a convolution integral, known as the memory function and based on Boltzmann's superposition principle. This approach is described in detail in Section 4.1.4 and essentially limited to linear viscoelasticity in its original form (various approaches of a modified superposition principle exist to overcome this limitation, Section 4.1.7). If the hereditary integral is converted to its incremental form (Section 4.1.5), it is reduced to a simple recursive formulation, in which the state of strain needs to be inherited from the previous to the current time increment, resulting in a very efficient numerical method which is suitable for the analysis of the very large models of this work. The three dimensional incremental form is derived in Section 4.1.6. It is suitable for numerical implementation of the classical linear viscoelastic Burgers material, in which the recursive approach corresponds to a variety of viscoelastic models presented in the literature [Tay70, Lai96, Haj04, Ric06, Hua08, Wol11]. In incremental form, the limitation to linear viscoelastic behavior only affects the current time increment Δt by assumption of a constant stress rate $\dot{\sigma} = \Delta\sigma/\Delta t$ and constant model parameters E, η for the current time increment. Thus, the overall nonlinear viscoelastic behavior as observed for the investigated polymeric matrix (Section 5.2.1) can be approximated by numerical integration of the load history with sectional linear time increments. The nonlinear modification of the model and its range of validity is described in Section 4.1.7. A detailed flowchart and the equations of the nonlinear model ready for implementation by means of a user subroutine (UMAT) are presented in Section 4.1.8.

4.1.2 Burgers four parameter model

The Burgers model is a composition of a viscous Maxwell model, represented by the spring E_0 and the dashpot η_0 and a viscoelastic Kelvin-Voigt model with the parameters E_1 and η_1 . Fig. 19 shows its rheological notation as it can be found in various lecture books (e.g. by Brinson [Bri08]). The Maxwell model describes a fluid whereas the Kelvin-Voigt model represents a solid.

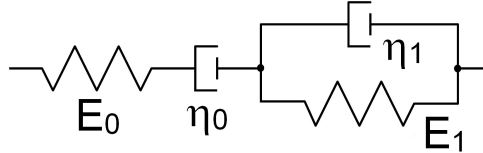


Figure 19: Schematic notation of the viscoelastic Burgers model as a combination of a viscous Maxwell model with the parameters E_0 and η_0 and a viscoelastic Kelvin-Voigt model with the parameters E_1 and η_1 .

By combining both elementary models, the Burgers model represents the characteristic mechanical behavior of an ideal thermoplastic as illustrated in Fig. 20 for a creep-recovery experiment under application of a constant stress σ_0 at time t_0 and removal of the stress at t_1 . The stationary creep rate $\dot{\epsilon} = \sigma_0/\eta_0$ of the second phase after relaxation of the Kelvin-Voigt element as well as the irreversible strain ϵ_{irr} after unloading correspond to the assumption of unlimited, continuous sliding of the polymeric chains under load.

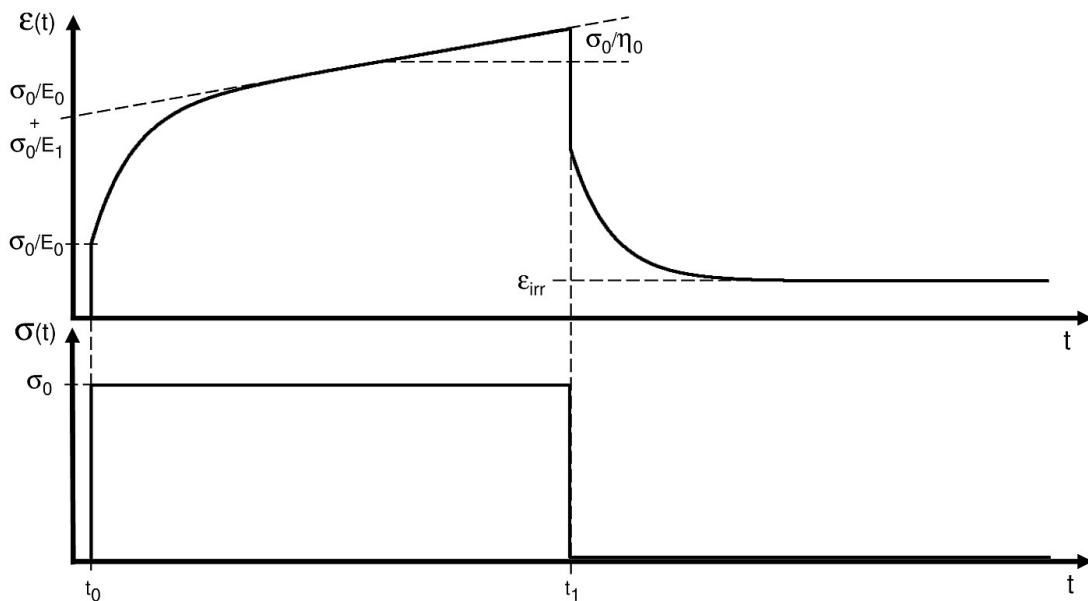


Figure 20: Response of the Burgers model to a constant stress σ_0 applied at time t_0 and recovery behavior of the unloading period after t_1 .

4.1.3 Differential equation

The one dimensional constitutive equation of the Burgers model in the form of an ODE is given by

$$\frac{E_1}{\eta_0} \sigma + \left(1 + \frac{E_1}{E_0} + \frac{\eta_1}{\eta_0}\right) \dot{\sigma} + \frac{\eta_1}{E_0} \ddot{\sigma} = E_1 \dot{\varepsilon} + \eta_1 \ddot{\varepsilon} . \quad (14)$$

The derivation (as described by Brinson [Bri08] amongst others) is carried out in the appendix (Section A.1.1).

The analytical solution of the ODE (Eq. 14) under the boundary condition of a constant stress σ_0 is given by

$$\varepsilon(t) = \sigma_0 \left[\frac{1}{E_0} + \frac{t}{\eta_0} + \frac{1}{E_1} \left(1 - e^{-\frac{t}{\tau_r}}\right) \right] = \sigma_0 C(t) , \quad (15)$$

where τ_r denotes the relaxation time of the Kelvin-Voigt element: $\tau_r = \eta_1/E_1$.

In this case, the creep behavior is independent of load and can be separated in the form of the creep compliance $C(t)$, defined as

$$C(t) = \frac{1}{E_0} + \frac{t}{\eta_0} + \frac{1}{E_1} \left(1 - e^{-\frac{t}{\tau_r}}\right) . \quad (16)$$

4.1.4 Hereditary integral

Besides the differential form as described in the previous section, a viscoelastic material behavior can be expressed in terms of a hereditary integral based on the Boltzmann superposition principle. The validity of the superposition principle in its original form is limited to linear viscoelasticity, where the creep response is independent of load.

The memory function of viscoelasticity is defined by the convolution integral

$$\varepsilon(t) = \int_0^t C(t - \tau) \dot{\sigma} \, d\tau , \quad (17)$$

where C is the creep compliance, $\dot{\sigma}$ the stress rate at time τ and τ the time integration variable. The derivation of the memory function is specified in the appendix (Section A.1.2).

4.1.5 Incremental form

The hereditary form offers some advantages with respect to numerical implementation as in incremental formulation, the model reduces to a simple recursive formulation in which the strain components of the Kelvin-Voigt element need to be inherited from the previous time increment to the current. Numerical implementation of such an approach was first published by Taylor *et al.* [Tay70]. The derivation as specified in the appendix (Section A.1.3) was described by Woldekidan [Wol11]. A similar procedure for the Maxwell body was presented by Richter [Ric06]. Furthermore, a variety of implementations of viscoelastic models in the literature are based on a comparable recursive algorithm [Lai96, Haj04, Hua08].

The total strain increment $\Delta\varepsilon^{\text{tot}}$ is decomposed into an elastic $\Delta\varepsilon^e$, a viscous $\Delta\varepsilon^v$ and a viscoelastic $\Delta\varepsilon^{\text{ve}}$ component:

$$\Delta\varepsilon^{\text{tot}} = \Delta\varepsilon^e + \Delta\varepsilon^v + \Delta\varepsilon^{\text{ve}} . \quad (18)$$

The elastic component is given by

$$\Delta\varepsilon^e = \frac{\Delta\sigma}{E_0} . \quad (19)$$

Under knowledge of the stress value at the beginning of the time increment $\sigma(t - \Delta t)$, the viscous component is defined as

$$\Delta\varepsilon^v(t) = \frac{\Delta t}{\eta_0} \left[\sigma(t - \Delta t) + \frac{\Delta\sigma}{2} \right] . \quad (20)$$

The following recursive expression applies to the viscoelastic component, where $\varepsilon^{\text{inh}}(t - \Delta t)$ is the viscoelastic strain which is inherited from the previous time increment:

$$\Delta\varepsilon^{\text{ve}}(t) = \frac{\Delta\sigma}{E_1} - \left[e^{\frac{-\Delta t}{\tau_r}} - 1 \right] \varepsilon^{\text{inh}}(t - \Delta t) - \frac{1}{E_1} \frac{\Delta\sigma}{\Delta t} \tau_r \left[1 - e^{\frac{-\Delta t}{\tau_r}} \right] . \quad (21)$$

4.1.6 3D generalization

The incremental form of the one dimensional model needs to be generalized to three dimensions as described by Lai and Bakker [Lai96] and Woldekidan [Wol11]. Some abbreviations are introduced with respect to a compact notation suitable for numerical implementation by means of a user subroutine (UMAT). The equations of this section can be directly used for numerical implementation of the linear 3D Burgers model.

Two general ways to model the 3D behavior of a viscoelastic body are known:

- **Type A: Constant Poisson's ratio**

For this type of 3D behavior of time-dependent deformation, a constant Poisson's ratio is assumed over the complete time history. The time-dependent deformation is therefore considered as compressible and treated in the same way as the instantaneous, elastic response of a solid with a constant Poisson's ratio $\nu_e = \nu_t < 0.5$. The one dimensional creep compliance $C(t)$ (Eq. 16) can then be divided into a shear $J(t)$ and a bulk $B(t)$ component as follows:

$$J(t) = 2(1 + \nu)C(t) , \quad (22)$$

$$B(t) = 3(1 - 2\nu)C(t) , \quad (23)$$

$$\nu = \text{const.} . \quad (24)$$

- **Type B: Time-dependent Poisson's ratio**

The second type of 3D behavior assumes only the shear component of viscoelastic deformation to be time-dependent, whereas the bulk part remains constant and equal to the bulk component of the instantaneous elastic response. Whereas the elastic response is assumed to be compressible with a Poisson's ratio $\nu_e < 0.5$, the time-dependent part of deformation is considered as incompressible ($\nu_t = 0.5$ and thus $\text{tr}(\boldsymbol{\varepsilon}_t) = 0$). As a consequence, the overall Poisson's ratio of time dependent deformation with an elastic and viscoelastic component becomes time-dependent:

$$J(t) = \frac{BC(t)}{3} \left[\frac{9}{B} - \frac{1}{C(t)} \right] , \quad (25)$$

$$B = \text{const.} , \quad (26)$$

$$\nu(t) = \frac{1}{2} - \frac{B}{6C(t)} . \quad (27)$$

For glassy or semi-crystalline, thermoplastic polymers as the investigated matrix material, *type A* of time-dependent 3D behavior is commonly assumed [Lai96] and was therefore applied in the following. In contrast, *type B* is used to model materials like bituminous mastic, where the shear deformation is considered to be dominant [Wol11].

The three dimensional equations of the following sections refer to the Voigt form of stress $\boldsymbol{\sigma}$ and strain $\boldsymbol{\varepsilon}$ - their tensors are reduced to six dimensional vectors in favor of a compact notation:

$$\boldsymbol{\sigma} = \left[\begin{array}{cccccc} \sigma_{11} & \sigma_{22} & \sigma_{33} & \sigma_{23} & \sigma_{13} & \sigma_{12} \end{array} \right] , \quad (28)$$

$$\boldsymbol{\varepsilon} = \left[\begin{array}{cccccc} \varepsilon_{11} & \varepsilon_{22} & \varepsilon_{33} & 2\varepsilon_{23} & 2\varepsilon_{13} & 2\varepsilon_{12} \end{array} \right] . \quad (29)$$

The elastic shear and bulk compliances J_0 and B_0 can be expressed in terms of Young's modulus E and Poisson's ratio ν by

$$J_0 = \frac{2(1 + \nu)}{E_0} , \quad (30)$$

$$B_0 = \frac{3(1 - 2\nu)}{E_0} , \quad (31)$$

where E_0 denotes the stiffness of the Maxwell element and ν the Poisson's ratio of the overall Burgers material.

The same is done for the Kelvin-Voigt element by the following:

$$J_1 = \frac{2(1 + \nu)}{E_1} , \quad (32)$$

$$B_1 = \frac{3(1 - 2\nu)}{E_1} . \quad (33)$$

The reciprocal value of the relaxation time τ_r is defined as

$$\lambda_r = \frac{E_1}{\eta_1} = \frac{1}{\tau_r} , \quad (34)$$

with E_1 and η_1 being the stiffness and viscosity of the Kelvin-Voigt element, respectively.

Some additional abbreviations are introduced to avoid cumbersome terms:

$$\beta = e^{-\lambda_r \Delta t} , \quad (35)$$

$$\alpha = \beta - 1 , \quad (36)$$

$$x = \frac{\Delta t}{\eta_0} , \quad (37)$$

where η_0 is the viscosity of the Maxwell element.

The time-dependent shear compliance J^* and bulk compliance B^* are given by

$$J^* = \frac{1}{2} \left[J_0 + J_1 \left(1 + \frac{1}{\lambda_r \Delta t} \alpha \right) \right] , \quad (38)$$

$$B^* = \frac{1}{3} \left[B_0 + B_1 \left(1 + \frac{1}{\lambda_r \Delta t} \alpha \right) \right] . \quad (39)$$

The model's constitutive equation to express the incremental stress $\Delta\boldsymbol{\sigma}$ in terms of the incremental strain $\Delta\boldsymbol{\varepsilon}$ at the time t is defined as

$$\begin{aligned} \Delta\boldsymbol{\sigma}(t) = & \left[\frac{1}{J^*}\mathbf{M}_d^* + \frac{1}{B^*}\mathbf{M}_b \right] \Delta\boldsymbol{\varepsilon}(t) - x \left[\frac{1}{J^*}\mathbf{M}_d^{**} + \frac{1}{B^*}\mathbf{M}_b \right] \boldsymbol{\sigma}(t) \\ & -\alpha \left[\frac{1}{J^*}\mathbf{M}_d^{***} \boldsymbol{\varepsilon}_d^{\text{inh}}(t - \Delta t) + \frac{1}{B^*}\mathbf{M}_b \boldsymbol{\varepsilon}_b^{\text{inh}}(t - \Delta t) \right] . \end{aligned} \quad (40)$$

The coupling matrix for the deviatoric strain components (\mathbf{M}_d , \mathbf{M}_d^* , \mathbf{M}_d^{**} and \mathbf{M}_d^{***}) is given by

$$\mathbf{M}_d = \begin{bmatrix} 2/3 & -1/3 & -1/3 & 0 & 0 & 0 \\ -1/3 & 2/3 & -1/3 & 0 & 0 & 0 \\ -1/3 & -1/3 & 2/3 & 0 & 0 & 0 \\ 0 & 0 & 0 & a & 0 & 0 \\ 0 & 0 & 0 & 0 & a & 0 \\ 0 & 0 & 0 & 0 & 0 & a \end{bmatrix}, \quad (41)$$

where $a = 2$ for \mathbf{M}_d , $a = 1$ for \mathbf{M}_d^* , $a = 3/2$ for \mathbf{M}_d^{**} and $a = 1/2$ for \mathbf{M}_d^{***} .

For the bulk components, it takes the form of

$$\mathbf{M}_b = \begin{bmatrix} 1/3 & 1/3 & 1/3 & 0 & 0 & 0 \\ 1/3 & 1/3 & 1/3 & 0 & 0 & 0 \\ 1/3 & 1/3 & 1/3 & 0 & 0 & 0 \\ 0 & 0 & 0 & 0 & 0 & 0 \\ 0 & 0 & 0 & 0 & 0 & 0 \\ 0 & 0 & 0 & 0 & 0 & 0 \end{bmatrix}. \quad (42)$$

Some additional abbreviations are introduced:

$$\gamma = -\frac{J_1}{2\lambda_r\Delta t}(1 - \beta), \quad (43)$$

$$\delta = -\frac{B_1}{3\lambda_r\Delta t}(1 - \beta). \quad (44)$$

The strain of the Kelvin-Voigt element $\boldsymbol{\varepsilon}^{\text{inh}}$ is inherited from the previous timestep. Its bulk and deviatoric components are stored separately and updated at the end of each time increment by the following equations:

$$\boldsymbol{\varepsilon}_d^{\text{inh}}(t) = \beta\boldsymbol{\varepsilon}_d^{\text{inh}}(t - \Delta t) + \gamma\mathbf{M}_d\Delta\boldsymbol{\sigma}(t), \quad (45)$$

$$\boldsymbol{\varepsilon}_b^{\text{inh}}(t) = \beta\boldsymbol{\varepsilon}_b^{\text{inh}}(t - \Delta t) + \delta\mathbf{M}_b\Delta\boldsymbol{\sigma}(t). \quad (46)$$

4.1.7 Nonlinear modification and range of validity

As a strong nonlinear viscoelastic behavior of the investigated polypropylene matrix material was observed experimentally, the classical, linear viscoelastic Burgers model is not applicable within reasonable accuracy (studies on several variants of the model formulation, including a linear viscoelastic one, are presented in Section 5.6.9). Thus, the formulation of the linear viscoelastic model according to the Boltzmann superposition principle had to be modified. Similar approaches were made by Leaderman [Lea43], who introduced the modified superposition principle (MSP) to account for nonlinear viscoelastic effects and Schapery [Sch69], who extended the MSP theory to account for more nonlinear functions, a reduced time and a shift factor in analogy to the thermodynamically motivated time-temperature superposition principle. In the original form of the model, the shift factor accounts exclusively for stress. Temperature and aging effects can be incorporated by additional shift factors [Lai96]. The creep function of the Schapery model, specified in the form of a time-dependent uniaxial strain $\varepsilon(t)$ is defined as

$$\varepsilon(t) = g_0 C_0 \sigma + g_1 \int_0^t \Delta C(\psi_t - \psi'_t) \frac{dg_2 \sigma}{d\tau} d\tau, \quad (47)$$

where C_0 is the instantaneous and ΔC the time-dependent part of the creep compliance and ψ_t the reduced time, given by

$$\psi_t = \int_0^t \frac{dt'}{a_\sigma(\sigma(t'))}, \quad (48)$$

and $\psi'_t = \psi_t(\tau)$. The functions $g_0(\sigma)$, $g_1(\sigma)$ and $g_2(\sigma)$ correspond the nonlinear material properties and $a_\sigma(\sigma)$ is the shift factor of the reduced time with respect to stress. For the 3D representation of the model, the von Mises equivalent stress, the hydrostatic pressure or a combination of both are usually chosen as measures of the effective stress based on which the nonlinear functions are expressed, as described by Lai and Bakker [Lai96]. In this way, it is also possible to account for a tension-compression asymmetry of the material. For $g_0 = g_1 = a_\sigma = 1$, the model reduces to the modified superposition principle of Leaderman:

$$\varepsilon(t) = C_0 \sigma + \int_0^t \Delta C(\psi_t - \psi'_t) \frac{dg_2 \sigma}{d\tau} d\tau, \quad (49)$$

and further simplification with $g_2 = 1$ yields the linear viscoelastic form. In this work, a similar approach of modification of the superposition principle was implemented. The Burgers model was retained as the underlying framework since empirical functions, which explicitly describe the stress-dependence of the Burgers parameters, could be found while

interpreting the experimental results (Section 5.2.1). It therefore seems to be more adequate to apply a bottom-up approach and to directly use these functions instead of fitting the Schapery model to the experimental data. Moreover, the Schapery model is predestined for thermosetting materials with a decaying secondary creep rate and no irreversible strain in the recovery phase [Bri08], since it is usually based on a generalized Maxwell model. The application of a generalized Maxwell model to the experimental data as alternative to the Burgers model is described in Section 5.2.2, Paragraph '*3D behavior*'. For the Burgers model, only one relaxation time had to be considered to accurately reproduce the experimental data (Fig. 42), whereas a multitude of relaxation times were necessary to describe the experimental curves with the generalized Maxwell body. Furthermore, the presence of an irreversible part of strain in the recovery period of the experiments indicates that the viscous character of the Burgers model is justified and therefore, the Burgers model was retained as the framework for the nonlinear version.

Finally, the stress-dependence of the Kelvin-Voigt spring E_1 and dashpot η_1 as well as the Maxwell dashpot η_0 is expressed by empirically determined equations specified in the results section (Section 5.2.1), whereas the spring E_0 was not found to be stress dependent (the parameters are defined in Fig. 19). For each time increment of the load history, the model parameters E_1 , η_0 and η_1 therefore need to be recalculated. An explicit calculation of these parameters is not possible: The material routine needs to compute the stress increment for a given strain increment by application of stress-dependent model parameters. Thus, the general framework of the material model must be extended by an iterative Newton-Raphson algorithm to determine the model parameters implicitly as described in detail in the following section. A similar approach was chosen by Lai and Bakker [Lai96] and Woldekidan [Wol11] for the implementation of the Schapery model.

The nonlinear approach and its numerical time integration scheme as presented in the following is based on the incremental form of the linear viscoelastic Burgers model (Section 4.1.5). In order that the time integration scheme is applicable, the assumption is made that the model parameters E , η remain constant for each time increment Δt and stress is assumed to vary linearly over each time increment, $\dot{\sigma} = \Delta\sigma/\Delta t$, in accordance to the implementations of Lai and Bakker [Lai96] and Woldekidan [Wol11]. These simplifications affect the range of validity of the nonlinear viscoelastic model. Further discussion and a method to improve the accuracy by the application of an extended predictor-corrector approach in combination with the recursive formulation can be found in the publication of Haj-Ali [Haj04]. Due to the need for a computational efficient model which is suitable for the analysis of very large microstructures, the model was kept as simple as possible and no such additional corrector steps were considered. The model is therefore not necessarily applicable to scenarios with a fast variation of load (e.g. cyclic loading), but sufficiently accurate to analyze creep scenarios without abrupt changes in load. Further analysis and discussion can be found in Section 5.6.9 and 6.2.2.

4.1.8 Numerical implementation of nonlinearity

A flowchart of the numerical implementation by means of a user subroutine (UMAT) is shown in Fig. 21. The stress dependent parameters are calculated implicitly by an iterative loop. As a significant part of the model is identical to its linear form, some abbreviations used in the following were already defined in Section 4.1.6.

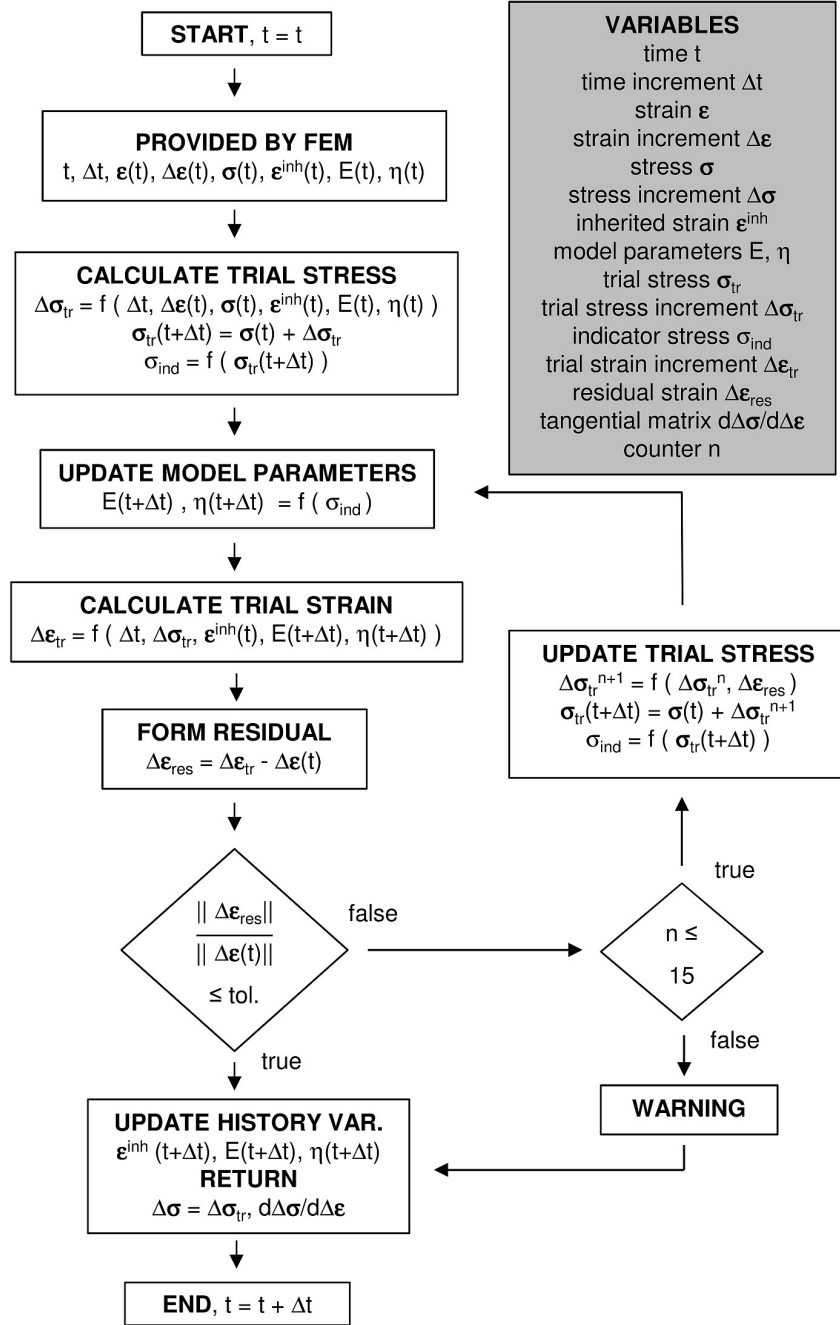


Figure 21: Flowchart of the numerical implementation of the nonlinear Burgers model.

- **Calculate trial stress with parameters from previous converged state**

Applying Eq. 50 (identical to the linear model, Eq. 40), a trial stress increment $\Delta\boldsymbol{\sigma}_{\text{tr}}$ is computed with the model parameters from the previous converged state based on the strain increment $\Delta\boldsymbol{\varepsilon}$ which is provided by the FE software at the beginning of the UMAT call (the coupling matrices are defined by Eq. 41 and 42):

$$\begin{aligned} \Delta\boldsymbol{\sigma}_{\text{tr}}(t) = & \left[\frac{1}{J^*} \mathbf{M}_d^* + \frac{1}{B^*} \mathbf{M}_b \right] \Delta\boldsymbol{\varepsilon}(t) - x \left[\frac{1}{J^*} \mathbf{M}_d^{**} + \frac{1}{B^*} \mathbf{M}_b \right] \boldsymbol{\sigma}(t) \\ & - \alpha \left[\frac{1}{J^*} \mathbf{M}_d^{***} \boldsymbol{\varepsilon}_d^{\text{inh}}(t - \Delta t) + \frac{1}{B^*} \mathbf{M}_b \boldsymbol{\varepsilon}_b^{\text{inh}}(t - \Delta t) \right]. \end{aligned} \quad (50)$$

- **Update model parameters based on trial stress**

The trial stress is formed by addition of the trial stress increment to the previous value of stress:

$$\boldsymbol{\sigma}_{\text{tr}}(t + \Delta t) = \boldsymbol{\sigma}(t) + \Delta\boldsymbol{\sigma}_{\text{tr}}(t). \quad (51)$$

The hydrostatic stress σ_{H} and the von Mises equivalent stress σ_{M} are calculated at each material point by

$$\sigma_{\text{H}} = \frac{1}{3} \sigma_{kk}, \quad (52)$$

$$\sigma_{\text{M}} = \sqrt{\frac{3}{2} \sigma'_{ij} \sigma'_{ij}}, \quad (53)$$

where σ'_{ij} denotes the deviatoric stress, defined as

$$\sigma'_{ij} = \sigma_{ij} - \frac{1}{3} \delta_{ij} \sigma_{kk}, \quad (54)$$

and δ_{ij} being the Kronecker delta (Eq. 3).

The indicator stress σ_{ind} is defined as the largest absolute value of σ_{M} and σ_{H} :

$$\sigma_{\text{ind}} = \begin{cases} \sigma_{\text{M}} & \text{if } |\sigma_{\text{M}}| \geq |\sigma_{\text{H}}| \\ \sigma_{\text{H}} & \text{if } |\sigma_{\text{H}}| > |\sigma_{\text{M}}| \end{cases}. \quad (55)$$

The indicator stress σ_{ind} is then used to determine the stress-dependent model parameters E_1 , η_0 , η_1 (defined by Eq. 118 - 120 in Section 5.2.1). For stress levels outside the experimentally investigated range, the material behavior is assumed to be linear viscoelastic. Thus, the model parameters remain constant at their respective values for stresses lower (higher) than 2.5 (12.5) MPa. The variables J^* , B^* , x , α , β , γ , δ then need to be recalculated with the new values of model parameters under application of the equations defined in Section 4.1.6.

- **Calculate backwards to trial strain and form residual**

Applying Eq. 56, the trial stress increment $\Delta\boldsymbol{\sigma}_{\text{tr}}$ is converted into a trial strain increment $\Delta\boldsymbol{\varepsilon}_{\text{tr}}$ using the updated model parameters:

$$\begin{aligned} \Delta\boldsymbol{\varepsilon}_{\text{tr}}(t) = & [J^* \mathbf{M}_d + B^* \mathbf{M}_b] \Delta\boldsymbol{\sigma}_{\text{tr}}(t) + x \mathbf{M}_x \boldsymbol{\sigma}(t) \\ & + \alpha [\mathbf{M}_d \boldsymbol{\varepsilon}_d^{\text{inh}}(t - \Delta t) + \mathbf{M}_b \boldsymbol{\varepsilon}_b^{\text{inh}}(t - \Delta t)] . \end{aligned} \quad (56)$$

The coupling matrix for the deviatoric \mathbf{M}_d and bulk components \mathbf{M}_b was already defined (Eq. 41 and 42). For the Maxwell dashpot (\mathbf{M}_x), it takes the form of

$$\mathbf{M}_x = \begin{bmatrix} 1 & 0 & 0 & 0 & 0 & 0 \\ 0 & 1 & 0 & 0 & 0 & 0 \\ 0 & 0 & 1 & 0 & 0 & 0 \\ 0 & 0 & 0 & 3 & 0 & 0 \\ 0 & 0 & 0 & 0 & 3 & 0 \\ 0 & 0 & 0 & 0 & 0 & 3 \end{bmatrix} . \quad (57)$$

A residual strain vector $\Delta\boldsymbol{\varepsilon}_{\text{res}}$ is computed by subtraction of the strain increment $\Delta\boldsymbol{\varepsilon}$ (provided by the FE software at the beginning of the subroutine call):

$$\Delta\boldsymbol{\varepsilon}_{\text{res}} = \Delta\boldsymbol{\varepsilon}_{\text{tr}} - \Delta\boldsymbol{\varepsilon} . \quad (58)$$

- **Minimize residual with updated trial stress**

The residual strain vector $\Delta\boldsymbol{\varepsilon}_{\text{res}}$ is minimized by an iterative Newton-Raphson procedure until the following criterion is satisfied:

$$\frac{\|\Delta\boldsymbol{\varepsilon}_{\text{res}}\|}{\|\Delta\boldsymbol{\varepsilon}\|} \leq 10^{-6} , \quad (59)$$

where $\|\cdot\|$ is the Euclidean norm (Eq. 6).

A maximum of $n = 15$ iterations is performed for the following recursive formulation to calculate the updated trial stress increment $\Delta\boldsymbol{\sigma}_{\text{tr}}^{n+1}$:

$$\Delta\boldsymbol{\sigma}_{\text{tr}}^{n+1} = \Delta\boldsymbol{\sigma}_{\text{tr}}^n - \left(\frac{1}{J^*} \mathbf{M}_d^{***} + \frac{1}{B^*} \mathbf{M}_b \right) \Delta\boldsymbol{\varepsilon}_{\text{res}} . \quad (60)$$

If the procedure did not converge after 15 iterations, the recursive loop is aborted and a warning message is written to the message file. The material routine is then continued in the same way as if convergence would have been obtained.

- **Update history variables and return the tangential matrix**

Before exiting the UMAT subroutine, the strain of the Kelvin-Voigt element needs to be stored in state variables. The values are updated by Eq. 45 and 46. 9 state variables are necessary to save the deviatoric (6) and bulk (3) components separately.

The current values for the stress-dependent model parameters E_1 , η_0 and η_1 are stored in three more variables.

The maximum value of indicator stress σ_{ind} over the time history is also saved: If the current value of σ_{ind} is larger than the value of the state variable, the state variable is updated (otherwise not).

Another two state variables store the hydrostatic strain ε_{H} and the equivalent deviatoric strain ε'_{eq} for postprocessing purposes:

$$\varepsilon_{\text{H}} = \frac{1}{3}\varepsilon_{kk} , \quad (61)$$

$$\varepsilon'_{\text{eq}} = \frac{1}{1+\nu} \sqrt{\frac{3}{2}\varepsilon'_{ij}\varepsilon'_{ij}} , \quad (62)$$

with $\varepsilon'_{ij} = \varepsilon_{ij} - \frac{1}{3}\delta_{ij}\varepsilon_{kk}$ being the deviatoric strain.

The equivalent deviatoric strain (Eq. 62) is calculated in analogy to the von Mises form in order to provide a scalar measure of the deviatoric part of strain. The factor $1/(1+\nu)$ effects that under uniaxial load, the equivalent strain is equal to the uniaxial strain, since a constant and equal Poisson's ratio of instantaneous and time-dependent deformation (Eq. 22 - 24) is considered by the model.

In total, 15 state variables at each material point are used by the material subroutine.

At the end, the tangential matrix $\frac{d\Delta\sigma}{d\Delta\varepsilon}$ is updated with

$$\frac{d\Delta\sigma}{d\Delta\varepsilon} = \frac{1}{J^*}\mathbf{M}_{\text{d}}^{***} + \frac{1}{B^*}\mathbf{M}_{\text{b}} . \quad (63)$$

4.2 Plastic matrix model

The von Mises plasticity model is based on the second invariant J'_2 of the deviatoric stress tensor σ'_{ij} (Eq. 54). The invariant defines a scalar stress intensity value as a function of the six dimensional space of stress which is independent of the rotation of the underlying coordinate system. Because only the deviatoric stress is considered, the model implies that plastic deformation is exclusively effected by distortional deformation modes, whereas the material response to volumetric deformation remains purely elastic. The derivation, as carried out in the following, can be found in various lecture books (e.g. Bower [Bow10]) and the *Abaqus* manual [Aba11].

The invariants J'_i represent the coefficients in the characteristic equation to extract the three principal stresses σ of the deviatoric stress tensor σ'_{ij} (Eq. 54):

$$\sigma^3 - J'_1\sigma^2 + J'_2\sigma - J'_3 = 0 . \quad (64)$$

The three invariants J'_i of the deviatoric stress tensor are given by

$$J'_1 = \sigma'_{kk} = 0 , \quad (65)$$

$$J'_2 = \frac{1}{2}\sigma'_{ij}\sigma'_{ij} = \frac{1}{6} [(\sigma_{11} - \sigma_{22})^2 + (\sigma_{22} - \sigma_{33})^2 + (\sigma_{33} - \sigma_{11})^2] + \sigma_{12}^2 + \sigma_{23}^2 + \sigma_{31}^2 , \quad (66)$$

$$J'_3 = \frac{1}{3}\sigma'_{ij}\sigma'_{jk}\sigma'_{ki} . \quad (67)$$

Based on J'_2 , the von Mises equivalent stress $\bar{\sigma}$ is defined as

$$\bar{\sigma} = \sqrt{3J'_2} = \sqrt{\frac{3}{2}\sigma'_{ij}\sigma'_{ij}} = \sigma_M . \quad (68)$$

To differentiate between the elastic and plastic part of deformation, the total strain $\boldsymbol{\varepsilon}^{\text{tot}}$ is decomposed into its elastic $\boldsymbol{\varepsilon}^e$ and plastic $\boldsymbol{\varepsilon}^p$ part:

$$\boldsymbol{\varepsilon}^{\text{tot}} = \boldsymbol{\varepsilon}^e + \boldsymbol{\varepsilon}^p . \quad (69)$$

The equivalent plastic strain $\bar{\varepsilon}^p$ can be obtained by integration of the equivalent plastic strain rate $\dot{\bar{\varepsilon}}^p$ over the time t :

$$\bar{\varepsilon}^p = \int_0^t \dot{\bar{\varepsilon}}^p dt . \quad (70)$$

The equivalent plastic strain rate $\dot{\bar{\epsilon}}^p$ is defined as

$$\dot{\bar{\epsilon}}^p = \sqrt{\frac{2}{3} \dot{\epsilon}_{ij}^p \dot{\epsilon}_{ij}^p} . \quad (71)$$

The yield stress $\bar{\sigma}_Y$ defines the critical limit of equivalent stress to cause plastic flow:

$$\bar{\sigma}(\boldsymbol{\sigma}) = \bar{\sigma}_Y(\bar{\epsilon}^p) . \quad (72)$$

The yield surface in the six dimensional stress space is defined by its normal \mathbf{n} :

$$\mathbf{n} = \frac{\sqrt{3/2}}{\bar{\sigma}} \boldsymbol{\sigma}' . \quad (73)$$

Plastic flow occurs if the equivalent stress reaches the yield stress and if the stress rate $\dot{\boldsymbol{\sigma}}$ points outside the yield surface:

$$\bar{\sigma}(\boldsymbol{\sigma}) = \bar{\sigma}_Y \quad \text{and} \quad \mathbf{n}^T \dot{\boldsymbol{\sigma}} > 0 . \quad (74)$$

An associated flow rule is assumed which induces the plastic flow rate to be parallel to the normal of the yield surface:

$$\dot{\boldsymbol{\epsilon}}^p = \Lambda \mathbf{n} . \quad (75)$$

The proportionality constant Λ is always larger than or equal to zero in the case of plastic flow. For negative values of Λ , the material response is elastic. Plastic flow is assumed to be isochoric, which implies a Poisson's ratio of 0.5 (incompressible solid). For an exemplary case of uniaxial loading, this results in

$$\dot{\epsilon}_{11}^p = \dot{\epsilon} , \quad \dot{\epsilon}_{22}^p = -\frac{1}{2} \dot{\epsilon} , \quad \dot{\epsilon}_{33}^p = -\frac{1}{2} \dot{\epsilon} . \quad (76)$$

The above equations are numerically implemented by an iterative *elastic predictor / plastic corrector* approach. The evolution of the yield surface (isotropic hardening) is defined in the form of tabular value pairs of equivalent plastic strain $\bar{\epsilon}^p$ and corresponding yield stress $\bar{\sigma}_Y$. Interpolation between two values is performed linearly, whereas the yield stress outside the specified range is assumed to remain constant. The model is available in *Abaqus* under the keyword **PLASTIC*, which was applied in the simulations accounting for plasticity.

4.3 Interface model

4.3.1 Simulation of fiber push-out

Reverse determination of the fiber-matrix interface properties was performed by FE simulation of the fiber push-out experiments in *Abaqus Explicit*. The parameters describing the mechanical behavior of the interface were manually adjusted in a way that the force-displacement curves of the push-out experiments could be reproduced (Section 5.4). The obtained description of the interface was then implemented into the RVE models to investigate their effect on the global deformation behavior of LFT. The fiber push-out scenario was modeled using the same coarse representation of the fibers by a single hexahedral element (*C3D8R*) as applied to model the LFT structures. Cohesive zone elements (*COH3D8*) were added between the fiber and the matrix. They are assigned to material properties in the form of a traction-separation law (Section 4.3.2) representing the debonding behavior. To simulate the effects of post-debonding friction, a contact formulation (Section 4.3.3) was optionally activated which captures the surface interactions after deletion of the cohesive zone elements, representing interface failure. Fig. 22 shows the model featuring the same thickness (85 μm) and support diameter (60 μm) as the experiments (Section 3.4). A cylindrical section of the push-out specimen was modeled with the inner circle representing the whole diameter of the perforated plate. The nodes outside the whole diameter are constrained in their DOF parallel to the push-out direction (support area in Fig. 22). The nodes of the fiber elements were displaced in fiber direction to model the fiber push-out. The fiber and matrix elements were given the same elastic properties as used for the LFT simulations ($E_m = 1250 \text{ MPa}$, $\nu_m = 0.35$, $E_f = 72000 \text{ MPa}$, $\nu_f = 0.22$).

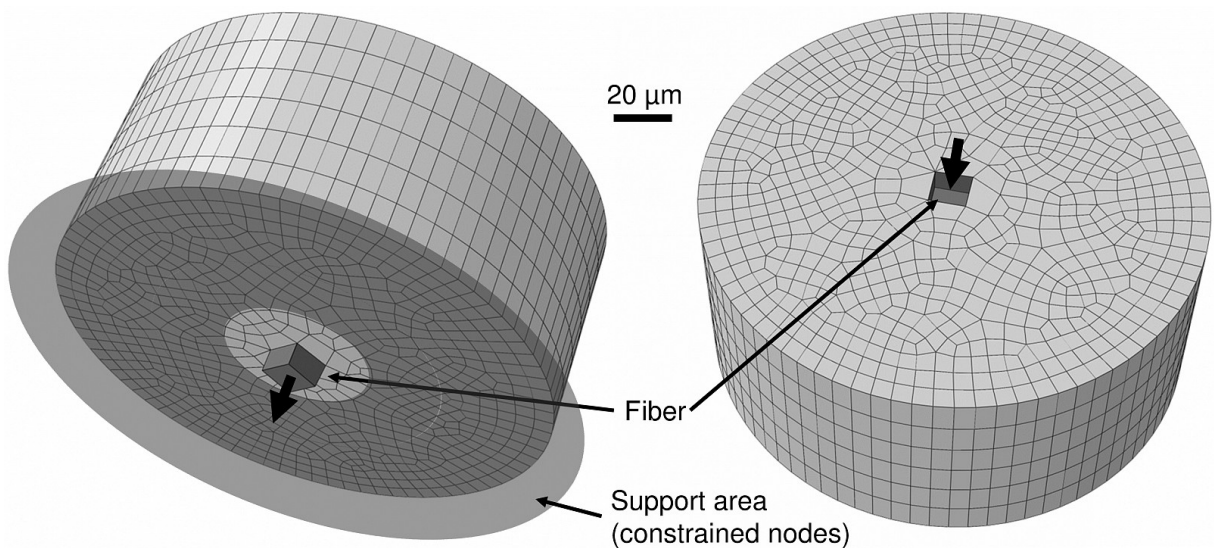


Figure 22: Simulation of the single fiber push-out tests for the reverse determination of the interface properties (left: bottom / right: top view). The black arrow shows the push-out direction.

4.3.2 Traction-separation law

Due to the thickness of the interface region being infinitesimally small and its stiffness being infinitesimally high, stress singularities would occur if the interface was modeled with continuum elements. A common method to overcome this problem is the use of a simplified model, which describes the effective mechanical behavior of the interface in terms of traction and separation between the two surfaces of the interface. The model is based on the work of Dugdale [Dug60] and Barenblatt [Bar62]. During the elastic period of separation of the two cohesive surfaces, the traction stress increases linearly until a critical value, representing the threshold of damage initiation, is reached. With ongoing separation, the traction stress is decreased continuously until complete separation is reached and finally the cohesive element is deleted from the mesh, breaking the nodal connectivity between the adjacent parts of the finite element model. The traction-separation law has no physical background and is therefore in general not transferable to other material systems without re-calibration. Furthermore, the initial stiffness K represents a numerical aid rather than a realistic material property.

The traction \mathbf{t} and separation $\boldsymbol{\delta}$ vector both have three components, in which the n-component represents the normal direction of the interface and the s- and t-components represent both shear directions. No coupling between the normal and the shear components was considered. Thus, the traction-separation law takes the form of

$$\begin{pmatrix} t_n \\ t_s \\ t_t \end{pmatrix} = \begin{bmatrix} K_n & & \\ & K_s & \\ & & K_t \end{bmatrix} \begin{pmatrix} \varepsilon_n \\ \varepsilon_s \\ \varepsilon_t \end{pmatrix}. \quad (77)$$

where $\boldsymbol{\varepsilon} = \boldsymbol{\delta}/h$ is the nominal strain defined by the quotient of separation and the nominal thickness of the interface h . The stiffness components of the elasticity matrix \mathbf{K} were set to an equal value since they do not have any physical meaning: $K_n = K_s = K_t = K$.

A quadratic nominal strain criterion defines the threshold of damage initiation:

$$\left(\frac{\langle \varepsilon_n \rangle}{\varepsilon_n^0} \right)^2 + \left(\frac{\varepsilon_s}{\varepsilon_s^0} \right)^2 + \left(\frac{\varepsilon_t}{\varepsilon_t^0} \right)^2 = 1, \quad (78)$$

where the superscript 0 denotes the respective threshold for each strain component and the $\langle \cdot \rangle$ - operator effects that a compressive normal strain does not initiate any damage (a compressive strain counteracts the separation of the interface, $\langle \varepsilon_n \rangle = 0$ if $\varepsilon_n < 0$). Because of the lack of mode-dependent experimental data, the threshold was set to an equal value for all strain components: $\varepsilon_n^0 = \varepsilon_s^0 = \varepsilon_t^0 = \varepsilon^0$.

The damage evolution is described by the scalar damage variable D , which has the initial value of 0 and increases monotonically with ongoing damage until the value of 1 is reached, representing a completely damaged interface. The traction stress of the damaged interface $\bar{t}_{n,s,t}$ depends on the damage variable in the following way:

$$\bar{t}_{n,s,t} = (1 - D)t_{n,s,t} , \quad (79)$$

where $t_{n,s,t}$ represents the traction component of the undamaged interface.

The evolution of the damage variable D was specified to increase linearly until a maximum effective displacement $\bar{\delta}$ is reached:

$$\bar{\delta} = \sqrt{\langle \delta_n \rangle^2 + \delta_s^2 + \delta_t^2} . \quad (80)$$

The above equations are implemented in *Abaqus Explicit*. The cohesive zone elements of the fiber push-out model as well as the multidirectional RVEs accounting for interface damage were assigned to section properties referring to the traction-separation law.

4.3.3 Contact formulation

To simulate the effects of post-debonding friction during fiber push- or pullout, mechanical contact was activated for the simulations considering friction. Invoking the contact prevents penetration between the fibers and the matrix after the cohesive elements are deleted from the mesh and enables the incorporation of a friction coefficient during the relative motion of the contact surfaces.

The *general contact* of *Abaqus Explicit* was activated for all simulations considering post-debonding friction. The contact algorithm tracks all exterior element surfaces, nodes and edges. Thus, node-into-surface and edge-into-edge penetrations are prevented by imposing a normal reaction force. Newly exposed surfaces (after elements are deleted from the mesh) are automatically detected and included in the list of active contact pairs. To consider edge-into-edge penetrations, the *feature edge* parameter was applied. A nominal thickness equal to the geometric value of the cohesive elements was considered by a *global thickness* property assignment to compensate the clearance between fibers and matrix which develops after deletion of the cohesive elements. The tangential behavior of the contact pair was defined under specification of the coefficient of friction, whereas the normal behavior was specified with the *hard contact* parameter.

4.4 Unidirectional fiber arrangement

In order to study the effects of a varying fiber length in detail, a unidirectional fiber model consisting of four fibers with square packing arrangement was investigated. A nominal fiber volume fraction of 13.22 % (corresponding to PPGF30) was chosen for all UD models. To ensure compatibility to the multidirectional RVEs and for the sake of reasonable computation times, the coarse mesh variant with a single hexahedral element (*C3D8R*) over the (square) fiber cross section was chosen for most of the models. To study the mesh dependency, a model with round fibers and a multitude of elements over the fiber cross section (*C3D8R*) was created for the smallest investigated variant with 1 mm length of the periodic RVE. A clearance of 40 μm representing approx. two fiber diameters was chosen between the fiber ends of all variants with finite fiber length. The nominal fiber volume fraction of 13.22 % is referred to the variant of infinite fiber length where the model contains no fiber ends. The same mesh is used for the variants with finite fiber length - the elements between the fiber ends are then assigned to the matrix properties. This causes a deviation from the nominal fiber volume fraction, which was found to be negligible in particular for the variants with a fiber length above 1 mm. Fig. 23 shows both mesh variants of the 1 mm long RVE, whereas the respective fiber structures are depicted in Fig. 24.

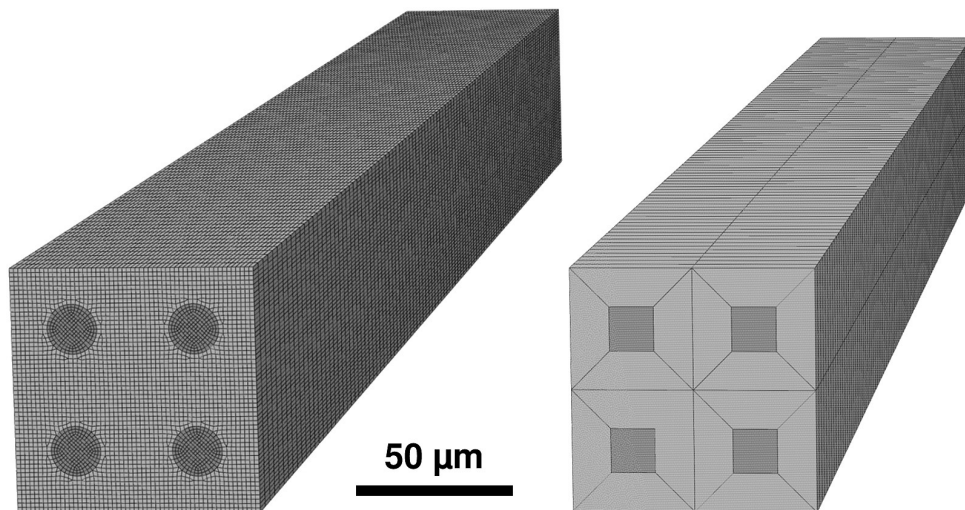


Figure 23: Periodic UD fiber arrangement (1 mm RVE length, 13.22 % vol. frac.): Fine mesh with round fibers (left) compared to coarse mesh with square fibers (right).

Periodic boundary conditions were applied to all investigated variants of the UD fiber arrangement. The constrained regions are marked in Fig. 25 showing the deformed RVE whose shape results from the discontinuous fibers and strain concentrations at the fiber ends. Each pair of corresponding nodes (n_a/n_b) of each of the six RVE surfaces is constrained by the following boundary conditions (Eq. 81 - 86).

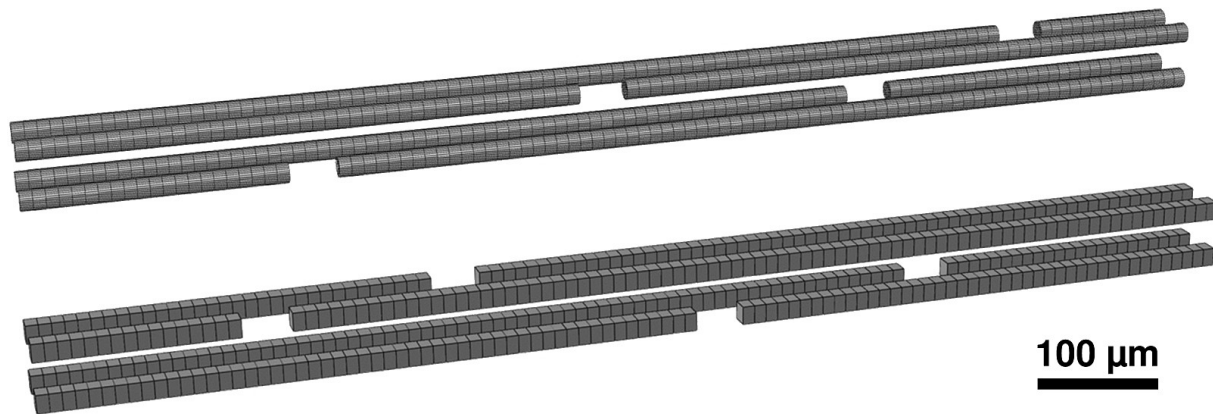


Figure 24: Round fiber structure (top) compared to the square variant (bottom).

- Surfaces *left* and *right* / *top* and *bottom*

$$u_1(n_a) - u_1(n_b) = 0, \quad (81)$$

$$u_2(n_a) - u_2(n_b) = 0, \quad (82)$$

$$u_3(n_a) - u_3(n_b) = 0, \quad (83)$$

- Surfaces *start* and *end*

$$u_1(n_a) - u_1(n_b) = 0, \quad (84)$$

$$u_2(n_a) - u_2(n_b) = 0, \quad (85)$$

$$u_3(n_a) - u_3(n_b) = d_3, \quad (86)$$

with d_3 being the displacement of a dummy node on which the load in x_3 -direction was applied and which was used for calculation of the effective strain.

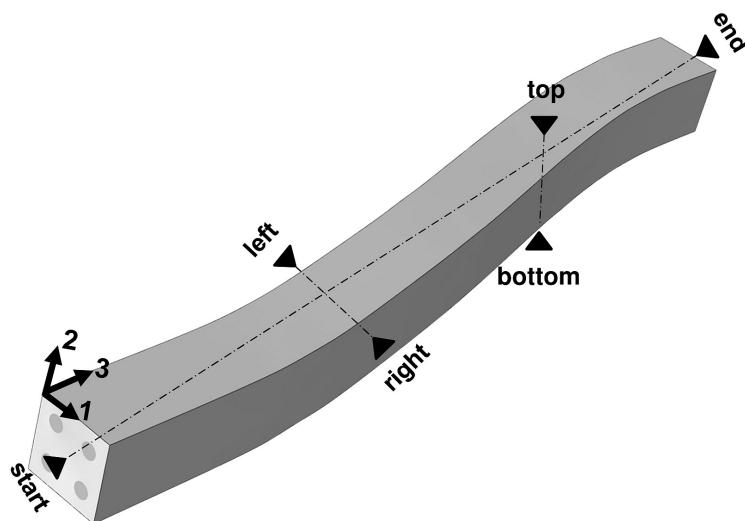


Figure 25: Periodic boundary conditions illustrated on deformed RVE.

4.5 Multidirectional LFT structure

The numerical LFT modeling procedure as described in the following, its validation with respect to the elastic properties and preliminary studies of creep and damage scenarios were previously published by the author [Fli15,Fli14,Fli13a,Fli13b,Fli12]. The procedure is divided into three steps: First, a fiber generator tool creates a stack of planar fibers with given length and orientation distributions. This stack is then compressed until the desired fiber volume fraction is reached. In the last step, the remaining gaps are filled with elements representing the matrix to complete the RVE. The procedure is illustrated in Fig. 26 for an exemplary RVE with 5 mm edge length.

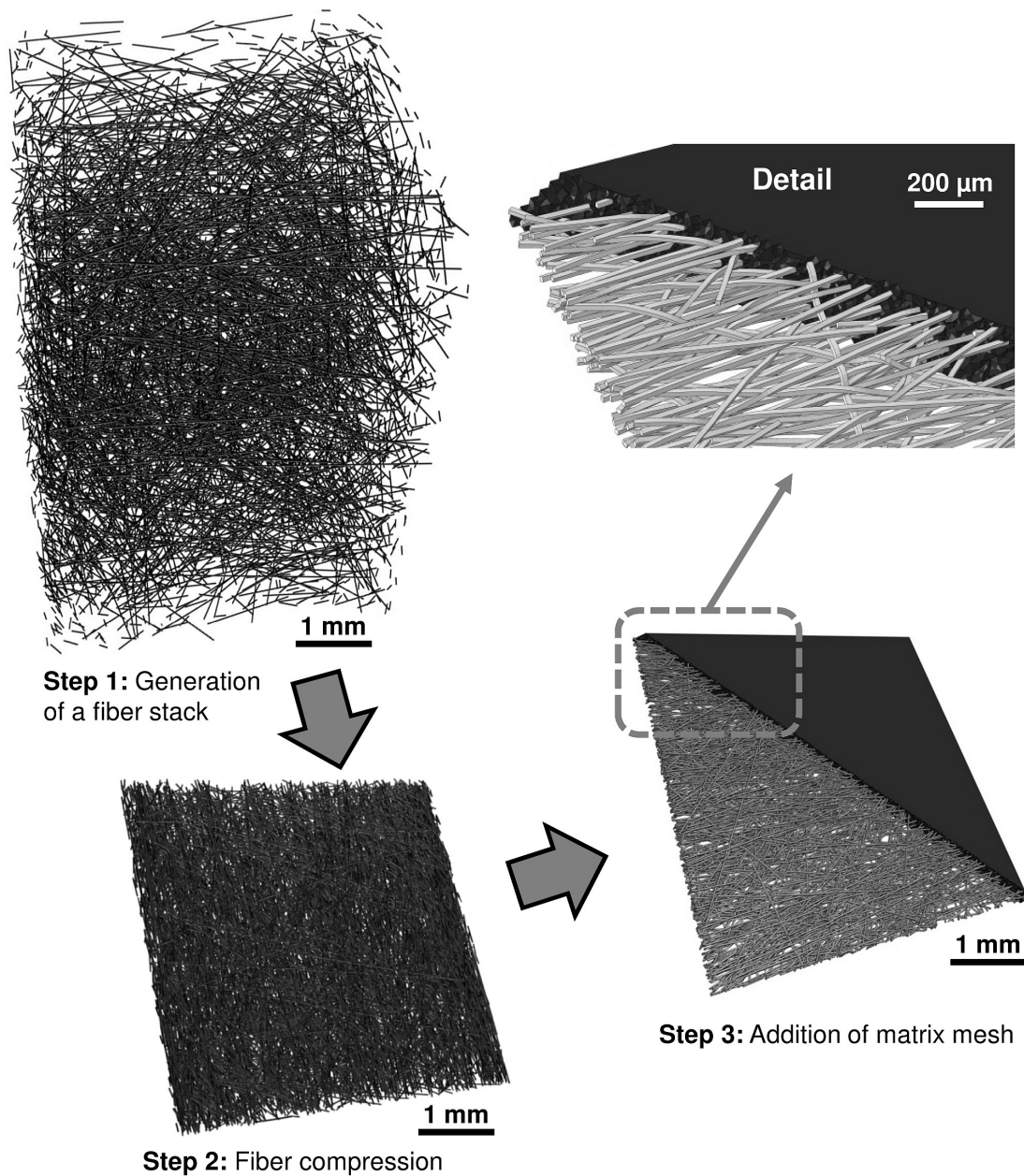


Figure 26: Three step procedure of the RVE generation: 1. Generation of a fiber stack, 2. Fiber compression and 3. Addition of the matrix mesh.

4.5.1 Generation of a fiber stack

The structure of the fiber generator tool is shown in Fig. 27 as a flowchart. The program generates a stack of layers in which each layer contains multiple planar, straight fibers according to the statistics provided by the user. These are the desired fiber orientation distribution $L(\alpha_c)_{\text{des}}$, the desired fiber length distribution $L(l_c)_{\text{des}}$, the desired total fiber length L_{tot} , the RVE dimensions X , Y , the limit of fiber length per layer L^* as well as several other variables which control the process of the algorithm. First the length distribution $L(l_c)_{\text{des}}$ given in terms of desired cumulative fiber length L for each length class l_c is scanned for its maximum value of l_c in which the desired value of L is still larger than the length sum of the currently generated fibers $\Sigma L(l_c)$. If necessary, the value of l_c is decreased by the length interval Δl until a length class is found which is not fully occupied. In the next step, a random in-plane fiber angle α_f is chosen and the orientation distribution $L(\alpha_c)_{\text{des}}$ is checked whether the desired cumulative length L for each class of angle α_c is still larger than the current value of fiber length $\Sigma L(\alpha_c)$ plus the current fiber length l_f . If a value of α_f is found, but the fiber does not fit inside the RVE dimensions X and Y , a finite number of attempts (limited by the re-orientation limit o) to re-orientate the fiber by choosing an alternate value of α_f is carried out. The practical meaning of this procedure is to prevent any cropping of longer fibers and to preserve their length by aligning them preferably in the direction of the largest RVE dimension (this issue is discussed in Section 6.1.4). In the next step, a random value for the fiber layer coordinate z is chosen. If the cumulative length per layer $\Sigma L(z)$ plus l_f is larger than the length per layer limit L^* , another layer is randomly chosen. L^* is given by the user as a parameter to control the packing density for each layer. The number of layers is calculated by dividing the total fiber length L_{tot} by L^* . The planar fiber position, defined by the fiber start and end points x_s , y_s is chosen randomly within the RVE borders and the end points x_e , y_e are calculated. The fiber location is then checked for intersection with any other fiber of the current layer, and, if necessary, the fiber is translated to another location. If such a location cannot be found in a number of attempts which is smaller than the re-position limit p , another random value for z will be chosen. If all checks were successfully performed, the fiber is generated. If L^* is set to a high value, too many fibers are packed into too few layers and too many attempts are then needed to find a fiber position where no collision with any other fiber in the specific layer occurs. Consequently the calculation time for the fiber generation procedure raises drastically. If the value for L^* is set too low, e.g. resulting in only a single fiber per layer, the fiber stack increases in height which increases the calculation time for the following fiber compression procedure. Fiber placement is repeated until the total generated fiber length reaches the desired amount L_{tot} . If the desired fiber length is generated, the program ends with the automatic generation of an *Abaqus* input file for the following step of fiber compression.

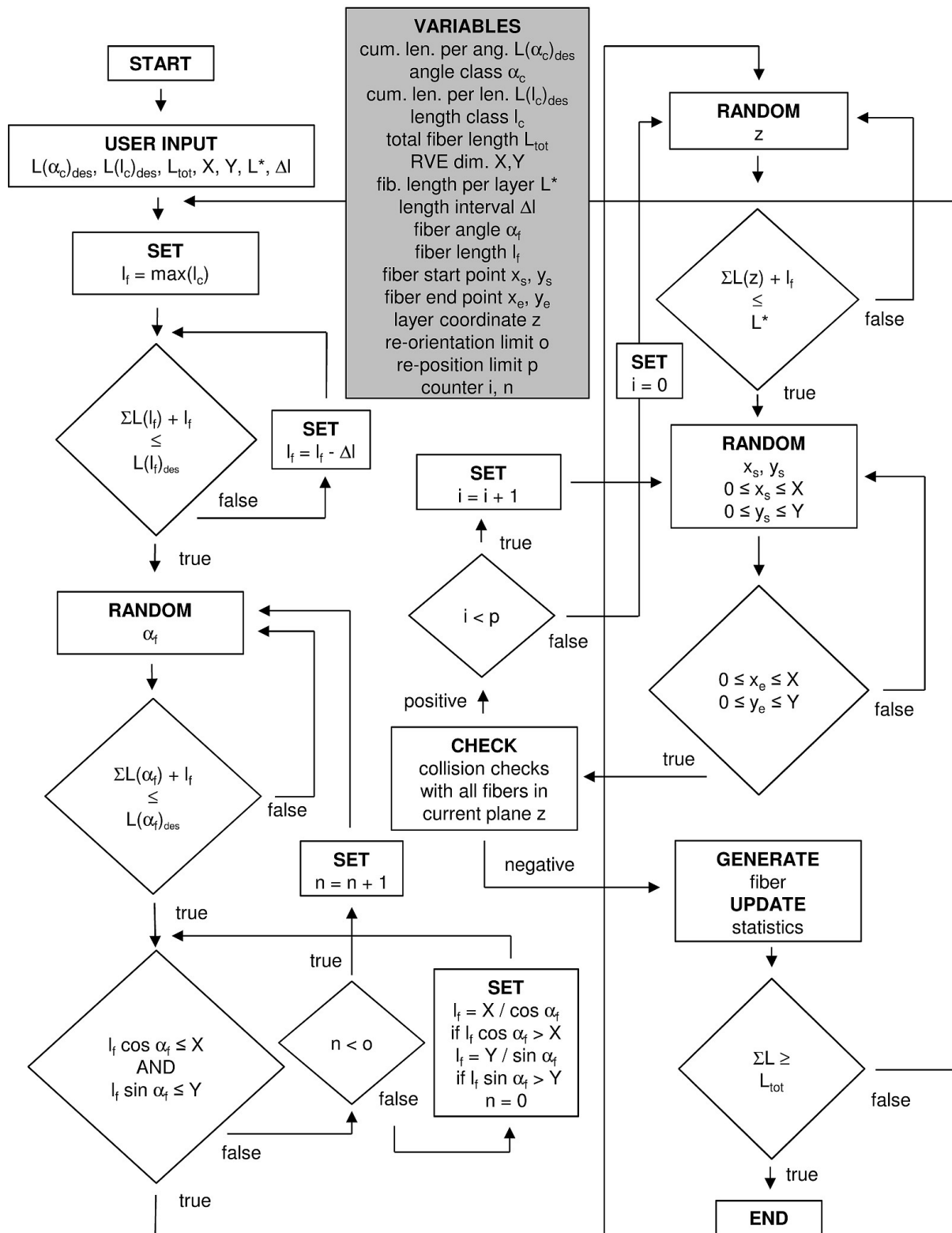


Figure 27: Structure of the fiber generator tool to create a stack of planar, straight fibers according to the given fiber orientation and length distribution.

4.5.2 Fiber compression

The fiber stack is compressed by an explicit FE simulation until the desired value of the fiber volume fraction is reached. Fully integrated, hexahedral elements (*C3D8*) are chosen to model the fiber compression scenario (which turned out to be beneficial to avoid penetration between the contact surfaces of the elements), whereas the element type is changed to reduced integration (*C3D8R*) in the following step of structural analysis (which is essential to avoid shear locking in fiber bending modes). The procedure as well as the coordinate system which defines the mean fiber orientation as the flow direction (x_1), the transverse direction (x_2) and the layer stacking or pressing direction (x_3) is illustrated in Fig. 28. The fiber stack is positioned between two rigid shell elements whose distance is continuously decreased until the desired fiber volume fraction is reached.

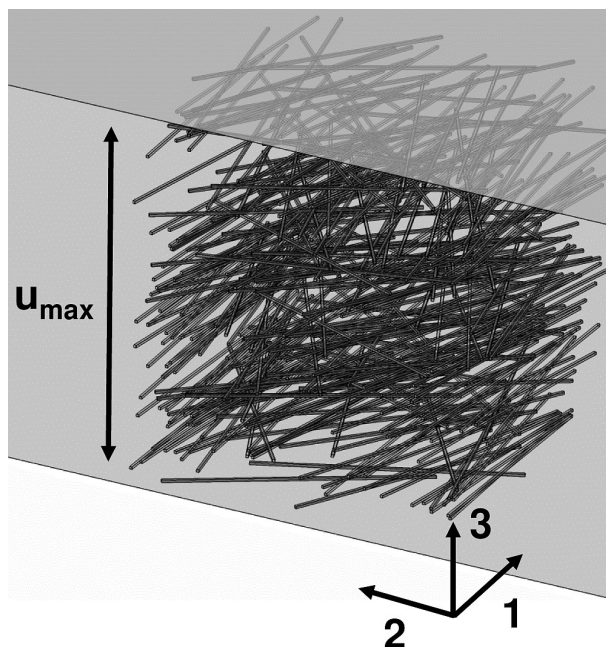


Figure 28: Illustration of the fiber compression scenario showing the maximum displacement of the pressing plates u_{\max} , the mean fiber orientation or flow direction x_1 , the transverse direction x_2 and the pressing direction x_3 .

The typical values of fiber volume fraction of LFT materials in applications for structural parts are in the range of 5 to 25 %. Due to their non-unidirectional alignment, their high aspect ratio and fiber volume fraction the fibers cannot remain straight to realize the required dense packing. This was investigated in detail by others [Eva86, Tol98] for randomly oriented fiber structures. In order to retain the fiber orientation distribution as well as possible, the pressing procedure is divided into two phases with different boundary conditions as specified in Table 3.

Phase	BC regions	BCs	Plate displacement
A	All nodes of each fiber	$u_1, u_2 = 0$ $u_3 = \text{free}$	0 to 0.9 u_{\max}
B	Only nodes of first and last fiber element	$v_1 > 0$ $u_2 = 0$ $u_1, u_3 = \text{free}$	0.9 u_{\max} to u_{\max}

Table 3: Boundary conditions for the two phases of the fiber compression procedure.

In *phase A* of the compression procedure, active for 90 % of the total displacement of the rigid plates u_{\max} , all nodes of each fiber are constrained in their planar displacements u_1 and u_2 , whereas u_3 was left unconstrained. This ensures that the orientation distribution in the 12-plane remains unchanged and fiber waviness develops only in thickness direction. For the structures presented here the achievable fiber volume fraction at the end of *phase A* is approx. 5 to 7.5 % before the simulation aborts due to excessive element distortion. To generate a higher volume fraction, the fiber constraints must then be relaxed.

The following scenario for *phase B* turned out to be suitable for reaching higher volume fractions up to approx. 25 % (depending on the orientation distribution and aspect ratio) with only minor distortion to the planar orientation distribution. Only the nodes of the first and last element of each fiber are constrained by boundary conditions, which set their displacement in x_2 -direction to zero and apply a non-zero velocity in x_1 -direction. A certain value of velocity parallel to the mean fiber direction as well as a non-zero friction coefficient of the contact formulation was beneficial to keep fiber waviness at a minimum.

Different scenarios were investigated with the result that the two phase procedure is indeed needed in order to allow just the mandatory intensity of fiber waviness as a consequence of the dense packing, but to avoid major distortion of the orientation distribution. In detail, the boundary conditions must not be relaxed until contact between any fiber and its neighbors is ensured because otherwise fiber waviness increases excessively. To keep a minimum distance between the fibers, the general contact formulation in *Abaqus Explicit* was given a non-zero value for the *global thickness* parameter and the *feature edge* parameter was enabled to avoid interpenetration of the fibers. Table 4 shows the parameters of the contact formulation as well as additional parameters of the explicit fiber compression simulation.

Parameter	Value	Unit
Element edge length	0.0151	mm
Mass density	$2 \cdot 10^{-9}$	t/mm ³
Elastic modulus	5000	MPa
Poisson's ratio	0.22	
Coefficient of friction	0.3	
Contact measure of overclosure	0.001	mm
Contact stiffness scale factor	100	
Global surface thickness assignment	0.01	mm
Global surface feature assignments	PERIMETER	
Step time	0.001	s
Automatic mass scaling target increment size	10^{-7}	s

Table 4: Additional parameters of the fiber compression procedure.

4.5.3 Meshing and boundary conditions

In the last step of the RVE generation procedure, the deformed fiber mesh is imported into the FE preprocessing software *HyperMesh* (Version 11.0) [Hyp14] to fill the remaining gaps between the fibers with a tetrahedral mesh representing the matrix. First, the fiber mesh is positioned into a cuboid with the desired dimensions of the RVE. The faces of the three dimensional fiber elements (*C3D8R*) act as seeds for the tetrahedral matrix elements (*C3D4*) in order to let the matrix mesh grow from each fiber surface. The desired element size of the matrix mesh can either be set to a constant value or the element size is chosen automatically by the meshing algorithm resulting in very small elements in regions near or between several fibers and larger elements toward the RVE borders, where the fiber density decreases. For the RVEs analyzed in this work, the latter option was able to keep the total element count below 10 million. Details of the resulting mesh for RVEs of all three investigated fiber volume fractions are shown in Fig. 29 with a part of the matrix mesh removed. The corresponding fiber structure (1/4 of the total RVE) is depicted in Fig. 30. The fiber meshes of two RVE variants with different fiber volume fraction are compared to the respective CT scans in Fig. 31.

Due to the complexity of the structure and the fact that the fibers need to be enclosed by the RVE boundary surfaces in order to create the matrix mesh, it is currently not possible to consider periodic BCs for the RVE simulations. Thus, displacement BCs are applied. The displacement value for each node of the constrained region u_1, \dots, u_n is set to zero for one side and to an equal non-zero value for the opposite side. Since the surfaces where the BCs are applied are forced to remain planar, stress and strain concentrations occur in the RVE boundary region which would distort the result if the boundary displacements would directly be used to calculate the averaged properties. Therefore, two node sets outside these stress concentrations are defined to determine the averaged effective properties of the RVE, as it can be seen in Fig. 32.

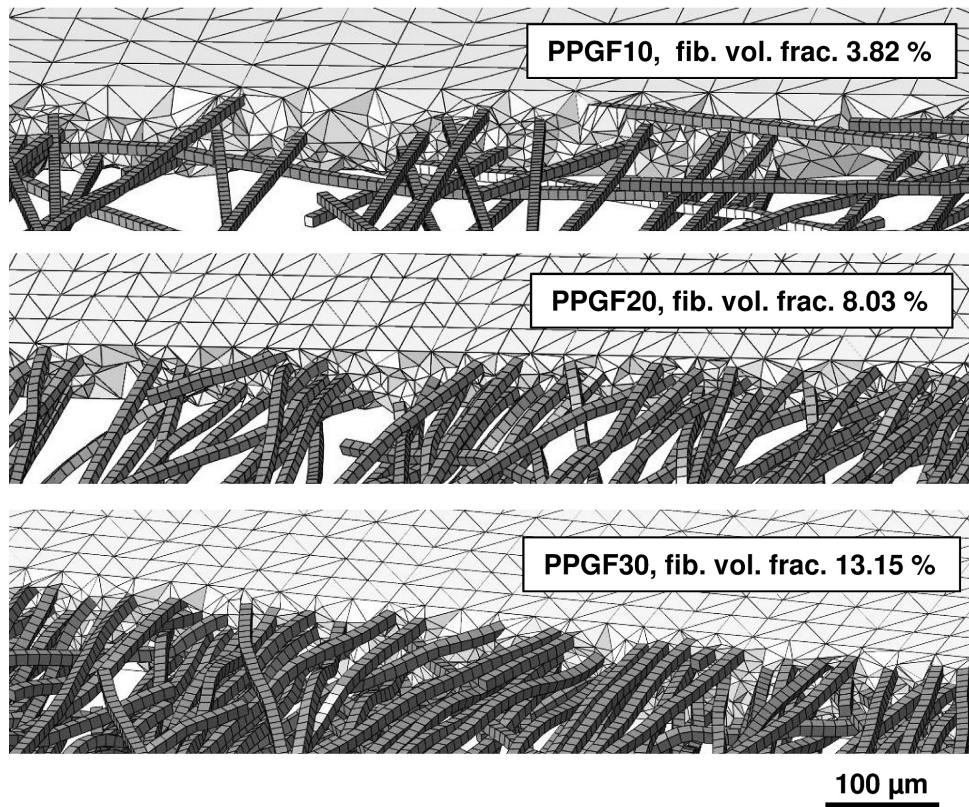


Figure 29: Mesh details of typical RVEs with varying fiber volume fractions. Some of the matrix elements were removed for illustration purposes.

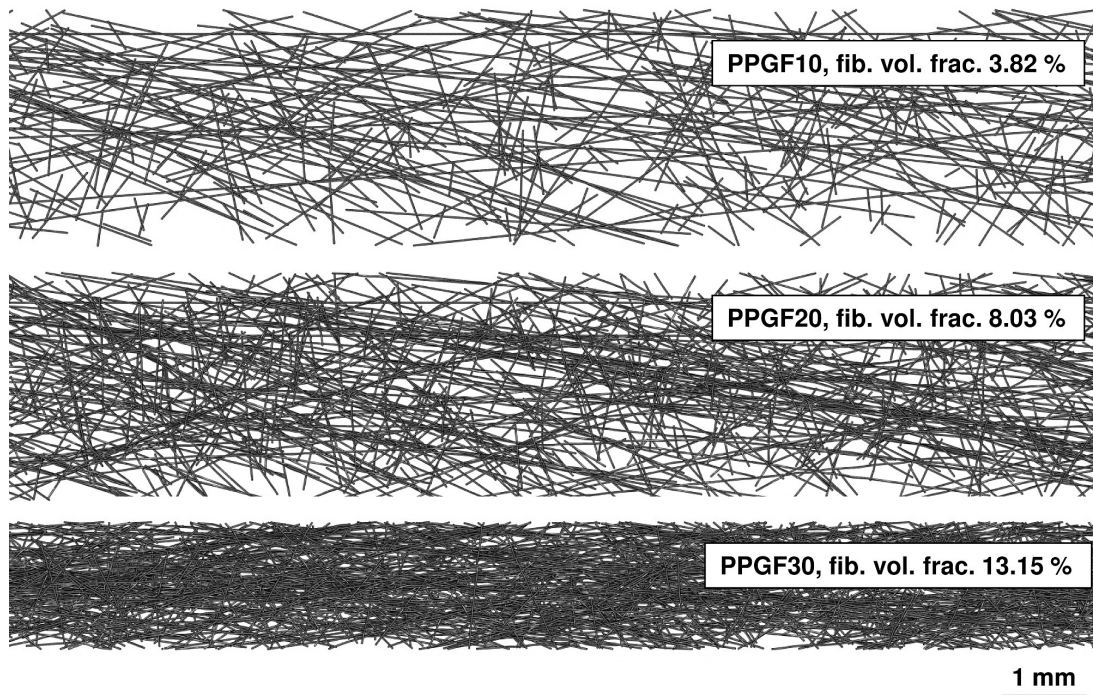


Figure 30: Details of typical fiber structures with varying fiber volume fraction. One quarter of the RVE length is depicted for each variant. All matrix elements were removed.

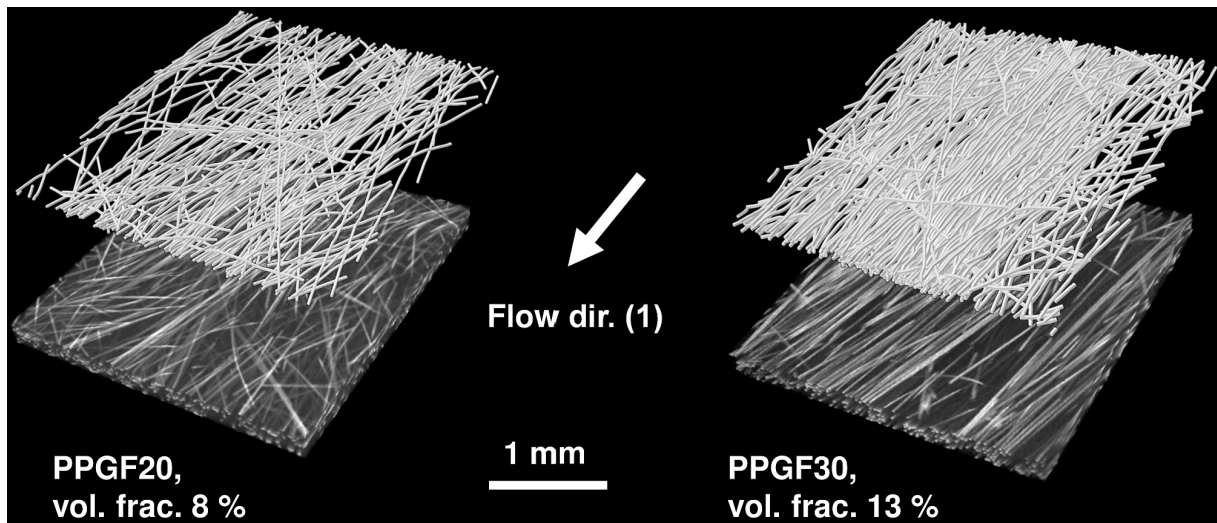


Figure 31: Comparison between fiber structures and CT scans for two values of fiber volume fraction.

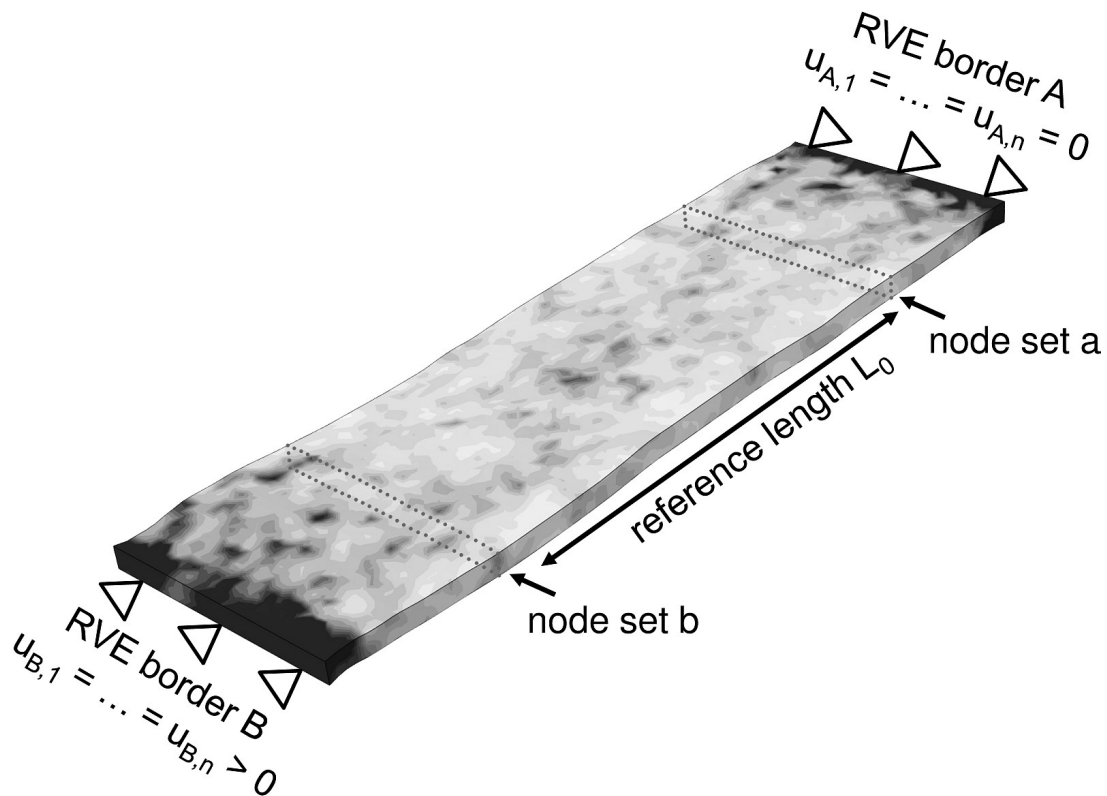


Figure 32: Applied BCs to determine the effective properties (RVE LD6 with dimensions of $5 \times 1.5 \text{ mm}^2$ and an exemplary reference length $L_0 = 3 \text{ mm}$ is shown). The displacement values for all nodes of each RVE border u_1, \dots, u_n are set to zero for one side (A) and to a non-zero value for the opposite side (B). The node sets outside the stress concentrations (a,b) are used to determine the averaged properties. The color scale visualizes the equivalent stress and strain, respectively (the darker the color, the higher its magnitude).

4.5.4 Elasticity

To determine the elastic stiffness, displacement boundary conditions (also known as Dirichlet BCs) were applied at the RVE borders as detailed in Fig. 32. The resulting displacement values for each node of the node sets a and b were then averaged: $\bar{u}_a = \text{avg}(u_{a,1}, \dots, u_{a,n})$ resp. $\bar{u}_b = \text{avg}(u_{b,1}, \dots, u_{b,n})$ with $\text{avg}()$ being the arithmetic mean and the engineering strain was calculated by $\varepsilon = (\bar{u}_b - \bar{u}_a)/L_0$ with the reference length L_0 being the initial distance between the node sets a and b. The elastic modulus was finally determined according to Hooke's law by calculation of the quotient of engineering stress and strain: $E = \sigma/\varepsilon$. The stress σ was obtained by dividing the sum of nodal reaction force $F_B = \Sigma F_{B,1}, \dots, F_{B,n}$ at the RVE border B by the initial RVE cross section area.

To obtain the stiffness values presented in Section 5.6.2 - 5.6.4, the RVEs were computed by implicit FE simulations with *Abaqus Standard* (Version 6.11) [Aba14]. Here, the static equilibrium equations derived from the principle of virtual work ensure equilibrium between outer and inner forces of the model. The equations need to be solved at the structural or geometrical level in order to compute values of the model's inner force variables which can then be translated into values of strain and stress for each element by application of the constitutive law at the material level. Effects of nonlinearity at the structural level are addressed by incremental application of the boundary conditions (e.g. load or displacement). The deviation of the linearized approximation to the exact solution is controlled at each increment of the simulation step. Therefore, the residual vector \mathbf{r} in the form of $\mathbf{r} = \mathbf{K}\mathbf{u} - \mathbf{F}$ (with \mathbf{F} being the force vector, \mathbf{K} being the stiffness matrix and \mathbf{u} being the displacement vector) is formed and minimized by an iterative Newton procedure until a specific level of tolerance is reached (e.g. the initial prediction of the displacement vector \mathbf{u} was corrected in a way that the residual \mathbf{r} is sufficiently small). Then, equilibrium between inner and outer forces is obtained and the increment has converged. The global solution process can now continue with the following increment. For each iteration of the Newton procedure, activated at each increment of the simulation step, the equation system ($\mathbf{r} = \mathbf{K}\mathbf{u} - \mathbf{F}$) must be solved for \mathbf{u} . Therefore, the stiffness matrix \mathbf{K} must be inverted, which requires enormous computational memory. The solution is either computed directly by a so-called *direct sparse* equation solver (to overcome the inefficiency of a classical Gaussian method for sparsely occupied matrices) or is approximated by a second iterative procedure in the form of a Krylov subspace method, the so-called *iterative solver*. An approximated solution is then searched in a subspace of the original set of equations with a much smaller number of mathematical operations and memory than necessary for the direct sparse solver to compute the complete equation system. If convergence cannot be reached using the first subspace, the subspace is sequentially en-

larged with each iteration until convergence is reached (an approximated solution could be found with the corresponding residual being sufficiently small). Krylov's subspace method is in particular efficient for the analysis of blocky structures like the investigated RVEs, where each element can interact with each other via an existing connection over a path of remaining elements (high degree of mesh connectivity). This causes the stiffness matrix \mathbf{K} to be occupied to a much higher degree than for most cases of analysis of rather shell-like components with a sparse stiffness matrix [Aba11].

The *iterative solver* with the default settings for convergence criteria (relative convergence tolerance of 10^{-3} and maximum number of iterations of 300) was applied to all implicit simulations of elasticity presented in Section 5.6.2 - 5.6.4. Small deformation theory was used and due to the linear elastic constitutive law of fibers and matrix (the values are specified in the results section), only one increment was needed for the simulation step.

Due to the direct relation between the size of the model and occupied computational memory for all implicit simulations (here the stiffness matrix \mathbf{K} must be inverted, which is very costly), element studies with quadratic elements (which are much more computationally expensive than linear elements because of more DOFs) could not be carried out on the 50 mm long RVEs. Thus, the results presented in Section 5.6.5 were generated by application of *Abaqus Explicit* (Version 6.11). In explicit FEM, the equation of motion $\mathbf{F} = \mathbf{M}\ddot{\mathbf{u}} + \mathbf{C}\dot{\mathbf{u}} + \mathbf{K}\mathbf{u}$ (where \mathbf{F} is the force vector, \mathbf{M} the mass matrix defining the mass assigned to each integration point corresponding to the material's density and $\ddot{\mathbf{u}}$ the acceleration vector) is solved for $\ddot{\mathbf{u}}$. Thus, the mass matrix \mathbf{M} must be inverted instead of \mathbf{K} (implicit FEM), which is much less expensive (the mass matrix mostly features only diagonal components and therefore, the inverse is trivial). Neither the equilibrium of the system is ensured, nor the convergence is controlled by evaluation of a residual. Thus, the increments of the simulation step must be chosen several orders of magnitudes smaller than for the implicit solution procedure with the benefit that computational cost is influenced by the model size to a much lower degree (no expensive inversion of the stiffness matrix) and therefore, the analysis of the full size 50 mm RVEs with quadratic elements is technically feasible. However, the results have to be interpreted with care as the solution might be affected by the effects of inertia (if the total amount of kinetic energy of the model is not negligible compared to its strain energy) as well as round-off errors, if a huge number of increments respectively floating point operations is needed to compute models with a small characteristic element length resulting in a small stable increment size. The latter problem was addressed by application of the double-precision executable of *Abaqus Explicit* whereas energetic issues are further analyzed in Section 5.6.5 and the discussion.

4.5.5 Viscoelasticity

Creep simulations of a total time period of $6 \cdot 10^5$ s were carried out at the respective RVEs under application of load controlled boundary conditions. Therefore, the nodes of the RVE border B (Fig. 32) were coupled to a reference dummy node (kinematic coupling in all DOFs) and the load (equal to the product of RVE cross section and desired stress level) was applied to the dummy node over a ramp of 1 s at the beginning of the simulation. For the remaining part of the creep simulation, the load was kept constant. Determination of effective strain was performed in the same form as described in Section 4.5.4 by averaging the displacement values of both node sets a and b (Fig. 32) which were recorded as history output at every increment.

Abaqus Standard (Version 6.11) with the *iterative solver* option and small deformation theory was applied to generate the results presented in Section 5.6.6 - 5.6.10. The size of the time increments was chosen automatically by *Abaqus* based on several criteria (e.g. numbers of Newton iterations made to reach convergence for the previous increment), which were kept to the default values (e.g. number of iterations resulting in a cutback (10) or increase of increment size (4)). An initial increment size of 0.1 s and a maximum increment size of 10^4 s was always chosen, if not specified otherwise. No cutback in increment size could be observed (the increment size chosen by *Abaqus* was increasing monotonically until the upper limit of 10^4 s was reached and 9 Newton iterations were necessary to obtain convergence for the largest increments). The viscoelastic model (Section 4.1 and 5.2) was assigned to the matrix elements, whereas the fibers were modeled as linear elastic (same values as specified in Section 5.6.2). A perfect interface between fibers and matrix was assumed.

4.5.6 Plasticity and damage

Virtual tensile tests including the effects of nonlinear deformation due to matrix plasticity and interface damage were carried out until the onset of fiber damage, which is assumed to represent the composite's strength. Effects of matrix damage could not be investigated because of the varying element size of the tetrahedral matrix elements which precludes modeling of material failure due to damage localization within the smallest elements. The RVE border B (Fig. 32) was coupled to a dummy node in all DOFs where a constant displacement rate corresponding to a nominal strain rate of $10 \cdot 1/s$ was applied. The reaction force of the dummy node was recorded in the form of history output at 200 equally spaced intervals over the step time of 0.01 s and divided by the nominal RVE cross section area to obtain the values of engineering stress. Engineering strain was determined in the same way as described in Section 4.5.4 based on averaged displacement values of both node sets a and b (Fig. 32).

Abaqus Explicit (Version 6.11) was applied to generate the results presented in Section 5.6.11 - 5.6.15. Finite deformation theory was applied. A semi-automatic mass scaling with a target increment size of $5 \cdot 10^{-9}$ s was activated, if not specified otherwise. To ensure the validity of the results, the values of kinetic and internal energy for the entire model were analyzed and the kinetic energy was always found to be sufficiently small compared to the internal energy. To avoid localization of plastic deformation and interface / fiber damage at the constrained RVE borders, where stress concentrations occur, the regions of the RVE outside the distance between the node sets (Fig. 32) were assigned to linear elastic material properties as illustrated in Fig. 33. The calibration of the matrix plasticity model, the cohesive zone model and the contact formulation representing post-debonding friction between fibers and matrix is described in Section 5.3 and 5.4.

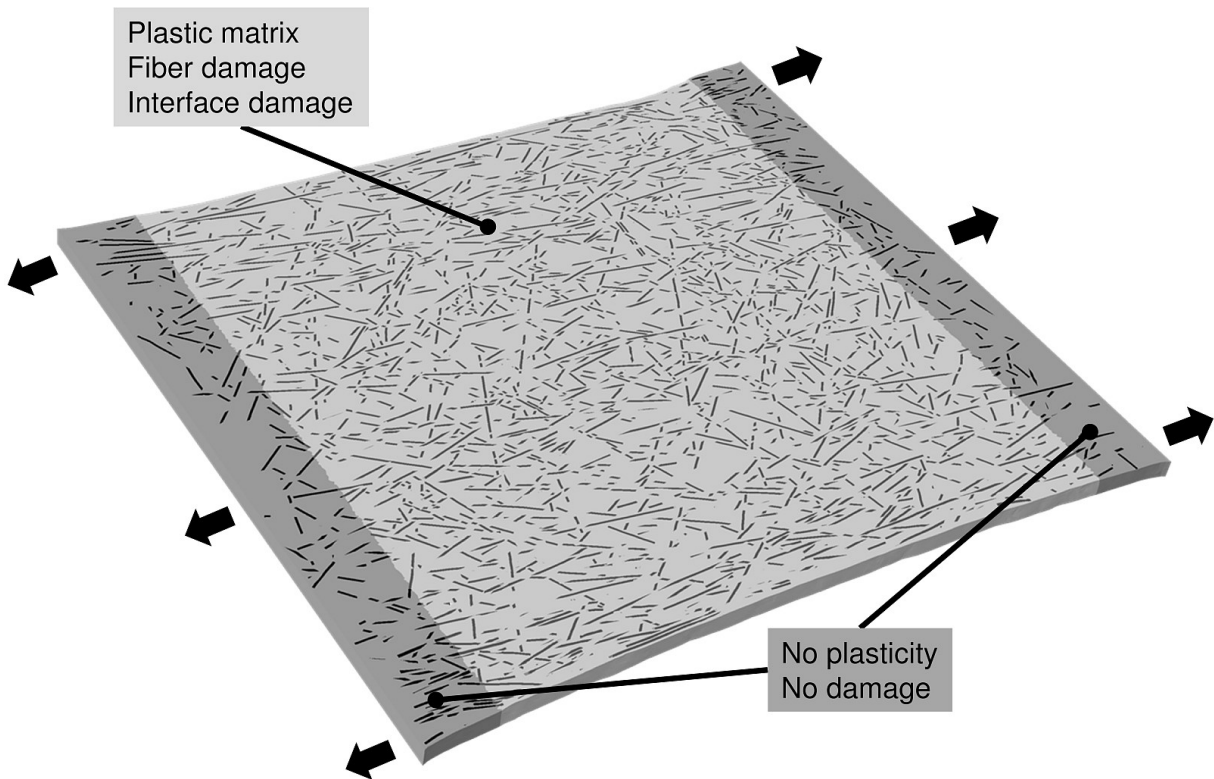


Figure 33: Assignment of material properties within an exemplary LFT structure (a cut at half wall thickness of the RVE LD7 with lateral dimensions of $5 \times 5 \text{ mm}^2$ is shown). The elastic RVE boundary ensures that no damage localization occurs at the RVE borders where the displacement BCs are applied and therefore stress concentrations occur (Fig. 32).

4.6 Analytical homogenization

To predict the effective properties of LFT, its complex nonwoven structure is approximated by virtual decomposition into a laminate of transversely isotropic unidirectional layers which are arranged according to the given fiber orientation distribution. This procedure is called orientation averaging and was introduced by Advani and Tucker [Adv87]. The Halpin-Tsai equations are used to predict the properties of the virtual unidirectional layer (Section 4.6.1). The fiber orientation tensor is formed in order to apply the orientation averaging procedure (Section 4.6.2). Orientation averaging is then carried out for each pseudo-grain with fibers of equal aspect ratio (Section 4.6.3). The term pseudo-grain is often used in context with multiple-step homogenization to combine microstructural entities (e.g. fibers) with similar properties (e.g. orientation, aspect ratio or both) to a sub-unit for which the first homogenization step is performed [Ada09, Kam11]. In the following, fibers with equal aspect ratio are combined to virtual pseudo-grains. For LFT with a non-uniform fiber length, a length averaging also needs to be performed (Section 4.6.4). As shown by Garesci and the author [Gar13], a suitable procedure is characterized by performing the orientation averaging at first to determine the orientation averaged properties for pseudo-grains of uniform fiber length and then to weigh the contributions of each pseudo-grain with the given fiber length distribution to obtain the final orientation and length averaged LFT stiffness value. The three-step procedure is illustrated in Fig. 34.

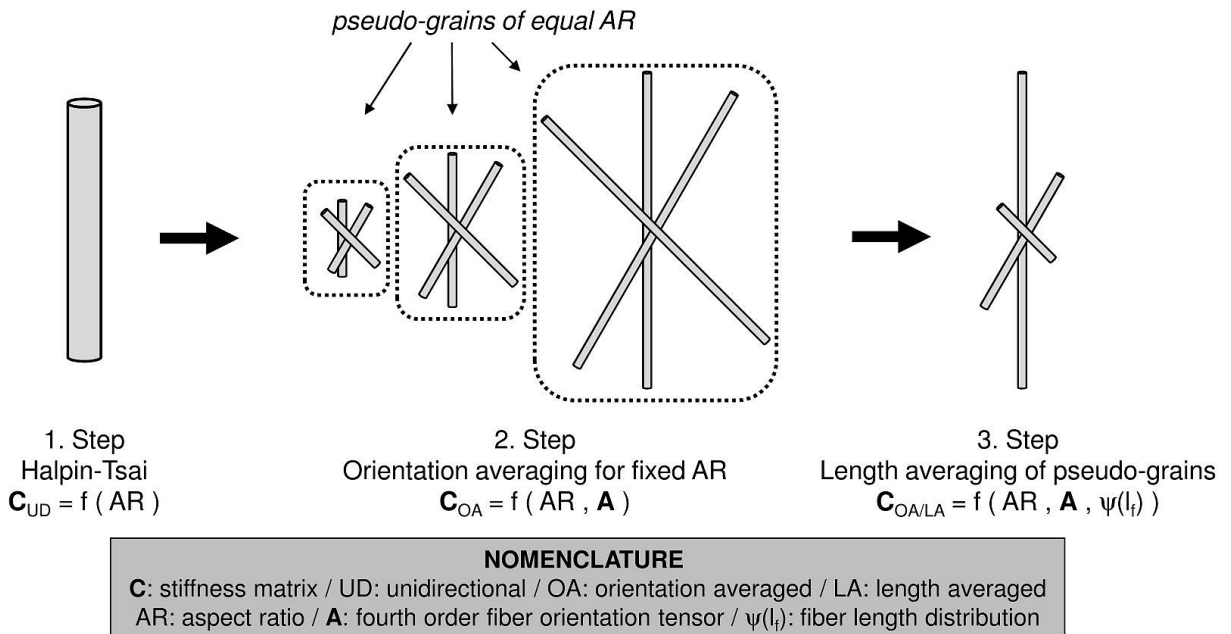


Figure 34: Scheme of the analytical homogenization procedure: At first, the stiffness matrix of the unidirectional reference composite is determined by the Halpin-Tsai equations (left). Orientation averaging is then carried out for each individual pseudo-grain of equal aspect ratio (middle). Finally, the influence of the fiber length distribution is addressed by averaging over all pseudo-grains (right).

4.6.1 Halpin-Tsai equations

The Halpin-Tsai equations [Hal76] are widely used to model the elastic properties of a transversely isotropic, unidirectional and discontinuous fiber composite. The semi-empirical equations were derived from Hill's self-consistent scheme [Hil63]. (An overview about micromechanics is presented in Section 2.2.2.) The ratio of the composite property P^c (Young's modulus E_{11}^c , E_{22}^c or shear modulus G_{12}^c) to the matrix property P^m (E_{11}^m , E_{22}^m , G_{12}^m) is defined by the following expression, with the index 1 referring to the fiber direction and 2, 3 referring to the transverse directions, respectively:

$$\frac{P^c}{P^m} = \frac{1 + \zeta_{\text{HT}} \eta_{\text{HT}} f_v}{1 - \eta_{\text{HT}} f_v}, \quad (87)$$

where f_v denotes the fiber volume fraction. The parameter η_{HT} is defined as

$$\eta_{\text{HT}} = \frac{P^f/P^m - 1}{P^f/P^m + \zeta}, \quad (88)$$

with P^f being the fiber property (E_{11}^f , E_{22}^f , G_{12}^f). The geometry factor ζ_{HT} is given by

$$\zeta_{\text{HT}}^{E_{11}} = 2AR + 40f_v^{10}, \quad (89)$$

$$\zeta_{\text{HT}}^{E_{22}} = 2 + 40f_v^{10}, \quad (90)$$

$$\zeta_{\text{HT}}^{G_{12}} = 1 + 40f_v^{10}, \quad (91)$$

where AR is the fiber aspect ratio and the term $40f_v^{10}$ an extension to improve the model accuracy at high volume fractions [Hew70, Hal76, Tuc99]. The remaining values needed to form the compliance matrix (Section 4.6.3) can be derived by application of the following relations of transverse isotropy and the rule of mixture:

$$E_{33} = E_{22}, \quad (92)$$

$$G_{13} = G_{12}, \quad (93)$$

$$G_{23} = \frac{E_{22}}{2(1 + \nu_{23})}, \quad (94)$$

$$\nu_{12} = \nu_f f_v + \nu_m (1 - f_v), \quad (95)$$

$$\frac{\nu_{12}}{E_1} = \frac{\nu_{21}}{E_2}, \quad (96)$$

$$\nu_{31} = \nu_{21}, \quad (97)$$

$$\nu_{32} = \nu_{23} = \frac{1}{\frac{f_v}{\nu_f} + \frac{1-f_v}{\nu_m}}, \quad (98)$$

with ν_f , ν_m being the Poisson's ratio of the isotropic fiber and matrix, respectively.

4.6.2 Orientation tensor

In order to apply the orientation averaging scheme for the first step of homogenization of each pseudo-grain with equal aspect ratio (Fig. 34), the fiber orientation distribution in the form of 2D probability density functions (Section 3.1.2) needs to be converted to orientation tensors after Advani and Tucker [Adv87]. With the orientation tensors, a compressed description of orientation information is available, which allows the storage of orientation information at every material point (e.g. mesh of a process simulation and mapping to a FE-mesh for structural simulation). When the second order orientation tensor \mathbf{a} (or a_{ij} in index notation) is applied, only five independent parameters are needed to describe a 3D orientation state (two independent parameters for 2D) instead of a probability density function with a magnitude of variables, while retaining a sufficiently accurate description of the orientation state for engineering applications.

The fundamental properties of \mathbf{a} are:

- $\text{tr}(\mathbf{a}) = 1$ - The trace of the tensor equals one. This is a consequence of the probability density function being normalized (Eq. 102).
- The diagonal components a_{11}, a_{22}, a_{33} represent the relative fiber amount aligned in the principal directions of \mathbf{a} .
- The off-diagonal components $a_{ij}, i \neq j$ have values ranging from $-1/2$ to $1/2$. They represent a measure of the degree of misalignment between the coordinate axes (x_1, x_2 and x_3) and the principal directions of the tensor and vanish if they coincide.
- One can visualize the orientation tensor as an ellipsoid in which the diagonal components define its shape by the three principal semi-axes and the off-diagonal components effect the rotation of these axes against the coordinate system.

The derivation of the fiber orientation tensors from the fiber orientation functions is carried out in the following. If a fiber is modeled as rigid cylinder, its orientation in 3D space can be described by the two angles θ, ϕ in a spherical coordinate system (Fig. 35). The orientation distribution can then be defined as probability density function $\psi(\theta, \phi)$. In order to introduce the vector \mathbf{p} (unit length) to describe the fiber position in Cartesian coordinates, the following transformations are applied:

$$p_1 = \sin \theta \cos \phi , \quad (99)$$

$$p_2 = \sin \theta \sin \phi , \quad (100)$$

$$p_3 = \cos \theta . \quad (101)$$

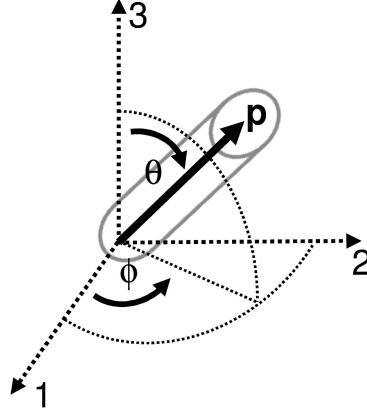


Figure 35: \mathbf{p} vector to describe the fiber orientation in Cartesian coordinates (x_1, x_2, x_3) and corresponding spherical coordinates (θ, ϕ) .

The probability density function $\psi(\theta, \phi)$ can then be converted to its Cartesian representation $\psi(\mathbf{p})$. The integral over all possible directions of \mathbf{p} (Cartesian coordinates) or over the surface of the unit sphere (spherical coordinates) must equal 1 since the probability density function must be normalized [Adv87]:

$$\oint \psi(\mathbf{p}) \, d\mathbf{p} = \int_{\phi=0}^{2\pi} \int_{\theta=0}^{\pi} \psi(\theta, \phi) \sin \theta \, d\theta \, d\phi = 1 . \quad (102)$$

Second, due to the symmetry of a fiber, the following conditions for periodicity apply:

$$\psi(\theta, \phi) = \psi(\pi - \theta, \phi + \pi) , \quad (103)$$

$$\psi(\mathbf{p}) = \psi(-\mathbf{p}) . \quad (104)$$

Orientation tensors are then defined by forming dyadic products of the vector \mathbf{p} and integrating the product with the probability distribution function over all possible directions [Adv87]. Because of the symmetry condition (Eq. 104), only the even-order tensors are different from zero. The second order (\mathbf{a}, a_{ij}) and fourth order (\mathbf{A}, A_{ijkl}) orientation tensors have practical importance and are given by

$$\mathbf{a} = \oint \mathbf{p} \otimes \mathbf{p} \, \psi(\mathbf{p}) \, d\mathbf{p} , \quad (105)$$

$$\mathbf{A} = \oint \mathbf{p} \otimes \mathbf{p} \otimes \mathbf{p} \otimes \mathbf{p} \, \psi(\mathbf{p}) \, d\mathbf{p} . \quad (106)$$

It is worth mentioning that in the literature, the fourth order orientation tensor is usually written in lower case (a_{ijkl}) [Adv87]. However, to ensure compatibility with the notational conventions (Section 1.3), an upper case letter is used in this work (\mathbf{A}, A_{ijkl}) .

To describe orientation states, the second-order tensor \mathbf{a} is usually accurate enough (e.g. to visualize the fiber orientation in mold-filling process simulation software). The fourth order tensor \mathbf{A} is needed for the following step of orientation averaging.

4.6.3 Orientation averaging

First, the transversely isotropic compliance matrix \mathbf{S}_{UD} is formed:

$$\mathbf{S}_{\text{UD}} = \begin{bmatrix} \frac{1}{E_{11}} & \frac{-\nu_{12}}{E_{11}} & \frac{-\nu_{12}}{E_{11}} & 0 & 0 & 0 \\ \frac{-\nu_{12}}{E_{11}} & \frac{1}{E_{22}} & \frac{-\nu_{23}}{E_{22}} & 0 & 0 & 0 \\ \frac{-\nu_{12}}{E_{11}} & \frac{-\nu_{23}}{E_{22}} & \frac{1}{E_{22}} & 0 & 0 & 0 \\ 0 & 0 & 0 & \frac{2(1+\nu_{23})}{E_{22}} & 0 & 0 \\ 0 & 0 & 0 & 0 & \frac{1}{G_{12}} & 0 \\ 0 & 0 & 0 & 0 & 0 & \frac{1}{G_{12}} \end{bmatrix}. \quad (107)$$

\mathbf{S}_{UD} describes the properties of the virtual unidirectional composite as calculated by the Halpin-Tsai equations (Section 4.6.1) or another suitable homogenization method.

The stiffness matrix \mathbf{C}_{UD} is defined as the inverse of \mathbf{S}_{UD} :

$$\mathbf{C}_{\text{UD}} = \begin{bmatrix} C_{11} & C_{12} & C_{13} & 0 & 0 & 0 \\ C_{21} & C_{22} & C_{23} & 0 & 0 & 0 \\ C_{31} & C_{32} & C_{33} & 0 & 0 & 0 \\ 0 & 0 & 0 & C_{44} & 0 & 0 \\ 0 & 0 & 0 & 0 & C_{55} & 0 \\ 0 & 0 & 0 & 0 & 0 & C_{66} \end{bmatrix} = \mathbf{S}_{\text{UD}}^{-1}. \quad (108)$$

The parameters B'_i are calculated from the components of the stiffness matrix \mathbf{C}_{UD} [Adv87]:

$$B'_1 = C_{11} + C_{22} - 2C_{12} - 4C_{66}, \quad (109)$$

$$B'_2 = C_{12} - C_{23}, \quad (110)$$

$$B'_3 = C_{66} + \frac{1}{2}(C_{23} - C_{22}), \quad (111)$$

$$B'_4 = C_{23}, \quad (112)$$

$$B'_5 = \frac{1}{2}(C_{22} - C_{23}). \quad (113)$$

The orientation averaged stiffness matrix \mathbf{C}^{OA} can now be obtained by [Adv87]

$$\begin{aligned} C_{ijkl}^{\text{OA}} = & B_1'(A_{ijkl}) + B_2'(A_{ij}\delta_{kl} + A_{kl}\delta_{ij}) + B_3'(A_{ik}\delta_{jl} + A_{il}\delta_{jk} + A_{jl}\delta_{ik} + A_{jk}\delta_{il}) \\ & + B_4'(\delta_{ij}\delta_{kl}) + B_5'(\delta_{ik}\delta_{jl} + \delta_{il}\delta_{jk}) \quad , \end{aligned} \quad (114)$$

with $i, j, k, l = 1, 2, 3$ and δ_{ij} being the Kronecker delta.

4.6.4 Length averaging

The stiffness values obtained by the application of the orientation averaging scheme were analyzed for each individual pseudo-grain (aspect ratio of 10, 50, 100, 500, 1000, 2000, 3000 and 4000) for each volume fraction of 3.8 % (PPGF10), 8.2 % (PPGF20) and 13.2 % (PPGF30). To obtain the final values as specified in Table 12 (Section 5.6.2), averaging over all pseudo-grains with respect to fiber length was performed by weighing the orientation-averaged stiffness value of each pseudo-grain with the respective fiber length fraction of the fiber length distribution (Eq. 115). The fiber length distribution (Section 5.1.2) had therefore to be coarsened to the intervals of fiber length corresponding to the values of aspect ratio of the pseudo-grains.

$$\mathbf{C}^{\text{OA/LA}} = \sum_{i=1}^n \frac{n_i l_i}{L_{\text{tot}}} \mathbf{C}^{\text{OA}}(AR_i) \quad , \quad (115)$$

where $\mathbf{C}^{\text{OA/LA}}$ denotes the orientation and length averaged stiffness matrix,

$n_i l_i / L_{\text{tot}}$ the length fraction of the number n_i of fibers with the length l_i ,

$L_{\text{tot}} = \sum_i n_i l_i$ the total fiber length and

$\mathbf{C}^{\text{OA}}(AR_i)$ the orientation averaged stiffness matrix (Eq. 114) of a pseudo-grain with fixed fiber aspect ratio AR_i .

In analogy to a probability distribution function, the sum over all fiber length fractions must necessarily be normalized: $\sum_{i=1}^n \frac{n_i l_i}{L_{\text{tot}}} = 1$.

5 Results

5.1 Material and microstructure

5.1.1 Fiber orientation distribution

The planar fiber orientation distributions of the PPGF30 and PPGF20 material (13.22 / 8.16 vol-%) are specified in Fig. 36. The distributions are averaged over the material thickness as described in Section 3.1.2. Analytical fit curves of the probability density function of the pattern $\psi(\phi) = a e^{b \sin(c\phi+d)} + e$ with the parameters $a \dots e$ were applied to calculate the second order orientation tensors a_{ij} as described in Section 4.6.2. The values of a_{ij} as well as the functions $\psi(\phi)$ are specified in the figure.

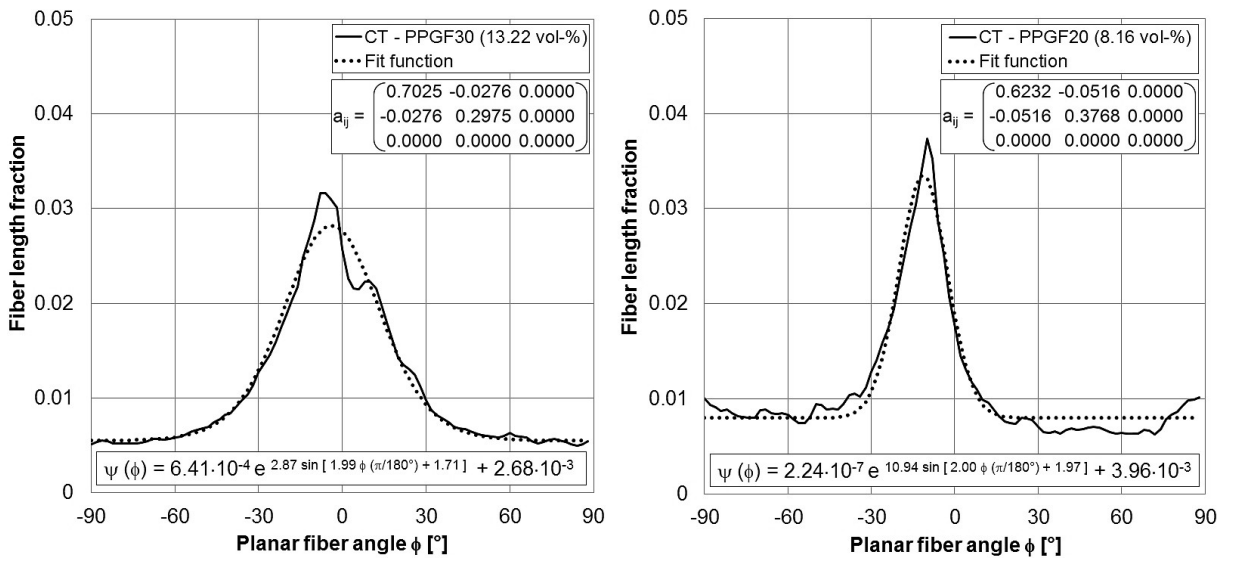


Figure 36: Experimental planar fiber orientation distributions of PPGF30 and PPGF20, fit functions $\psi(\phi)$ and orientation tensors a_{ij} .

5.1.2 Fiber length distribution

The fiber length distribution of an incinerated specimen of PPGF30 was analyzed by the automatic procedure described in Section 3.1.3. The resulting distribution (normalized by number and weighted by length) is specified in Fig. 37, 38 and 39 (a second analysis is presented in the appendix, Section A.2). The original distribution as depicted in the figures features approx. 3000 length classes which is not suitable to realize both orientation distribution and length distribution in the FE model (multidirectional RVEs) with a reasonable number of fibers. The length distribution was therefore coarsened to 33 length classes with an interval of 200 μm for fibers below 2 mm length and an interval of 2 mm for 2 - 48 mm fiber length. No significant deviation in mean fiber length can be observed comparing the original and coarsened distributions (Table 5). Furthermore, the distributions were cropped to a maximum fiber length of 48 mm, so that the longest fibers can

fit inside the largest RVEs with a length of 50 mm. The few fibers which feature a length between 50 and 60 mm were therefore shortened to 48 mm, resulting in the peak at the right end of the distribution (Fig. 37 - 38).

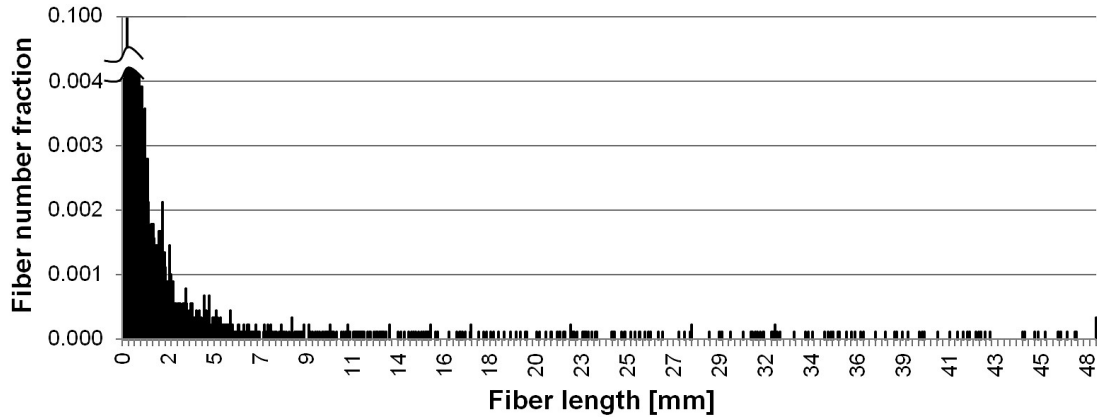


Figure 37: Fiber length distribution (normalized by number) of PPGF30.

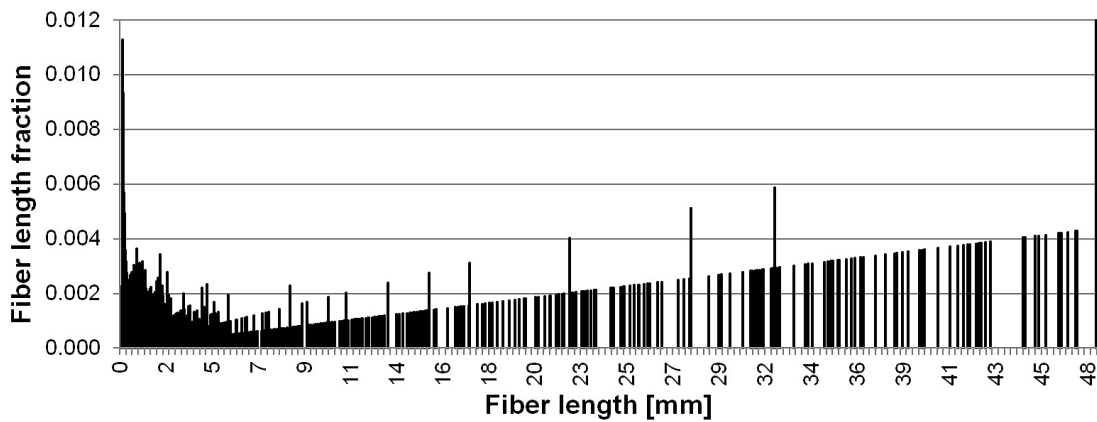


Figure 38: Fiber length distribution (weighted by length) of PPGF30.

Length distribution	Mean length (by number) \bar{l}_n [mm]	Mean length (weighted) \bar{l}_w [mm]	Length class [mm]
Original	1.2	15.0	0.015
Coarsened	1.3	14.5	0.2 (< 2 mm) 2 (2 - 48 mm)

Table 5: Characteristic values of original and coarsened fiber length distributions.

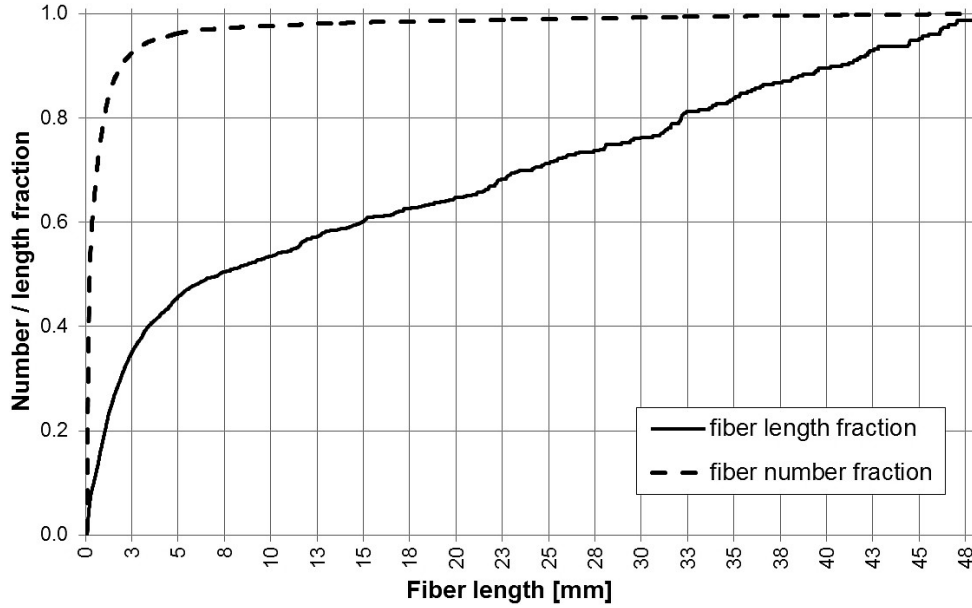


Figure 39: Cumulative depiction of fiber length distribution (normalized by number / length) of PPGF30.

5.1.3 Fiber volume fraction

The fiber volume fraction f_v was calculated from the weight fraction f_w as described in Section 3.1.4. The values are given in Table 6.

Material	Fiber weight fraction f_w [%]	Fiber volume fraction f_v [%]
PPGF10	10	3.80
PPGF20	20	8.16
PPGF30	30	13.22

Table 6: Fiber weight fraction f_w and volume fraction f_v of the investigated materials.

5.1.4 Fracture surfaces

Fig. 40 - 41 show scanning electron microscopy (SEM) images of the fracture surface of a PPGF30 specimen. Because of the backscattered electron (BSE) contrast, the fibers appear brighter than the matrix due to their higher mass density. The specimen was broken at cryogenic temperature to ensure brittle fracture in order to expose the specimen's inner structure in its original state and to avoid ductile deformation of the matrix, which would smear the fracture surface. The characteristic LFT structure with the fibers being aligned within layers parallel to the specimen surface and a low degree of fiber orientation in thickness direction can be observed in Fig. 40. A high degree of fiber pullout (represented by the amount of free fiber surfaces and holes of the pulled out fibers from the opposite surface, respectively) can be seen in Fig. 41.

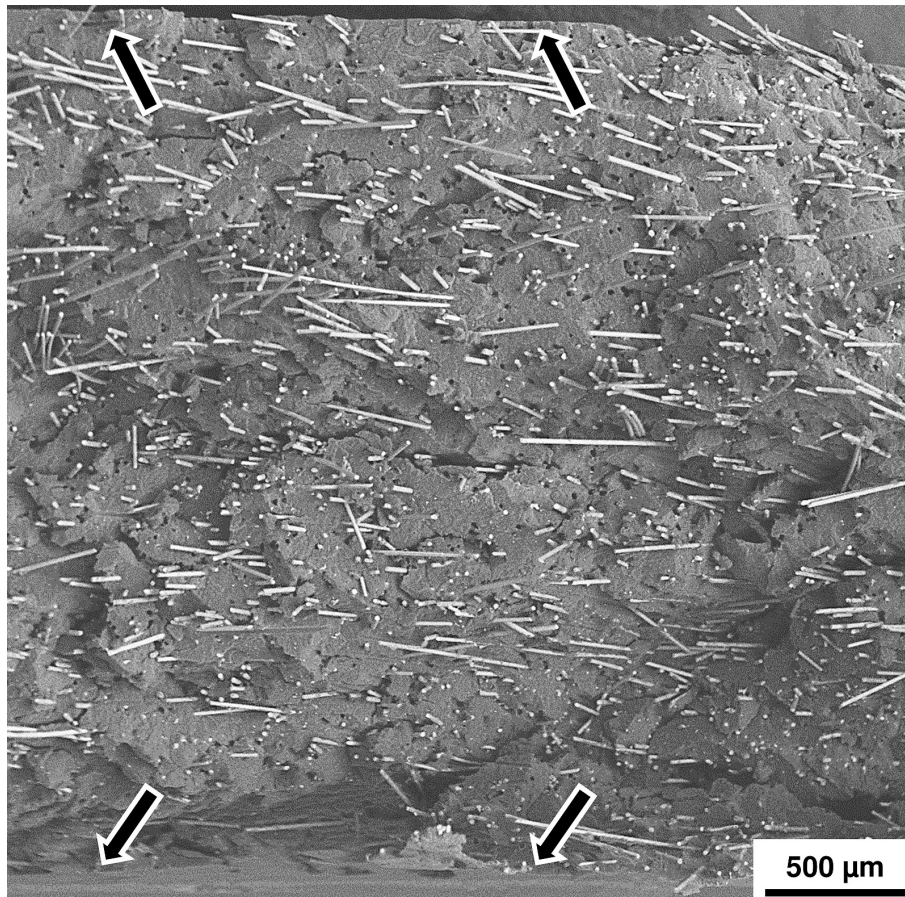


Figure 40: Fracture surface of PPGF30 specimen. The wall surfaces are marked by the arrows. A layer-wise alignment of the fibers parallel to the surfaces can clearly be seen.

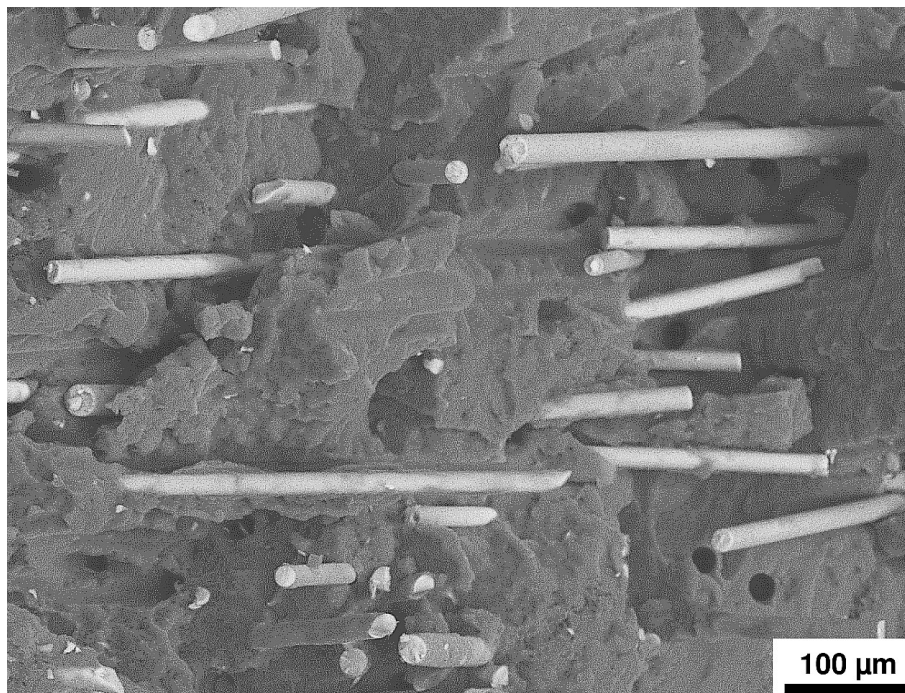


Figure 41: Fracture surface of a PPGF30 (13.2 vol-%) specimen (detail). A high degree of fiber pullout can be observed.

5.2 Viscoelastic matrix model

5.2.1 Model calibration

To determine the parameters of the Burgers model (E_0 , E_1 , η_0 and η_1), the ODE (14) was solved for the boundary condition of a constant stress σ_0 :

$$\varepsilon = \sigma_0 \left[\frac{1}{E_0} + \frac{t}{\eta_0} + \frac{1}{E_1} \left(1 - e^{-\frac{E_1}{\eta_1} t} \right) \right]. \quad (116)$$

Equation (116) was fitted to uniaxial creep and recovery experiments at varying stress levels from 2.5 to 12.5 MPa under application of the least squares method to determine the model parameters for each discrete stress level. Exclusively the creep period of the experimental data (up to $6 \cdot 10^5$ s) was used to fit the parameters, since the abrupt removal of the load affects the strain measurement to become imprecise. The fit curves are presented together with the experimental data in Fig. 42. For the stress levels of 2.5, 5 and 10 MPa, the experimental data is reproduced with high accuracy by the fit curves. For 7.5 and 12.5 MPa, a slightly overrated creep rate can be observed for the second period of creep (above $2 \cdot 10^5$ s). The experimental data for the highest stress level of 12.5 MPa is missing above $3 \cdot 10^5$ s due to a failure of the strain measurement device. It is worth mentioning that multiple experiments for each stress level were carried out. The creep curves used for parameter identification (which are shown in the figure) were manually selected from the middle of the scatter band. To evaluate the stress-dependence of the model parameters, the values of E_1 , η_0 and η_1 are plotted in Fig. 43 as symbols for each investigated stress level. E_0 as instantaneous elastic stiffness of the material is treated as stress-independent. For the remaining parameters, the stress dependence can be described by a power law of the pattern $a(\sigma) = b c^\sigma$ for E_1 and logarithmic functions of the pattern $a(\sigma) = b + c \ln(\sigma + d)$ for η_0 and η_1 , respectively. The functions are represented through the solid lines in Fig. 43. Overall, the experimental data can be described with high accuracy by the empirical functions. Only the value of E_1 is slightly underestimated at a stress of 5 MPa. The stress level or indicator stress refers to the unidirectional stress for the creep experiments and the equivalent stress (Eq. 55) for the three dimensional model, respectively. The stress dependent model parameters are finally given by the following equations:

$$E_0 = 1250, \quad (117)$$

$$E_1 = 3292.34 \cdot 0.86788^{\sigma_{\text{ind}}/\text{MPa}}, \quad (118)$$

$$\eta_0 = 3.0602 \cdot 10^9 - 1.11126 \cdot 10^9 \ln(\sigma_{\text{ind}}/\text{MPa} - 0.4369), \quad (119)$$

$$\eta_1 = 5.38979 \cdot 10^7 - 1.78557 \cdot 10^7 \ln(\sigma_{\text{ind}}/\text{MPa} - 1.73967), \quad (120)$$

where σ_{ind} is the indicator stress (Eq. 55).

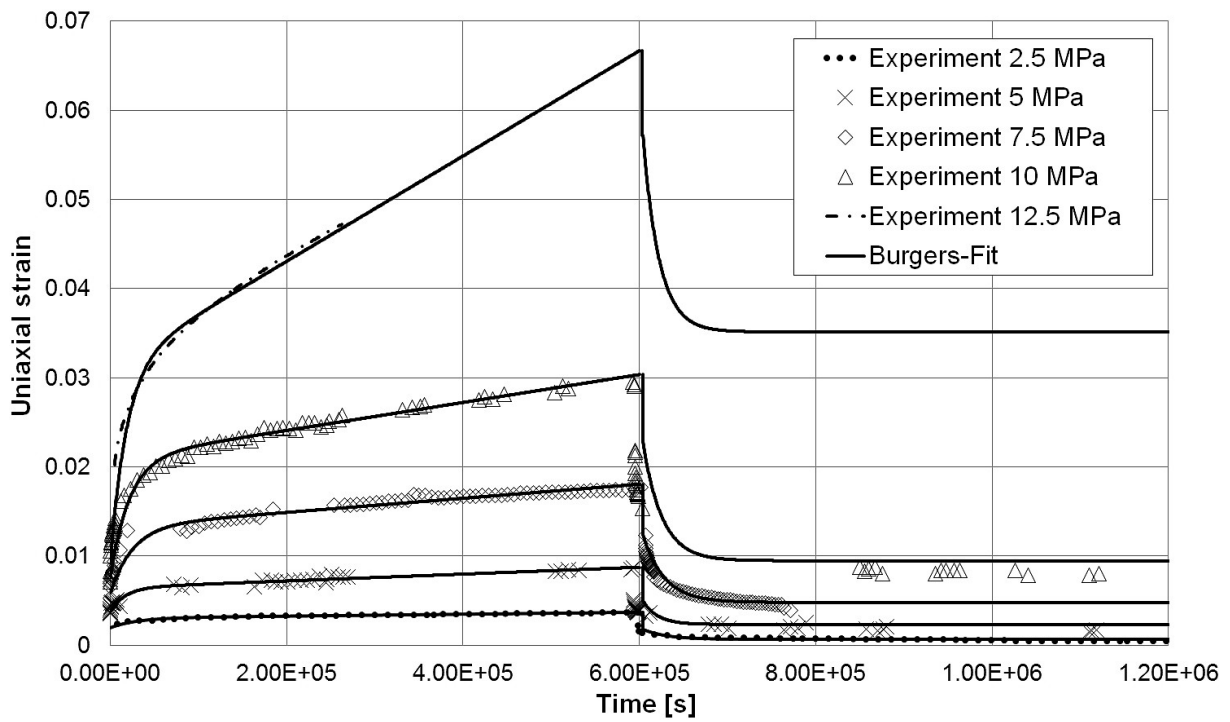


Figure 42: Experimental creep-recovery tests on matrix substance specimens under varying stress levels and fit curves of the Burgers model to determine the model parameters.

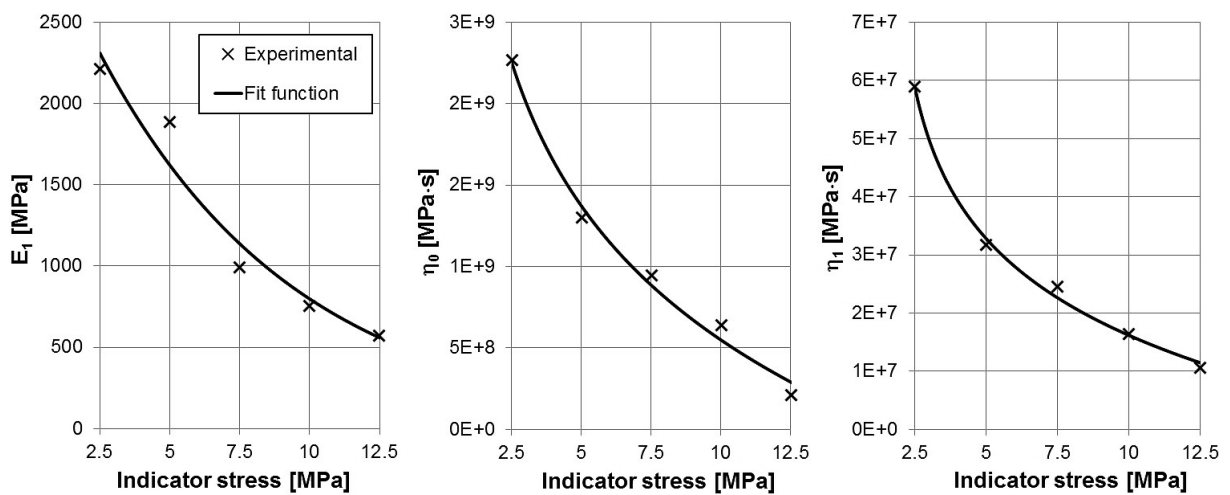


Figure 43: Stress dependence of three of the four Burgers parameters as determined experimentally and fit functions.

5.2.2 Model validation

The model validation is divided into two parts: First, the suitability of the nonlinear modified Burgers model (as derived in Section 4.1.8, in the following denoted by *Burgers UMAT*) to describe a complex load sequence was validated against an experiment for the uniaxial case. Second, the 3D behavior of the linear viscoelastic Burgers model was validated against the viscoelastic model which is implemented in *Abaqus*.

Load history

To validate the *Burgers UMAT* with respect to a complex load history emphasizing the nonlinear viscoelastic behavior, an exemplary sequence was investigated. The sequence consists of three load controlled periods and one strain controlled period. The response of the model is compared to that of a matrix substance specimen in Fig. 44. Overall, the model is well able to describe the experimental data for all periods. It is worth mentioning that the model was calibrated with experimental data of specimens which were selected from the middle of the scatter band, whereas a single specimen was used for the validation sequence. Thus, the minor differences in absolute strain of the third period can likely be explained by experimental scatter. With respect to the shape of the curves, a systematic underprediction of the curvature of the experimental data by the model is existent.

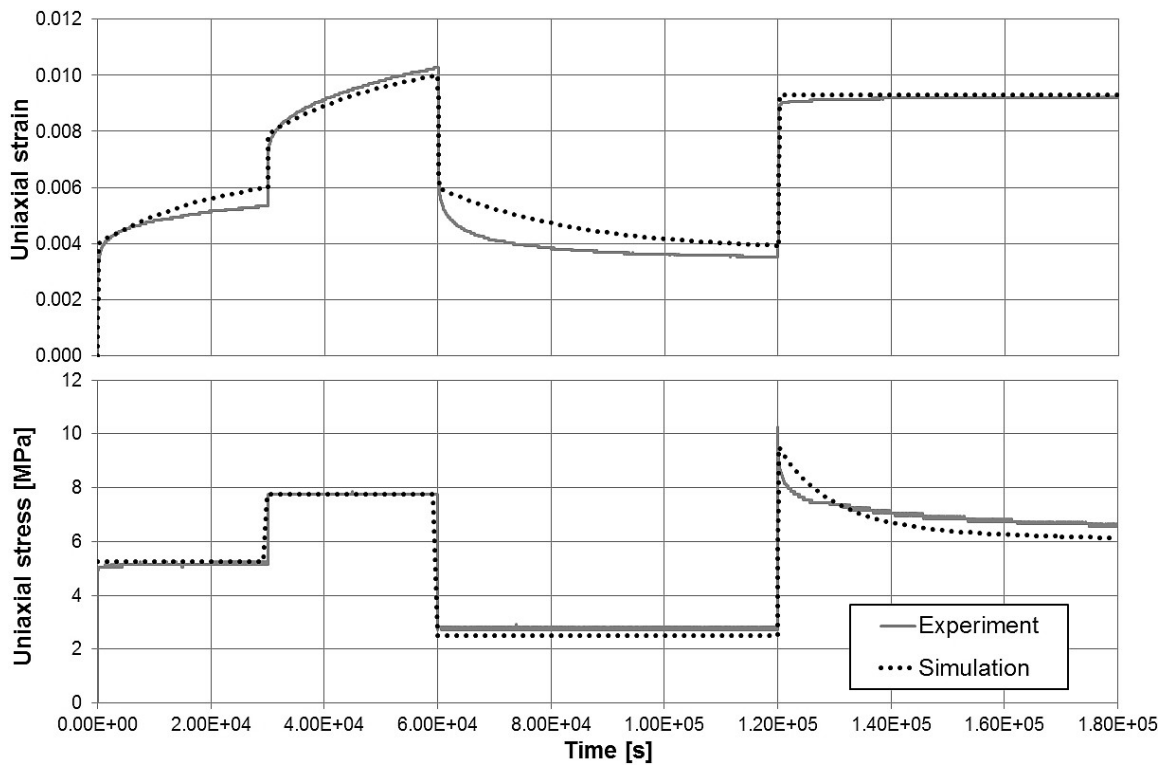


Figure 44: Complex load sequence of a matrix substance specimen compared to the response of the nonlinear viscoelastic matrix model (*Burgers UMAT*).

3D behavior

To validate the 3D behavior of the *Burgers UMAT*, it was compared to the viscoelastic material model which is implemented in *Abaqus* under the keyword **VISCOELASTIC* (referred to as *Abaqus* model in the following). The latter represents a generalized Maxwell model. The schematic notations of both models are compared in Fig. 45.

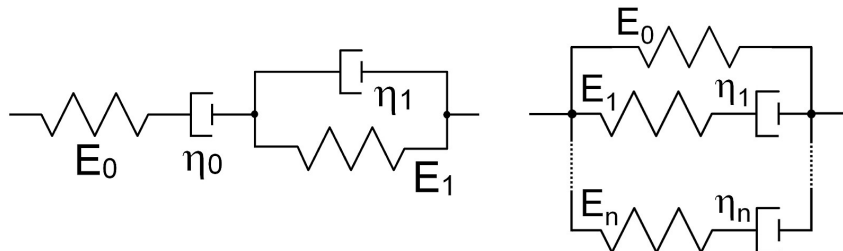


Figure 45: Schematic notation of the Burgers model (*Burgers UMAT*, left) compared to the generalized Maxwell model (*Abaqus *VISCOELASTIC*, right).

The creep compliance of the Burgers model is defined as

$$C_{Burgers}(t) = \frac{1}{E_0} + \frac{t}{\eta_0} + \frac{1}{E_1} \left(1 - e^{-\frac{t}{\tau_1}}\right). \quad (121)$$

For the generalized Maxwell model, it takes the form of

$$C_{Maxwell}(t) = \left[E_0 + \sum_{i=1}^n E_i e^{-\frac{t}{\tau_i}} \right]^{-1}, \quad (122)$$

with $\tau_i = \eta_i/E_i$ being the relaxation time.

Due to the free dashpot η_0 of the Burgers model, the viscous properties are dominant in contrast to the generalized Maxwell model, which represents a viscoelastic body due to the spring E_0 being parallel to all dashpots. Thus, the model formulations are incompatible and simple conversion of the parameters is not feasible. Therefore, the *Abaqus* model needs to be fitted to the strain response of the *Burgers UMAT*. Several Maxwell elements are needed in the form of coefficients of the Prony series (the relaxation times τ_i in the summation term of Eq. 122) to capture the shape of the curve. These were computed automatically by *Abaqus* under specification of the time-dependent strain values. The 3D behavior was assumed to feature a constant Poisson's ratio as described in Section 4.1.6. The applicability of the *Abaqus* model is restricted to linear viscoelasticity. Therefore, the model parameters of the *Burgers UMAT* were forced to remain constant for this study to mimic a linear viscoelastic response. The parameters were fixed to the respective values for an indicator stress σ_{ind} of 10 MPa. Fig. 46 shows the response of the *Abaqus* model and the *Burgers UMAT* for an uniaxial tension of 10 MPa. It was not possible to identify parameters for the *Abaqus* model which reproduce exactly the results of the *Burgers UMAT*. Therefore, a small deviation can be seen in the figure. In

the following, the 3D behavior of the *Burgers UMAT* was validated against the *Abaqus* model for two different load cases: Four of the eight nodes of a single hexahedral element (*C3D8*) were fixed in all DOFs whereas the remaining four nodes were subjected to pure shear loading respectively distortion with a different load applied to each node in an arbitrary direction. Both load cases are illustrated in Fig. 47. The time-dependent nodal displacements for both scenarios are shown in Fig. 48. The small deviation between the *Burgers UMAT* and the *Abaqus* model results from the different and incompatible model formulations and is negligible. Thus, the 3D behavior of the *Burgers UMAT* could be successfully verified against the commercial implementation of *Abaqus*.

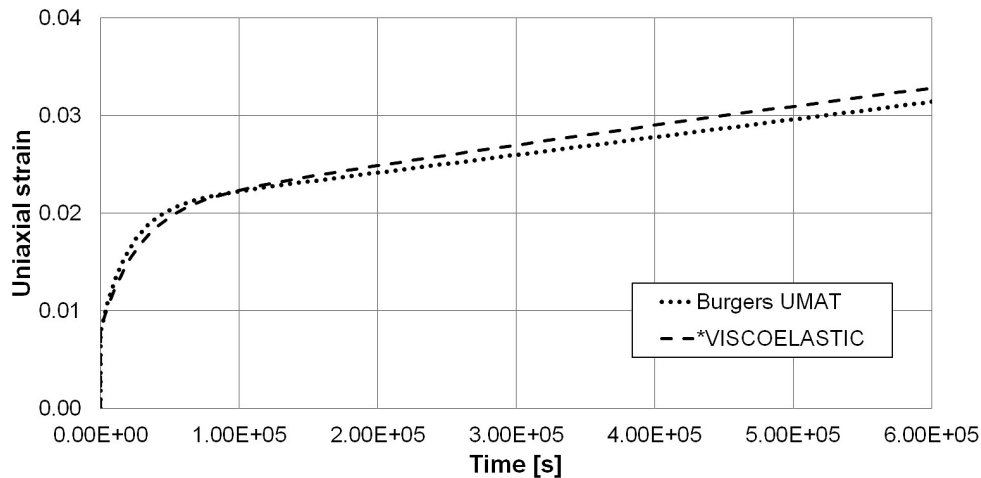


Figure 46: Comparison between the *Abaqus* model and the *Burgers UMAT* for uniaxial tension of 10 MPa.

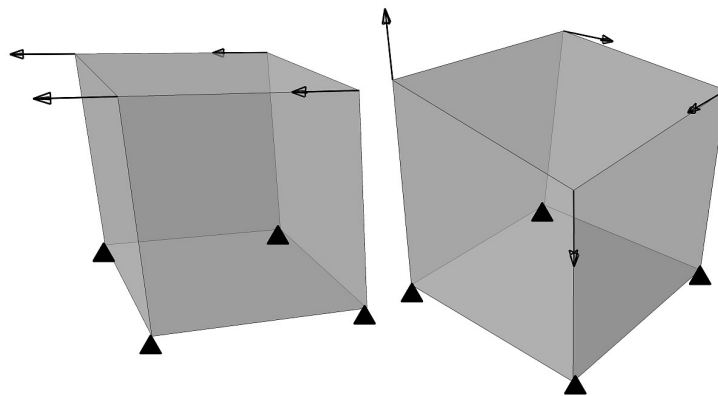


Figure 47: Load scenarios of the single element tests: shear (left) and distortion (right).

5.2.3 Modified parameters

This section deals with the derivation of modified parameters of the nonlinear viscoelastic matrix model to compensate the effects of the coarse matrix mesh in the multidirectional LFT structures (RVEs) to a certain degree. Due to their enormous size, it

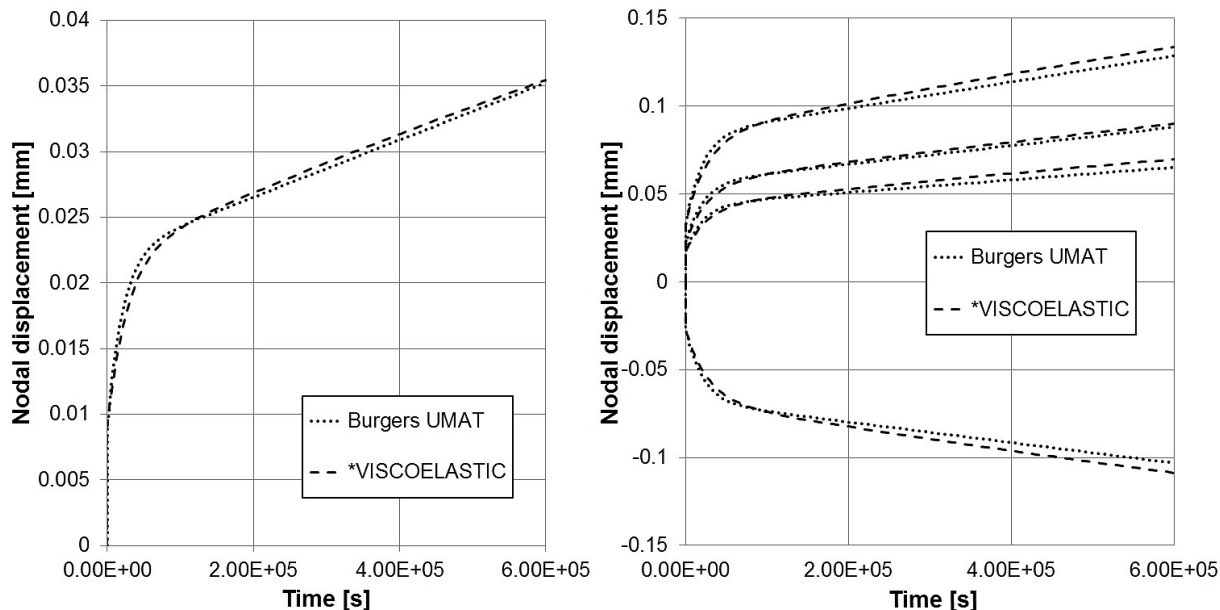


Figure 48: Comparison between the *Abaqus* model and the *Burgers UMAT* for the load case of shear (left) and distortion (right).

was not technically feasible to carry out element studies on the 50 mm long RVEs with the implicit FEM (A respective study under application of the explicit solver is presented in Section 5.6.5). A very small RVE of $1 \times 1 \text{ mm}^2$ was therefore chosen to study the effects of varying mesh densities and element types applying the implicit solver. Table 7 specifies the investigated variants. The column labeled *Element order* refers to both fiber and matrix elements, whereas the one denoted by *Integration* applies to the fiber elements only. In the column *Elements per fiber*, the number of elements over the fiber cross section is specified. The column *Matrix material* defines the parameters of the viscoelastic matrix model (Fig. 50). The fiber elements were chosen to hexahedral elements for *variant A, B, D, E* (tetrahedral elements for *variant C*), whereas the matrix was always represented by tetrahedral elements. The response of the $1 \times 1 \text{ mm}^2$ RVE is specified in Fig. 49 (left) for a stress of 50 MPa. No difference in effective behavior could be observed for mesh *variants C* and *D*; therefore convergence is assumed for both variants. In the following, the parameters of the viscoelastic matrix model were varied until the effective behavior of the converged mesh variants under application of the original model parameters could be reproduced with the coarse mesh (*variant E*). The resulting modified model parameters are plotted in Fig. 50 and specified by Eq. 123 - 126. To validate the modified model parameters, a second RVE with $5 \times 1 \text{ mm}^2$ base section was analyzed under two different stress levels of 10 and 50 MPa. The effective behavior for mesh *variant C* and *E* is shown in Fig. 49 (right). No significant difference can be observed between the modified matrix model with the coarse mesh (*variant E*) and the original material with the quadratic mesh (*variant C*). Thus, the effects of the coarse mesh can indeed partially be compensated by the modified parameters.

Variant	Element order	El. type fiber	Integration	El. type matrix	Elements per fiber	Matrix material
A	linear	<i>C3D8</i> (hex.)	full	<i>C3D4</i> (tet.)	1	original
B	linear	<i>C3D8R</i> (hex.)	reduced	<i>C3D4</i> (tet.)	1	original
C	quadratic	<i>C3D10</i> (tet.)	full	<i>C3D10</i> (tet.)	2	original
D	linear	<i>C3D8R</i> (hex.)	reduced	<i>C3D4</i> (tet.)	16	original
E	linear	<i>C3D8R</i> (hex.)	reduced	<i>C3D4</i> (tet.)	1	modified

Table 7: Investigated mesh variants of the element studies.

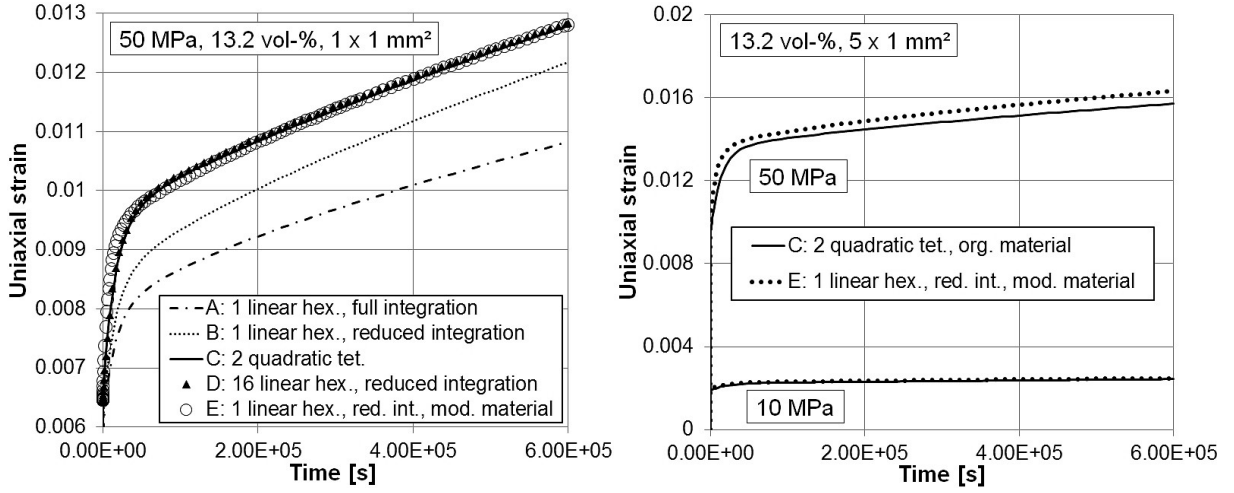


Figure 49: Element study on small RVE (left) and validation on second RVE (right).

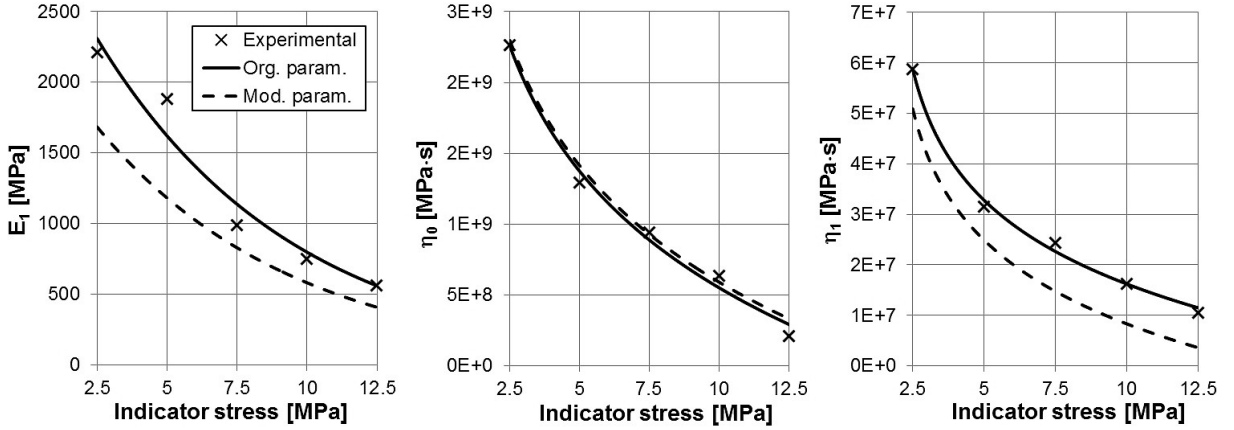


Figure 50: Functions of original and modified parameters of the nonlinear Burgers model.

$$E_0^{\text{mod}} = 1050 , \quad (123)$$

$$E_1^{\text{mod}} = 2400 \cdot 0.86788 \sigma_{\text{ind}}/\text{MPa} , \quad (124)$$

$$\eta_0^{\text{mod}} = 3.1 \cdot 10^9 - 1.11126 \cdot 10^9 \ln(\sigma_{\text{ind}}/\text{MPa} - 0.4369) , \quad (125)$$

$$\eta_1^{\text{mod}} = 4.6 \cdot 10^7 - 1.78557 \cdot 10^7 \ln(\sigma_{\text{ind}}/\text{MPa} - 1.73967) , \quad (126)$$

where σ_{ind} is the indicator stress (Eq. 55).

5.3 Plastic matrix model

This section deals with the calibration of the von Mises plasticity model to describe the plastic deformation of the thermoplastic matrix to model the deformation and damage behavior of LFT. It is worth noting that the plastic model is completely independent of the viscoelastic model of the previous sections - no viscoelastic effects are considered here. The evolution of the multilinear hardening in the form of strain-dependent values of yield stress was fitted to the stress-strain curve of a characteristic matrix substance specimen (Fig. 51). The experiment which was used to calibrate the matrix model was performed at the same effective strain rate as the LFT validation experiments ($\dot{\epsilon} = 7 \cdot 10^{-4}$ 1/s). The apparent softening of the experimental curve beyond a value of total strain of approx. 0.04 is likely caused by specimen necking which is not captured by the engineering notation of stress and strain. Consequently, no such softening is considered in the numerical data of the LFT simulations. An additional study about the effect of a varying strain rate of $7 \cdot 10^{-5}$ 1/s $\leq \dot{\epsilon} \leq 7 \cdot 10^{-3}$ 1/s and the effects of a supposed softening of the matrix material can be found in the appendix (Section A.3). Table 8 shows the tabular data used

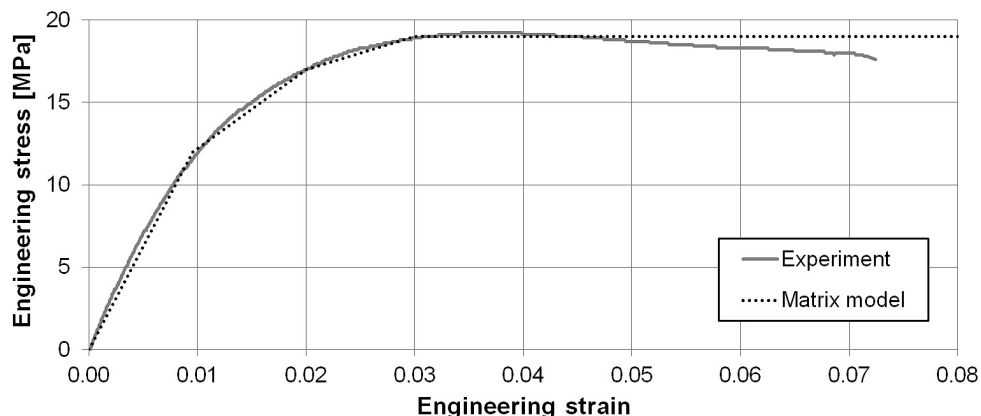


Figure 51: Calibration of the von Mises plasticity model with experimental data.

to define the multilinear, isotropic hardening of the plasticity model in terms of equivalent plastic strain $\bar{\epsilon}^p$ and yield stress $\bar{\sigma}_Y$. The values of total strain ϵ^{tot} were calculated under consideration of the elastic properties from the manufacturer's data sheet [DOW03] ($E_m = 1250$, $\nu_m = 0.35$). In Fig. 51, $\bar{\sigma}_Y$ is plotted against ϵ^{tot} in order to compare the response of the model with the calibration experiment.

Total uniaxial strain ϵ^{tot}	Equivalent plastic strain $\bar{\epsilon}^p$	Yield stress $\bar{\sigma}_Y$ [MPa]
0.0096	0	12
0.02	0.0104	17
0.03	0.0204	19

Table 8: Tabular values for isotropic hardening of the matrix plasticity model.

5.4 Interface model

This chapter describes the inverse modeling of single fiber push-out experiments with the aim to extract interface parameters which can then be fed into the multidirectional LFT models (RVEs) to investigate their effect on the global deformation and damage behavior. In Fig. 52, the load-displacement curves of the fiber push-out experiments (Section 3.4) are plotted together with the simulation results (Section 4.3).

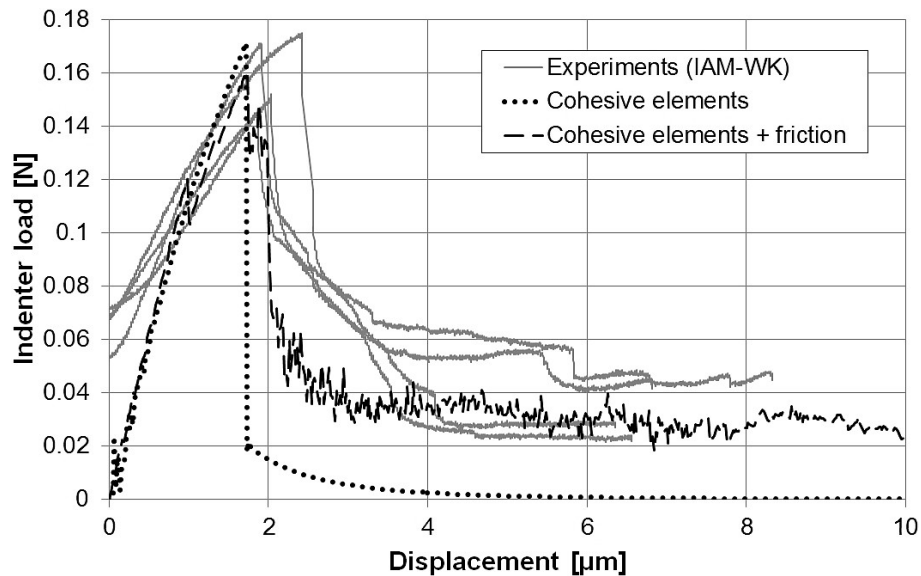


Figure 52: Load-displacement curves of fiber push-out (experimental and numerical data).

Table 9 shows the parameters of the traction-separation law (assigned to the cohesive elements), which were obtained by fitting the numerical curves to the experimental data as described in Section 4.3. The curve denoted by *cohesive elements* in Fig. 52 features only cohesive elements and considers no post-debonding friction, whereas an additional contact formulation was activated for the variant labeled *cohesive elements + friction*. The failure displacement of the cohesive zone elements then needs to be reduced to the specified value in the table.

Parameter	Cohesive el.	Coh. el. + fric.	Unit
Nominal thickness of cohesive section	$1 \cdot 10^{-5}$	$1 \cdot 10^{-5}$	mm
Mass density	$2 \cdot 10^{-9}$	$2 \cdot 10^{-9}$	t/mm ³
Stiffness of elastic traction (K)	10	10	N/mm
Displacement of damage initiation	0.005	0.005	mm
Displacement of damage evolution (corresponding stiffness degradation of 1)	0.00025	0.00015	mm
Coefficient of friction	-	2	
Global surface thickness assignment (general contact formulation)	-	$1 \cdot 10^{-5}$	mm

Table 9: Parameters of the cohesive law (debonding) and contact formulation (friction).

5.5 Unidirectional fiber arrangement

Several variants of an unidirectional fiber arrangement (Section 4.4) were studied to investigate the principle relation between the fiber length and the effective elastic and viscoelastic properties, respectively. The microstructural properties of the examined variants of the model are specified in Table 10.

Variant	AR	Length [mm]	Vol. frac. [%]	Fiber ends	Mesh
1-f	27	1	12.10	8	round fibers, fine
1-c	27	1	12.16	8	square fibers, coarse
2-f	57	1	12.63	4	round fibers, fine
2-c	57	1	12.69	4	square fibers, coarse
3-c	145	5	13.01	8	square fibers, coarse
4-c	292	5	13.11	4	square fibers, coarse
5-c	586	10	13.17	4	square fibers, coarse
6-c	2939	50	13.21	4	square fibers, coarse
7-f	∞	1	13.15	0	round fibers, fine
7-c	∞	1	13.22	0	square fibers, coarse

Table 10: Characteristic values of the investigated variants of the UD fiber arrangement: The column *AR* denotes the corresponding fiber aspect ratio (∞ for continuous fibers), *Length* the lateral RVE dimension, *Vol. frac.* the actual value of fiber volume fraction, *Fiber ends* the number of fiber ends within the RVE and *Mesh* the investigated mesh variants as described in Section 4.4.

In Fig. 53, the elastic properties of the UD fiber arrangements (nominal vol. frac. 13.22 %) are compared to the predictions of the Halpin-Tsai equations (Section 4.6.1, 13.22 % and 15 %). The constituent properties are: $E_m = 1250$ MPa, $\nu_m = 0.35$, $E_f = 72000$ MPa, $\nu_f = 0.22$. It can be seen that the saturation behavior of the elastic stiffness with increasing fiber length is very similarly predicted by the FE and analytical approach, whereas its absolute value is underestimated if the Halpin-Tsai equations are fed by a realistic value of fiber volume fraction of 13.22 %. This issue can be addressed by choosing a slightly increased value of 15 % which yields a very good agreement to the FE model.

In addition to the elastic studies, the viscoelastic properties of the unidirectional fiber arrangements were investigated with the aim to identify a fiber length of saturation similar to one with respect to the elastic properties. The results were generated under application of the nonlinear viscoelastic matrix model with its original parameters (Section 5.2) and elastic fiber properties ($E_f = 72000$ MPa, $\nu_f = 0.22$). At first, the deviation between the coarse mesh with square fiber cross section and the fine mesh with round fibers was investigated. Fig. 54 shows the response of both variants for aspect ratios of 27, 57 and ∞ for a constant stress of 50 MPa. Similar to the elastic behavior (Fig. 53), the difference between the two mesh variants is large for an aspect ratio of 27, decreases for an AR of 57 and vanishes for an infinite AR.

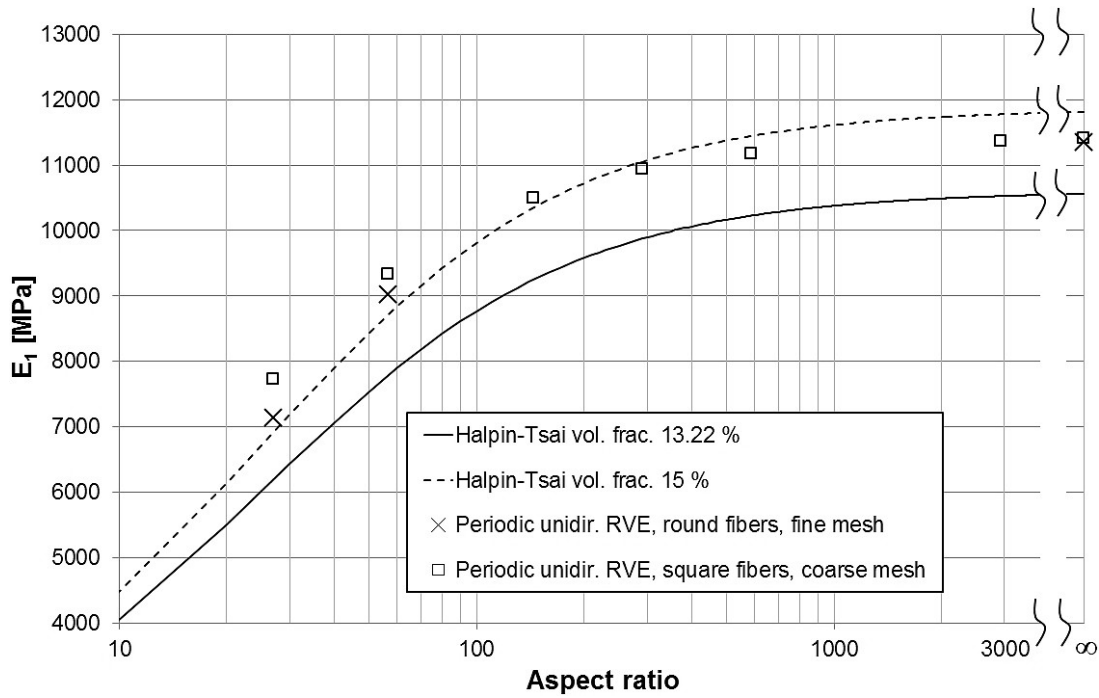


Figure 53: Elastic properties of the UD fiber models compared to the Halpin-Tsai predictions. The different mesh variants are described in Section 4.4.

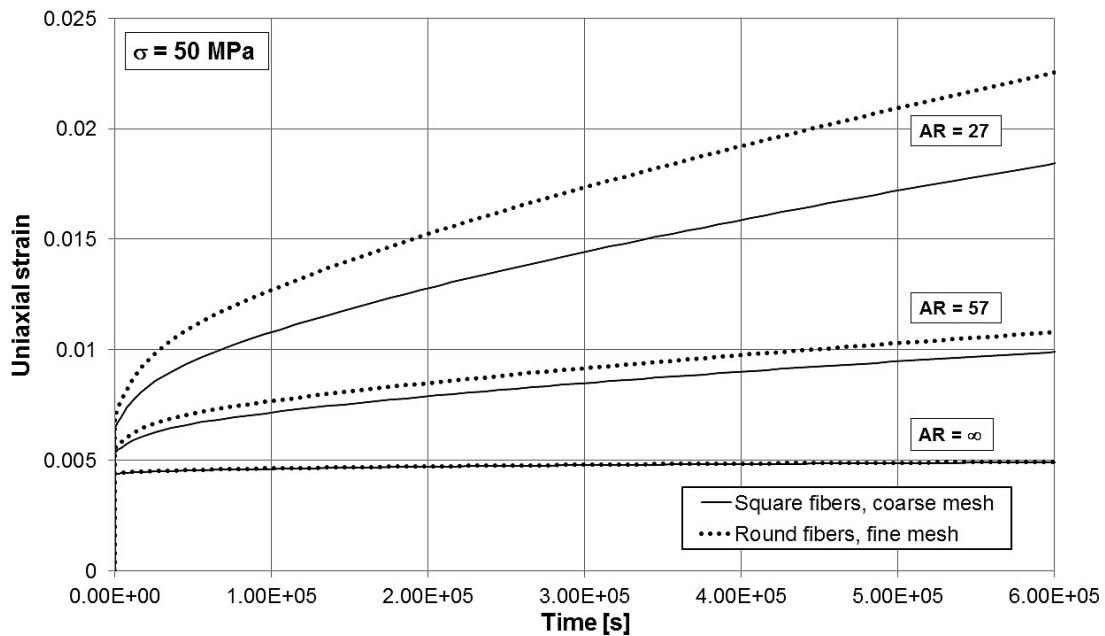


Figure 54: Creep properties of the UD fiber arrangement (nominal vol. frac. 13.22 %) for a stress of 50 MPa and a varying AR of 27, 57 and ∞ . The creep response of the coarse mesh (square fibers) is compared to the fine mesh (round fibers).

In the following, a characteristic measure needs to be defined in order to quantify the creep behavior and to relate it with the fiber length. Therefore, the creep rate $\dot{\epsilon}$ of the secondary period was evaluated by linear fit functions applied to the creep curves between $2 \cdot 10^5$ and $6 \cdot 10^5$ s using the least squares method. Fig. 55 shows the normalized creep strain $\epsilon(t)/\epsilon_0$ of the UD fiber model with the coarse mesh and varying aspect ratios from 27 to ∞ for a stress of 50 MPa in together with the corresponding linear fits of the second period of creep.

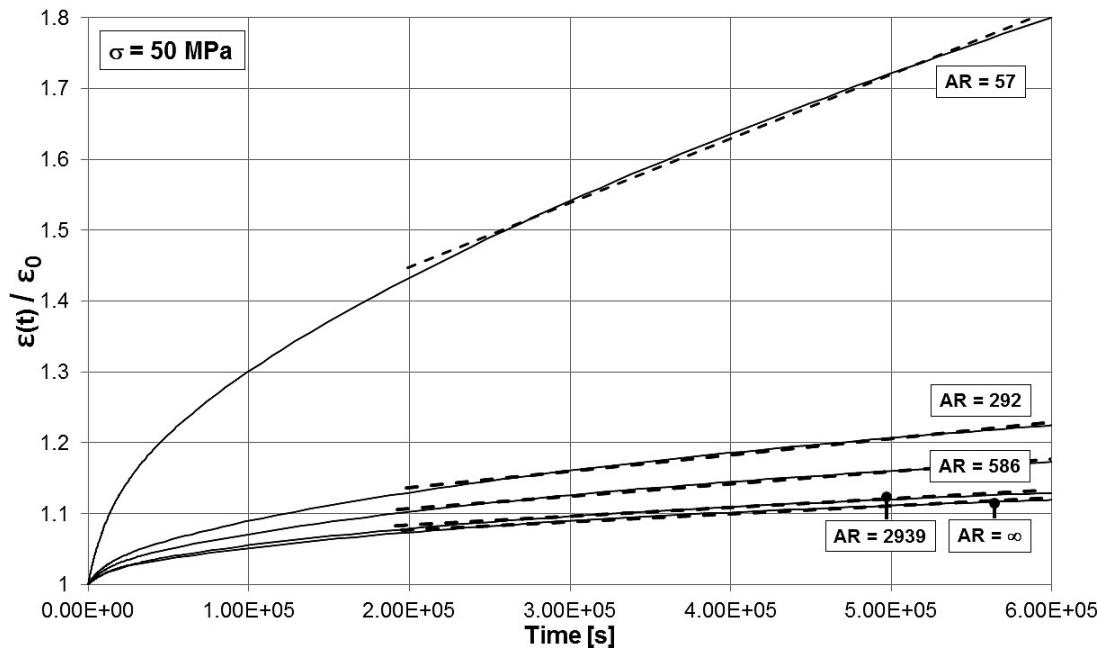


Figure 55: Creep properties of the UD fiber arrangement (nominal vol. frac. 13.22 %) for a stress of 50 MPa and varying AR from 57 to ∞ . The dashed lines represent linear fits to the second period of creep between $2 \cdot 10^5$ and $6 \cdot 10^5$ s used to determine the creep rate.

In Fig. 56, the saturation behavior of the creep rate is compared to that of the elastic stiffness. For this purpose, the normalized creep rate $\dot{\epsilon}_{\text{norm}} = \dot{\epsilon}(AR)/\dot{\epsilon}_{\infty}$ is visualized in together with the normalized elastic compliance $C_{\text{norm}} = C(AR)/C_{\infty}$ based on the data of Fig. 53 and 55. In order to interpolate between the data points (symbols), logarithmic fit functions were applied (continuous lines). The creep properties are presented for two stress levels of 5 and 50 MPa, which delimit a reasonable application range of such a material, because the saturation fiber length with respect to the creep rate is stress dependent. The aspect ratio of saturation is then determined to the AR where the corresponding property deviates less than 10 % from its saturation value (a value of 1.1 for the y-axis in Fig. 56). The saturation AR is finally evaluated to $AR_{\text{elastic}}^{\text{sat}} \approx 100$ with respect to the elastic stiffness and $AR_{\text{creep}}^{\text{sat}} \approx 1600$ to 2600 for the creep rate (depending on stress).

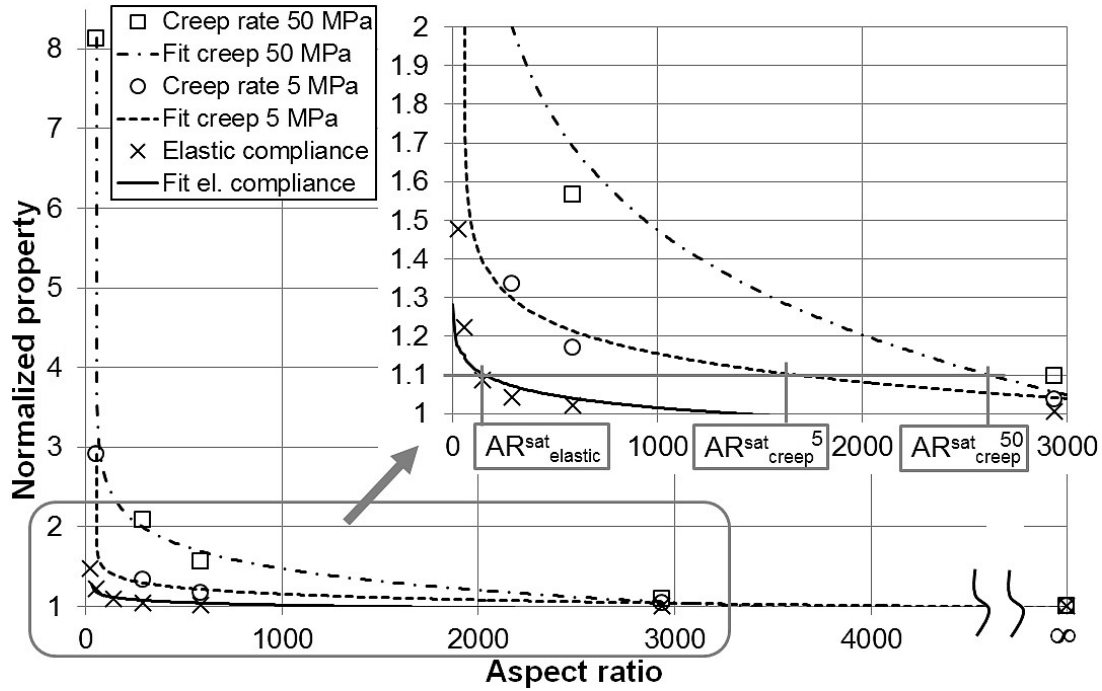


Figure 56: Saturation behavior of the elastic compliance and creep rate: The effective properties are normalized to their respective values for an infinite fiber aspect ratio. The aspect ratio of saturation is then defined as the corresponding value to the elastic compliance resp. creep rate for an infinite fiber aspect ratio multiplied by a factor of 1.1.

5.6 Multidirectional LFT structure

In this chapter, the results of the multidirectional LFT models (RVEs) are presented. First, the microstructural characteristics of the investigated structures are compared to the corresponding experimental data (Section 5.6.1).

Then, the elastic properties of the RVEs are studied and compared to experimental data as well as to the results of an analytical homogenization scheme (Section 5.6.2 - 5.6.5). In this context, multiple aspects, such as the variation of the RVE size, the fiber length and the FE mesh are examined.

In Section 5.6.6 - 5.6.10, the findings with respect to the viscoelastic properties are presented under investigation of the same aspects as for the elastic properties which are completed by studies with regard to varying formulations of the viscoelastic matrix model. Finally, the multidirectional RVEs are used to model the deformation and damage behavior of LFT under application of constitutive models for the plasticity of the matrix, interface and fiber damage (Section 5.6.11 - 5.6.15). It is worth mentioning that the latter results were generated under application of the explicit FEM and are thus completely independent of the elastic and viscoelastic modeling (implicit FEM).

5.6.1 Nomenclature and microstructure characteristics

The microstructure characteristics of the investigated RVEs are specified in Table 11.

The value which is modified between adjacent rows is printed in ***bold italic***.

Each RVE was assigned to an identifier as follows:

LDx - RVEs with implemented measured fiber Length Distribution

CLx - RVEs with Constant fiber Length.

RVE	Volume frac. f_v [%]	Dimensions [mm ³]	Elem. count	Tot. fib. len. [mm]	Mean fiber length \bar{l}_w [mm]
LD1	3.82 (PPGF10)	50 x 2.75 x 0.125	$7.4 \cdot 10^6$	3056	10.1 (15 - distr.)
LD2	8.03 (PPGF20)	50 x 2.75 x 0.099	$8.7 \cdot 10^6$	5048	9.4 (15 - distr.)
LD3	13.15 (PPGF30)	50 x 1.5 x 0.134	$9.7 \cdot 10^6$	6067	8.1 (15 - distr.)
LD4	13.50 (PPGF30)	20 x 1.5 x 0.132	$3.9 \cdot 10^6$	2498	5.5 (15 - distr.)
LD5	13.10 (PPGF30)	10 x 1.5 x 0.137	$2.0 \cdot 10^6$	1241	4.2 (15 - distr.)
LD6	13.34 (PPGF30)	5 x 1.5 x 0.135	$1.0 \cdot 10^6$	622	2.5 (15 - distr.)
LD7	12.95 (PPGF30)	5 x 5 x 0.265	$6.9 \cdot 10^6$	3806	2.4 (15 - distr.)
CL1	13.09 (PPGF30)	50 x 1.5 x 0.143	$10 \cdot 10^6$	6075	1.2 (1.2 - const.)
CL2	12.91 (PPGF30)	50 x 1.5 x 0.139	$9.8 \cdot 10^6$	6061	6.1 (15 - const.)

Table 11: Microstructural characteristic values of the investigated RVE variants: The column *RVE* denotes the RVE identifier, *Volume frac.* is the actual fiber volume fraction, *Dimensions* the lateral RVE dimensions, *Elem. count* the number of elements of the RVE, *Tot. fib. len.* the total fiber length within the RVE and *Mean fiber length* the actual mean fiber length of the RVE followed by the input value in brackets.

The right column (Mean weighted fiber length \bar{l}_w , Eq. 12) shows the actual value of the RVE realization followed by the given value in brackets. If the RVE dimensions are significantly smaller than the max. fiber length (e.g. RVEs with 1.5 mm width), the resultant mean length deviates significantly from the given value as the fibers aligned in the short RVE dimension will be cropped automatically by the fiber generator tool (Section 4.5). The RVEs LD1 - LD7 were generated with the measured fiber length distribution (Section 5.1.2) as input, whereas the RVEs CL1 - CL2 were given a constant fiber length of 1.2 and 15 mm, respectively. The value of 1.2 mm (15 mm) corresponds to the arithmetic mean \bar{l}_n (weighted mean \bar{l}_w) of the measured length distribution. The fiber orientation distributions of all RVEs are compared to the corresponding CT scans in Fig. 57 and 58. No CT data was available for the material with the lowest fiber fraction. Therefore, the RVE LD1 (PPGF10) was generated with the fiber orientation distribution of PPGF20. The RVEs were analyzed under application of the same image correlation technique as for the CT scans. Fifty view cuts, equally spaced over the RVE thickness were analyzed. The screenshots were taken with the fibers being displayed in white, whereas the matrix was given a black color in analogy to the CT scans. In general, a good agreement between the orientation distributions of the RVEs and the experimental ones can be observed.

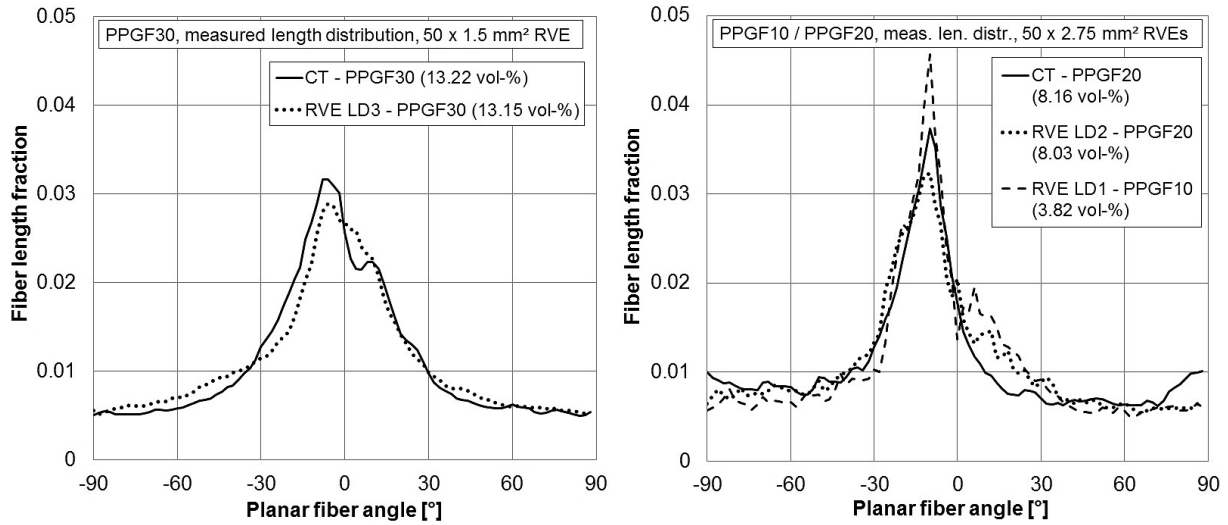


Figure 57: Planar fiber orientation distributions of the RVEs with measured fiber length distribution and dimensions of $50 \times 1.5 \text{ mm}^2$ (PPGF30, left) respectively $50 \times 2.75 \text{ mm}^2$ (PPGF10 and PPGF20, right) compared to the corresponding CT data (Section 5.1.1).

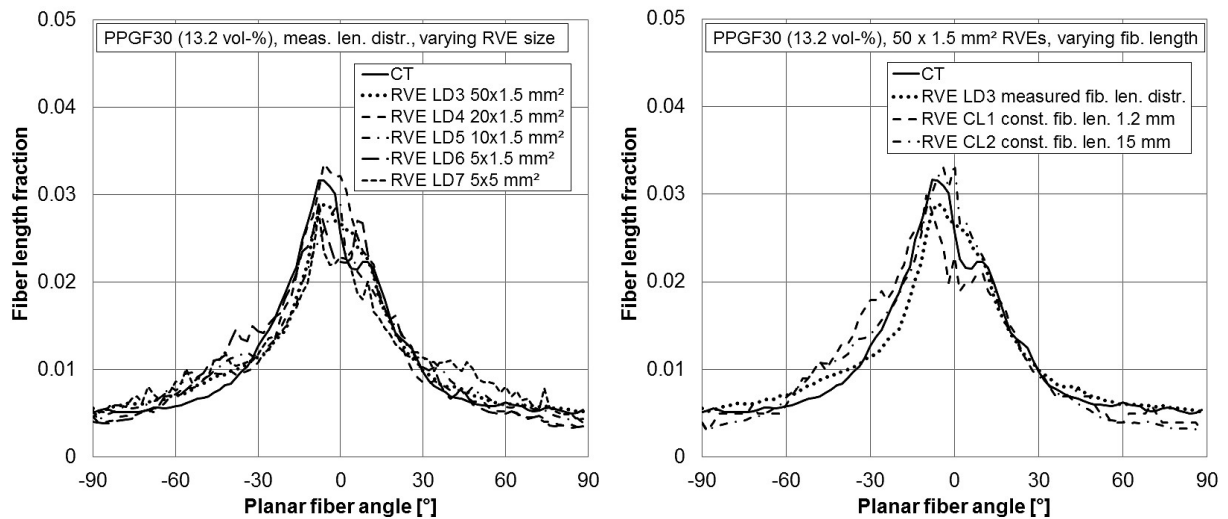


Figure 58: Planar fiber orientation distributions of the RVEs with varying RVE length (PPGF30, measured fiber length distribution, left) and with varying fiber length (PPGF30, $50 \times 1.5 \text{ mm}^2$ RVE dimensions, right) compared to the corresponding CT data (Section 5.1.1).

5.6.2 Elasticity - general

The elastic stiffness of the multidirectional RVEs of the three investigated materials is compared to the experimental (Section 3.2.2) and analytical (Section 4.6) results in Table 12. The 50 mm long RVEs LD1, LD2 and LD3 were analyzed by implicit FE simulations as described in Section 4.5.4. The table specifies the effective elastic modulus of LFT in flow (E_1) and transverse direction (E_2). The same data is illustrated as bar chart in Fig. 59.

The constituent properties were taken from the manufacturer's data sheet [DOW03] respectively from the literature [Kim98, Gom96, Ngu08, Hin02]:

$$E_m = 1250 \text{ MPa}, \nu_m = 0.35, E_f = 72000 \text{ MPa}, \nu_f = 0.22.$$

Material	Fib. vol. frac. [%]	E_1 exp. [MPa]	E_1 num. [MPa]	E_1 an. [MPa]	E_2 exp. [MPa]	E_2 num. [MPa]	E_2 an. [MPa]
PPGF10	3.8	3052	2968	2568	2054	1999	2000
PPGF20	8.1	4435	4431	4025	2432	2568	2841
PPGF30	13.2	6649	6841	6508	3074	3148	3323

Table 12: Elastic stiffness: Experimental vs. numerical vs. analytical data. RVEs LD1, LD2 and LD3 (50 mm length) were analyzed.

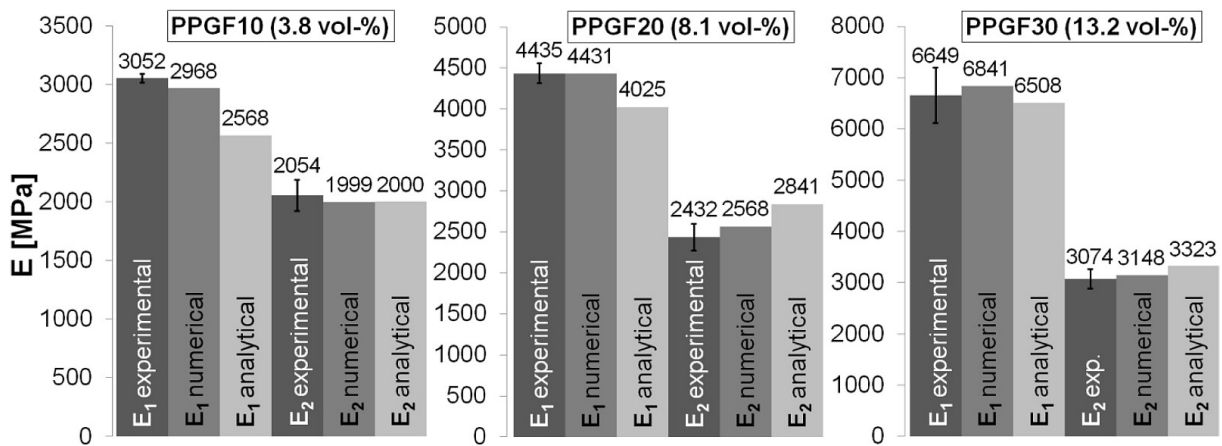


Figure 59: Elastic stiffness: Experimental vs. numerical vs. analytical data.

Overall, a good agreement between the numerical approach and the experimental values can be seen (Fig. 59). The deviation between the analytical values and the experimental ones is somewhat higher, where the values of E_1 tend to be under- and the values of E_2 to be overestimated by the analytical model. The standard deviation of the experimental values (illustrated with error bars) is in general low, whereas the values of E_2 of PPGF10 and of E_1 of PPGF30 are slightly increased.

5.6.3 Elasticity - variation of RVE size

The effect of a varying RVE length on the elastic compliance in flow direction was analyzed for RVEs with a length of 5, 10, 20 and 50 mm. The results are presented in Fig. 60. The ratio of reference length to RVE length was set to a constant value of $L_0/L_{RVE} = 0.8$, with the reference length L_0 being the distance between the node sets of Fig. 32. The elastic compliance was normalized to the value of the 50 mm RVE: $C_{norm} = C/C_{50mm}$. All RVEs feature a fiber volume fraction of 13.2 % (PPGF30) and the measured fiber length distribution.

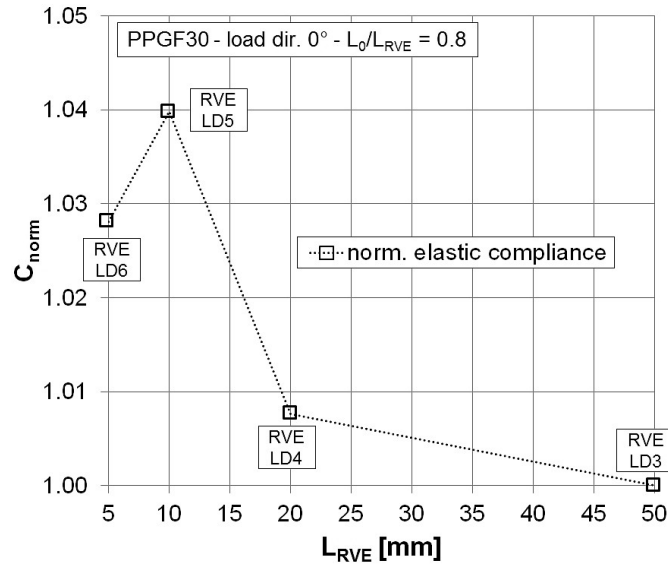


Figure 60: Effect of the RVE length on the normalized elastic compliance.

The absolute effective elastic modulus in flow (E_1) and transverse direction (E_2) of the RVEs is specified in Table 13. The relative deviation to the reference RVE (LD3, 50 mm length) is also given.

RVE	RVE length [mm]	RVE width [mm]	E_1 [MPa]	Dev. to LD3 [%]	E_2 [MPa]	Dev. to LD3 [%]
LD3	50	1.5	6841	0	3148	0
LD4	20	1.5	6789	0.77	3180	1.02
LD5	10	1.5	6579	3.99	3082	2.14
LD6	5	1.5	6654	2.81	3028	3.96

Table 13: Effect of the RVE length on the elastic stiffness of PPGF30.

From both depictions of the data (Fig. 60 and Table 13), a rather weak effect (approx. 1 % deviation) can be observed if the RVE length is reduced from 50 to 20 mm, whereas the error increases significantly (approx. 4 %) for a further reduction to 10 and 5 mm, respectively.

The fluctuation of the elastic compliance within different sized RVEs was studied by analysis of different ratios of reference length to RVE length $L_0/L_{\text{RVE}} = 0.2, 0.4, 0.6, 0.8$ for RVEs of 5, 10, 20 and 50 mm length. The results are presented in Fig. 61. The elastic compliance was normalized to the maximum value of each RVE $C_{\text{norm}} = C/C_{\text{max}}$. For the RVEs LD5 and LD6 (10 and 5 mm, respectively), a rather strong fluctuation of the value of C_{norm} can be observed, whereas the larger RVEs LD3 and LD4 (50 and 20 mm, respectively) show significantly less variation of elastic compliance.

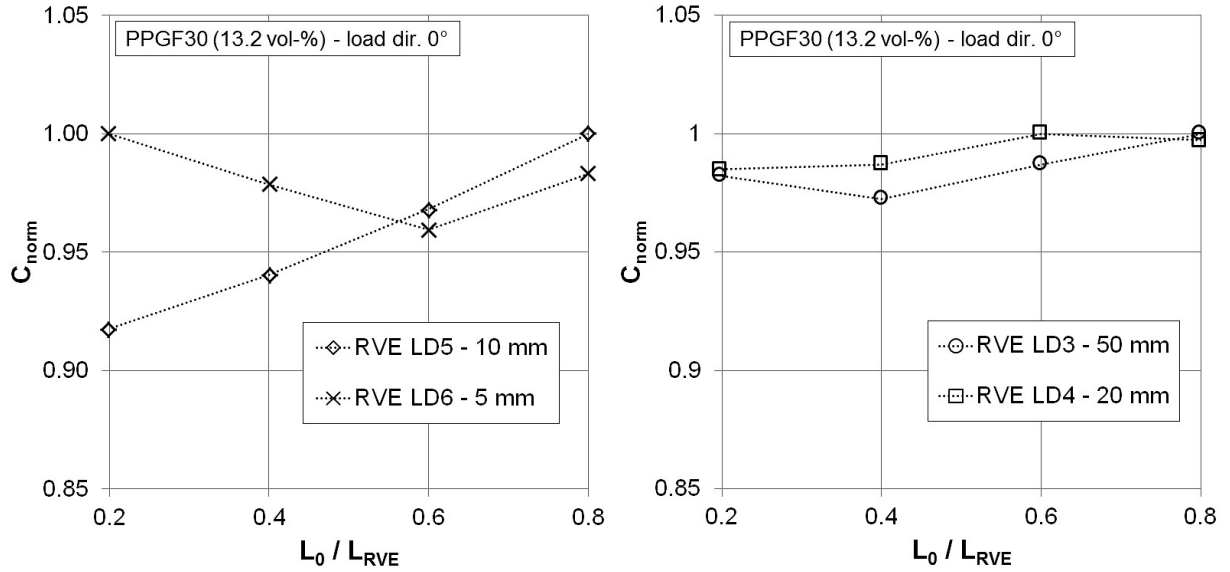


Figure 61: Fluctuation of the normalized elastic compliance within different sized RVEs.

5.6.4 Elasticity - variation of fiber length

The effect of a varying fiber length on the elastic properties of various RVEs with 13.2 % fiber volume fraction (PPGF30) is shown in Table 14.

RVE	Mean weighted fiber length \bar{l}_w [mm]	Length distribution	E_1 [MPa]	Dev. to LD3 [%]	E_2 [MPa]	Dev. to LD3 [%]
LD3	8.1 (15)	Measured distr.	6841	0	3148	0
CL1	1.2 (1.2)	Constant length	5872	16.50	3315	5.30
CL2	6.1 (15)	Constant length	6551	4.43	3262	3.62

Table 14: Effect of a varying fiber length on the elastic properties of PPGF30.

The second column (*Mean weighted fiber length*) shows the actual value of the RVE realization followed by the value of the input distribution in brackets. In this respect, the deviation of the variants LD3 and CL2 is caused by the anisotropic RVE dimensions with the RVE width being significantly smaller than the fiber length (Section 5.6.1).

Substitution of the length distribution (RVE LD3) by fibers of uniform length equal to the mean weighted length \bar{l}_w of the distribution yields only moderate deviation in elastic modulus (RVE CL2), whereas a large deviation (16.5 % in E_1) can be observed for a uniform fiber length equal to the number average \bar{l}_n of the distribution (RVE CL1).

5.6.5 Elasticity - variation of FE mesh

Aim of this study is to investigate the effects of the coarse FE mesh of the RVEs on their elastic properties. Due to the enormous size of the models, element studies of the 50 mm long RVEs could not be performed with the implicit solver (A study on much smaller structures using the implicit solver is presented in Section 5.2.3). A linear and a quadratic mesh variant of the RVE LD3 (50 x 1.5 mm², PPGF30, 13.2 vol-%) was therefore analyzed by *Abaqus Explicit* (Section 4.5.4, last paragraph).

Fig. 62 shows the stress-strain curves of 0° and 90° load direction to derive the elastic modulus whereas in Fig. 63, the kinetic energy E_{kin} is plotted against the internal energy E_{int} to ensure that E_{kin} is sufficiently small against E_{int} in order that the effects of inertia do not significantly affect the solution. E_{int} is equivalent to the strain energy for a linear-elastic material: $U = \frac{1}{2}V\sigma\varepsilon = \frac{1}{2}VE\varepsilon^2$ (with U being the strain energy, V the volume of the model, σ the stress, ε the strain and E the modulus).

In 0° load direction, the kinetic energy has approx. the same magnitude as the internal energy at the very beginning of the simulation step ($t \leq 0.0001$ s, Fig. 63 left) whereas it becomes negligible for the further progress of the simulation. Thus, the effect can be tolerated but affects the stress-strain curve to oscillate significantly. The stiffness value can finally be determined by linear approximations of the stress-strain data. Comparison of the resulting elastic moduli (Table 15) for a different increment size (the target increment size of mass scaling) reveals that no significant difference in elastic modulus can be observed, whereas the degree of oscillation is directly affected by the increment size.

In 90° load direction, no oscillation can be seen for the larger increment size of $5 \cdot 10^9$ s and therefore no additional simulation with a decreased increment size was investigated.

The resulting elastic moduli of all mesh variants of RVE LD3 are finally compared to the implicit simulation results in Table 15. The same elastic properties of the constituents were used as for the implicit calculations ($E_m = 1250$ MPa, $\nu_m = 0.35$, $E_f = 72000$ MPa, $\nu_f = 0.22$). It can be seen that a significant influence of the mesh exists for E_2 (in this case, the stiffness value of the quadratic mesh variant is about 10 % smaller than the value of the linear mesh) whereas no significant influence can be observed for E_1 .

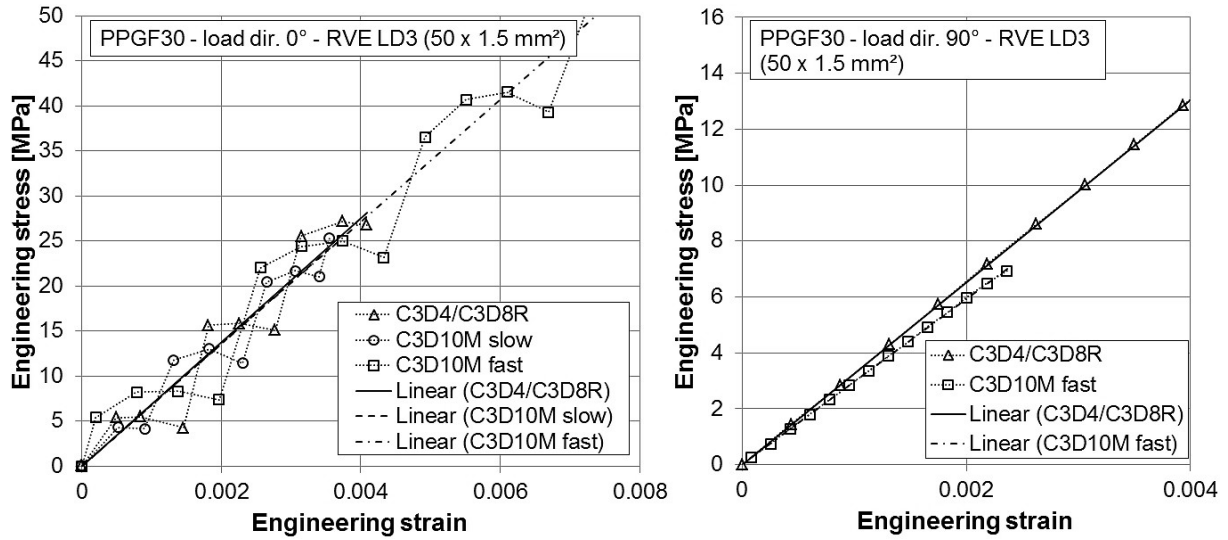


Figure 62: Stress-strain curves of the explicit element studies (left: 0° load direction, right: 90° load direction).

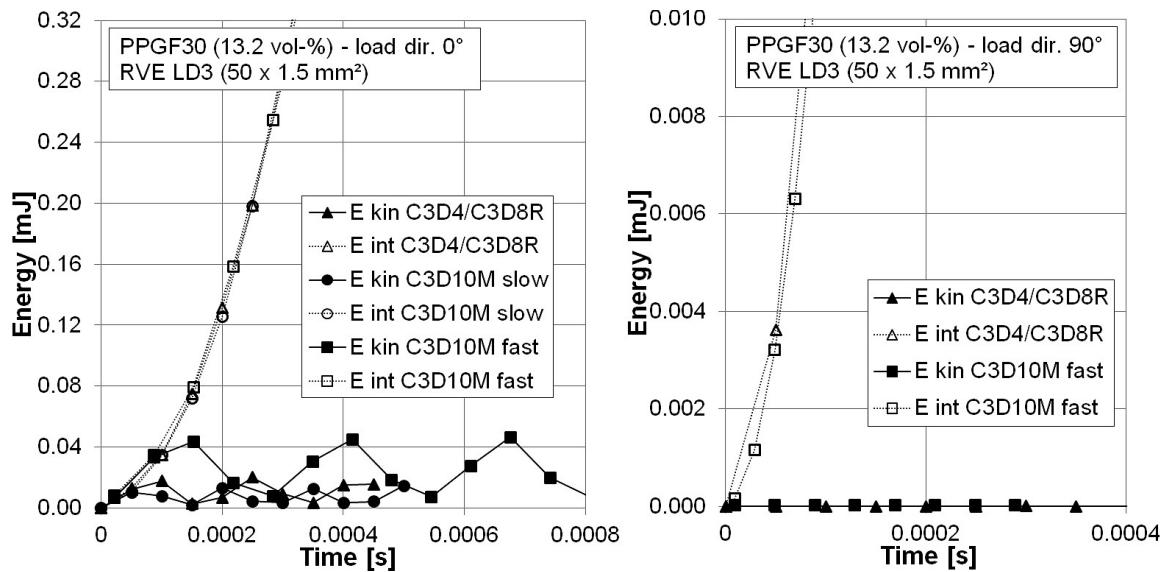


Figure 63: Development of kinetic and internal energy of the explicit element studies (left: 0° load direction, right: 90° load direction).

Element type	Simul. techn.	Increment size [s]	E_1 [MPa]	Dev. to impl. [%]	E_2 [MPa]	Dev. to impl. [%]
linear $C3D8R/C3D4$	Implicit	-	6841	0	3148	0
linear $C3D8R/C3D4$	Explicit	$1 \cdot 10^{-8}$	6879	0.56	3130	0.58
quadratic $C3D10M$	Explicit	$2.5 \cdot 10^{-9}$ (slow)	6797	0.65	-	-
quadratic $C3D10M$	Explicit	$5 \cdot 10^{-9}$ (fast)	6790	0.75	2891	8.89

Table 15: Resulting elastic moduli for different mesh variants of RVE LD3.

5.6.6 Viscoelasticity - general

In the following sections, the results of the creep simulations are presented, which were performed on several variants of the multidirectional RVEs (representing the LFT material) with the implicit FEM. The methodology is further described in Section 4.5.5. The fibers are modeled linear elastic ($E_f = 72000$ MPa, $\nu_f = 0.22$), whereas the matrix was assigned to a viscoelastic behavior by incorporation of the viscoelastic matrix model described in Section 5.2. The following results were generated under the assumption of a perfect fiber-matrix interface and are limited to the viscolastic region. The simulations therefore exclude (visco-)plastic or damage effects. Furthermore, no extrapolation to times outside the range of the underlying experimental data of the matrix model (up to $6 \cdot 10^5$ s) is legitimate, since otherwise, additional relaxation times had to be included in the model. Therefore, most of the creep results are evaluated based on their absolute uniaxial strain ε within time range from 0 to $6 \cdot 10^5$ s. A more detailed description of the range of validity of the modeling approach can be found in Section 6.2.2.

The creep curves of the RVE simulations of all investigated material variants (PPGF10, PPGF20 and PPGF30), two load directions (0 and 90° relative to flow direction) and various stress levels (three in 0° , two in 90°) are compared to their corresponding validation experiment on a LFT specimen in Fig. 64 - 69.

The creep curve of each experiment was offset by a constant value of strain in such a way that its elastic strain at the time of the load application (instantaneous strain at the beginning of the creep experiment) was equal to the corresponding mean value of elastic stiffness for each material variant, specified in Table 12 and Fig. 59 and determined by quasi-static tensile tests. This procedure was necessary since the tactile strain measurement by means of a clip-on extensometer is not reliable at the time of the sudden load application in contrast to the creep period, where no abrupt changes in load or vibrations occur.

The RVE simulations were carried out under application of two different sets of parameters of the viscoelastic matrix model (denoted by *original* and *modified* in the following). The original parameters are exclusively based on experimental findings and are described in Section 5.2.1. The derivation of the modified paramaters is detailed in Section 5.2.3. The modified parameters were inversely determined based on element studies and compensate the observed effect of the coarse matrix mesh of the RVEs to a certain amount.

Overall, a good agreement between the validation experiments and the simulations can be observed (Fig. 64 - 69). In most cases, the experimental creep curves lie in between the simulations under application of the original and modified parameters, respectively. In 0° load direction, the difference between the simulations with the original and modified parameters is rather small, whereas in 90° load direction, the properties of the matrix are more dominant (less fibers are aligned in load direction) and consequently, the difference between the two sets of parameters is larger.

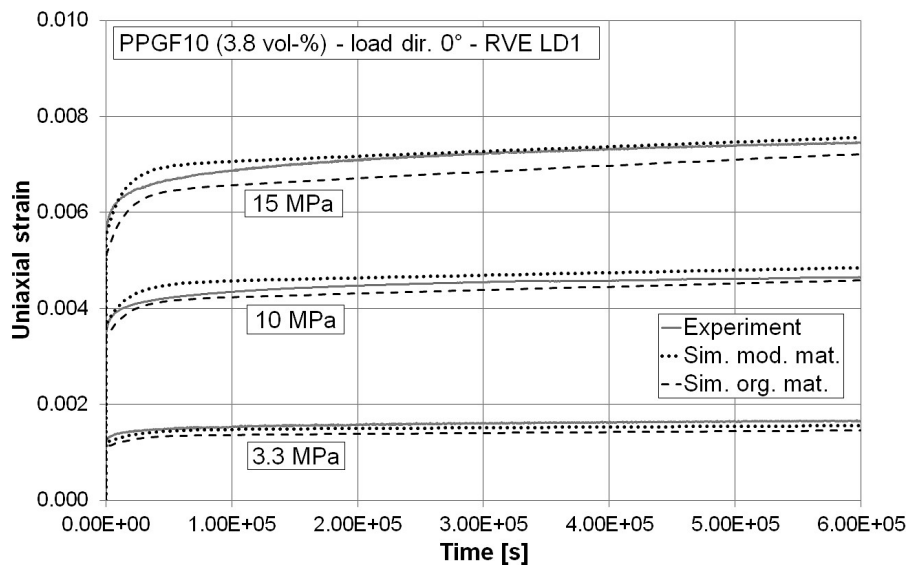


Figure 64: Creep curves of PPGF10 (3.8 vol-%) and 0° load direction. *Sim. org. mat.* and *Sim. mod. mat.* refer to the original / modified parameters of the matrix model.

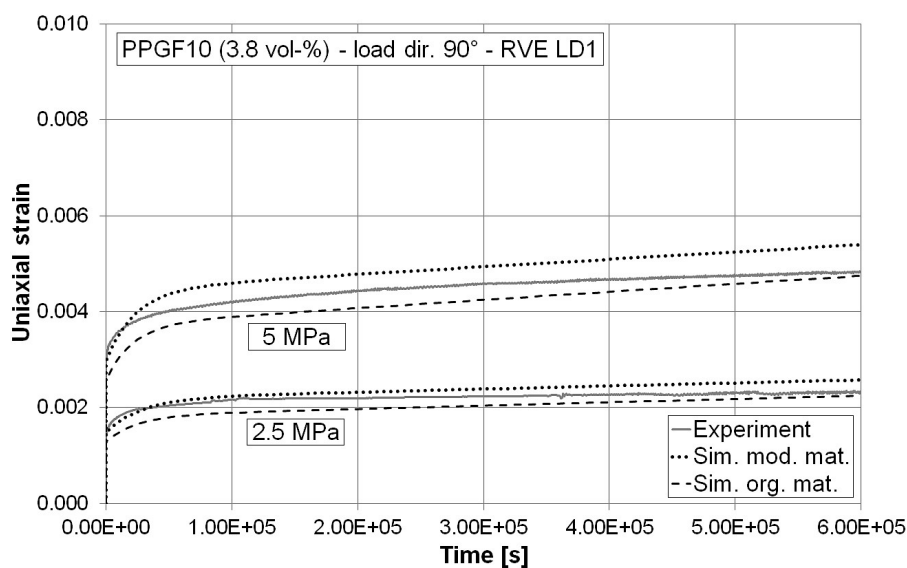


Figure 65: Creep curves of PPGF10 (3.8 vol-%) and 90° load direction. *Sim. org. mat.* and *Sim. mod. mat.* refer to the original / modified parameters of the matrix model.

In 0° load direction, the creep rates are rather well predicted for the lower and medium stress levels (PPGF10: 3.3 and 10 MPa - PPGF20: 10 and 20 MPa - PPGF30: 15 and 25 MPa) whereas they tend to be overestimated by the model for the highest stress levels (PPGF10: 15 MPa - PPGF20: 30 MPa - PPGF30: 40 MPa).

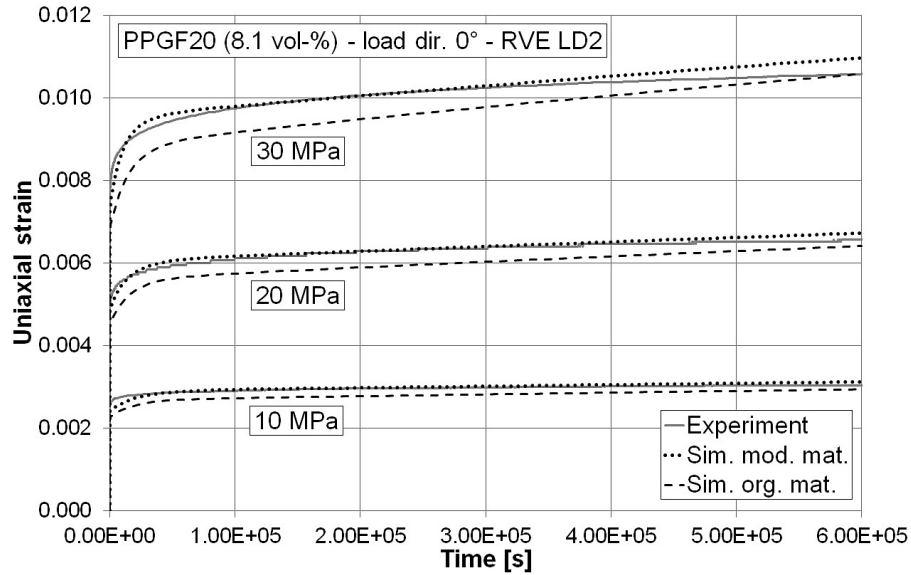


Figure 66: Creep curves of PPGF20 (8.1 vol-%) and 0° load direction. *Sim. org. mat.* and *Sim. mod. mat.* refer to the original / modified parameters of the matrix model.

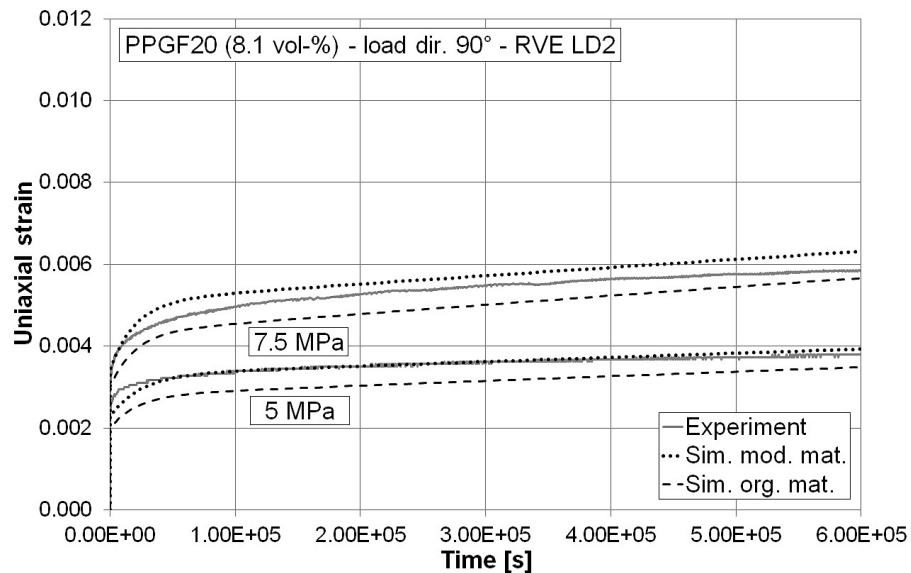


Figure 67: Creep curves of PPGF20 (8.1 vol-%) and 90° load direction. *Sim. org. mat.* and *Sim. mod. mat.* refer to the original / modified parameters of the matrix model.

In 90° load direction, the creep rates are significantly overestimated by the simulations for all material variants and stress levels. This is likely due to the drastically reduced RVE dimensions in transverse direction (PPGF30: 1.5 mm - PPGF20 & PPGF10: 2.75 mm, see Table 11) compared to the flow direction (50 mm for all materials). Thus, the structures do not represent the fiber length distribution adequately in 90° direction which likely explains the overestimated creep rates in this case.

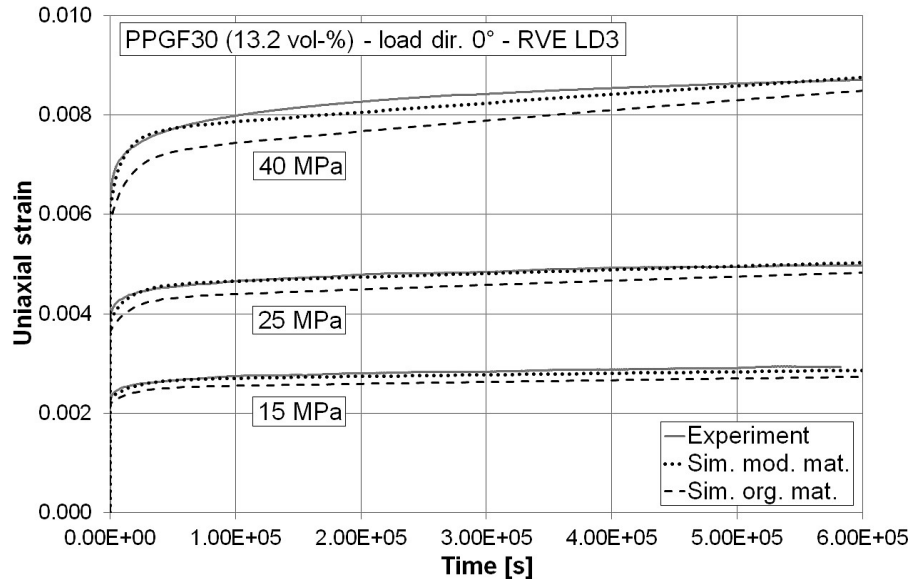


Figure 68: Creep curves of PPGF30 (13.2 vol-%) and 0° load direction. *Sim. org. mat.* and *Sim. mod. mat.* refer to the original / modified parameters of the matrix model.

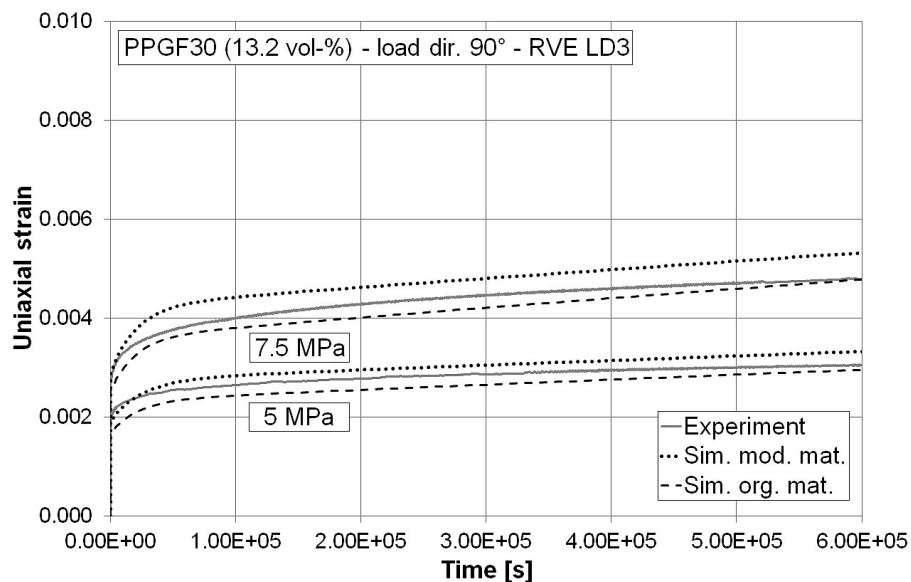


Figure 69: Creep curves of PPGF30 (13.2 vol-%) and 90° load direction. *Sim. org. mat.* and *Sim. mod. mat.* refer to the original / modified parameters of the matrix model.

5.6.7 Viscoelasticity - variation of RVE size

The effect of a varying RVE length on the creep rate in flow direction was analyzed for RVEs with a length of 5, 10, 20 and 50 mm. The results are presented in Fig. 70. The ratio of reference length to RVE length was set to a constant value of $L_0/L_{\text{RVE}} = 0.8$, with the reference length L_0 being the distance between the node sets of Fig. 32. The creep rate of the second period between $2 \cdot 10^5$ and $6 \cdot 10^5$ s (determined by linear fits to the creep curves of the RVEs in analogy to Fig. 55) was normalized to the value of the 50 mm RVE: $\dot{\epsilon}_{\text{norm}} = \dot{\epsilon}/\dot{\epsilon}_{50\text{mm}}$. The simulations were performed at a stress level of 40 MPa and with the modified material parameters of the viscoelastic matrix model (Section 5.2.3).

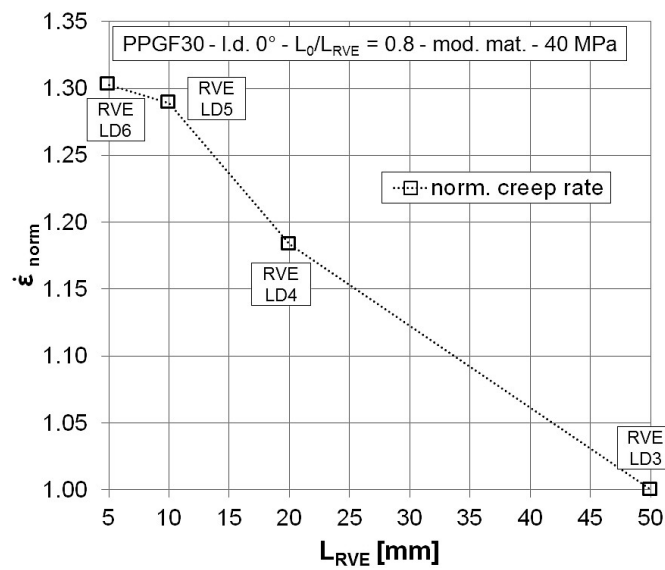


Figure 70: Effect of the RVE length on the normalized creep rate.

In Fig. 71, the effect of a varying RVE length on the creep curves in flow direction is shown (the same parameters were used as for Fig. 70).

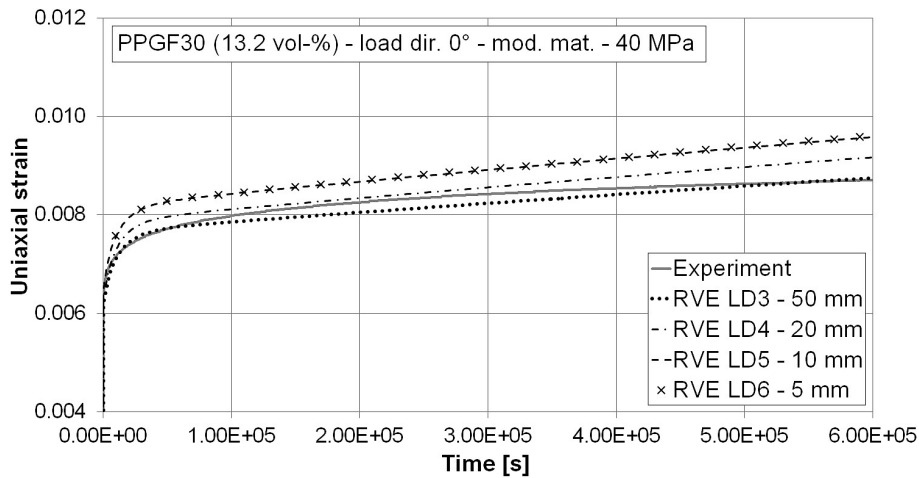


Figure 71: Creep curves of multiple RVEs with a varying RVE length.

Both figures show a large effect of the RVE size on the creep rate: Decreasing the RVE length from 50 to 20 mm affects the creep rate to increase approx. 20 %. Further reduction to 10 mm still has a significant effect, whereas only negligible deviation between 10 and 5 mm can be observed.

The fluctuation of the creep rate within different sized RVEs was studied by analysis of different ratios of reference length to RVE length $L_0/L_{RVE} = 0.2, 0.4, 0.6, 0.8$ and RVEs of 5, 10, 20 and 50 mm length. The results are presented in Fig. 72. The creep rate is normalized to the maximum value of each RVE $\dot{\epsilon}_{\text{norm}} = \dot{\epsilon}/\dot{\epsilon}_{\text{max}}$.

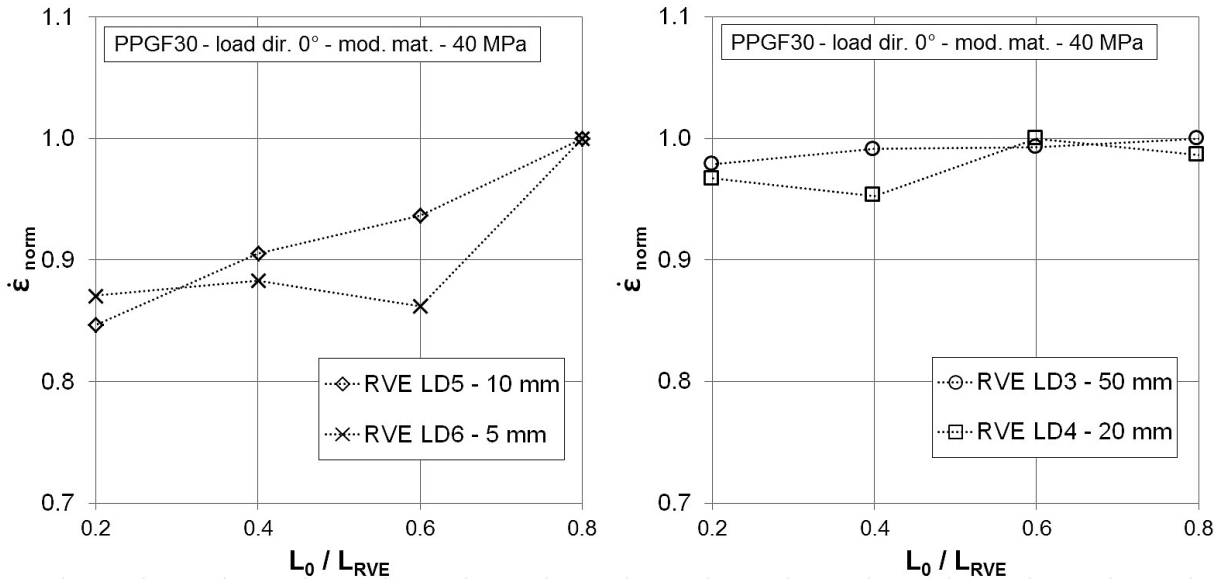


Figure 72: Fluctuation of normalized creep rate within different sized RVEs.

A strong variation of the creep rate within the RVEs LD5 and LD6 (10 and 5 mm, respectively) can be observed, whereas the fluctuation is significantly weaker within the longer RVEs LD3 and LD4 (50 and 20 mm, respectively).

5.6.8 Viscoelasticity - variation of fiber length

Fig. 73 shows the effect of a varying fiber length on the creep curves of PPGF30 in 0° load direction at a stress level of 40 MPa.

A significant, but rather moderate deviation in their creep behavior can be observed if the fiber length distribution (RVE LD3) is substituted by a uniform fiber length of 15 mm (RVE CL2, representing the mean weighted length \bar{l}_w of the distribution), whereas a huge difference can be seen for RVE CL1 with a uniform fiber length of 1.2 mm, representing the number average fiber length \bar{l}_n of the length distribution. It is worth mentioning that the deviations always effect the creep rate of the second period (where the rate is approx. constant) in together with an offset of the curves which is larger than the pure difference in instantaneous elastic strain. If the creep rates are evaluated by linear fits of the creep curves between $2 \cdot 10^5$ and $6 \cdot 10^5$ s, a relative increase of $\dot{\epsilon}_{\text{CL1}}/\dot{\epsilon}_{\text{LD3}} = 1.94$

is found comparing RVE CL1 and LD3, whereas the increase is significantly smaller for RVE CL2 which amounts to $\dot{\epsilon}_{CL2}/\dot{\epsilon}_{LD3} = 1.16$.

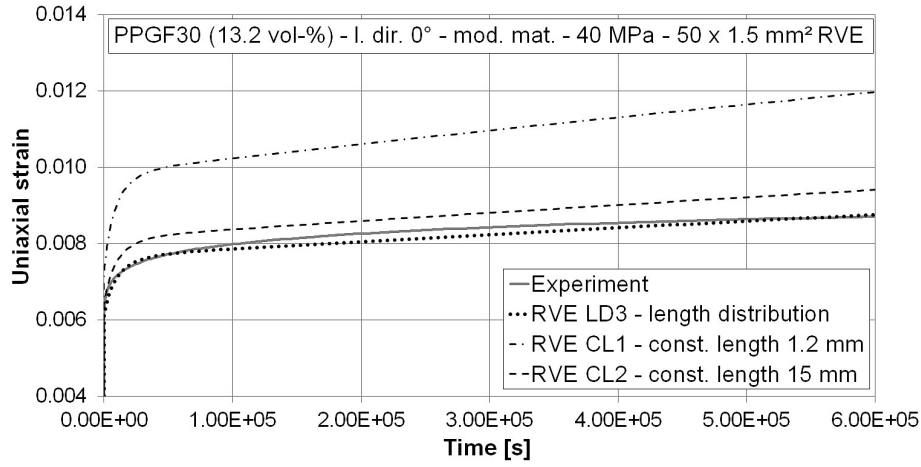


Figure 73: Creep curves of RVEs with varying fiber length.

5.6.9 Viscoelasticity - variation of model formulation

In order to study the effects of stress redistribution within the matrix due to its nonlinear viscoelastic behavior (regions exposed to a higher stress will relax faster, see Fig. 42), the model formulation was varied for one RVE variant and the highest investigated stress level of 40 MPa. The highest stress level was chosen, since here, the nonlinear effects can be expected to be large.

Fig. 74 compares the RVE response under application of the *fully nonlinear* material model as derived in Section 4.1.8 with a so-called *pseudo nonlinear* variant: An elastic trial stress was applied at the first increment ($t = 0$). The viscoelastic model parameters for each material point were then determined based on the trial stress and were kept constant for the remaining part of the simulation. In contrast, the *fully nonlinear* model determines the parameters for each time increment anew.

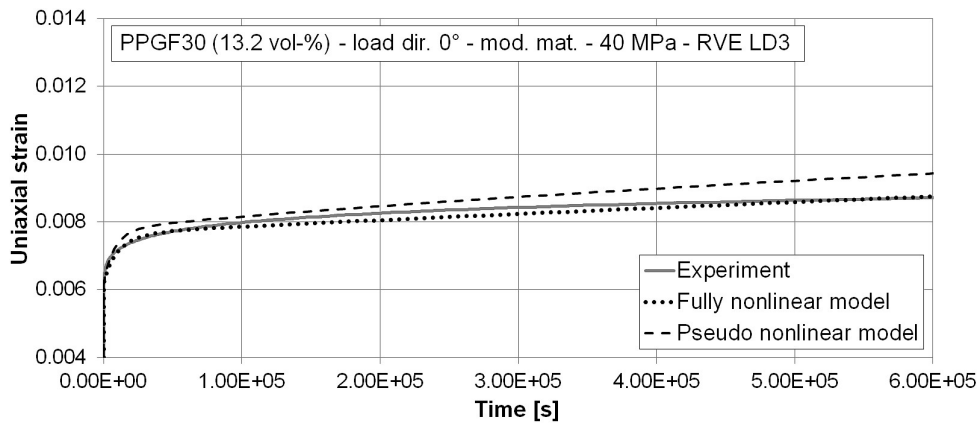


Figure 74: Creep curves under variation of the formulation of the matrix model.

The deviations between both model formulations are indeed significant and affect mostly the creep rate. As expected, the stress redistribution within the matrix, which is exclusively described by the *fully nonlinear* model, slows the creep rate down compared to the *pseudo nonlinear* variant, where this kind of stress redistribution is deactivated. Evaluation of the creep rates between $2 \cdot 10^5$ and $6 \cdot 10^5$ s reveals a relative increase of $\dot{\epsilon}_{\text{pseudo}}/\dot{\epsilon}_{\text{fully}} = 1.37$ which supports the visual impression of the curves.

In order to investigate further simplifications of the model, a pure *linear viscoelastic* variant was also applied. Here, the model parameters remain constant and equal for all material points. Fig. 75 shows the RVE response under a creep load of 40 MPa, where the *linear viscoelastic* model was applied with prescribed values of indicator stress from 2.5 to 12.5 MPa which define the model parameters E_1 , η_0 and η_1 (Fig. 50).

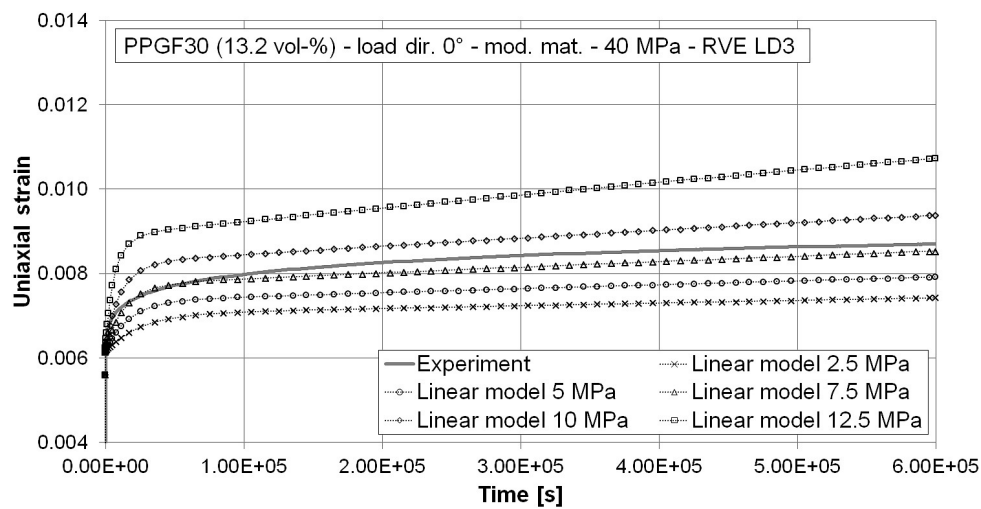


Figure 75: Creep curves for varying parameters of the linear viscoelastic matrix model.

As it can be seen in Fig. 75, the range covered by all variants of model parameters is large. This is supported by the evaluation of the creep rates, which reveals a relative deviation between the two boundary curves of $\dot{\epsilon}_{2.5 \text{ MPa}}/\dot{\epsilon}_{12.5 \text{ MPa}} = 4.65$. It is therefore not possible to apply a *linear viscoelastic* model within reasonable accuracy to reproduce the creep experiments - the stress dependence of the model parameters must somehow be considered.

Since an explicit time integration scheme is used for all variants of the viscoelastic model, the solution might be affected by the size of the time increments of the FE simulation. If the variation of load is too fast within a time increment, the assumption of a constant stress rate $\dot{\sigma} = \Delta\sigma/\Delta t$ and constant model parameters E , η for the current increment - as considered by all variants of the viscoelastic model - might be an incorrect simplification (Section 4.1.7). Motivated by these facts, the effect of a varying increment size was investigated by an exemplary study, in which the increment size was limited to a very small value of 5 s. RVE LD4 with dimensions of $20 \times 1.5 \text{ mm}^2$ was chosen due to computational performance (Computation of the

50 mm long RVE LD3 would have been too expensive since the limitation to 5 s increment size extensively increases the total number of increments). In Fig. 76, the simulation with the limited increment size of 5 s is compared to the variant where the increment size was chosen automatically by *Abaqus*, as applied for all presented creep studies: Here, the initial size of the increment was specified to 0.1 s and successively increased until the upper limit of 10^4 s was reached (more details are specified in Section 4.5.5). Therefore, the increment size remains sufficiently small in the beginning of the creep period (first phase) with a considerable change of strain over time, whereas the increments are chosen larger for the second period after relaxation of the Kelvin-Voigt element (exclusively governed by the viscous strain component and characterized by a smaller and constant strain rate).

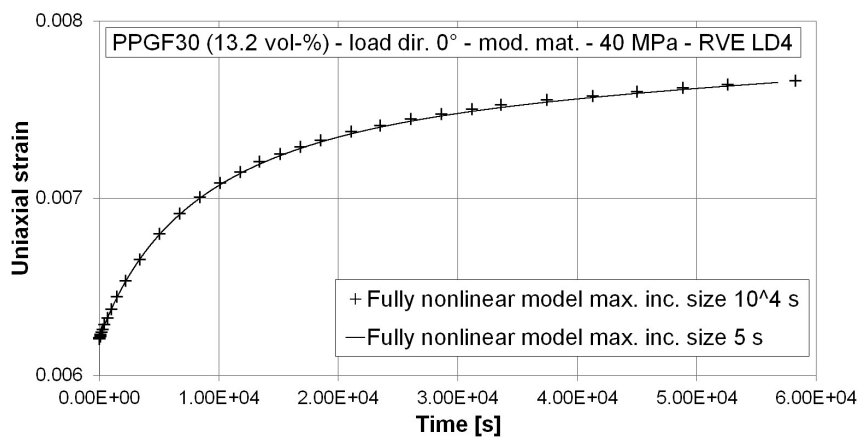


Figure 76: Creep curves of simulations with a varying size of the time increments.

As it can be seen in Fig. 76, no significant deviation between both variants with different sized time increments exists and thus, the automatically chosen time increments (max. size of 10^4 s) are sufficiently small for the investigated creep scenarios.

5.6.10 Viscoelasticity - contour plots

Fig. 77 shows the stress redistribution after the application of a creep load of 40 MPa within a section of RVE LD3 (view cut at half thickness). The upper plot depicts the von Mises stress at $t = 600$ s with a maximum value within the fibers of approx. 1200 MPa. The lower plot shows the state at $t = 600\,000$ s with a maximum fiber stress of approx. 2000 MPa. The observed stress redistribution from the matrix to the fibers happens because of the steady softening of the matrix during the creep period and is similar for all variants of the matrix model (the *fully nonlinear* model was applied here).

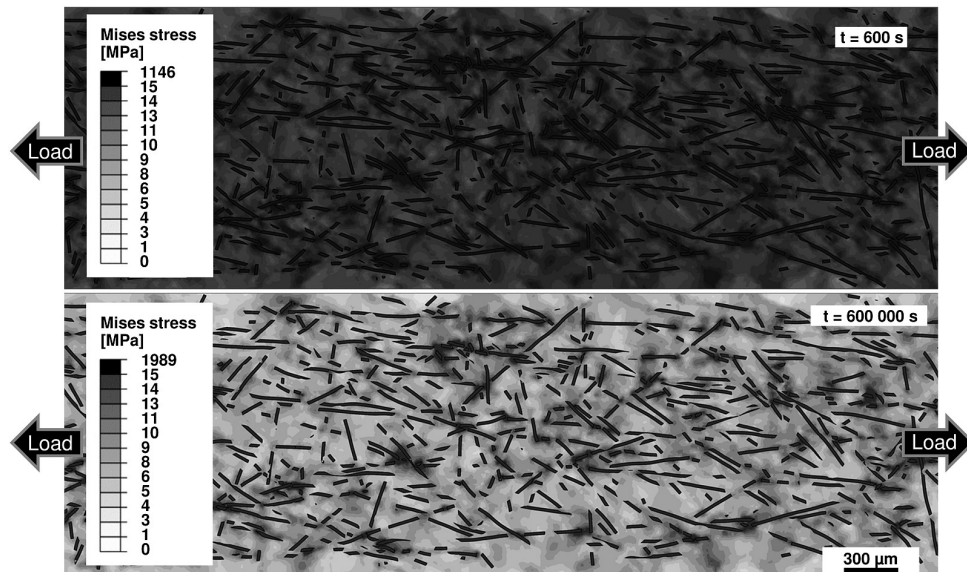


Figure 77: Redistribution of Mises stress σ_M (Eq. 53) within RVE LD3.

Similar plots of the equivalent deviatoric strain resp. the hydrostatic strain of the same structure under the same boundary conditions are depicted in Fig. 78 and 79. It is worth noting that the maximum value of the color scale is chosen to 0.05 for Fig. 78 (equivalent deviatoric strain) and significantly smaller to 0.01 for Fig. 79 (hydrostatic strain). Thus, it can be concluded that the hydrostatic strain is significantly smaller anywhere and to any time within the investigated structure. Furthermore, the regions under a high hydrostatic strain are significantly smaller than those of a high equivalent deviatoric strain. Hence, the hydrostatic strain decays within a shorter distance.

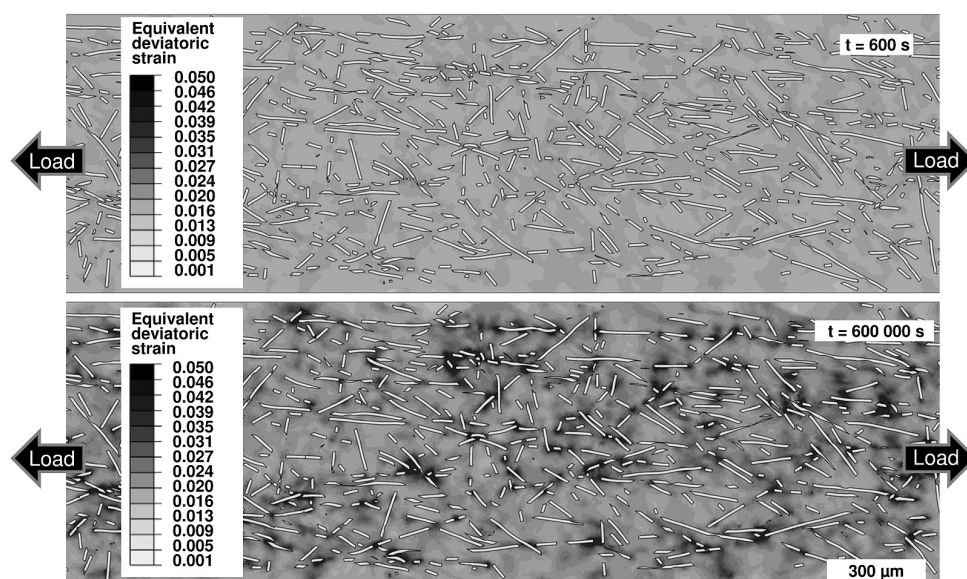


Figure 78: Redistribution of eq. dev. strain ε'_{eq} (Eq. 62) within RVE LD3.

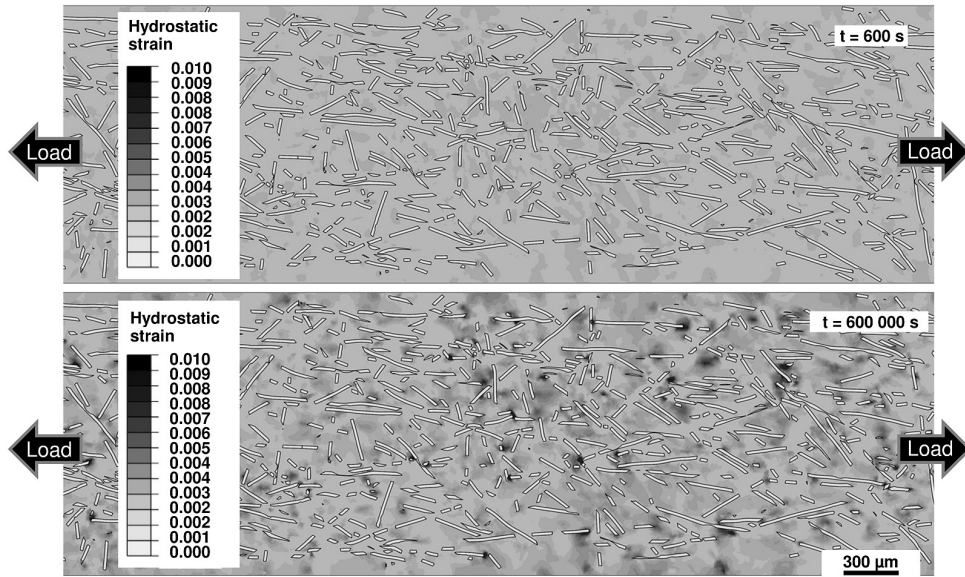


Figure 79: Redistribution of hydrostatic strain ε_H (Eq. 61) within RVE LD3.

5.6.11 Plasticity and damage - deformation and damage mechanisms

In this section, the results of the modeling of the deformation and damage behavior of LFT are shown. The material with the highest fiber fraction (PPGF30, 13.2 vol-%) was investigated in this respect under application of the explicit FEM (Section 4.5.6), the plastic matrix model (Section 4.2), the interface model (Section 4.3) and a brittle fracture model of the fibers. It is worth noting that the applied models in this section are completely independent of the ones used for the implicit simulations of elastic and viscoelastic properties.

The matrix and interface properties were chosen as described in Section 5.3 and 5.4. The fibers were assigned to elastic properties ($E_f = 72000$ MPa, $\nu_f = 0.22$). A brittle fracture model with a mean value of failure stress ($\sigma_f = 2500$ MPa) from the middle of the range which is specified in the literature [Kim98, Adv14, And02, Tho14, Zha00a, Zha00b, Wan97] was activated in all simulations accounting for fiber damage: If the failure stress is reached for an element, it is immediately deleted.

Fig. 80 compares the stress-strain curve of a characteristic LFT validation experiment with the simulations for a load direction of 0° , whereas the results for 90° are presented in Fig. 81. The 50 mm long RVE LD3 was analyzed in 0° load direction, the 5 mm long RVE LD7 in 90° .

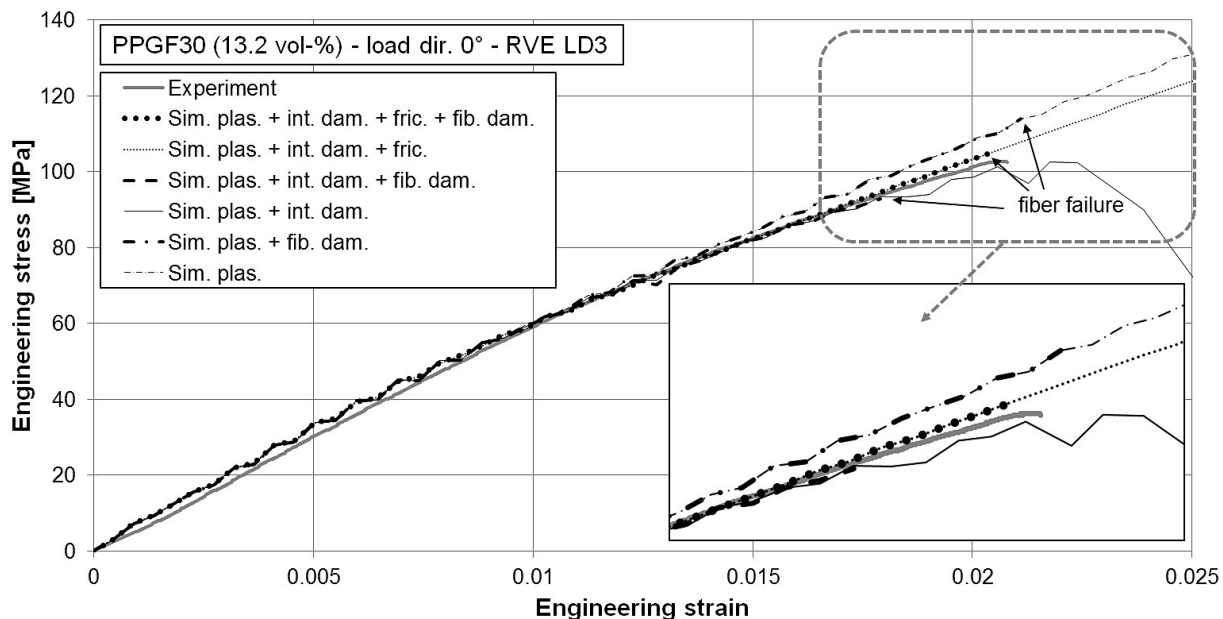


Figure 80: Simulation of the deformation and damage mechanisms of PPGF30 in 0° load direction. The different mechanisms are denoted by: *Sim. plas.*: Matrix plasticity and elastic fibers / *Sim. plas. + fib. dam.*: Matrix plasticity and brittle fiber failure / *Sim. plas. + int. dam.*: Matrix plasticity and interface debonding / *Sim. plas. + int. dam. + fib. dam.*: Matrix plasticity, interface debonding and brittle fiber failure / *Sim. plas. + int. dam. + fric.*: Matrix plasticity, interface debonding and post-debonding friction / *Sim. plas. + int. dam. + fric. + fib. dam.*: Matrix plasticity, interface debonding, post-debonding friction and brittle fiber failure (all mechanisms).

In general, similar effects of the different mechanisms can be observed for both load directions (Fig. 80 and 81): At higher strains close to the point of fracture, the slope of the experimental stress-strain curve is overestimated by the simulations which do not account for interface damage and thus consider a perfect interface. If interface debonding is active, the slope of the experimental curve can be accurately reproduced until the point of fracture. For the simulations, the point of fracture is determined by the first occurrence of failure of fiber elements since no matrix damage can currently be modeled. This point is marked by the arrows. For the simulations where fiber damage was deactivated, the further development of the stress-strain curves beyond the point of fracture is depicted by the thin lines. The variants which account for interface damage but no post-debonding friction then feature a drop of load (thin lines), whereas no such drop can be observed if friction was activated.

It is remarkable that in 0° load direction (Fig. 80), the best agreement between the simulations and the experiment can be observed for the variant which accounts for all mechanisms (matrix plasticity, interface damage, post-debonding friction and fiber damage), whereas the point of fracture is significantly underestimated if post-debonding friction is deactivated (only matrix plasticity, interface damage and fiber damage are considered).

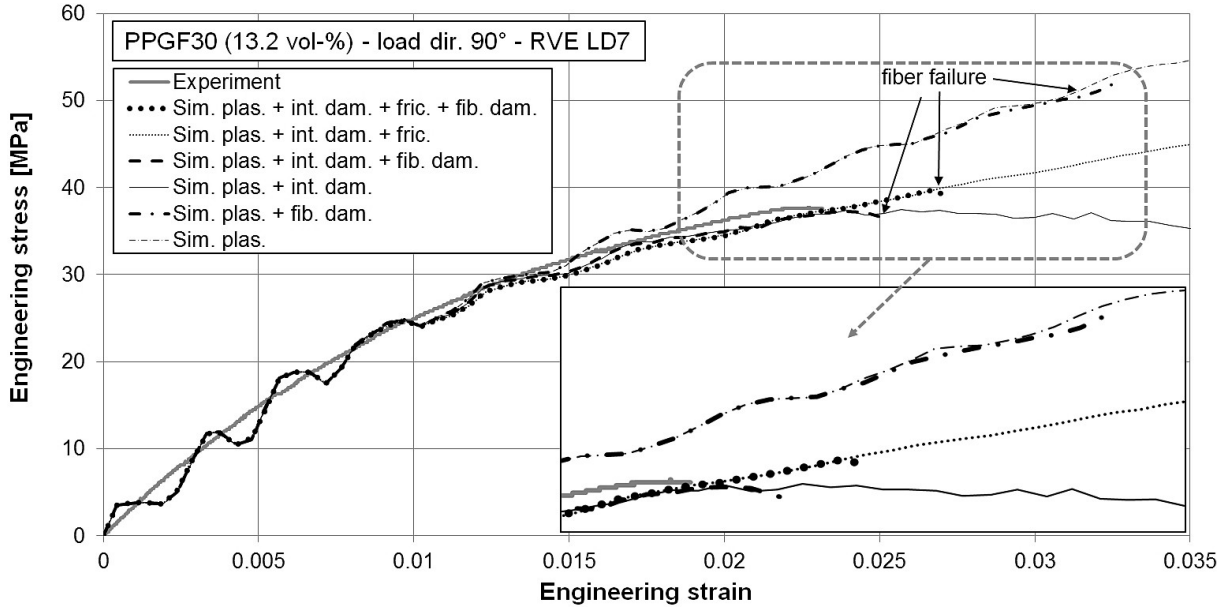


Figure 81: Simulation of the deformation and damage mechanisms of PPGF30 in 90° load direction. The different mechanisms are the same as in Fig. 80.

The variant accounting exclusively for matrix plasticity and fiber damage (perfect interface) does not reproduce the shape of the stress-strain curve accurately, but the point of fracture is only weakly overestimated.

In 90° load direction (Fig. 81), the difference between the variant with a perfect interface (no interface damage) deviates very strongly from the remaining variants and the experiment: The softening of the curve toward the point of fracture is not captured and the values of fracture stress and strain are strongly overestimated. Based on the agreement with the experimental data, the simulation variant with matrix plasticity, interface damage and fiber damage (but no post-debonding friction) seems to be the most realistic one, even if the effect of activating post-debonding friction is very weak in this case.

5.6.12 Plasticity and damage - experimental scatter

In the following, the degree of experimental scatter is visualized by depicting three experimental curves in together with the simulations (accounting for all mechanisms). For this purpose, the data of 0° load direction is shown in Fig. 82, whereas the results for 90° are presented in Fig. 83. Furthermore, the degree of nonlinearity of the stress-strain curves is emphasized by additional plots of the mean values of the elastic moduli in both directions (E_1 and E_2 , respectively, see Table 12). It is worth noting that the elastic moduli were determined on different specimens than the ones which were loaded until fracture.

In 0° load direction (Fig. 82), the observed scatter with respect to the point of fracture is rather low, whereas significant deviation in the shape of the curves can be observed. It is remarkable that two of the three curves almost coincide, which furthermore agree

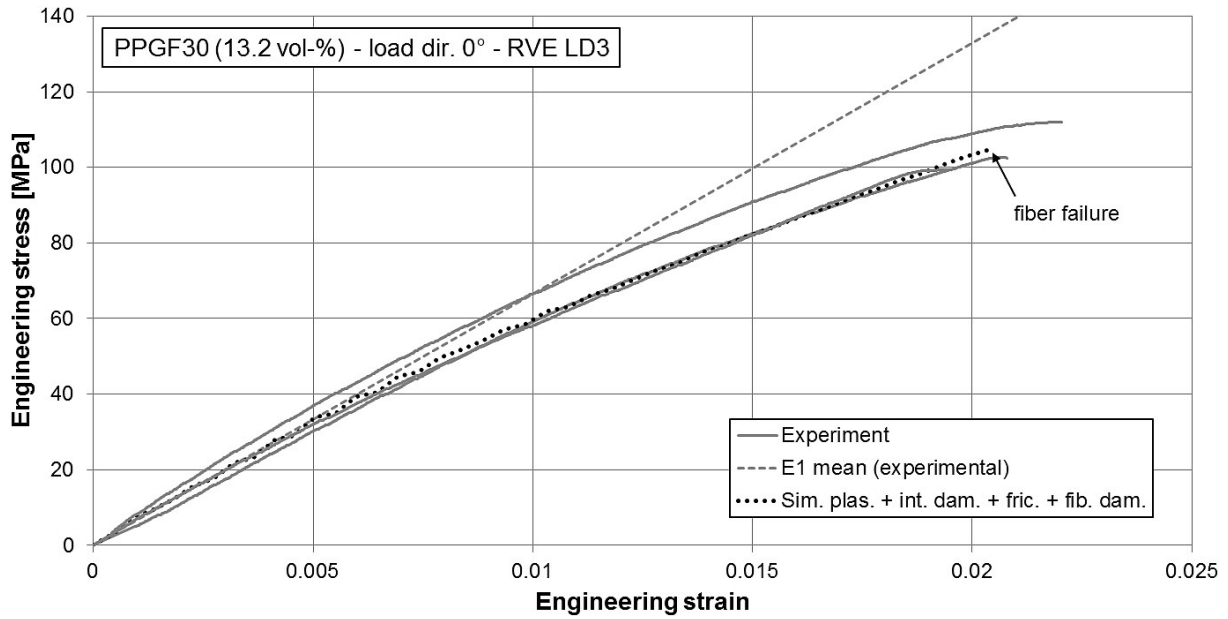


Figure 82: Experimental scatter of PPGF30 for 0° load direction.

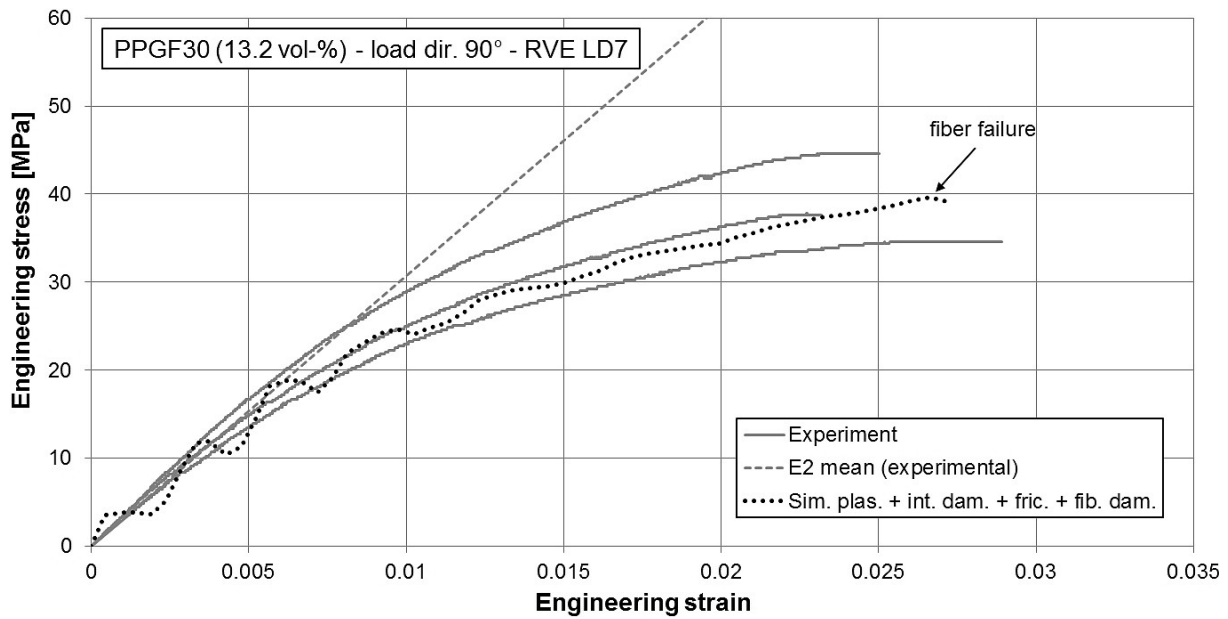


Figure 83: Experimental scatter of PPGF30 for 90° load direction.

very well with the mean value of elastic stiffness in their initial phase at low strains. Therefore, the third experiment with larger deviations likely represents an outlier. The degree of nonlinearity of the curves is rather weak, but significant: If the material would be modeled linear elastic, the stress would be overestimated by approx. 30 % at a strain of 0.02.

For a load direction of 90° (Fig. 83), the scatter is significantly larger than for 0° . The middle curve which was considered as the representative experiment for the validation of the simulation agrees very well with the mean value of elastic stiffness in its initial phase. Therefore, the choice seems to be justified. It is remarkable that the degree of nonlinearity is very large for this load direction: An elastic modeling of the material would result in an overprediction of stress of approx. 100 % at a strain of 0.02.

5.6.13 Plasticity and damage - variation of RVE size

A variation of the RVE size was also studied with respect to plasticity and damage, even if no systematic variation in multiple steps was performed as for the elastic and viscoelastic properties. Fig. 84 shows the effects of a varying RVE size (5 vs. 50 mm length) for a load direction of 0° . Both RVEs feature the measured fiber length distribution and account for all mechanisms.

It can be clearly observed that the stress-strain curve of the RVE with reduced dimensions (LD7, 5 mm) deviates significantly from the large one (LD3, 50 mm) above a strain value of approx. 0.01. The fracture strain is overestimated, whereas the fracture stress does not significantly deviate from the large RVE and the experiment. Furthermore, the initial stiffness of both RVEs is very similar.

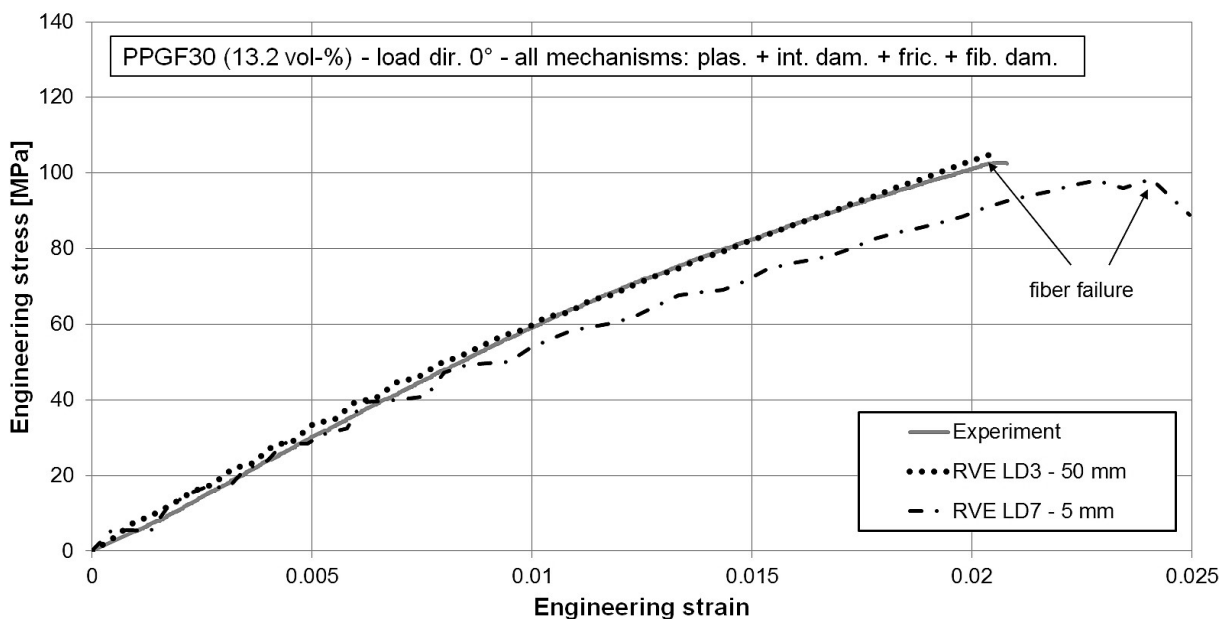


Figure 84: Effect of RVE size analyzed for PPGF30 and 0° load direction.

5.6.14 Plasticity and damage - variation of fiber length

In analogy to the elastic and viscoelastic properties, a variation of the fiber length was studied. Substituting the fiber length distribution (RVE LD3), a uniform fiber length of 1.2 mm (equal to the number average fiber length \bar{l}_n of the distribution) is implemented into RVE CL1, whereas RVE CL2 features a uniform fiber length of 15 mm (representing the weight average fiber length \bar{l}_w of the distribution). Fig. 85 shows the effects of a varying fiber length for 0° load direction and a RVE size of $50 \times 1.5 \text{ mm}^2$. The simulations represented by the bold lines account for all mechanisms, whereas the thin lines refer to the simulations which exclusively account for matrix plasticity and interface damage to visualize the additional load transfer which is enabled under consideration of post-debonding friction (bold lines).

It can be seen (Fig. 85, bold lines) that the difference between RVE LD3 and CL2 is very small and thus, the weight average fiber length \bar{l}_w seems to be an appropriate substitute for the length distribution, whereas the number average fiber length \bar{l}_n (RVE CL1) yields a strong underprediction of the failure stress and the shape of its stress-strain curve deviates significantly from the remaining variants. If post-debonding friction is deactivated (thin lines), the failure strain of RVE CL1 collapses to approx. half of its initial value (under consideration of friction, bold line) and the composite fails catastrophically by fiber pullout. No such drastic effect can be observed for the remaining RVEs, where the level of the maximum stress remains similar if friction is deactivated.

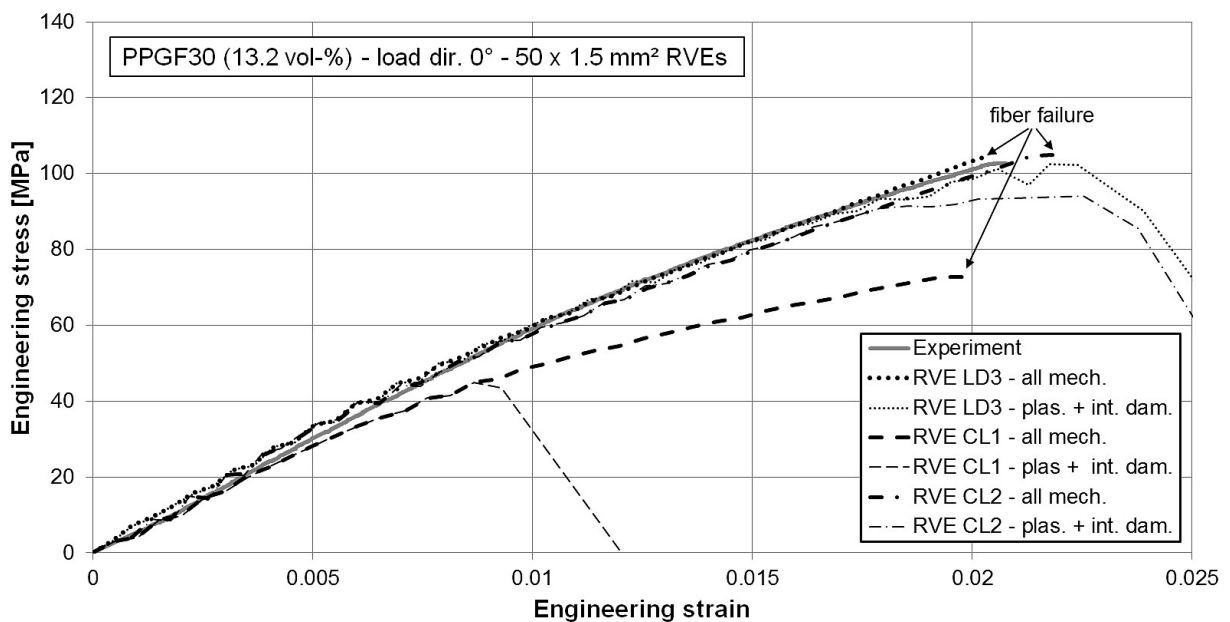


Figure 85: Effect of fiber length analyzed for PPGF30 and 0° load direction.

5.6.15 Plasticity and damage - contour plots

Fig. 86 shows the damage localization within the cohesive zone elements of the RVE CL1 at the time of its failure by fiber pullout, when no post-debonding friction was considered (thin line in Fig. 85), which would prevent such localization within the cohesive zones. The legend represents the scalar stiffness reduction factor D of the damage evolution law (Section 4.3.2). A value of 1 corresponds to a completely degraded element. Matrix and fiber elements were removed for illustration purposes.

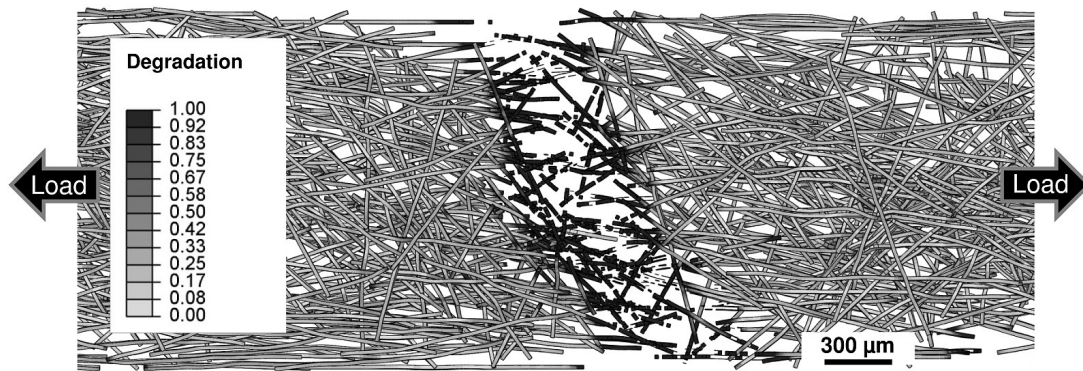


Figure 86: Damage localization within the cohesive elements of RVE CL1.

Fig. 87 shows the damage localization within the fiber elements of RVE LD3 at a nominal strain of approx. 0.02 (at the point of fracture, Fig. 80). All mechanisms (matrix plasticity, fiber-matrix debonding, post-debonding friction and fiber failure) were activated for the simulation. The legend represents the von Mises stress. Some fiber elements can actually feature a value slightly above the nominal failure stress of 2500 MPa due to their non-zero (but very small) value of damage evolution energy (a certain amount of energy must be dissipated before the element is deleted).

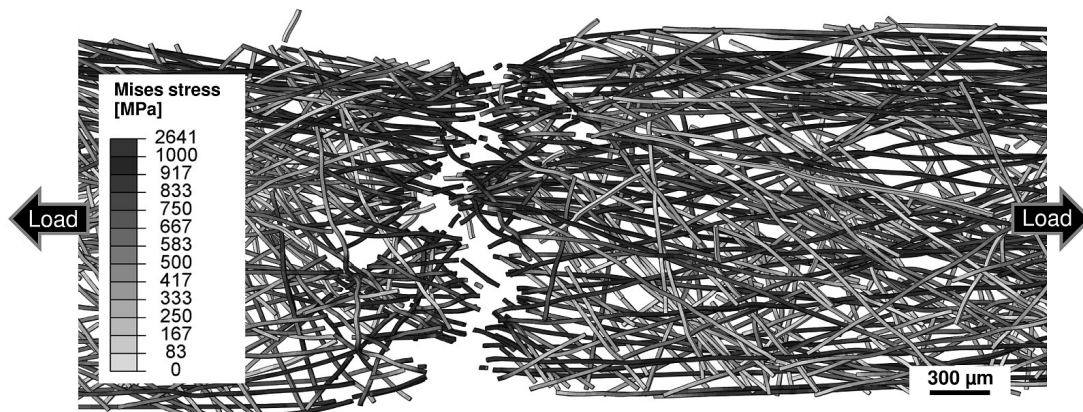


Figure 87: Damage localization within the fiber elements of RVE LD3.

6 Discussion

The discussion is divided into three main sections.

First, the *Microstructural aspects* are treated (Section 6.1) with respect to the identification and evaluation of sources of uncertainty which affect the experimental determination of the characteristic values (fiber volume fraction, fiber orientation distribution, fiber length distribution). Besides the discussion of the single aspects it is very important to incorporate their correlation and interaction. The last part of this chapter deals with the artificial reproduction of the microstructure in the form of computer models and highlights their promising features as well as current shortcomings.

The part *Constitutive models* (Section 6.2) deals with the mechanical continuum models which were applied to describe multiple aspects of the behavior of the components fiber, matrix and interface within the simulation of the LFT material. It is mandatory to clearly define their respective range of validity and limitations in order to evaluate their roles within the microstructural simulation of LFT. The treated models are the viscoelastic matrix model, which was applied to reproduce the creep behavior, the plastic matrix model used to describe the quasi-static deformation, the brittle fracture model of the fibers and the interface model to represent debonding phenomena.

Finally, the chapter *Multidirectional LFT structure* (Section 6.3) highlights the relationship between the microstructure and the effective mechanical behavior of LFT. Multiple partial models are now combined to describe different phenomena of the material. The principle effect of several characteristics, e.g. the fiber length or the size of the structures is evaluated and compared with respect to different mechanical properties. The knowledge of such relations, which is gained by the virtual laboratory, is important for the design and development of new material variants. A mechanism-based interpretation of the deformation and damage behavior of LFT is fundamental for the future development of effective mechanical models which can then be used to simulate components made from the material.

6.1 Microstructural aspects

6.1.1 Fiber volume fraction

In this work, the nominal fiber volume fraction was calculated based on the values of the mass flow rate of the manufacturing process (Section 3.1.1). The accuracy of this procedure was investigated by Tröster [Tro03] and Radtke [Rad08] amongst others. Differential weighing of multiple specimens taken from varying positions of a LFT plate support that the uncertainty with respect to the calculated values of fiber volume fraction can

be considered as low and that the nominal values are sufficiently accurate [Tro03]. For example, analysis of a 400 x 400 mm² specimen plate manufactured by compression molding with a nominal volume fraction of 13.22 % (PPGF30) revealed a minimum value of 12.41 % and a maximum value of 13.77 % [Rad08]. For most regions of the plate, the agreement to the calculated value was even better.

On the microscale, a significant fluctuation of the fiber volume fraction (the local fiber density) could be observed. In Fig. 88, the CT data of Fig. 12 is rearranged so that an exemplary fiber agglomeration is clearly visible. Such fiber agglomerations form within the material possibly as a relict of fractions of fiber rovings which were not homogeneously dispersed and infiltrated with the polymeric melt during the compounding procedure. The agglomerations can be classified as internal flaws of the material and possibly act as crack starters due to the locally missing bonding to the matrix and thus, an imperfect load transfer to the fibers.

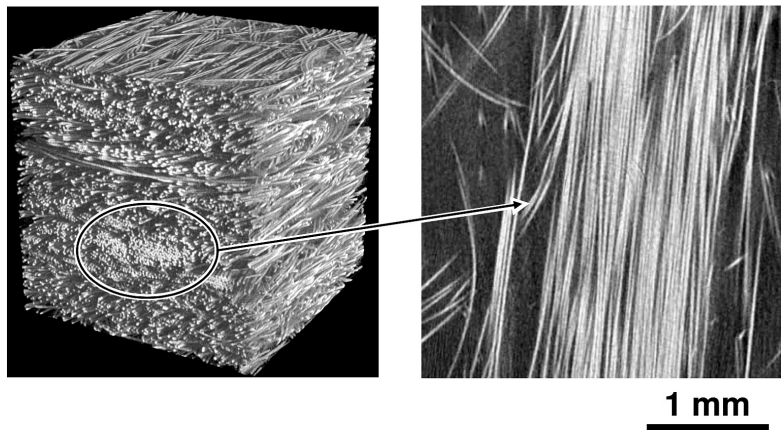


Figure 88: Fiber agglomeration observed in the 3D (left) and 2D (right) depiction of the rearranged CT data of Fig. 12.

6.1.2 Fiber orientation distribution

The applied image correlation technique (*ImageJ*) does not perform any segmentation of fibers. Each 2D slice of the CT data is analyzed independently and no connectivity of the fiber fragments can be detected. Thus, the obtained fiber orientation data represents area fractions of each single 2D image with a preferred direction. The method was validated against computer generated images containing multiple lines in which the orientation state is known and found to be suitable for an accurate reproduction of their orientation state [Fij14]. Moreover, similar methods to analyze the fiber orientation were reported in the literature. For example, the commercial fiber analysis software *FibreShape* [Fib14] was applied to analyze the planar fiber orientation in natural fiber composites and validated against manual measurements with *ImageJ* [Gra14].

The general limit of the applied image correlation technique is reached when a high degree of fiber waviness or orientation in thickness direction causes the cut through the fibers visible in the 2D slice to degrade to an ellipsoid or in the worst case, to a circle. If the majority of the fibers of the section to be analyzed show the latter phenomenon, the method becomes inaccurate and no reliable evaluation of the orientation state can be performed. However, the structure of the investigated material features layer-wise alignment of fibers with a low degree of fiber orientation in thickness direction (Fig. 12, 40, 88). Visual screening of the 2D slices of each CT scan ensured that no such circular degradation of the fibers was dominant and that the majority of the slices feature linear fiber segments (exemplary slices are depicted in Fig. 12 and 89). The procedure can therefore be considered as suitable for the analysis of the investigated material.

The studied LFT material produced by compression molding does not show a significant change of fiber orientation over the thickness of the specimen plates (An exemplary plot is shown in Fig. 13). It is therefore well justified to average the fiber orientation over the complete material thickness, resulting in a single 2D histogram or probability density function to describe the orientation state. For injection molded LFTs, a characteristic structure with three layers over the cross section is commonly assumed [Ngu08, Ngu09] with the outer layers featuring a high degree of orientation in flow direction and the inner layer being transversely oriented. The modeling procedure could be extended to account for such a structure by averaging the orientation over the respective layer, followed by generation of a partial RVE for each layer. Due to the equivalent mesh of the boundary, the partial RVEs could then easily be joined to form the complete RVE of a layered structure. A possible restriction concerns the size of the resulting model, because the size of the investigated structures of a single layer is already very close to the limit which is processable with common computational resources.

The characteristic values of the microstructure were determined by random samples. The CT screening section of 3^3 mm^3 used to extract the fiber orientation distribution can be considered as relatively small compared to the analysis section of the tensile specimens of $50 \times 10 \times 3 \text{ mm}^3$. A possible variation of the orientation distribution within the specimens is not considered in the current data and cannot be captured due to the extensive effort which would be necessary to analyze the fiber orientation at multiple positions within a single specimen. To minimize this source of uncertainty, a process simulation of the compression molding of the LFT plates could provide additional information about the variation of the microstructure characteristics within the specimens and between several specimen positions of the LFT plate. The simulation could then be validated with CT scans at several positions. For injection molded, short fiber reinforced thermoplastics, this procedure is currently technically feasible. A process simulation of the injection molding of LFTs is a topic of ongoing research. Only few works about compression molding of LFTs are currently available [Jin13].

6.1.3 Fiber length distribution

To extract the fiber length distribution (Section 3.1.3 and 5.1.2), a part of the specimen plate (Fig. 11) was incinerated so that the matrix was burned off and the pure fiber structure remains. A characteristic sample of fibers was introduced into an automatic scanning procedure after the fibers were dispersed in a dilute solvent. The incinerated specimen needs to be large enough to avoid distortion of the length distribution due to cutting of too many fibers at its edges and therefore features a multitude of fibers which cannot be analyzed completely by the scanning procedure. Thus, a sample of fibers had to be selected for the analysis, which was chosen to contain approx. 10000 fibers. Because of gravitational effects, short fibers tend to sink down through the fiber structure toward the bottom of the ceramic crucible containing the specimen during the incineration procedure in a muffle furnace. To avoid the exclusion of the short fibers from the analysis, the fibers were manually selected from the top as well as the bottom of the fiber structure. A second analysis was performed under application of the same parameters, resulting in a negligible deviation to the first analysis, which supports the robustness of the procedure (Fig. 94, Section A.2). However, the procedure is based on experience and is not statistically proven. A method to overcome this problem and to perform a more systematic sampling was presented by Kunc [Kun07]. Kunc infiltrated the incinerated fiber structure with epoxy resin by applying a cylinder-shaped droplet reaching from the bottom to the top of the fiber structure. A syringe was used to let the droplet grow from the bottom toward the top. Then, the droplet with all captured fibers was separated from the remaining part of the structure. The epoxy droplet was burned off and the fiber sample was introduced into the scanning procedure.

6.1.4 Correlation between fiber orientation and length distribution

Uncertainties remain concerning the correlation between the fiber length and orientation distributions. Experimental determination of such correlation is currently not possible since the orientation distributions and length distributions are determined by different and independent measurements, which cannot be related. It was therefore necessary to assume that the longest fibers are preferably aligned in flow direction for the generation of the fiber structures. Although this assumption seems reasonable it is not validated by independent measurements. In the RVE generation procedure, this issue is represented by the finite number of attempts to re-orient a fiber preserving its length (Section 4.5.1). This re-orientation only affects the correlation between the length and orientation distributions but does not modify the orientation distribution itself. A reliable simulation of the compression molding process under incorporation of a fiber fracture model would be extremely helpful to further investigate this aspect. As mentioned before, such simulation methods are current research topics.

The application of a probabilistic approach represents an alternative way to treat the uncertainty of the microstructure characteristics as demonstrated by Hohe *et al.* [Hoh15]: The standard deviations of the local fiber orientation and density (volume fraction) were described by stochastic variables and their effect on the distribution of the effective elastic properties was evaluated by analytical homogenization.

6.1.5 Microstructure generation

The semi-automatic microstructure generation procedure (Section 4.5) needs to be classified as a tool to realize the given statistical data. It does not represent a profound description of the physics which govern the mechanisms during the compression molding of the material in reality. Nevertheless, it provides an approximation to the real structure at a much more sophisticated level than conventional methods (e.g. analytical homogenization), which consider straight fibers and cannot capture fiber interactions like e.g. fiber crossings or entanglements.

The fiber compression procedure (Section 4.5.2) is numerically implemented under application of an extensive degree of mass scaling in order to be computable. In the explicit FE simulation, the size of the stable time increment Δt depends on the characteristic element length l , the elastic constants E , ν and the mass density ρ : $\Delta t = l/\sqrt{E/(1-\nu^2)\rho}$. Due to the characteristic element length of the fibers (15.1 μm) being extremely small, a significant, virtual increase in the material's density is mandatory, which is performed automatically by the mass scaling algorithm of the FE software. The effects of inertia are therefore strongly overestimated in the simulations. Additionally, the elastic modulus of the fibers during the fiber compression simulation needed to be chosen significantly below its real value (5000 MPa vs. 72000 MPa) to further increase the stable increment size. Both procedures affect that the fiber waviness, which develops in the last step of the compression (*phase B*, Section 4.5.2), features a characteristic bending radius significantly smaller than the one which was experimentally observed. This phenomenon can be seen in Fig. 89, where a characteristic slice of a CT scan is compared to the computer generated structure. No remedy can currently be identified to avoid the mass scaling with today's computational resources. An exemplary study of a fiber compression scenario with a reduced degree of mass scaling and an increased elastic modulus of the fibers turned out to be numerically unstable so that the simulation aborted at an early stage.

The characteristic bending radius of the fibers as observed in the CT scans (e.g. Fig. 89 left, the characteristic fibers are marked by the arrows) could be mimicked by assigning respective initial stresses to the straight fibers at the beginning of the pressing process and let the eigenstresses relax, resulting in a bending deformation. The change in orientation distribution then needs somehow to be compensated.

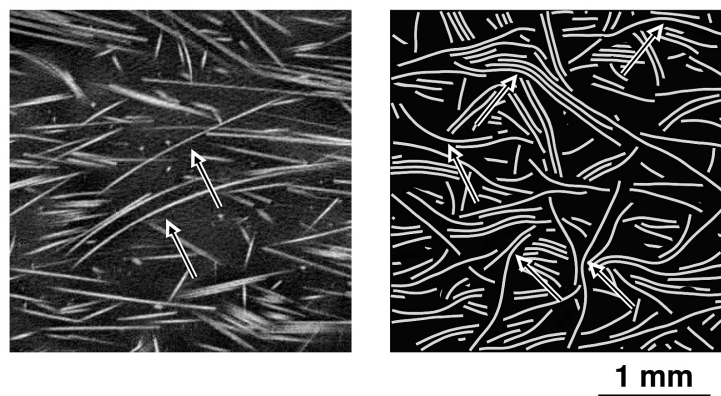


Figure 89: Exemplary slice of a CT scan (left) vs. generated structure (right).

In this work, no variation of fiber density or fiber agglomerations (Fig. 88) were analyzed or incorporated into the models. The fiber generator tool (Section 4.5.1) could be modified to account for such agglomerations by mimicking a nucleation process while generating the seeds of the fibers. Most likely, the RVE dimensions then need to be chosen much larger in particular in thickness direction in order to represent the gradient of fiber density within the RVE. With the current computational resources, this is not technically feasible due to the required size of the models.

6.2 Constitutive models

6.2.1 General aspects

The applied constitutive models, which are discussed in the following, represent appropriate descriptions of the mechanical behavior of the matrix, fibers and interface for the investigated validation scenarios of the LFT model. However, they describe single aspects which were analyzed independently and isolated from each other. For arbitrary loading conditions, some aspects cannot be treated as independent. This is in particular important for the constitutive law of the matrix. Here, a comprehensive model would be needed which describes the nonlinear viscoelastic behavior at different time scales together with viscoplastic effects and progressive damage as a function of the variables stress σ , strain ε , time t and temperature T . It needs to be emphasized that the investigated load cases, which include quasi static tensile tests (e.g. Fig. 51) to characterize the plastic behavior besides creep and relaxation experiments (e.g. Fig. 44) to measure the viscoelastic properties, represent idealized cases within the general framework of stress, strain, time and temperature. Their position in the space of stress, strain and time at a constant temperature is illustrated in Fig. 90, where the quasi static tensile tests can be described in the *isochronous* plane ($t = \text{const.}$), the creep tests are associated with the *iso-stress* plane ($\sigma = \text{const.}$) and the relaxation behavior lies within the *iso-strain* plane ($\varepsilon = \text{const.}$). The application of a model which would accurately describe any arbitrary scenario in the

three ($T = \text{const.}$) or four dimensional space represents a very complex task which could not be treated in this thesis. It is therefore very important to be aware of the general framework when single aspects of the models are evaluated in the following sections.

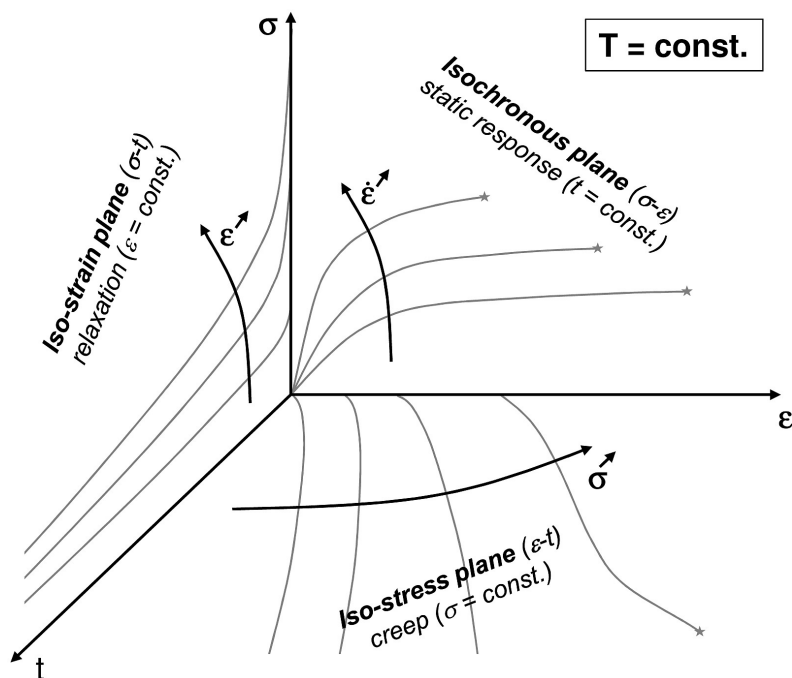


Figure 90: The three characteristic planes (isochronous, iso-stress and iso-strain) in the space of stress σ , strain ϵ and time t at a constant temperature T to classify the investigated load cases in the framework of an arbitrary viscoelastic viscoplastic response.

Furthermore, a varying structure of the polymer within the composite should be considered for the correct representation of the physical properties of the matrix. The degree of crystallinity changes in the vicinity of a fiber due to the surface tension of the fiber which acts as a nucleus for the crystallization process during solidification of the polymeric melt. Hence, the mechanical properties vary locally within the matrix polymer, which cannot be captured by the applied continuum models. To account for such phenomena, the crystallization kinetics must be simulated within a multi-scale framework. Such models are topics of ongoing research [Rua12, Rua11, Ben98, Meh93] and could not be treated within the scope of this work.

6.2.2 Viscoelastic matrix model

Range of validity

In Fig. 91, the *iso-stress* plane of Fig. 90 is described in more detail to illustrate the range of validity of the viscoelastic matrix model, which includes the linear and nonlinear viscoelastic regime with respect to the stress axis and the range of the calibration experiments with respect to the time axis ($0 \leq t \leq 6 \cdot 10^5$ s). Depending on the corresponding stress level of the creep curves, the figure can be divided into three characteristic regions:

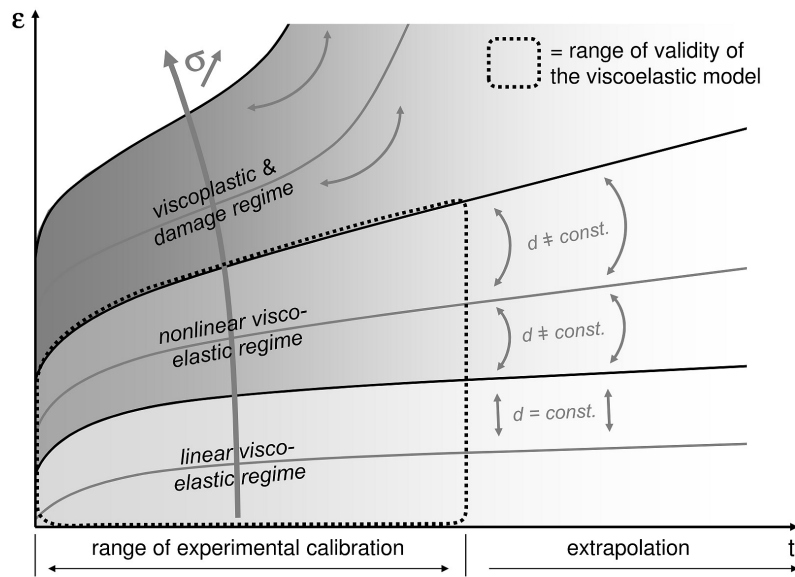


Figure 91: Range of validity of the viscoel. model (*iso-stress* plane of Fig. 90).

Within the *linear viscoelastic* regime, the time response is independent of stress. Thus, the creep curves of different stress levels simply feature a parallel offset - the creep rate of the second period ($\dot{\epsilon} \approx \text{const.}$) remains equal and independent of the stress level.

The *nonlinear viscoelastic* regime is characterized by increasingly spreading creep curves with a growing stress level since the time response is no more independent of the load. The nonlinearity usually affects exclusively the viscoelastic, time-dependent response [Sch69]: The stress is still low enough to remain within the elastic part of a corresponding stress-strain curve in the *isochronous* plane at $t = 0$.

The *viscoplastic and damage* regime can feature a tertiary creep period which is characterized by an increasing creep rate after the second period, where the creep is stationary. The corresponding stress levels would be outside the elastic and within the plastic region of the stress-strain curves at $t = 0$. The tertiary creep period is associated with severe inelastic deformations which finally induce creep fracture.

The time axis shows the range for which the model was experimentally calibrated. To describe the mechanical behavior outside this range, it is in principle feasible to apply extrapolation schemes such as the time-temperature superposition principle. For thermorheologically simple materials (e.g. unreinforced polymers as the polypropylene matrix) such methods are widely used and justified, whereas they are in general not applicable to thermorheologically complex materials (e.g. fiber reinforced thermoplastics) [Bri08]. Since no temperature-dependent data was available for the polypropylene matrix, no such extrapolation could be applied and thus, the use of the viscoelastic matrix model is restricted to the range of time which is covered by the calibration experiments.

Model choice and numerical implementation

The Burgers model was chosen for the representation of the viscoelastic effects of the thermoplastic matrix. Its free dashpot effects the viscous behavior of the model to be dominant, resulting in a constant creep rate during the second period (Fig. 20) and a irreversible strain component during the recovery phase. The model therefore represents the continuous sliding of the polymeric chains of an amorphous or semi-crystalline thermoplastic. The creep curves of the calibration experiments could be described by the Burgers model to a high degree of accuracy (Fig. 42) with only a single Kelvin-Voigt element. Furthermore, the existence of an irreversible strain component of the recovery period of the calibration experiments indicates that the feature of a free viscous dashpot in the model representation is legitimated (Fig. 42). Thus, the model choice seems to be well justified. Additionally, as supported by the validation scenario, the nonlinear modification of the model is in general well able to reproduce the nonlinear viscoelastic, time-dependent deformation behavior of the polypropylene matrix for the investigated load range and time scale (Fig. 44). It needs to be emphasized that the model was calibrated with characteristic specimens (Fig. 42), which were selected from the middle of the observed scatter band. In contrast, a single specimen was investigated for validation (Fig. 44). Thus, the observed deviation between the model prediction and the validation experiment can be considered as low.

The formulation of the applied nonlinear viscoelastic matrix model (Section 4.1.8) is restricted to small deformation theory which implies that the deformation of each element remains sufficiently small compared to its reference configuration and that the engineering definition of stress and strain is sufficiently accurate. Deformations of glass-fiber reinforced plastics are mostly considered as small because of the value of fracture strain of the glass fibers (approx. 3.5 %) which delimits their application-relevant range of strain. In contrast, the matrix polymers feature very high strains to failure. Analysis of the microscopic strains within an exemplaric LFT structure revealed a maximum value of the local equivalent deviatoric strain of approx. 5 % after a creep period of $6 \cdot 10^5$ s at the highest investigated stress level of 40 MPa (Fig. 78). The hydrostatic strain was found to be significantly lower (Fig. 79). Thus, the application of the small deformation theory seems to be well justified for the investigated load range.

A second restriction of the model concerns the limitation to a single relaxation time (only one Kelvin-Voigt element is considered). A semi-crystalline thermoplastic is characterized by a spectrum of relaxation times, where each value of relaxation time corresponds to a specific length of a polymeric chain (Section 2.1.5). Depending on the time period or frequency of the loading, a different relaxation time of the spectrum is activated. In order to generalize the model to arbitrary time scales, the whole spectrum of relaxation times must be screened e.g. by means of dynamic-mechanical-analysis (DMA). The

spectrum of relaxation times is then implemented by means of a *generalized* viscoelastic model, where several units of the respective model are connected in parallel and each sub-unit represents a single value of relaxation time (e.g. the generalized Maxwell model, Fig. 45). The latter can be addressed numerically by using a Prony series of relaxation times rather than a single value (Eq. 122). If the Burgers model based on the form presented in Section 4.1.8 is extended to a generalized formulation, this results in 9 history variables of decoupled deviatoric and volumetric strain components at each integration point per relaxation time or element of the Prony series. For the analysis of the large structures of this work, this would require an extensive amount of memory: For example, 10 elements of the Prony series would result in 90 floating point variables per integration point of 10 million elements and thus, a total of 900 million state variables. In order to keep the computational cost as low as possible, only one relaxation time was implemented, which corresponds to the time scale of the creep scenarios ($6 \cdot 10^5$ s). Thus, the model cannot describe other time periods or frequencies without re-calibration. This partially affects the validation sequence of Fig. 44: The time period of each sequence of constant stress or constant strain was chosen somewhat smaller than the calibration period of $6 \cdot 10^5$ s, with the shortest investigated period being $3 \cdot 10^4$ s. Thus, precision is lost with respect to the reproduction of the curvature of the creep curves (Fig. 92).

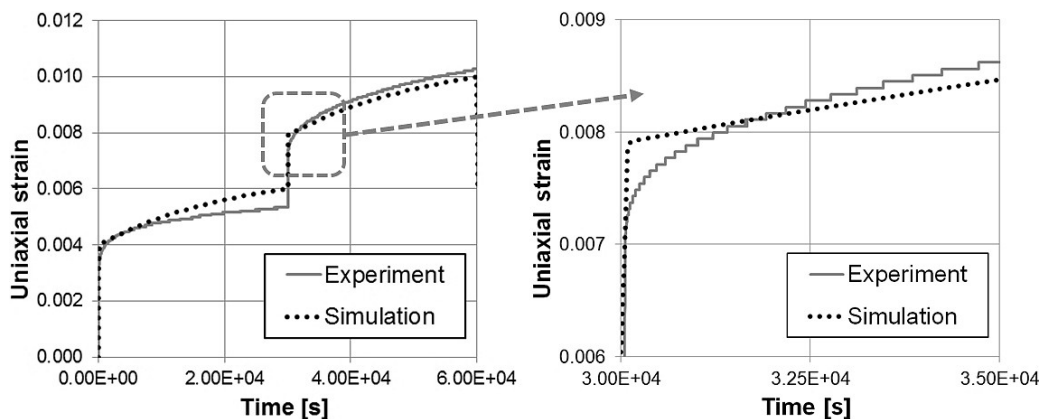


Figure 92: First two phases of the matrix validation sequence (Fig. 44, left) and close-up of the beginning of the second phase (right).

As mentioned in Section 4.1.7, the third restriction of the model concerns the applicability to fast variations of load. Due to the chosen scheme of time integration, a global non-linear viscoelastic load history is approximated by a series of sectional linear viscoelastic increments, represented by constant model parameters for each increment. Hence, the model is not suited for load scenarios with a fast variation of load as e.g. cyclic loading, whereas applicability to creep scenarios with a constant external load and rather slow re-distribution of stresses within the microstructure is not problematic. This is supported by the validation scenario (Fig. 44). Furthermore, the size of the time increments was varied in an exemplary study (Fig. 76). The results were found to be insensitive with respect

to the increment size. This supports that the variation of load of the investigated creep scenarios is sufficiently small to ensure the validity of the applied model formulation.

Effects of stress redistribution due to nonlinear viscoelasticity

Two variants of stress redistribution are active within the LFT structures under creep load: The stress redistribution from the matrix to the fibers is caused by the creep of the matrix (an increasing compliance over time) and applies to both linear and nonlinear viscoelastic matrix behavior, whereas the stress redistribution within the matrix is exclusively effected by nonlinear viscoelasticity. Here, the stress redistribution causes a stabilization of the material, since the regions under higher stress relax faster, so that the load is transferred to other regions and hot spots vanish over time. In the end, the redistribution of stresses within the matrix due to its nonlinear viscoelastic behavior decelerates the effective creep response of the composite. To investigate the extent of this effect, two variants of the model formulation were applied: For the *pseudo nonlinear* model, the stress-dependent parameters are determined at the beginning of the simulation, where the elastic load is applied. They are set to their respective values in dependence of the value of the indicator stress (Eq. 55) at each integration point. Then, the model parameters are kept constant over the creep period and thus, stress redistribution within the matrix was deactivated. In contrast, for the *fully nonlinear* model, the parameters are determined for each time increment anew and the effects of nonlinear viscoelasticity are fully active.

The results of the *pseudo nonlinear* and the *fully nonlinear* model are compared in Fig. 74 for the highest investigated stress level of 40 MPa and an exemplary structure of PPGF30. The observed extent of stress redistribution is indeed significant and mostly affects the creep rate of the second creep period (where the creep rate is stationary). The increase in creep rate of the *pseudo nonlinear* compared to the *fully nonlinear* model was found to amount approx. 37 %. Comparison with the experimental data shows that even the *fully nonlinear* model slightly overestimates the creep rate in this specific case (Fig. 74). The *pseudo nonlinear* model therefore represents a conservative estimate, which could be sufficiently accurate for engineering purposes containing a safety margin. A computationally very efficient implementation of such a model would be in principle feasible as here, the time-dependency can be separated from the load (as for linear viscoelasticity). In contrast, the *fully nonlinear* variant is necessary when accurate information of the microscopic stress and strain state is mandatory, which can exclusively be provided by this variant of the model. For example, such information would be required if the microstructural model would be extended to account for a tertiary creep period at higher loads, which would induce local damage at the microstructural scale.

As further simplification, results generated under application of the *linear viscoelastic* model variant (constant and equal model parameters at every integration point) were compared for different, prescribed values of model parameters specified in the form of a

given value of indicator stress (Eq. 55). The same exemplary structure of PPGF30 under the highest stress level was investigated as for the *pseudo nonlinear* and *fully nonlinear* variant. The resulting creep curves presented in Fig. 75 vary over a rather broad range (the difference in creep rate between the boundary curves amounts to approx. 365 %) and deviate significantly from the experimental curve. Therefore, a purely *linear viscoelastic* material model with constant and equal parameters at each integration point cannot be applied within acceptable precision.

To conclude the investigations of the influence of the nonlinear viscoelastic behavior of the matrix, it can be stated that:

- the *linear viscoelastic* model is not applicable within reasonable accuracy,
- the *pseudo nonlinear* model represents a conservative estimate of the effective creep behavior of the composite which is suitable for engineering applications,
- the *fully nonlinear* model is mandatory when precise information about the microstructural stress-strain state is required.

Three dimensional formulation, deviatoric vs. volum. deformation

In contrast to the creep mechanisms of most metals, the viscoelastic behavior of thermoplastics is not based on the motion of dislocations, which can in general be considered as independent of hydrostatic stress. In particular, the amorphous regions of the semi-crystalline matrix material (polypropylene) can actually feature a viscoelastic behavior which is explicitly dependent on hydrostatic stress. As a consequence, the applied model formulation considers an indicator stress which is chosen to the von Mises stress or the hydrostatic stress, respectively, based on the maximum absolute value of both (Section 4.1.8, Eq. 55). Additionally, both the deviatoric and the volumetric components of the inelastic deformation were assumed to be time-dependent, resulting in a constant Poisson's ratio over time (Section 4.1.6). (In contrast, the time-dependent deformation of metals is commonly assumed to be incompressible, i.e. only the deviatoric components are time-dependent). For the load case of uniaxial tension (all creep scenarios), the value of hydrostatic strain was never larger than the equivalent deviatoric strain within the analysis section of the investigated structures (within L_0 of Fig. 32). Exemplary contour plots at the time of the load application and at an advanced stage of the creep scenarios can be seen in Fig. 78 and 79. It can be clearly observed that the equivalent deviatoric strain is significantly larger than the hydrostatic strain at any location and anytime within the investigated structure. For severely deformed elements at the RVE border, where the displacement boundary conditions were applied (outside L_0 , see Fig. 32), a larger value of the hydrostatic strain than the equivalent deviatoric strain could be sporadically found. This indicates that volumetric deformations at the microscopic level might become significant for multiaxial load states, whereas they have apparently only negligible effect for the load case of uniaxial tension.

6.2.3 Plastic matrix model

Model choice and simplifications

Due to the lack of a generally accepted plasticity model for thermoplastics, the classical von Mises model (Section 4.2) was chosen for the explicit simulations of the quasi static deformation and damage behavior of LFT (denoted by *plasticity and damage*). Thus, the plastic deformation is assumed to be purely deviatoric. As discussed in Section 6.2.2, this assumption is not necessarily adequate for the polypropylene matrix material. However, the negligence of a volumetric part of the inelastic deformation can be justified with the results from the viscoelastic modeling, where the volumetric component was found to be rather negligible within the matrix of LFT structures for loading in uniaxial tension. If the range of application is extended to arbitrary load states, this simplification might become inappropriate and a plasticity model should be chosen which accounts for a volumetric component of inelastic deformation. Furthermore, a tension-compression asymmetry of the matrix material could then become significant. Such effects were reported by Rybicki and Kanninen [Ryb73] for investigations on polypropylene. However, no significant compressive stress is expected for the investigated structures under tensile loading.

Effects of strain rate

It needs to be emphasized that the applied plasticity model which is included in the explicit FE software package (*Abaqus Explicit*) is independent of the viscoelastic model of the previous section (which was implemented into an implicit FE framework by a user subroutine). The plasticity model therefore does not feature a dependence on strain rate. To overcome this issue in a pragmatic way, the nominal strain rate was chosen equally for the calibration experiments (matrix substance specimens) and validation experiments (LFT specimens) to approx. $7 \cdot 10^{-4}$ 1/s. Nevertheless, due to the inhomogeneous strain field at the microstructural level, the microscopic strain rate can also vary. No such strain-rate dependency is considered by the current plasticity model. The initial stiffness, the yield stress and the hardening behavior of the stress-strain curves of the matrix specimens is likely affected by the strain rate. To investigate the extent of this dependency, the strain rate of several experiments on matrix substance specimens was varied over three orders of magnitude (Section A.3). The plasticity model was then calibrated with the three different experimental stress-strain curves and the effect on the response of the composite was investigated by an exemplary microstructural simulation (Fig. 97). The effects can be assessed as weak, in particular under consideration that the change of strain rate everywhere within the matrix represents a rather extreme assumption. Furthermore, the response in Fig. 97 refers to a sample structure which is loaded in 90° direction, where the matrix properties are dominant (for a load direction of 0° , the effect can be expected to be even weaker). By comparison of Fig. 97 with Fig. 83, one can clearly observe that the

deviations of the stress-strain curves due to the variation of the strain rate are within the range of experimental scatter. Due to these facts and the excellent agreement between LFT validation experiments and microstructural simulations (under consideration of a constant strain rate, see e.g. Fig. 80 and 81), the negligence of a strain rate dependency of the plasticity model seems to be appropriate as long as a very slow effective strain rate (corresponding to the quasi static case) is existent. Of course, strain-rate dependent material parameters are of great importance for the simulation of highly dynamic processes, such as the load case of crash.

6.2.4 Fiber fracture model

For the simulations of plasticity and damage of the multidirectional LFT structures, the fibers were assigned to a brittle fracture model with a uniform value of failure stress. Values of fiber strength in the literature vary over a range from approx. 1800 to 3500 MPa [Kim98, And02, Tho14, Zha00a, Zha00b, Wan97] for the type of E-glass (the fibers of the investigated material). A mean value of 2500 MPa from the middle of this range was therefore considered for the simulations of this work. Furthermore, this value is commonly assumed if a mean, uniform value of strength needs to be specified [Kim98, Adv14]. More comprehensive investigations of fiber strength were carried out by Andersons *et al.* [And02] amongst others. A variation of the gauge length of the single fiber tests revealed a dependence of the strength from fiber length according to Weibull's weakest-link theory (the larger the volume of a brittle material, the higher the probability that it contains a flaw which will cause catastrophic failure). Such dependence could be implemented into the simulations in future to represent the fiber strength properties more accurately. A similar approach was made by Mishnaevsky to include the effects of a strength distribution for particle reinforced composites [Mis07].

6.2.5 Interface model

The interface properties were assigned to the cohesive zone elements between the fibers and the matrix in the form of a traction-separation law. The traction-separation model needs to be considered as a simplified approach to mimic the effective behavior of the interface. The model is not based on a physical background and cannot be transferred to other material systems without re-calibration. Furthermore, no mode-dependent parameters could be determined with the fiber push-out experiments, since they are restricted to shear loading of the interface. It was therefore necessary to assume equal parameters for the normal and both shear deformation modes. Another micromechanical testing method would be necessary to determine the parameters in normal direction (e.g. the Broutman test [Age99, Bro69]).

6.3 Multidirectional LFT structure

6.3.1 General aspects

In this chapter, the general suitability of the LFT model to describe different mechanical properties is discussed with respect to elasticity, viscoelasticity and plasticity and damage. The most fundamental aspects are highlighted for each property in no particular order. More specific problems will then be treated in a more systematic way within the following chapters.

Elasticity

For all three investigated materials with varying fiber fractions (PPGF10, PPGF20, PPGF30) and two respective load directions, the LFT model is suitable to reproduce the experimental results within a maximum error below 10 % which can in general be rated as very promising (Table 12, Fig. 59) and represents a necessary precondition to apply the model to predict mechanical properties beyond linear elasticity. The deviation to the analytical approach is somewhat higher with the analytical values of E_1 systematically being smaller than the numerical results and E_2 being larger. This is likely caused by a certain degree of underestimation of E_1 and overestimation of E_2 , respectively, by the Halpin-Tsai equations [Hal76], which was reported by Tucker and Liang for aspect ratios larger than 10 by systematic comparison of the results of analytical and numerical models of unidirectional fiber composites [Tuc99]. A similar behavior could be observed for the FE models of an unidirectional fiber arrangement of this work (Fig. 53). For the exact value of 13.22 % fiber volume fraction, the Halpin-Tsai equations clearly underestimate the FE results, whereas a slightly increased value of 15 % yields good agreement. These results support the findings of Tucker and Liang and in the end the assumption that the minor deviations between analytical and numerical results of the LFT model are caused by inaccuracies of the Halpin-Tsai equations.

Viscoelasticity

The viscoelastic LFT simulations were validated against characteristic creep experiments of all three investigated materials under two load directions at multiple stress levels (Fig. 64 - 69). Two sets of parameters of the viscoelastic matrix model were considered. The *original* parameters are exclusively based on experimental findings (Section 5.2.1), whereas the *modified* parameters were determined inversely to compensate the observed effects of the coarse matrix mesh to a certain amount (Section 5.2.3). Overall, a good agreement between the simulations and the validation experiments can be observed in Fig. 64 - 69. The initial offset of the curves is governed by the elastic stiffness which has found to deviate less than 10 % from the experiments (previous paragraph). Furthermore, the creep behavior of the first period up to the relaxation time of the Kelvin-Voigt element

($0 \leq t \leq 2 \cdot 10^5$ s), characterized by a decreasing strain rate and a high curvature of the graphs, deviates from the experiments only to a minor degree, as it can be seen in the figures. A more complex situation exists for the second creep period after the relaxation of the Kelvin-Voigt element ($2 \cdot 10^5 \leq t \leq 6 \cdot 10^5$ s), characterized by an approximately constant creep rate:

In 0° load direction, the creep rates of the low and medium stress levels of the three materials are well reproduced, whereas the creep rate of the highest stress level of each material is significantly overpredicted by the LFT model. A possible explanation is that the stress dependency of the creep rate is overestimated by the matrix model for higher stresses: As it can be seen in Fig. 42, the experimental data of the highest stress level of 12.5 MPa (which was used to calibrate the model) is fragmentary. In this context, it needs to be mentioned that the depicted creep curves were manually selected from the middle of the scatter band of multiple experiments per stress level. It was observed that the experimental scatter drastically increased for the higher stress levels. It is therefore possible that the experimental data which was chosen to calibrate the model is not completely representative, even if the middle curves of the scatter band were selected. More creep experiments with finer increments for the higher stress levels (e.g. 10, 10.5, 11, 11.5, 12, 12.5 MPa) would be helpful to identify possible inaccuracies of the model. Furthermore, the validation sequence of the matrix model does not contain the highest stress level of 12.5 MPa (Fig. 44). As a consequence, a possible inaccuracy of the model at higher stress levels cannot be detected by the validation scenario.

In 90° load direction, the creep rates are in general overpredicted to a higher degree for all investigated materials and stress levels. This is likely caused by the anisotropic RVE dimensions: The length of the RVEs is shortened to 1.5 mm (PPGF30) and 2.75 mm (PPGF10, PPGF20) in transverse direction in contrast to the length of 50 mm in longitudinal direction. As it can be seen in Fig. 70, the creep rate is strongly affected by a variation in RVE size (the study revealed approx. 30 % deviation for a size reduction from 50 to 5 mm). Therefore, it is very likely that the elongated RVEs are not suitable for an accurate prediction of the creep rate in transverse load direction. In contrast, the elastic properties are only weakly affected by a change in length of the RVEs (Fig. 60).

The difference in creep behavior of the *original* and *modified* model parameters is in general small (Fig. 64 - 69). In detail, the respective curves feature a very similar shape and creep rate, but a significant offset. This offset is larger for 90° than for 0° load direction since in transverse direction, less fibers are aligned in load direction and therefore, the properties of the matrix are more dominant. This agrees well to the results with respect to the elastic properties, where a significant mesh influence could exclusively be detected in 90° load direction (Section 5.6.5). Overall, the use of the *modified* parameters yields

a slightly better agreement to the experiments. Furthermore, the *modified* model tends to overpredict the time-dependent strain of the experiments slightly and is thus more conservative than the *original* variant.

Plasticity and damage

The investigated LFT material features a very complex deformation and damage behavior which is characterized by a high degree of nonlinearity in transverse direction (where less fibers are aligned in load direction and thus, the matrix properties become dominant which are the source of the nonlinearity). In contrast, the behavior in longitudinal direction is effected by the significantly higher amount of long fibers parallel to the load (Fig. 36) and thus features a clearly increased stiffness and strength of the stress-strain curves with a smaller degree of nonlinearity, as it can be seen in Fig. 82 and 83. Furthermore, the effects of the fiber-matrix interface damage need to be considered since the bonding between the thermoplastic matrix and the glass fibers is in general rather weak because of the absence of covalent bonds (Section 2.1.5). The broad fiber length distribution, reaching from fragments well below 1 mm length up to very long fibers of approx. 50 mm (Fig. 37) affects that their failure behavior is quite complex and not uniform, since short fibers will fail by fiber pullout, whereas fibers with a sufficient length will fail by normal fracture. Below that critical length, the point of failure by fiber pullout is reached earlier for shorter fibers and further delayed for longer ones. Moreover, the complex mechanical behavior of the thermoplastic matrix plays an important role. Besides its significant strain-rate dependency due to its viscoelastic and viscoplastic nature, the influence of hydrostatic pressure and the material's tension-compression asymmetry might be relevant for the investigation of arbitrary load cases. Again, it is worth noting that the applied modeling approaches feature severe restrictions in this respect, as mentioned in Section 6.2.

Against this background, it is remarkable that the experimental stress-strain curves can be reproduced by the LFT model quite accurately under application of very simple constitutive laws (the strain rate independent von Mises plasticity model, a mode independent traction-separation interface model and a brittle fracture model of the fibers). The resulting curves of the simulations which account for all investigated mechanisms (matrix plasticity, fiber-matrix debonding, post-debonding friction and fiber failure) agree very well with the validation experiments and are located at the middle of the observed scatter band (Fig. 82 and 83). It is worth noting that these results were generated under consideration of a matrix behavior which was determined at the same effective strain rate as the LFT validation experiments. At lower nominal strain rates (quasi-static case) this assumption is obviously justified because of the good agreement between the simulations and validation experiments. Furthermore, an exemplary study of the strain rate depen-

dency of the matrix revealed a rather weak effect for the investigated range of strain rates (Section 6.2.3, Paragraph '*Effects of strain rate*').

6.3.2 Effects of RVE size

In this section, the variation of the RVE size is discussed with respect to different mechanical properties. If the effective properties of the RVEs are not significantly affected by a change in size, the structures are likely sufficiently large to be representative, since the mechanical properties in general tend to converge to a saturation value with increasing RVE size. Because of the extreme aspect ratio of the fibers of the investigated material, it is not possible to generate arbitrarily large structures due to the related computational cost. Thus, a variation of the RVE size can only be performed within a rather small range which likely excludes the value of saturation. To circumvent this systematic problem in a pragmatic way, the numerical values can be compared to the experimental data, where it can be assured that the structures are large enough to be representative.

Elasticity

The variation of the RVE size in x_1 -direction (flow direction) was systematically investigated in the range of 5 to 50 mm with the result that the effective stiffness is rather weakly affected (Fig. 60 and Table 13). A maximum deviation of approximately 4 % for E_1 could be observed. An increase in stiffness with decreasing RVE length would be reasonable, since every fiber long enough to connect the analysis node sets (L_0 of Fig. 32) contributes to the effective stiffness in the same way as an endless fiber and the shorter the RVE, the larger the overestimation of fibers which are shorter than the saturation length (Fig. 53). In contrast, an opposite trend can be observed in Fig. 60), where the compliance increases with smaller dimensions. This is likely because the smallest RVE investigated (5 mm edge length and 4 mm reference length L_0) is still close to the the saturation fiber length ($E_{4\text{mm}}/E_\infty = 0.93$ according to the Halpin-Tsai equations [Hal76]). Thus, statistical effects of the microstructure predominate the effective stiffness and the effects of pure fiber length are rather negligible. This is a direct consequence of Hill's rule [Hil51, Bis51] and in particular, Eq. 10: Even for the largest investigated RVEs with 50 mm length, the condition is not met: Here, the RVE length L_{RVE} is just equal to the microstructural characteristic length L_{micro} , which can be considered as the maximum fiber length of 50 mm. To satisfy the condition, the RVE dimensions would have to be significantly larger. This was not technically feasible since RVEs larger than 50 mm are currently not computable with the available resources.

The effect of a varying reference length L_0 within the 5 to 50 mm long RVEs was also studied to quantify the fluctuation of the value of stiffness within these RVEs. No significant influence could be observed for different ratios of reference length to RVE length L_0/L_{RVE} for the 50 and 20 mm long RVEs (Fig. 61, right): They appear both to be large enough so that statistical fluctuations of the microstructure, which would result in a locally varying stiffness value, are rather weak. The RVEs with a length of 10 and 5 mm show a different behavior (Fig. 61, left). In this case, the results indicate that fluctuations of stiffness within these RVEs are significant.

It can be concluded that although even the largest investigated structures are too small to be representative in a strict statistical sense according to Hill's condition, the effect of the RVE size on the elastic properties is rather weak and within an acceptable precision for engineering applications ($< 5\%$). The weak sensitivity is likely caused by the fact that even rather short fibers are close to the saturation length of the elastic stiffness and therefore, a cropping of the long fibers as necessary for the small RVEs has only a negligible effect. A different situation exists for the fluctuation of the stiffness values within the RVEs. Here, a significant increase of the range of variation can be observed for the small structures.

Viscoelasticity

The influence of the RVE size on the viscoelastic properties was investigated by the same scenario as for the elastic properties. The effect of a varying RVE length (Fig. 70) is significantly larger than observed for the elastic properties. In detail, the relative deviation of the normalized creep rate reaches values up to 30 % for the smallest RVE with 5 mm length compared to a deviation of max. 4 % of the normalized elastic compliance. Besides the variation in creep rate, the respective creep curves (Fig. 71) feature a significant offset which is larger than the one resulting from their difference in initial stiffness, which is, as mentioned before, very low. A possible explanation of the large effect lies in the difference in the saturation lengths of the fibers with respect to the elastic and viscoelastic properties, because - as mentioned in the last paragraph - the reduction of the RVE size affects that the longer fibers are cropped to fit inside the RVE boundary. Whereas the saturation fiber length with respect to the elastic properties can be estimated based on the Halpin-Tsai equations (amongst other homogenization methods), no common approach exists for the viscoelastic properties, which motivates the FE studies on a unidirectional fiber arrangement (Section 5.5). These investigations imply that the saturation length of elastic stiffness is at least one order of magnitude smaller than the one of the creep behavior: A saturation aspect ratio of approx. 100 (corresponding fiber length of approx. 2 mm), which furthermore agrees well to the Halpin-Tsai predictions, was found for the elastic properties, whereas the saturation AR for creep amounts to approx. 2000 (corresponding fiber length of approx. 40 mm) according to Fig. 56. Therefore, it seems to

be reasonable that the 50 mm RVEs agree well with the creep experiments, whereas a reduction in RVE size results in quite considerable deviation in viscoelastic properties.

Investigations under variation of the ratio of reference length to RVE length L_0/L_{RVE} to quantify the fluctuation of the creep rate within the structures revealed a very similar behavior for the normalized creep rate (Fig. 72) as for the elastic compliance. The creep rate does not significantly vary within the larger RVEs, whereas considerable variation can be observed within the smaller ones.

It can be concluded that the RVE dimensions need to be chosen significantly larger to accurately predict the creep behavior than necessary for an accurate prediction of the elastic properties. With respect to the viscoelastic properties, the maximum investigated RVE length of 50 mm represents the lower limit which is necessary to yield a reasonably accurate prediction of the creep rate, since the saturation length for creep (approx. 40 mm) is very close to the RVE length. Therefore, no reduction in RVE size is acceptable if accurate results should be obtained - in contrast to the elastic properties, where even the shortest RVE of 5 mm length yields very reasonable results.

Plasticity and damage

No such systematic investigations of the effects of RVE size as for the elastic and viscoelastic properties were carried out for the deformation and damage behavior. Nevertheless, two different RVEs of 50 and 5 mm length were analyzed (Fig. 84). The simulations were conducted under activation of all treated mechanisms (matrix plasticity, fiber-matrix interface debonding, post debonding friction and fiber failure). As it can be seen in the figure, the composite strength is rather weakly affected, whereas a significant effect on the fracture strain can be observed. Furthermore, the slope of the stress-strain curve of the smaller RVE is significantly reduced for the second half of the graph (yielding an underprediction of the experimental curve), whereas its initial elastic stiffness is almost identical to the one of the large RVE. This agrees well to the elastic results, where a deviation in stiffness of approx. 4 % was found for the decreased RVE dimensions, which can certainly not be visually observed in the graph. The deviation toward the end of the curves can be explained by a higher extent of fiber-matrix debonding for the small RVE due to its shorter fibers which will debond at a lower value of effective composite strain than the ones of the large RVE: The load transfer between the matrix and the fibers after the debonding is exclusively conducted by friction, and therefore, a higher fraction of debonded fibers results in a decrease in effective stiffness of the material. With respect to Schemme's graph of fiber effectiveness (Fig. 6), it seems furthermore to be reasonable that the results are somehow affected for RVE dimensions of 5 mm because here, the length is significantly smaller than Schemme's value of saturation fiber length with respect to strength, which is approx. 10 mm.

6.3.3 Effects of fiber length

In order to further simplify various kinds of LFT models, the substitution of a fiber length distribution by a uniform mean length is of great interest. This motivates the investigations which are discussed in the following. Here, the fiber length distribution was replaced by fibers of a uniform length equal to the number average mean fiber length \bar{l}_n (Eq. 11) and the volume average or weighted mean fiber length \bar{l}_w (Eq. 12) of the length distribution. Because of the constant fiber cross section, the volume average means the same as the average with respect to the fiber length. If the deviation between the respective modeling results under incorporation of the uniform fiber length and the length distribution is sufficiently small, a substitution of the fiber length distribution by a uniform fiber length can be justified.

Elasticity

The resulting values of effective stiffness (Table 14) indicate that the volume average fiber length represents a legitimate substitute for the length distribution with a small deviation (< 5 %) between the stiffness values of the RVEs containing fibers with a varying length and a constant length, respectively. This agrees to the numerical studies of injection-molded LFTs which were carried out by Nguyen *et al.* [Ngu08], who justify the use of the weighted (or volume related) distributions with the fact that the process of averaging over the fiber length essentially represents a volume average. In contrast, Hine *et al.* found the number average fiber length to be the most accurate substitute for a length distribution of unidirectional short fiber composites [Hin02]. However, the current studies reveal that for the investigated LFT material, the use of the number average length clearly underestimates the value for E_1 by approx. 20 % (Table 14). It is worth mentioning that the results need to be interpreted as related to the investigated material with a specific fiber length distribution. Generality and transferability to other materials with arbitrary fiber length distributions cannot be ensured.

In order to identify the principle effect of the fiber length, an unidirectional fiber arrangement was also studied (Section 5.5). The results of the FE models were found to be in good agreement to the Halpin-Tsai equations, if they are fed by a slightly increased value of fiber volume fraction as discussed before (Section 6.3.1, Paragraph 'Elasticity'). A fiber aspect ratio of saturation was defined as the saturation threshold of the elastic stiffness in accordance with Schemme's notation of fiber effectiveness (Fig. 6). The saturation aspect ratio of the UD fiber structures amounts to approx. 100 (Fig. 56), whereas Schemme reports a value of approx. 50. An identical value cannot be expected since Schemme's value was determined by experimental investigations of multidirectional laminates (Section 2.1.4). Because of the validation by the Halpin-Tsai equations (Fig. 53), the numerical value can be considered as reliable.

Furthermore, these findings also agree to the results of the multidirectional LFT models with a uniform fiber length (which were discussed shortly before): The number average mean fiber length of the distribution ($\bar{l}_n = 1.2$ mm, corresponding AR of 60) is significantly smaller than the saturation threshold of the unidirectional structures of 100. Therefore, a significant deviation to the RVE with implemented length distribution can be observed (Table 14). In contrast, the weighted mean fiber length ($\bar{l}_w = 15$ mm, corresponding AR of 750) exceeds the saturation limit significantly and thus, the deviation in stiffness is very weak.

Viscoelasticity

The effect of the substitution of the fiber length distribution by the mean weighted fiber length of 15 mm and the number average length of 1.2 mm can be evaluated based on the data shown in Fig. 73. A moderate deviation is visible between the creep curves of the RVEs with the mean weighted fiber length and the length distribution. The deviation affects both the offset between the curves and the change in creep rate (approx. 16 %). For the number average fiber length, the offset between the creep curves is drastically increased. The difference in creep rate is affected in a similar manner (an increase of approx. 94 %). Therefore, the mean weighted fiber length can be chosen as a substitute of the length distribution within significant, but moderate deviations, whereas the number average fiber length yields improper results. In the end, the findings and their interpretation are similar to the ones with respect to the elastic properties (last paragraph) with the restriction that use of the weight average fiber length yields significantly more deviation for the creep rate (16 %) than for the elastic stiffness (< 5 %).

For principle investigations, the unidirectional fiber arrangement was also analyzed with respect to its viscoelastic behavior (Section 5.5). As it is shown in Fig. 56, a saturation fiber length is dependent on the stress level and not general as for the elastic properties. Therefore, a range of stress which represents a reasonable area of application of the virtual material was investigated (5 to 50 MPa). Finally, a fiber length of saturation with respect to the creep rate could be identified in the range of 32 to 52 mm with a corresponding aspect ratio of 1600 to 2600 (see also Section 6.3.2, Paragraph '*Viscoelasticity*'). The saturation threshold for the creep rate is therefore at least one order of magnitude larger (with a mean AR of approx. 2000) than for the elastic properties (with an AR of approx. 100).

For the multidirectional LFT structures, these findings might also explain that the use of the mean weighted fiber length of 15 mm (corresponding AR of 750) yields significantly more deviation for the creep rate than for elasticity: For elasticity, the mean weighted fiber length is much larger than the saturation threshold ($750 \gg 100$), whereas for the creep rate, it is significantly smaller ($750 < 2000$).

Plasticity and damage

Both RVEs with a uniform fiber length (1.2 mm and 15 mm) were also analyzed with respect to their deformation and damage behavior (Fig. 85). In accordance with the elastic results, the effect on the initial stiffness of the stress-strain curves is negligible for the mean weighted fiber length and significant for the number average fiber length. The nonlinear deformation of the second half of the stress-strain curve as well as the values of fracture stress and strain are in good agreement for the RVEs with implemented fiber length distribution and the mean weighted length of 15 mm under consideration of all damage mechanisms (matrix plasticity, fiber-matrix interface debonding, post-debonding friction and fiber fracture). In contrast, use of the number average fiber length of 1.2 mm yields a significant underprediction of the slope of the curves as well as the fracture stress. Again, the use of the mean weighted fiber length as a substitute for the length distribution is well justified and furthermore supported by the conclusions of Schemme: The mean weighted length of 15 mm is significantly larger than Schemme's critical fiber length with respect to static strength (approx. 10 mm, Fig. 6), whereas the number average length (1.2 mm) is much smaller.

The same LFT structures (length distribution, mean weighted length, number average length) were also simulated under activation of matrix plasticity and interface debonding, but no post-debonding friction and fiber fracture (thin lines in Fig. 85). It can be seen that the structures now fail catastrophically by fiber pullout instead of normal fiber fracture. This effect is in particular pronounced for the RVE with a uniform fiber length of 1.2 mm. The interface damage then localizes at the weakest point of the structure as it can be observed in Fig. 86. The failure stress drops to approx. half of its initial value for the variant which considers friction (Fig. 85). In contrast, no such drastic degree of fiber pullout can be observed if friction is activated. Then, the friction stabilizes the debonding and no localization occurs, so that finally the fiber fracture stress can be reached. For the variants with the fiber length distribution and a mean fiber length of 15 mm, respectively, the point of catastrophic fiber pullout of the variant which considers no friction (thin lines) is very similar to the point of fiber fracture under activation of friction (bold lines). For these RVEs, the point of fracture can obviously be reached without the additional load transfer by post-debonding friction because the fibers are sufficiently long.

It can be concluded that the substitution of the length distribution by the mean weighted fiber length (15 mm) yields very accurate results for the damage modeling and therefore agrees well with the findings for the elastic stiffness and - under restrictions - with the viscoelastic results. In contrast, the number average length of 1.2 mm yields a strong underestimation of the failure stress and distorts the shape of the nonlinear part of the stress-strain curve. It is therefore inappropriate.

6.3.4 Effects of the finite element mesh

The numerical results are affected by the relatively coarse mesh of the RVEs and in particular the representation of the matrix by linear tetrahedral elements which were chosen for computational efficiency. These elements are known to be less accurate at stress and strain concentrations which arise e.g. at the end of a fiber. This results from the element's linear shape function and the existence of only one integration point for the calculation of the stress and strain values. Thus, no variation of stress and strain can be described within the element and only by using a multitude of such elements, an accurate solution can be obtained. This is partially addressed by the meshing algorithm which decreases the element size in regions close to a fiber and increases the size toward regions of low fiber density, where no strain concentrations are present (Fig. 29). Nevertheless, the influence of the finite element mesh needs to be investigated in order to ensure the validity of the results.

Due to the enormous size of the models (10 million elements for the largest, 50 mm long RVEs), such element studies could not be performed with implicit FE simulations since here, a direct relation between the size of the model and the required memory exists. A mesh refinement would shift the value of memory outside the range of available computational resources. The use of quadratic elements instead of linear ones has the same effect due to more nodes per element, resulting in more DOFs of the quadratic elements.

As a consequence, two separate approaches to carry out element studies were made:

Implicit studies on small structures

For an exemplary structure of $1 \times 1 \text{ mm}^2$, element studies (varying element size and type) could be performed with the implicit FEM. The results are presented together with the derivation of the modified parameters for the viscoelastic matrix model in Section 5.2.3. It is shown that convergence is obtained for either the coarse mesh with quadratic elements (which can capture linear variations of stress and strain within the element due to the use of quadratic shape functions and four integration points) or a refined mesh with 16 linear elements over the fiber cross section, resulting in much smaller matrix elements in the vicinity of a fiber. The results of both variants deviate approx. 10 % in effective elastic strain from those of the coarse mesh with linear elements, which was also applied to analyze the 50 mm long RVEs. Because of the extensively reduced dimensions of the small RVE, on which the element studies were performed, the results are not significant for the effective behavior of the real material, because the structure is not statistically representative (Section 6.3.2).

Explicit studies on full-size structures

Since the size of the model has no such drastic effect on the calculation time of explicit FE simulations, element studies were technically feasible on the full-size, 50 mm long

structures with the drawback that the results can be distorted by the effects of inertia. To exclude such issues, the degree of mass scaling of the simulations, which directly influences the kinetic energy of the models, was varied for the results presented in Section 5.6.5 and found to be insignificant. Additionally, the stiffness values of the coarse, linear mesh agree very well between explicit and implicit simulations (less than 1 % deviation, Table 15). The explicit simulations seem therefore to be reliable enough to carry out element studies. Simulations of a quadratic mesh variant of the 50 mm long structure reveals equal values of effective stiffness to the coarse, linear mesh in x_1 direction (flow direction), whereas in x_2 direction (transverse direction), a significant deviation exists (approx. 10 %, Table 15). Thus, the coarse, linear mesh can be considered as convergent in x_1 direction, where a multitude of long fibers govern the deformation behavior and the influence of the matrix is rather weak. In contrast, the matrix properties are more dominant in transverse direction (x_2), where less fibers are aligned in load direction and consequently, a weak effect of the coarse mesh can be observed. This agrees well to the findings with respect to the viscoelastic properties (application of original and modified model parameters), which were discussed in Section 6.3.1, Paragraph '*Viscoelasticity*'.

6.3.5 Deformation and damage mechanisms

Within this section, the effects of progressive damage of the LFT structure are discussed. It is important to mention that the underlying results were generated with the explicit FEM and are therefore completely independent of the elastic and viscoelastic modeling (implicit FEM). The range of validity and the limitations of the applied constitutive models (plastic matrix model, fiber-matrix interface model, fiber fracture model) are specified in Section 6.2.

Mechanism-based interpretation of the stress-strain curves

With the microstructural simulations presented in Section 5.6.11, it is possible to relate the individual results of the calibration experiments of each mechanism (matrix plasticity, calibrated with tensile tests, fiber-matrix interface debonding and friction, fed by experimental data of fiber push-out tests and fiber fracture, which considers an experimental value from the literature). The resulting effective stress-strain curves of the simulations can then be compared to those of the LFT validation experiments, enabling an interpretation with respect to the active mechanisms at the microstructural level. In Fig. 80 and 81, the numerical stress-strain curves are shown together with those of a validation experiment for both load directions of 0° and 90° . Several numerical variants were investigated, in which different mechanisms were accounted for. The remaining mechanisms were then deactivated. The different mechanisms are the plastic deformation of the matrix, which was always active, the damage of the cohesive zone elements between fiber and matrix, which represents the fiber-matrix debonding, the post-debonding friction captured by a

contact formulation and a friction coefficient and the brittle fracture of the fibers. The effects are illustrated in Fig. 93 for two exemplary numerical variants under 90° load direction. The simulation labeled *realistic interface* accounts for all mechanisms, whereas the variant *perfect interface* considers no fiber-matrix debonding and no post-debonding friction. The deviation in fracture strain and stress between both curves can be interpreted as the potential increase of the respective property if the composite would feature an imaginary, perfect interface.

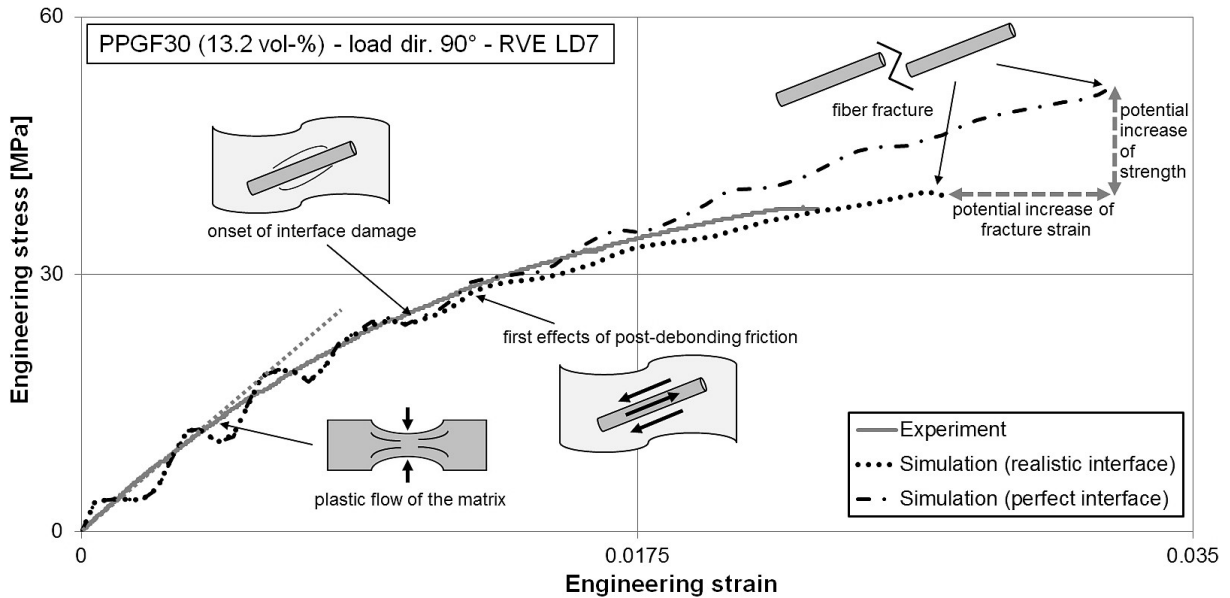


Figure 93: Interpretation of the different deformation and damage mechanisms based on the data of Fig. 81 (PPGF30, 90° load direction).

Effects of matrix plasticity

At the point where the stress-strain curve significantly deviates from its initial slope (Fig. 93), the effects of the plastic flow of the matrix become significant for the effective behavior of the composite. The numerical curve features a significant amount of oscillation due to the explicit simulation (this aspect was further analyzed by examination of energetic issues in Section 5.6.5). Thus, the point of onset of plastic flow is difficult to observe. During the further progress of the variant with a *perfect interface*, the shape of the curve becomes linear again and the simulation deviates significantly from the experiment. This is also the case for a load direction of 0° (Fig. 80) although here, the effect is weaker. At the point where the curve reaches linearity, all matrix elements which are in the vicinity of a fiber and are therefore loaded beyond their initial value of yield stress, have completed the process of hardening as specified by the plastic matrix model (Section 5.3) and have reached the final value of yield stress. The load is then predominantly carried by the fibers which govern the deformation of the composite by their linear elastic behavior until the fracture stress of the fibers is reached. In contrast, matrix elements far away from any fibers do not reach the initial value of yield stress and therefore remain elastic.

Fiber-matrix debonding and load transfer within the fiber structure

At the point where the curves of the variants *realistic interface* and *perfect interface* deviate for the first time, the effect of interface damage becomes visible in the mechanical response of the composite. During the further progress of fiber-matrix debonding, the area fraction of intact interface decreases steadily diminishing the load transfer from the matrix to the fibers. As a consequence, the shorter fibers are debonded at first and the load is transferred to the longer fibers, where a larger part of the interface is still intact. Successively more and more fibers are debonding and finally, only the fibers above the critical fiber length can carry the load. These fibers feature a length which is large enough so that their circumferential area available for load transfer causes the interfacial stresses to be small enough that no debonding occurs. The critical length $L_{KT} = \sigma_f D / 2\tau$ after Kelly and Tyson [Kel65] is defined by the quotient of normal fiber strength σ_f , the fiber diameter D and the interfacial strength τ . Fibers of super-critical length will break in normal tension mode whereas fibers of sub-critical length will be pulled out (this is also discussed in Section 2.1.4). The brittle failure of the super-critical fibers determines the end of the stress-strain curve. The range of validity of the simulations ends here, as due to the varying element size of the matrix mesh, no failure of matrix elements can be implemented, so that the fracture of the material over the complete cross section cannot be captured. The simulations were therefore aborted when fiber fracture occurred (Fig. 87). The point of first fiber fracture, which was considered as the strength of the composite, is reached significantly faster for the variants which consider debonding, because here, fibers of sub-critical length are pulled out and are not available for load transfer in contrast to the variants with the *perfect interface*. Consequently, the pullout of the sub-critical fibers causes a redistribution of load to the super-critical fibers and the fracture stress within the super-critical fibers is reached at a lower composite stress and strain than for the variants with a *perfect interface*. This is supported by the stress-strain curves of the LFT validation experiments, which agree very well to the fracture stress and strain values of the numerical variants accounting for debonding. Furthermore, a significant amount of fiber pull-out can be observed in SEM images of fracture surfaces of the LFT specimens (Fig. 40 - 41).

Influence of post-debonding friction

Two approaches were considered to model the interface properties. The more basic variant only accounts for the fiber-matrix debonding by means of cohesive zone elements which will be degraded in stiffness to model their damage evolution, calibrated with the fiber push-out experiments presented in Section 5.4, Fig. 52. The plateau after the force peak in the push-out curve of the indenter force against the indenter displacement is then ignored. This plateau can be accounted for in the model by the second variant, which considers an additional contact formulation capturing the friction between fiber and matrix after the

cohesive zone elements were deleted from the mesh. The friction also affects the shape of the curve before the force peak, because the cohesive zone elements fail successively (starting from the fiber ends), and as soon as an element is deleted, a part of the load which was initially carried by the element is now partially transferred by friction. Therefore, the damage evolution parameters of the cohesive zone law had to be modified for the variant accounting for friction, because otherwise, the maximum force in the push-out-curves was overestimated. The respective values of the traction-separation law of the cohesive zone elements and the friction formulation, respectively, can be found in Table 9. Fig. 52 shows no significant deviation in shape and size of the force peak for both variants, whereas the plateau after the peak is obviously only captured by the variant accounting for friction.

The effect on the stress-strain curve of the LFT structure with implemented fiber length distribution is shown in Fig. 80 and 81 for both variants (only debonding / debonding and friction) and is indeed significant. The additional load transfer because of the post-debonding friction affects the redistribution of stresses within the fiber structure in a way that also fibers with a sub-critical length can carry a specific amount of load transferred by friction. Consequently, the mechanism of load transfer to fibers with a super-critical length is less pronounced and the fracture stress within these fibers is reached at a later point of the stress-strain curve. Also the curves of the variants which do not account for fiber fracture are shown in the figures. The thin lines represent the theoretical progress of the stress-strain curves for all three variants (perfect interface, only debonding, debonding and friction), if no fiber fracture occurs. The stress-strain curves (accounting for friction but no fiber failure) are then monotonically increasing, even though their stiffness is significantly reduced compared to the variants accounting for a perfect interface.

In 0° load direction (Fig. 80) where the majority of fibers is aligned in load direction, the stress-strain curve of the variant considering post-debonding friction almost coincides with the variant of a *perfect interface*, which implies that the fibers are sufficiently long and the potential increase in composite strength, which could be exploited by an enhanced interface strength, is rather low.

In 90° load direction (Fig. 81), more fibers are transversely aligned and consequently loaded normal to their interface. Thus, friction has no effect for these fibers and only applies to those which are aligned in load direction, which are significantly less compared to the variant of 0° load direction. Therefore, the consideration of post-debonding friction has a negligible effect on the composite properties and the results of the variants accounting for debonding only / debonding and friction are very similar. The potential increase in composite strength by comparison with the variant of a *perfect interface* seems therefore to be relatively large and could be exploited by enhancement of the interface strength. In this context, it needs to be emphasized that the interface strength in normal direction, which is dominant here, was assumed to be equal to the shear direction, because

only fiber push-out experiments were available which exclusively provide data in shear mode. Thus, the validity of the simulations is not ensured and needs to be further supported by experimental data of the interface properties in normal direction (as discussed in Section 6.2.5).

6.3.6 Current limitations and future developments

In this section, the current limitations of the modeling of the investigated loading scenarios, which are mostly independent of each other, are elaborated by separate paragraphs. In the end, the potential to join the partial aspects to form a holistic model, is evaluated.

Elasticity

As discussed in Section 6.3.2, Paragraph '*Elasticity*', the investigated structures are too small to be representative in a strict statistical sense. Although the effects are rather weak and negligible for engineering applications, the computation of even larger structures would be beneficial to further validate the current findings. Furthermore, the microstructure generation procedure should be modified to account for a periodic fiber arrangement as well as to consider periodic boundary conditions. Even with the capabilities of state-of-the-art finite element software, the computation of such gigantic structures cannot be considered to be technically feasible. Current developments in alternative calculation methods, such as FFT based solvers, seem to be promising in this respect [Kab14].

Viscoelasticity

The viscoelastic studies were conducted under the assumption of a perfect interface and no presence of viscoplastic and/or damage effects. The stress levels of the validation experiments were chosen within a range which is relevant for the application of the materials, but are sufficiently small that no fracture occurred during the load period of $6 \cdot 10^5$ s. To extend the model to higher stress levels, the phenomena of a tertiary creep period and creep fracture will become significant. These cannot be captured by the applied implicit FE simulations since a stiffness reduction to describe the effects of damage would cause an excessive reduction of the increment size, prohibiting the computation of such models. As a consequence, the modeling of degradation and damage effects was pursued by explicit simulations (next paragraph). The stress levels of the implicit creep simulations were therefore chosen significantly smaller than the stresses for which the first occurrence of damage could be observed in the stress-strain curves of the explicit simulations (the points, where the curves of the simulations with and without consideration of interface damage deviate the first time in Fig. 80 and 81). Thus, the negligence of damage phenomena and the choice of a perfect fiber-matrix interface is well justified for the investigated creep scenarios. Other limitations of the viscoelastic modeling of LFT mostly affect the constitutive model of the matrix and were already discussed in Section 6.2.2.

Plasticity and damage

Current limitations with respect to the modeling of the deformation and damage behavior of LFT mostly affect the reproduction of the damage evolution of the matrix. The applied explicit FE simulations are in general suitable to describe such effects since the computational cost per time increment is much smaller than for implicit simulations. Therefore, the modeling of a damage evolution, described by a stiffness degradation is in principle feasible, since the resulting, very small increments can be accepted. However, the representation of the matrix by tetrahedral elements with a strongly varying element size (Fig. 29) would result in strong fluctuations of the damage energy within the mesh, which is physically incorrect. In contrast, the fibers and interface elements are not affected, since here, the element size and shape is constant. To incorporate a damage model of the matrix in future, respective sub-models could be generated with a significantly refined and uniform mesh. The weakest region of each RVE, where the damage is expected to be localized, could be identified by the current techniques and regenerated with a locally refined mesh, whereas the use of the refined mesh throughout the full size structures seems not to be feasible due to the drastically increased element count, which would even be problematic for the explicit simulations. Another promising area of enhancement is the extension of the model to higher strain rates to describe highly dynamical processes, such as crash and impact. As mentioned in Section 2.1.4, the systematic investigation of the relation between impact energy and fiber length by realistic microstructural models would represent an important topic of future research. Therefore, the constitutive models would have to be modified to account for strain rate effects, as discussed in Section 6.2.

Combination of the partial models

As discussed in the previous paragraphs, the different modeling approaches of the investigated load cases are currently independent of each other mainly due to the application of different simulation techniques (implicit and explicit FEM). Although the implicit approach offers advantages with respect to the elastic and viscoelastic properties mainly because of its higher accuracy, all attempts to include material degradation and damage into the implicit simulations have failed (the models were not computable). With respect to this situation, the transformation of the viscoelastic matrix model to the explicit FEM would likely represent a solution to overcome the current limitations and to extend the viscoelastic modeling to account for damage effects. For this purpose, it would be necessary to scale the time of the creep experiments down to a reasonably small period, which is not expected to be problematic. Furthermore, the viscoelastic matrix model would have to be extended to account for viscoplastic and damage effects and most certainly to be transformed to large deformation theory, which is mandatory to describe highly distorted, damaged elements. A comprehensive model would then be obtained which would be suitable for the investigation of quite complex scenarios as described in Section 6.2.1.

7 Conclusions

A novel microstructure modeling procedure was presented which is suitable for the generation of LFT structures with a maximum fiber aspect ratio of approx. 5000. The resulting mesh represents the fibers by a single element over their cross-section. The LFT model therefore closes the gap between conventional three dimensional finite element models of discontinuous fiber composites which describe each fiber by a multitude of elements over their cross section (high level of detail, computationally costly) and simplified models which use one dimensional truss elements for the representation of fibers, permitting fiber interpenetration (low level of detail, computationally efficient). The proposed model combines the advantages of both conventional approaches and allows the analysis of comparably large structures within state-of-the-art computational resources, but keeps the level of detail sufficiently high to include the detailed interactions of the microstructure. It also allows the analysis of fiber-matrix debonding phenomena under incorporation of cohesive zone elements.

Representative volume elements were generated for three material variants with varying fiber fractions, based on the experimentally measured fiber orientation and length distributions. The RVEs were then validated with respect to their elastic behavior as the most fundamental mechanical property. Excellent agreement between the model predictions and experimental results was found. Furthermore, an established, analytical homogenization scheme was applied under incorporation of the same microstructural information and constituent properties and resulted in very similar effective properties. Significant, but relatively weak effects of the coarse mesh could be observed in 90° load direction, whereas they were negligible in 0° orientation. The influence of the size of the LFT structures as well as the effects of fiber length were investigated. It was shown that the elastic properties are relatively insensitive to the length of the structures, as long as their minimum dimension is chosen larger than the fiber length of saturation in accordance to the literature. It is remarkable that substitution of the fiber length distribution by a uniform mean length yields negligible deviation in elastic stiffness if the volume or length average is used. Substitution by the number average length was found to be inappropriate.

As second part of the investigations, creep scenarios were modeled. The viscoelastic behavior of the matrix was characterized by experiments on substance specimens, which revealed a strong nonlinear viscoelastic response. A classical Burgers model was modified to account for the observed stress dependency by means of variable parameters. The model was implemented into the finite element framework as a user material subroutine and validated with respect to its suitability to reproduce an exemplary load history. The three dimensional formulation was compared to the behavior of a commercially implemented viscoelastic model. LFT simulations of all three investigated fiber fractions were

validated against respective LFT experiments under two different load directions and several stress levels, which were chosen in an industrial relevant range, but below the loads, where damage mechanisms and a tertiary creep period become significant. The influence of a varying RVE size and fiber length was found to be considerably different from the elastic behavior. The cause was found to lie in a significantly increased fiber length of saturation, which is at least one order of magnitude larger for the viscoelastic properties than for elasticity. This is supported by principle investigations on a unidirectional fiber arrangement. Furthermore, the effect of stress redistribution within the matrix due to its nonlinear viscoelastic behavior was studied and found to be indeed significant for the highest investigated stress level.

Finally, the modeling of the quasi static deformation and damage behavior of LFT was investigated by explicit simulations accounting for different mechanisms, which are the plastic deformation of the matrix, the fiber-matrix interface debonding, the post-debonding friction and the brittle failure of the fibers. Each individual part of the model was calibrated independently with respective experimental data or values from the literature. The interface properties, represented by a traction-separation law assigned to cohesive zone elements between fibers and matrix, were fed by single fiber push-out experiments. The friction between fibers and matrix during their pullout after debonding was accounted for by a contact formulation, which was also calibrated with the fiber push-out tests. The failure stress of the fibers was estimated based on data from the literature. Virtual tensile tests of the material with the highest fiber fraction could be reproduced with good accuracy. The mechanisms of interface debonding and post-debonding friction were found to have significant effects on the mechanical response of the material. Furthermore, the potential increase in composite strength and fracture strain for an imaginary, perfect fiber-matrix interface could be evaluated. The difference between the stress-strain curves of finite and infinite interface strength represents the potential of optimization of the material, which could be exploited by an improved bonding between the fibers and the matrix. The influence of RVE size and fiber length was also studied and agreement with models from the literature was found. A current limitation is the lack of a suitable damage model for the matrix due to a strongly varying element size. This issue could be addressed in future by the introduction of sub-models with a refined and uniform mesh.

The presented model provides a powerful tool to support the development and the validation process of new effective material models. These models will allow the simulation of LFT components in an industrial scope under incorporation of the mechanisms which were investigated by micromechanical simulations. Furthermore, the micromechanical model can be employed in a virtual laboratory to enable the design and optimization of new materials, precisely adapted to their respective application.

References

- [Aba11] Abaqus Version 6.11 Online Documentation. *Dassault Systèmes*, 2011.
- [Aba14] Abaqus Unified FEA. *Dassault Systèmes*.
<http://www.3ds.com/products-services/simulia/portfolio/abaqus/overview/>,
10-29-2014.
- [Ada09] Adam L, Depouhon A, Assaker R. Multi-Scale Modeling of Crash & Failure of Reinforced Plastics Parts with DIGIMAT to LS-DYNA interface. In *7th European LS-DYNA Conference*, 2009.
- [Adv87] Advani SG, Tucker CL. The use of tensors to describe and predict fiber orientation in short fiber composites. *Journal of Rheology*, 31:751–784, 1987.
- [Adv14] Advanced Lightweight Engineering (ALE). *Fiber properties E-glass*.
<http://www.ae.nl/?portfolio=fiber-types>, 07-24-2014.
- [Age99] Ageorges C, Friedrich K, Schüller T, Lauke B. Single-fibre Broutman test: fibre-matrix interface transverse debonding. *Composites Part A*, 30:1423–1434, 1999.
- [And02] Andersons J, Joffe R, Hojo M, Ochiai S. Glass fibre strength distribution determined by common experimental methods. *Composites Science and Technology*, 62:131–145, 2002.
- [Bar62] Barenblatt, GI. The mathematical theory of equilibrium cracks in brittle fracture. *Advances in applied mechanics*, 7:55–129, 1962.
- [Ben98] Benard A, Advani SG. An analytical model for spherulitic growth in fiber-reinforced polymers. *J. Appl. Polym. Sc.*, 70:1677–1687, 1998.
- [Bis51] Bishop JW, Hill R. A theory of the plastic distortion of a polycrystalline aggregate under combined stresses. *Philosophical Magazine Series 7*, 42:414–427, 1951.
- [Bow10] Bower AF. *Applied Mechanics of Solids*. CRC Press - Taylor & Francis Group, <http://www.solidmechanics.org>, 2010.
- [Bri08] Brinson HF, Brinson LC. *Polymer Engineering Science and Viscoelasticity - An Introduction*. Springer Science+Business media, LLC, 2008.
- [Bro69] Broutman, LJ. Measurement of the Fibre-Polymer Matrix Interfacial Strength. In *Interfaces in Composites*, pages 27–41. ASTM STP, 1969.
- [Bry10] Brylka B, Fritzen F, Böhlke T, Weidenmann KA. Study of Experimental Methods for Interface Problems Based on Virtual Testing. In *Proc. Appl. Math. Mech.*, volume 10, pages 109–110. PAMM, 2010.
- [Bry11] Brylka B, Fritzen F, Böhlke T, Weidenmann KA. Influence of micro-structure on fibre push-out tests. In *Proc. Appl. Math. Mech.*, volume 11, pages 141–142. PAMM, 2011.

- [Cot64] Cottrell AH. Strong solids. *Proc. Roy. Soc.*, 282:2–9, 1964.
- [Cox52] Cox HL. The elasticity and strength of paper and other fibrous materials. *British Journal of Applied Physics*, 3:72–79, 1952.
- [Dem07] Demiray S, Becker W, Hohe J. Numerical determination of initial and subsequent yield surfaces of open-celled model foams. *International Journal of Solids and Structures*, 44:2093–2108, 2007.
- [Dig14] Digimat - The nonlinear multi-scale material and structure modeling platform. *e-Xstream engineering*.
<http://www.e-xstream.com/en/digimat-software>, 05-13-2014.
- [DIN03] DIN EN ISO 3167: Plastics - Multipurpose test specimens, December 2003.
- [Dir14] Dirrenberger J, Forest S, Jeulin D. Towards gigantic RVE sizes for 3D stochastic fibrous networks. *International Journal of Solids and Structures*, 51:359–376, 2014.
- [DOW03] DOW® Chemical Company. *C711-70RNA Polypropylene Resin - Product Information*, 2003.
- [Dug60] Dugdale, DS. Yielding of steel sheets containing slits. *Journal of the Mechanics and Physics of Solids*, 8:100–104, 1960.
- [Esh57] Eshelby JD. The determination of the elastic field of an ellipsoidal inclusion and related problems. *Proc. Roy. Soc. A*, 241:376–396, 1957.
- [Eva86] Evans KE, Gibson AG. Prediction of the maximum packing fraction achievable in randomly oriented short-fibre composites. *Composites Science and Technology*, 25:149–162, 1986.
- [Fae05] Faessel M, Delisee C, Bos F, Castera P. 3D Modelling of random cellulosic fibrous networks based on X-ray tomography and image analysis. *Composites Science and Technology*, 65:1931–1940, 2005.
- [FAS14] FASEP®. *xyz high precision*. <http://www.fasep.de>, 01-13-2014.
- [Fib14] FibreShape. *IST AG - Innovative Sintering Technologies*.
<http://www.powdershape.ch>, 01-15-2014.
- [Fij14] Fiji / ImageJ plugin 'Directionality'. *Tinevez JY*.
<http://fiji.sc/wiki/index.php/Directionality>, 01-21-2014.
- [Fli12] Fliegner S, Luke M, Reif M. Microstructure-based modeling of the creep behavior of long-fiber-reinforced thermoplastics. In *Proc. of European Conference on Composite Materials ECCM 15*, volume 434. European Society for Composite Materials, 2012.
- [Fli13a] Fliegner S, Elmer D, Seifert T, Luke M. Multi-scale modeling of the viscoelastic properties of non-woven, thermoplastic composites. In *Proc. of International Conference on Composite Materials ICCM 19*, volume 202, pages 4061–4072. Canadian Association for Composite Structures and Materials, 2013.

- [Fli13b] Fliegner S, Luke M, Elmer D, Seifert T. Modellierung des Kriechverhaltens langfaserverstärkter Thermoplaste unter Berücksichtigung der prozessabhängigen Faserausrichtung (in German). In *Tagungsband 19. Deutsche Gemeinschaft für Materialkunde DGM Symposium Verbundwerkstoffe und Werkstoffverbunde*, volume 83. Wanner A, Weidenmann KA, 2013.
- [Fli14] Fliegner S, Luke M, Gumbsch P. 3D microstructure modeling of long fiber reinforced thermoplastics. *Composites Science and Technology*, 104:136–145, 2014.
- [Fli15] Fliegner S, Hohe J, Haspel B, Weidenmann KA. Micromechanical modeling of the nonlinear deformation of LFTs under consideration of the effects of interface damage. In *Proceedings of the 20th International Conference on Composite Materials ICCM 20*, Copenhagen, 19-24th July, 2015.
- [Fri09] Fritsch J, Hiermaier S, Strobl G. Characterizing and modeling the non-linear viscoelastic tensile deformation of a glass fiber reinforced polypropylene. *Composites Science and Technology*, 69:2460–2466, 2009.
- [Gar13] Garesci F, Fliegner S. Young’s modulus prediction of long fiber reinforced thermoplastics. *Composites Science and Technology*, 85:142–147, 2013.
- [Geo14] GeoDict - The Virtual Material Laboratory. *Math2Market GmbH*. <http://www.geodict.de>, 04-01-2014.
- [Gho08] Ghorbel E. A viscoplastic constitutive model for polymeric materials. *International Journal of Plasticity*, 24:2032–2058, 2008.
- [Glo07] Glomsaker T, Andreassen E, Polanco-Loria M, Lyngstad OV, Gaarder RH, Hinrichsen EL. Mechanical response of injection-moulded parts at high strain rates. In *Polymer Processing Society Europe/Africa regional meeting PPS07EA*, Ghotenburg, Sweden, 2007.
- [Gom96] Gommers B, Verpoest I, Van Houtte, P. Modelling the elastic properties of knitted-fabric-reinforced composites. *Composites Science and Technology*, 56:685–694, 1996.
- [Gra14] Graupner N, Beckmann F, Wilde F, Müssig J. Using synchrotron radiation-based micro-computer tomography for the measurement of fibre orientations in cellulose fibre-reinforced polyactide composites. *J Mater Sci*, 49:450–460, 2014.
- [Gus02] Gusev A, Heggli M, Lusti HR. Orientation averaging for stiffness and thermal expansion of short fiber composites. *Advance Engineering Materials*, 4 12:931–933, 2002.
- [Haj04] Haj-Ali RM, Muliana AH. Numerical finite element formulation of the Schapery non-linear viscoelastic material model. *International Journal for Numerical Methods in Engineering*, 59:25–45, 2004.
- [Hal76] Halpin JC, Kardos JL. The Halpin-Tsai Equations: A Review. *Polymer Engineering and Science*, 16-5:344–352, 1976.

- [Har09] Hartwich MR, Höhn N, Mayr H, Sandau K, Stengler R. FASEP ultra - automated analysis of fibre length distribution in glass-fibre-reinforced products. In *Proceedings of SPIE Conference*, volume 7389, page 66. Society of Photo-Optical Instrumentation Engineers (SPIE), 2009.
- [Har12a] Harper LT, Qian C, Turner TA, Li S, Warrior NA. Representative volume elements for discontinuous carbon fibre composites - Part 1: Boundary conditions. *Composites Science and Technology*, 72:225–234, 2012.
- [Har12b] Harper LT, Qian C, Turner TA, Li S, Warrior NA. Representative volume elements for discontinuous carbon fibre composites - Part 2: Determining the critical size. *Composites Science and Technology*, 72:204–210, 2012.
- [Has62] Hashin Z, Shtrikman S. On some variational principles in anisotropic and nonhomogeneous elasticity. *Journal of the Mechanics and Physics of Solids*, 10(4):335–342, 1962.
- [Hen05] Henning F, Ernst H, Brüssel R, Geiger O, Krause W. LFTs for automotive applications. *Reinforced Plastics*, 49:24–33, 2005.
- [Hew70] Hewitt RL, de Malherbe MC. An Approximation for the Longitudinal Shear Modulus of Continuous Fibre Composites. *Journal of Composite Materials*, 4:280–282, 1970.
- [Hil51] Hill R. The Elastic Behaviour of a Crystalline Aggregate. *Proceedings of the Physical Society Section A*, 65:349–354, 1951.
- [Hil63] Hill R. Elastic properties of reinforced solids: Some theoretical principles. *J. Mech. Phys. Solids*, 11:357–372, 1963.
- [Hin02] Hine PJ, Lusti HR, Gusev AA. Numerical simulation of the effects of volume fraction, aspect ratio and fibre length distribution on the elastic and thermoelastic properties of short fibre composites. *Composites Science and Technology*, 62:1445–1453, 2002.
- [Hof12] Hoffmann S. *Computational Homogenization of Short Fiber Reinforced Thermoplastic Materials*. PhD thesis, Technische Universität Kaiserslautern, ISBN 978-3-942695-05-3, 2012.
- [Hoh05] Hohe J, Becker W. A probabilistic approach to the numerical homogenization of irregular solid foams in the finite strain regime. *International Journal of Solids and Structures*, 42:3549–3569, 2005.
- [Hoh15] Hohe J, Beckmann C, Paul H. Modeling of uncertainties in long fiber reinforced thermoplastics. *Materials and Design*, 66:390–399, 2015.
- [Hua08] Huang CW. *Development and numerical implementation of nonlinear viscoelastic-viscoplastic model for asphalt materials*. PhD thesis, Texas A&M University, 2008.
- [Hyp14] HyperMesh. *Altair Engineering, Inc.*
<http://www.altairhyperworks.com/Product,7,HyperMesh.aspx>, 10-29-2014.

- [Jin13] Jin X, Wang J, Han S. Property calculation system for injection molding and compression molding of fiber-filled polymer composites. In *Proc. of International Conference on Composite Materials ICCM 19*, volume 202, pages 7211–7219. Canadian Association for Composite Structures and Materials, 2013.
- [Kab14] Kabel M, Böhlke T, Schneider M. Efficient fixed point and Newton-Krylov solvers for FFT-based homogenization of elasticity at large deformations. *Computational Mechanics*, 54:1497–1514, 2014.
- [Kam11] Kammoun S. *Micromechanical modeling of the progressive failure in short glass-fiber reinforced thermoplastics*. PhD thesis, Universite catholique de Louvain, <http://hdl.handle.net/2078.1/94334>, 2011.
- [Kel65] Kelly A, Tyson WR. Tensile properties of fibre-reinforced metals. *J. Mech. Phys. Solids*, 13:329–350, 1965.
- [Kim98] Kim JK, Mai YW. *Engineered interfaces in fiber reinforced composites*. Elsevier Science Ltd, 1998.
- [Kra03] Krause W, Henning F, Tröster S, Geiger O, Eyerer P. LFT-D - A Process Technology for Large Scale Production of Fiber Reinforced Thermoplastic Composites. *Journal of Thermoplastic Composite Materials*, 16:289–302, 2003.
- [Kre64] Krenchel H. *in Fibre Reinforcement, Akademisk Forlag, Copenhagen*, 1964.
- [Kun07] Kunc V, Frame B, Nguyen BN, Tucker CL, Velez-Garcia G. Fiber Length Distribution Measurement for Long Glass and Carbon Reinforced Injection Molded Thermoplastics. In *Proceedings of the 7th Annual SPE Automotive Composites Conference and Exposition*, Troy, Michigan, 2007. Society of Plastic Engineers.
- [Lai96] Lai J, Bakker A. 3-D schapery representation for non-linear viscoelasticity and finite element implementation. *Computational Mechanics*, 18:182–191, 1996.
- [Lea43] Leaderman H. Elastic and Creep Properties of Filamentous Materials and Other High Polymers. *Textile Foundation*, Washington, DC, 1943.
- [Liu91] Liu ZQ. Scale space approach to directional analysis of images. *Applied Optics*, 30:1369–1373, 1991.
- [Lu 14] Lu Z, Yuan Z, Liu Q. 3D numerical simulation for the elastic properties of random fiber composites with a wide range of fiber aspect ratios. *Computational Materials Science*, 90:123–129, 2014.
- [Mea69] Mears DR, Pae KD, Sauer JA. Effects of Hydrostatic Pressure on the Mechanical Behavior of Polyethylene and Polypropylene. *Journal of Applied Physics*, 40:4229–4237, 1969.

- [Meh93] Mehl NA, Rebenfeld, L. Computer simulation of crystallization kinetics and morphology in fiber-reinforced thermoplastic composites. II. Three-dimensional case. *J. Polym. Sci. B Polym. Phys.*, 31:1687–1693, 1993.
- [Mis07] Mishnaevsky L. *Computational Mesomechanics of Composites*. John Wiley and Sons Ltd., 2007.
- [Mor73] Mori T, Tanaka K. Average stress in matrix and average elastic energy of materials with misfitting inclusions. *Acta Metallurgica*, 21:571–574, 1973.
- [Ngu08] Nguyen BN, Satish KB, Holbery JD, Smith MT, Kunc V, Frame BJ, Phelps JH, Tucker CL. Fiber length and Orientation in Long-Fiber Injection-Molded Thermoplastics Part I Modeling of Microstructure and Elastic Properties. *Journal of Composite Materials*, 42:1003–1029, 2008.
- [Ngu09] Nguyen BN, Bapanapalli SK, Kunc V, Phelps JH, Tucker CL. Prediction of the Elastic-Plastic Stress/Strain Response for Injection-Molded Long-Fiber Thermoplastics. *Journal of Composite Materials*, 43:217–246, 2009.
- [Oka10] Okabe T, Nishikawa M, Takeda N. Micromechanics on the Rate-dependent Fracture of Discontinuous Fiber-reinforced Plastics. *International Journal of Damage Mechanics*, 19:339–360, 2010.
- [Oka14] Okabe T, Sasayama T, Koyanagi J. Micromechanical simulation of tensile failure of discontinuous fiber-reinforced polymer matrix composites using Spring Element Model. *Composites: Part A*, 56:64–71, 2014.
- [Pal14] Palmyra. *MatSim® Materials Simulation GmbH*. <http://www.matsim.ch/products/palmyra.html>, 04-01-2014.
- [Pan08a] Pan Y, Iorga L, Pelegri AA. Analysis of 3D random chopped fiber reinforced composites using FEM and random sequential adsorption. *Computational Materials Science*, 43:450–461, 2008.
- [Pan08b] Pan Y, Iorga L, Pelegri AA. Numerical generation of a random chopped fiber composite RVE and its elastic properties. *Composites Science and Technology*, 68:2792–2798, 2008.
- [Pan10] Pan, Y. *Stiffness and progressive damage analysis on random chopped fiber composite using FEM*. PhD thesis, The State University of New Jersey, 2010.
- [PPG13] PPG Fiber Glass. *TufRov® 4575 - Data Sheet*, 2013.
- [Rad08] Radtke A. *Steifigkeitsberechnung von diskontinuierlich faserverstärkten Thermoplasten auf der Basis von Faserorientierungs- und Faserlängenverteilungen (in German)*. PhD thesis, Fraunhofer Institut für Chemische Technologie, ISBN 978-3-8167-7852-3, 2008.
- [Reu29] Reuss A. Berechnung der Fließgrenze von Mischkristallen auf Grund der Plastizitätsbedingung für Einkristalle (in German). *Journal of Applied Mathematics and Mechanics*, 9(1):49–58, 1929.

- [Ric06] Richter F. *Upsetting and Viscoelasticity of Vitreous SiO₂: Experiments, Interpretation and Simulation*. PhD thesis, Technische Universität Berlin, 2006.
- [Rua11] Ruan C, Ouyang J, Liu S, Zhang L. Computer modeling of isothermal crystallization in short fiber reinforced composites. *Computers and Chemical Engineering*, 35:2306–2317, 2011.
- [Rua12] Ruan C, Ouyang J, Liu S. Multi-scale modeling and simulation of crystallization during cooling in short fiber reinforced composites. *International Journal of Heat and Mass Transfer*, 55:1911–1921, 2012.
- [Ryb73] Rybicki EF, Kanninen MF. *The effect of different behavior in tension than in compression on the mechanical response of polymeric materials*. Springer US, 1973. Deformation and Fracture of High Polymers (pp. 417-427).
- [Sau74] Sauer JA, Pae KD. The flow of solid polymers under high pressure. *Colloid & Polymer Sci.*, 252:680–695, 1974.
- [Sch69] Schapery RA. On the Characterization of Nonlinear Viscoelastic Materials. *Polymer Engineering and Science*, 9:295–310, 1969.
- [Sch00] Schijve W. Long glass fibre PP - High Performance at medium fibre length. In *3rd AVK Conference*, Baden-Baden, 2000.
- [Sch03] Schemme M. Langfaserverstärkte Thermoplaste (in German). *Kunststoffe*, 93:106–109, 2003.
- [See08] Seelig T, Latz A, Sanwald S. Modelling and crash simulation of long-fibre-reinforced thermoplastics. In *7. LS-DYNA Anwenderforum, Bamberg*, pages D–I 33–40, 2008.
- [Sol14] Soltani P, Johari MS, Zarrebini M. Effect of 3D fiber orientation on permeability of realistic fibrous porous networks. *Powder Technology*, 254:44–56, 2014.
- [Tan84] Tandon GP, Weng GJ. The effect of aspect ratio of inclusions on the elastic properties of unidirectionally aligned composites. *Polym. Compos.*, 5:327–333, 1984.
- [Tay70] Taylor RL, Pister KS, Goudreau, GL. Thermomechanical analysis of viscoelastic solids. *International Journal for numerical methods in engineering*, 2:45–59, 1970.
- [Tho96a] Thomason JL, Vlug MA. Influence of fibre length and concentration on the properties of glass fibre-reinforced polypropylene: 1. Tensile and flexural modulus. *Composites Part A*, 27A:477–484, 1996.
- [Tho96b] Thomason JL, Vlug MA, Schipper G, Krikor HGLT. Influence of fibre length and concentration on the properties of glass fibre-reinforced polypropylene: 3. Strength and strain at failure. *Composites Part A*, 27A:1075–1084, 1996.

- [Tho97] Thomason JL, Vlug MA. Influence of fibre length and concentration on the properties of glass fibre-reinforced polypropylene: 4. Impact properties. *Composites Part A*, 28A:277–288, 1997.
- [Tho14] Thomason JL, Yang L, Meier R. The properties of glass fibres after conditioning at composite recycling temperatures. *Composites: Part A*, 61:201–208, 2014.
- [Tol98] Toll S. Packing mechanics of fiber reinforcements. *Polymer Engineering and Science*, 38(8):1337–1350, 1998.
- [Tro03] Troester S. *Materialentwicklung und -charakterisierung für thermoplastische Faserverbundwerkstoffe im Direktverfahren (in German)*. PhD thesis, Fraunhofer Institut für Chemische Technologie, ISBN 3-8167-6643-9, 2003.
- [Tuc99] Tucker CL, Liang E. Stiffness predictions for unidirectional short-fiber composites: Review and evaluation. *Composites Science and Technology*, 59:655–671, 1999.
- [Voi89] Voigt W. Über die Beziehung zwischen den beiden Elastizitätskonstanten isotroper Körper (in German). *Wied. Ann.*, 38:573–587, 1889.
- [Wan97] Wang Z, Xia Y. Experimental evaluation of the strength distribution of fibers under high strain rates by bimodal weibull distribution. *Composites Science and Technology*, 57:1599–1607, 1997.
- [Wan07] Wang Q, Maze B, Tafreshi HV, Pourdeyhimi B. Simulating through-plane permeability of fibrous materials with different fiber lengths. *Modelling Simul. Mater. Sci. Eng.*, 15:855–868, 2007.
- [Wol11] Woldekidan MF. *Response Modelling of Bitumen, Bituminous Mastic and Mortar*. PhD thesis, Delft University of Technology, ISBN 978-90-8570-762-2, 2011.
- [Zha00a] Zhao FM, Okabe T, Takeda N. The estimation of statistical fiber strength by fragmentation tests of single-fiber composites. *Composites Science and Technology*, 60:1965–1974, 2000.
- [Zha00b] Zhao FM, Takeda N. Effect of interfacial adhesion and statistical fiber strength on tensile strength of unidirectional glass fiber/epoxy composites. Part I: experimental results. *Composites: Part A*, 31:1203–1214, 2000.

A Appendix

A.1 Derivation of viscoelastic matrix model

A.1.1 Differential equation

The derivation of the one dimensional constitutive equation in differential form can be found in various lecture books (e.g. by Brinson [Bri08]). To derive the ODE, the total strain ε^{tot} is decomposed into an instantaneous elastic part ε^e , a viscous part ε^v and a viscoelastic part of the Kelvin-Voigt branch ε^{ve} :

$$\varepsilon^{\text{tot}} = \varepsilon_{\text{Maxwell}} + \varepsilon_{\text{Kelvin-Voigt}} = \varepsilon^e + \varepsilon^v + \varepsilon^{\text{ve}} . \quad (127)$$

The stress σ remains constant in both branches of the model:

$$\sigma = \sigma_{\text{Maxwell}} = \sigma_{\text{Kelvin-Voigt}} . \quad (128)$$

The stress for the Kelvin-Voigt element equals the sum of the dashpot's and spring's contributions:

$$\sigma_{\text{Kelvin-Voigt}} = E_1 \varepsilon^{\text{ve}} + \eta_1 \dot{\varepsilon}^{\text{ve}} . \quad (129)$$

The derivative is formed to proceed:

$$\dot{\sigma} = E_1 \dot{\varepsilon}^{\text{ve}} + \eta_1 \ddot{\varepsilon}^{\text{ve}} . \quad (130)$$

The viscoelastic strain component ε^{ve} is substituted by the remaining parts:

$$\dot{\sigma} = E_1 (\dot{\varepsilon}^{\text{tot}} - \dot{\varepsilon}^e - \dot{\varepsilon}^v) + \eta_1 (\ddot{\varepsilon}^{\text{tot}} - \ddot{\varepsilon}^e - \ddot{\varepsilon}^v) . \quad (131)$$

The elastic and viscous strain of the Maxwell element spring resp. dashpot are expressed by the stress and their parameter E_0 resp. η_0 :

$$\dot{\sigma} = E_1 \left(\dot{\varepsilon}^{\text{tot}} - \frac{\dot{\sigma}}{E_0} - \frac{\sigma}{\eta_0} \right) + \eta_1 \left(\ddot{\varepsilon}^{\text{tot}} - \frac{\ddot{\sigma}}{E_0} - \frac{\dot{\sigma}}{\eta_0} \right) . \quad (132)$$

Expansion gives:

$$\dot{\sigma} = E_1 \dot{\varepsilon}^{\text{tot}} - \frac{E_1}{E_0} \dot{\sigma} - \frac{E_1}{\eta_0} \sigma + \eta_1 \ddot{\varepsilon}^{\text{tot}} - \frac{\eta_1}{E_0} \ddot{\sigma} - \frac{\eta_1}{\eta_0} \dot{\sigma} . \quad (133)$$

Rearrangement yields the final form of the ODE:

$$\frac{E_1}{\eta_0} \sigma + \left(1 + \frac{E_1}{E_0} + \frac{\eta_1}{\eta_0} \right) \dot{\sigma} + \frac{\eta_1}{E_0} \ddot{\sigma} = E_1 \dot{\varepsilon} + \eta_1 \ddot{\varepsilon} . \quad (134)$$

A.1.2 Hereditary integral

If a sudden change in stress $\Delta\sigma_0$ is applied at the time t_0 , the time-dependent strain $\varepsilon(t)$ can be expressed by

$$\varepsilon(t) = C(t - t_0)\Delta\sigma_0 , \quad (135)$$

with $C(t - t_0)$ being the creep compliance which describes the time-dependency of the material [Bri08].

A complex load history $\sigma(t)$ can be approximated by a sum of sudden load increments $\Delta\sigma_i$ as follows:

$$\sigma(t) = \sum_{i=1}^n \Delta\sigma_i . \quad (136)$$

The response of the material is then given by

$$\varepsilon(t) = \sum_{i=1}^n C(t - t_i)\Delta\sigma_i . \quad (137)$$

Generalization to infinitesimal time steps yields the so-called memory function of viscoelasticity given by the convolution integral

$$\varepsilon(t) = \int_{\sigma(0)}^{\sigma(t)} C(t - \tau) d\sigma(\tau) = \int_0^t C(t - \tau)\dot{\sigma} d\tau , \quad (138)$$

where $\dot{\sigma}$ denotes the stress rate at time τ and τ the time integration variable.

A.1.3 Incremental form

The derivation of the incremental form of the linear viscoelastic Burgers model as carried out in the following was described by Woldekidan [Wol11]. In analogy to the derivation of the differential form (Section A.1.1), the total strain ε^{tot} is decomposed into an instantaneous elastic part ε^e , a viscous part ε^v and a viscoelastic part ε^{ve} :

$$\varepsilon^{\text{tot}} = \varepsilon_{\text{Maxwell}} + \varepsilon_{\text{Kelvin-Voigt}} = \varepsilon^e + \varepsilon^v + \varepsilon^{\text{ve}} . \quad (139)$$

In the following, the incremental form $\Delta\varepsilon$ of each individual component ε is derived. The total strain increment $\Delta\varepsilon^{\text{tot}}$ can then be obtained by re-combination of the components:

$$\Delta\varepsilon^{\text{tot}} = \Delta\varepsilon^e + \Delta\varepsilon^v + \Delta\varepsilon^{\text{ve}} . \quad (140)$$

For the derivation of the incremental components, the memory function (Eq. 17) is applied to each strain component $\varepsilon(t)$:

$$\varepsilon(t) = \int_0^t C(t - \tau) \dot{\sigma} \, d\tau . \quad (141)$$

The overall creep compliance C^{tot} (Eq. 16) is divided into its individual components in a similar manner as the strain components:

$$C^{\text{tot}} = C^e + C^v + C^{\text{ve}} . \quad (142)$$

The components are then obtained by:

$$C^e = \frac{1}{E_0} , \quad (143)$$

$$C^v = \frac{t}{\eta_0} , \quad (144)$$

$$C^{\text{ve}} = \frac{1}{E_1} \left[1 - e^{-\frac{t}{\tau}} \right] . \quad (145)$$

- **Elastic component $\Delta\varepsilon^e$**

The solution for the time-independent elastic part is trivial:

$$\Delta\varepsilon^e = C^e \Delta\sigma = \frac{\Delta\sigma}{E_0} . \quad (146)$$

- **Viscous component $\Delta\varepsilon^v$**

The contribution of the serial dashpot is obtained by

$$\varepsilon^v(t) = \int_0^t C^v(t - \tau) \dot{\sigma} \, d\tau = \int_0^t \left[\dot{C}^v(t - \tau) \right] \sigma(\tau) \, d\tau , \quad (147)$$

with

$$C^v(t - \tau) = \frac{t - \tau}{\eta_0} \quad (148)$$

and

$$\dot{C}^v(t - \tau) = \frac{dC^v(t - \tau)}{d(t - \tau)} = \frac{1}{\eta_0} . \quad (149)$$

Substitution and dividing the integral into two parts yields:

$$\varepsilon^v(t) = \frac{1}{\eta_0} \left[\int_0^{t-\Delta t} \sigma(\tau) d\tau + \int_{t-\Delta t}^t \sigma(\tau) d\tau \right]. \quad (150)$$

The first integral corresponds to the viscous strain of the previous time step:

$$\frac{1}{\eta_0} \int_0^{t-\Delta t} \sigma(\tau) d\tau = \varepsilon^v(t - \Delta t). \quad (151)$$

Thus, the incremental form $\Delta\varepsilon^v(t)$ can be obtained by combining Eq. 150 and 151:

$$\Delta\varepsilon^v(t) = \varepsilon^v(t) - \varepsilon^v(t - \Delta t) = \frac{1}{\eta_0} \int_{t-\Delta t}^t \sigma(\tau) d\tau. \quad (152)$$

The above expression can be approximated by a trapezoidal rule and the incremental form of the viscous strain component $\Delta\varepsilon^v$ is finally given by

$$\Delta\varepsilon^v(t) = \frac{\Delta t}{\eta_0} \left[\sigma(t - \Delta t) + \frac{\Delta\sigma}{2} \right]. \quad (153)$$

- **Viscoelastic component $\Delta\varepsilon^{ve}$**

To derive the incremental form of viscoelastic strain of the Kelvin-Voigt element $\Delta\varepsilon^{ve}$, the memory function is applied to the viscoelastic creep compliance C^{ve} :

$$\varepsilon^{ve}(t) = \int_0^t C^{ve}(t - \tau) \dot{\sigma} d\tau = \int_0^t \frac{1}{E_1} \left[1 - e^{-\frac{(t-\tau)}{\tau_r}} \right] \dot{\sigma} d\tau. \quad (154)$$

The above expression is divided into a so-called instantaneous ε^i and inherited part ε^{inh} as follows:

$$\varepsilon^{ve}(t) = \varepsilon^i(t) - \varepsilon^{inh}(t) = \frac{1}{E_1} \int_0^t \dot{\sigma} d\tau - \frac{1}{E_1} \int_0^t \left[e^{-\frac{(t-\tau)}{\tau_r}} \right] \dot{\sigma} d\tau. \quad (155)$$

After transformation of each component to its incremental form as carried out below, the viscoelastic strain increment can then be obtained by

$$\Delta\varepsilon^{ve}(t) = \Delta\varepsilon^i(t) - \Delta\varepsilon^{inh}(t). \quad (156)$$

The solution for the instantaneous part is trivial:

$$\varepsilon^i(t) = \frac{1}{E_1} \int_0^t \dot{\sigma} \, d\tau = \frac{\sigma(t)}{E_1} . \quad (157)$$

Thus, the incremental form of the instantaneous component is obtained by

$$\Delta\varepsilon^i = \frac{\Delta\sigma}{E_1} . \quad (158)$$

Under consideration of a time step Δt , the second integral $\varepsilon^{\text{inh}}(t)$ can be divided into two parts:

$$\varepsilon^{\text{inh}}(t) = \frac{1}{E_1} \int_0^t \left[e^{-\frac{(t-\tau)}{\tau_r}} \right] \dot{\sigma} \, d\tau = \frac{1}{E_1} \left[\int_0^{t-\Delta t} \left[e^{-\frac{(t-\tau)}{\tau_r}} \right] \dot{\sigma} \, d\tau + \int_{t-\Delta t}^t \left[e^{-\frac{(t-\tau)}{\tau_r}} \right] \dot{\sigma} \, d\tau \right] . \quad (159)$$

The first part can be simplified to the following recursive formulation:

$$\frac{1}{E_1} \int_0^{t-\Delta t} \left[e^{-\frac{(t-\tau)}{\tau_r}} \right] \dot{\sigma} \, d\tau = e^{-\frac{\Delta t}{\tau_r}} \varepsilon^{\text{inh}}(t - \Delta t) . \quad (160)$$

To transform the second part, a constant stress rate $\dot{\sigma} = \frac{\Delta\sigma}{\Delta t} = \text{const.}$ is assumed during the incremental time step Δt :

$$\frac{1}{E_1} \int_{t-\Delta t}^t \left[e^{-\frac{(t-\tau)}{\tau_r}} \right] \dot{\sigma} \, d\tau = \frac{1}{E_1} \frac{\Delta\sigma}{\Delta t} \tau_r \left[1 - e^{-\frac{\Delta t}{\tau_r}} \right] . \quad (161)$$

By substitution of both integrals in Eq. 159 one obtains the recursive expression for the inherited strain component ε^{inh} :

$$\varepsilon^{\text{inh}}(t) = e^{-\frac{\Delta t}{\tau_r}} \varepsilon^{\text{inh}}(t - \Delta t) + \frac{1}{E_1} \frac{\Delta\sigma}{\Delta t} \tau_r \left[1 - e^{-\frac{\Delta t}{\tau_r}} \right] . \quad (162)$$

The increment of inherited strain $\Delta\varepsilon^{\text{inh}}$ can be calculated as

$$\Delta\varepsilon^{\text{inh}}(t) = \varepsilon^{\text{inh}}(t) - \varepsilon^{\text{inh}}(t - \Delta t) = \left[e^{-\frac{\Delta t}{\tau_r}} - 1 \right] \varepsilon^{\text{inh}}(t - \Delta t) + \frac{1}{E_1} \frac{\Delta\sigma}{\Delta t} \tau_r \left[1 - e^{-\frac{\Delta t}{\tau_r}} \right] . \quad (163)$$

Finally, the viscoelastic strain increment $\Delta\varepsilon^{\text{ve}}$ caused by a stress increment $\Delta\sigma$ is obtained by superposition of the incremental components according to Eq. 156:

$$\Delta\varepsilon^{\text{ve}}(t) = \frac{\Delta\sigma}{E_1} - \left[e^{-\frac{\Delta t}{\tau_r}} - 1 \right] \varepsilon^{\text{inh}}(t - \Delta t) - \frac{1}{E_1} \frac{\Delta\sigma}{\Delta t} \tau_r \left[1 - e^{-\frac{\Delta t}{\tau_r}} \right] . \quad (164)$$

A.2 Additional fiber length data

In Fig. 94, the fiber length distribution as implemented into the RVEs is compared to the data of a second analysis. Both measurements were carried out on PPGF30 (13.22 vol-%) using the same parameters. The mean fiber length (number and volume average, respectively) of both distributions are compared in Table 16.

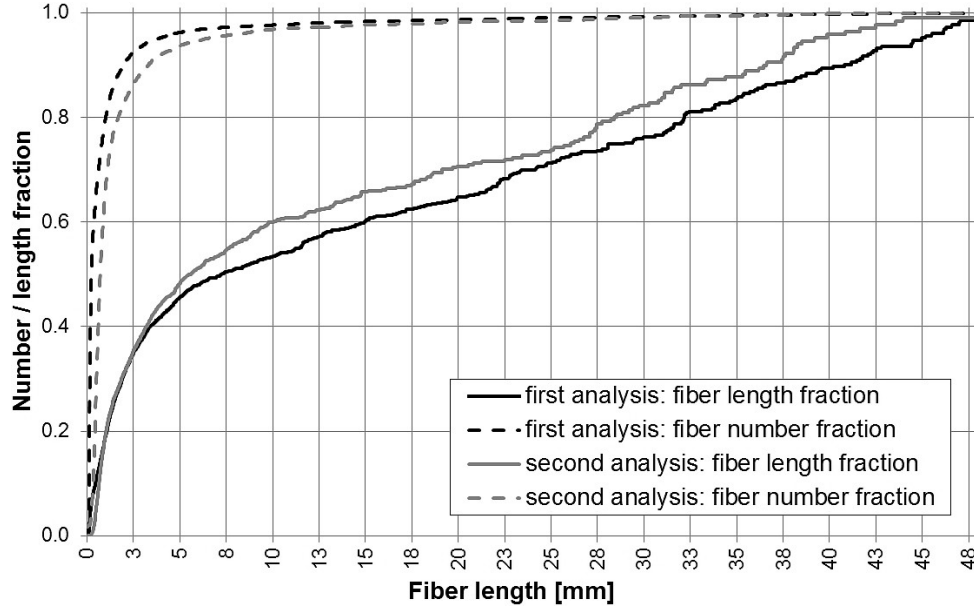


Figure 94: Comparison between the implemented fiber length distribution (first analysis) and the repeated measurement (second analysis) in cumulative depiction.

Length distribution	Mean length (by number) \bar{l}_n [mm]	Mean length (weighted) \bar{l}_w [mm]
first analysis	1.2	15.0
second analysis	1.9	13.1

Table 16: Characteristic values of first and second analysis of fiber length.

A.3 Variation of matrix strain rate

No strain rate dependence was considered for the LFT simulations accounting for plasticity and damage. To assess the effect of varying strain rate in a pragmatic way, the matrix model was calibrated with substance specimens which were tested at strain rates of $7 \cdot 10^{-5}$, $7 \cdot 10^{-4}$ and $7 \cdot 10^{-3}$ 1/s (Fig. 95). Also the apparent softening of the matrix substance specimens was considered (Fig. 96). In Fig. 97, the effects of the different constituent data on the effective behavior of RVE LD7 (PPGF30, 90° load direction) is shown (a perfect interface was considered).

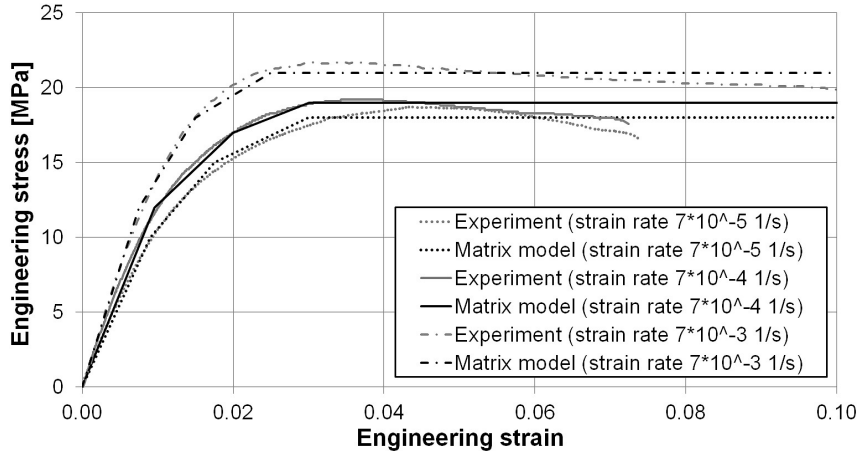


Figure 95: Stress-strain curves of matrix substance specimens under variation of strain rate and calibration of the plastic matrix model.

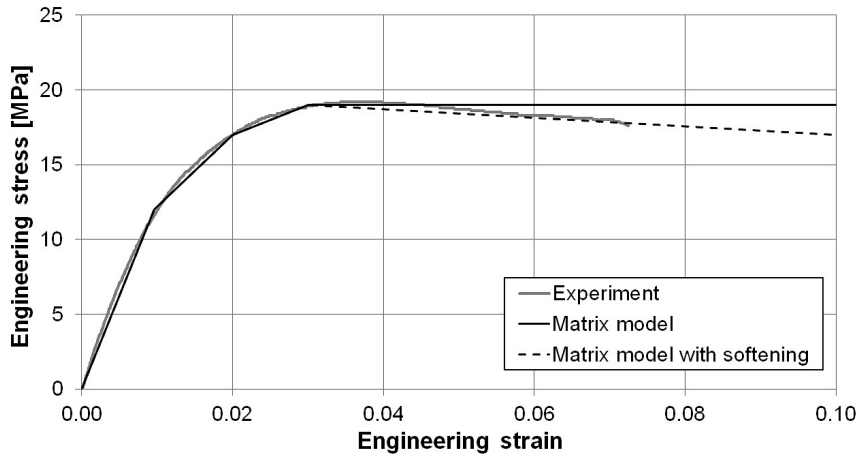


Figure 96: Stress-strain curves of matrix substance specimens (strain rate $7 \cdot 10^{-4}$ 1/s) and model calibration with and without consideration of softening.

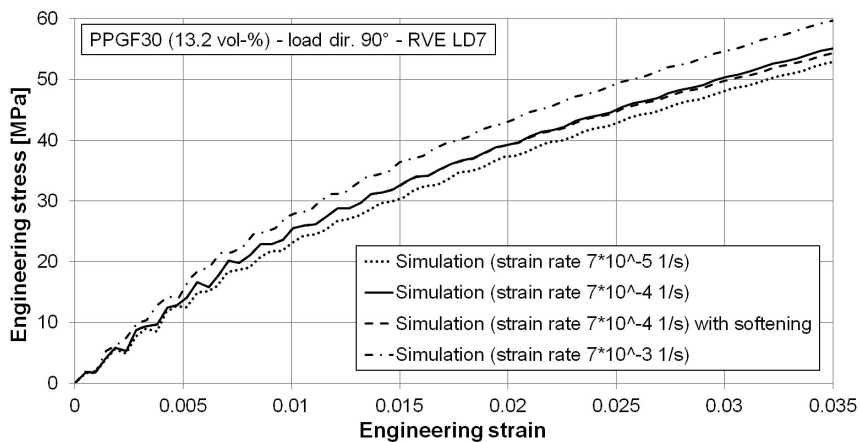


Figure 97: Effect of varying strain rate and softening on the stress-strain curve of RVE LD7 (PPGF30, 90° load direction).

Lebenslauf

Persönliche Daten

Name Sascha Torsten Fliegener
Geburtstag 18. Dezember 1981
Geburtsort Saarbrücken
Familienstand verheiratet
Staatsangehörigkeit deutsch
Anschrift Goethestr. 8, 79379 Müllheim

Beruf

ab Oktober 2010 Wissenschaftlicher Mitarbeiter
am *Fraunhofer-Institut für Werkstoffmechanik (IWM)*, Freiburg

Studium

September 2010 Erfolgreicher Studienabschluss (Diplom)
Oktober 2002 - September 2010 Studium des Maschinenbaus (*Allgemeiner Maschinenbau*)
am *Karlsruher Institut für Technologie (KIT)*
August 2010 Diplomarbeit am *Fraunhofer IWM*:
Mechanische Charakterisierung von oxidischen Faserkeramiken
Februar 2010 Studienarbeit am *Institut für Werkstoffkunde I, KIT*:
Charakterisierung von reibermüdungsbeanspruchten Hochleistungskeramiken

Praktika

Oktober 2008 - März 2009 Praktikum bei der Firma
Desert Aircraft (Tucson, Arizona, USA)
Januar 2006 - März 2006 Praktikum bei der Firma
G-Force Composites (Rayong, Thailand)

Zivildienst

September 2001 - Juni 2002 Zivildienst bei der *Lebenshilfe Saarland*,
Werkstatt für geistig Behinderte (Saarbrücken-Bübingen)

Schulbildung

Juni 2001 Allgemeine Hochschulreife (Abitur)
1992 - 2001 *Theodor-Heuss Gymnasium* (Sulzbach/Saar)
1988 - 1992 *Mellin-Schule* (Sulzbach/Saar)